2-23-2024 10:15 AM

The Development and Testing of a Gyroscope-Based Neck Strengthening Rehabilitation Device

Nicole D. Devos, *University of Western Ontario*

Supervisor: Trejos, Ana Luisa, *The University of Western Ontario*
Co-Supervisor: McIsaac, Ken, *The University of Western Ontario*
A thesis submitted in partial fulfillment of the requirements for the Master of Engineering Science degree in Electrical and Computer Engineering

Abstract

Neck pain can be debilitating, and is experienced by the majority of people at some point over the course of their life. Resistance training has been shown to have significant improvement in pain or disability for patients. There are few options available for telerehabilitation, and the use of gyroscope stabilizers is proposed for this use. A biomechanics model of a head–neck–gyroscope system was created. In order to also model the dynamics of such a system, this work proposes a blended method using the Denavit–Hartenberg (DH) convention, popular in the field of robotics, with the Lagrangian mechanics approach to analyze an unstable vehicle, the Spry–Girard derivation. A prototype single-gyroscope device was designed. A dynamics model was calculated with the proposed method validated using the prototype, with the model predicting the torques within 10% of measured values. This work will allow future optimization of both the design and any control system necessary.

Keywords: Wearable mechatronics, neck rehabilitation, gyrostabilizer, gyroscope, kinematic and dynamic modelling.

Lay Summary

Neck pain can be debilitating, and is experienced by the majority of people at some point over the course of their life. Strength training has shown to offer an improvement in pain or disability for patients. There are currently few options available for "smart" rehabilitation from home, and the use of gyroscopes was proposed to provide small resistance to neck movement for take-home use. A possible system that uses gyroscopes to resist small neck movements as a strength-training option for rehabilitation is described in this work. A mathematical model of a head–neck–gyroscope system was created. In order to also calculate the forces experienced by the user in this system, this work proposes a blended method using an approach popular in the field of robotics with a physics-based approach used previously to analyze the use of gyroscopes as stabilizers for monorail carts. A prototype single-gyroscope device was designed. The equations for force were calculated with the proposed method and validated using the prototype. The equations predicted the force within 10% of the measured torque in the experiment. This work will allow future designs for both the device design and any controls necessary, in order to provide the required resistance for strength training for at-home use.

for Fionna

Acknowledgments

To my co-supervisor and long-time supporter, Dr. Ken McIsaac, for supporting not just my master's thesis, but also all my academic and learning pursuits since 2012. Thank you for taking a chance with a wide-eyed second year undergraduate with lofty goals.

A special thank you to my co-supervisor Dr. Ana Luisa Trejos, for being so patient and supportive during this project as it evolved into a thesis. It would not be hyperbole to say that I would not have completed this without her guidance and encouragement.

I would like to recognize the help of Eugen Porter for assisting myself in how to program the motor used in the experiment, Dr. Aaron Price for allowing the use of his scales, Dr. Ryan Willing for providing the cervical spine CT files, Myles Lidka for creating and allowing the use of components from his old testing apparatus, and Dr. Brandon Edmonds for helping modify it to fit on my desk. Additionally, the advice from Dr. Victor Kwan to "use a rotational [sic] matrix on the whole object. [It's] magical" while working out the geometry of the Potential Energy in Chapter 4 was invaluable and saved me from many more weeks of over-thinking and over-complicating the problem.

My gratitude to Dr. Ilia Polushin for sitting on my advisory committee over the years, as his support was necessary for this project to be completed. And to the trainees, alumni, and postdoctoral fellows of WearME lab, as well as everyone in the TRASH lab, for their support and for making this journey so memorable. There's a special place in my heart for my undergrad classmates, Dr. Jacob Tryon and Dr. Brandon Edmonds, who both continued their education alongside myself in the WearME lab.

Special recognition is needed for Dr. David M. Walton, without whose invaluable collaboration this project would not have existed; and to Selin Denise Acar, for leaping on board with an excited graduate student and developing the neck

rehabilitation game.

And I would like to thank my best friend, Ayeda Sayeed, for only ever being one message away (even across the globe); to Lydia Balogh and my cats for being a shoulder to cry on and a ear to listen; to Naomi-Jean Q. Scherba for being an incredible sounding board and draft editor; and to Kate McDonald for labouring beside me as this document came to resemble its current iteration.

The final crunch to see this thesis completed required the assistance of friends and family members. From picking up the slack and making sure I (and the cats) were fed and had my coffee (thanks, Mom!), to reviewing the second-to-last chapter drafts.

And finally, words cannot express the gratitude I have for my partner, Tyler, who not only supported me in every and any way possible throughout this entire program, but had to learn the hard way to not "Ask about the thesis." A true partner in this endeavour: supporting and listening to all my academic and non-academic chatter, and allowing my math and drawn robot models to cover an entire wall of our living space, as if I was the main character in a mathematician's biopic... despite my questionable drawing skills.

Contents

List of Figures

List of Tables

Nomenclature

0	Relating to the base/world frame of a rigid link system representation
A	(As a superscript or subscript), relating to the Aurora/Aurora frame
$\mathbf{A}$	Intermediate Homogeneous Transformation Matrix for adjacent links using the DH convention in robotic applications
$\hat{\mathbf{a}}$	Coordinates expressed in the Aurora reference frame
a	A constant term in the dynamics equations; also the link length in the DH convention
$\mathbf{A}_i^{i-1}$	General form of the Homogenous Transformation Matrix, as applied to adjacent links using the DH convention
B	Relating to the Base/base frame. Analogous to the Neck frame
$\hat{\mathbf{b}}$	Coordinates expressed in the base reference frame
b	Damping coefficient
C	Relating to the cage/cage frame
$\mathbf{c}$	Cosine
$\vec{d}_p^a$	Displacement vector of point p with respect to frame a
d_i^*	The prismatic joint variable for joint i
$\boldsymbol{\mathcal{F}}_b^a$	Velocity Transformation Matrix for a 6×1 velocity vector ξ
$\mathbf{G}$	The Gimbals frame. As a sub/super script, relating to the Gimbals. (Also referred to as the gyroscope cage)

$\mathbf{H}_b^a$	General form of a Homogenous Transformation Matrix. Not derived from the DH convention
$\mathbf{H}$	The Head frame. As a sub/super script, relating to the Head
I	Mass moment of inertia
$\mathbf{J}$	The Jacobian of a given manipulator, from the DH convention
j	The number of gyroscopes in the system
JT_1	Relating to Joint 1/the frame of Joint 1 (the neck)
JT_2	Relating to Joint 2/the frame of Joint 2 (the gyroscope gimbal/cage)
$\mathcal{K}$	Kinetic Energy
k	The number of rigid link model representations for a given system
L	(As an addition to a subscript or superscript), relating to a landmark
$\mathcal{L}$	Lagrangian
m	The number of manipulator representations for each j gyroscope (typically 3)
m	Mass
$\mathbf{N}$	The Neck/World frame. As a sub/super script, relating to the Neck
O	Origin of a frame of reference, in the DH convention
$\mathcal{P}$	Potential Energy
Q	Resultant joint torques
q	generalized coordinate vector of the system (specifically the joint variables)
$\mathcal{R}$	Rayleigh Dissipation Function
$\mathbf{R}$	Rotation matrix
$\mathcal{S}$	Skew-symmetric matrix

s	Sine
s_1	Relating to *sensor1*/the frame of *sensor1* (the sensor on the head/the end effector for joint 1)
s_2	Relating to *sensor2*/the frame of *sensor2* (the sensor on the cage/the end effector for joint 2)
T	Transformation matrix for non-adjacent links, a resulting homogeneous transformation matrix using the DH convention
$\vec{v}$	Linear velocity
W	The Wheel frame. As a sub/super script, relating to the Wheel
$x_{\_}$	Distance between neck rotation point and Centre of Mass (COM) of the subscript along the neck x axis
$y_{\_}$	Distance between neck rotation point and COM of the subscript along the neck y axis
$z_{\_}$	Distance between neck rotation point and COM of the subscript along the neck z axis
α	Angle between the z axes of the head and the gyrostabilizer cage and wheel; the precession angle of the gyroscope
β	The nutation angle of a gyroscope; also the angle between the $-y$ axis of the Aurora and the x axis of the cage.
γ	The spin angle of a gyroscope
θ	1. Joint angle of a revolute joint. 2. Also Pitch: the angle of rotation about the y' axis. Angle of cervical flexion–extension.
ξ	The 6×1 velocities vector
ϕ	Roll: the angle of rotation about the x'' axis. Angle of lateral cervical flexion; the angle between the y axes of the head and the neck (world frame)
ω	Angular velocity

Units

cm	Centimetre
g	Gram
Hz	Hertz
kg	Kilogram
lbf	Pounds-force
m	Metre
mm	Millimetre
N	Newtons
N·m	Newton-metre
nN·m	Nano-Newton-metre
s	Second
V	Volts

Glossary

ATI ATI Industrial Automation. A company that develops robotic accessories and robot arm tooling, including Multi-Axis Force/Torque (FT) Sensing Systems. Company that produced the ATI F/T Gamma Sensor.

DICOM A file format. Stands for Digital Imaging and Communications in Medicine, and is a standardized file format for medical imaging.

NDI The company Northern Digital Inc., branded as NDI. The manufacturer of the Aurora sensor. *See also* NDI (Neck Disability Index) in Acronyms.

NI The company NI, previously known as National Instruments.

STL A file format. Used for stereolithography CAD files, generally for 3D printing.

Acronyms

3D	Three Dimension
ADL	Activity of Daily Living
BTE	Baltimore Therapeutic Equipment
CIRCLE	Collaboration for the Integration of Rehabilitation with Consumer Electronics
CMG	Control Moment Gyroscope
COM	Centre of Mass
CT	Computed Tomography
DAQ	Data Acquisition
DC	Direct Current
DH	Denavit–Hartenberg
DOF	Degree(s) of Freedom
EMI	Electromagnetic Interference
ESC	Electronic Speed Controller
F/T	Force/Torque
HMA	Hot Melt Adhesive
IDE	Integrated Development Environment
IQR	Interquartile Range
MCU	Multi-Cervical Unit
mmgs	Millimetre-Gram-Second
MSK	Musculoskeletal
MVA	Motor Vehicle Accident

NDI	Neck Disability Index
nRMSE	Normalized Root Mean Square Error
NRS	Numerical Rating Scale of Pain
PD	Parkinson's Disease
PT	Physical Therapist
RHR	Right Hand Rule
RHS	Right-Hand Side
RMSE	Root Mean Square Error
ROM	Range of Motion
SNAG	Self-Sustained Natural Apophyseal Glide
STD	Standard deviation
UAV	Unmanned Aerial Vehicle
US DoD HFE TAG	The United States Department of Defense Human Factors Engineering Task Force Group
UWO	the University of Western Ontario
VR	Virtual Reality
WAD	Whiplash Associated Disorder
WSIB	Workplace Safety and Insurance Board

Chapter 1

Introduction

The broad term "neck pain" is estimated to affect 60% of people (surveyed by British, Canadian, and American researchers) at some point over the course of their life, with the majority of this group experiencing neck pain during middle age [1]. Neck pain is caused by varying factors, including trauma, degenerative disease, and/or mechanical factors [1–3]. There are a number of interventions, and depending on the specific condition(s), are typically treated with physical therapy (manipulation and/or mobilization) to regain or increase full Range of Motion (ROM) or to reduce or manage the pain [4–10]. While the outcome varies based on the type of intervention provided, the combination of interventions, and source of neck pain [2,3,10–16], traditional physical therapy interventions can be considered boring by the patient [17], can have only short term benefits [11, 15, 18, 19], and can require a large time commitment and/or multiple trips to a therapist's office each week [3, 8, 18, 20–23]. The literature shows that strength training—especially from using large gym-like equipment such as the Multi-Cervical Unit (MCU) from Baltimore Therapeutic Equipment (BTE)—results in significant improvement in pain mitigation [13, 18, 24], but even a quick daily at-home resistance program can have positive outcomes compared to control groups [25]. An easy-to-use take-home strengthening neck rehabilitation device is hypothesized to help increase accessibility and patient outcomes.

1.1 Motivation

Physical therapy can be expensive and inconvenient for patients [23, 26]. Take home therapies (such as Theraband, an exercise band) are cost- and time-effective

but have been reported in some studies to have lower success rates for increased strength or pain mitigation [25,27], and are "low tech." These interventions require patients to either set up a neck traction contraption that does little to strengthen muscles, or have enough upper arm strength and mobility to use a resistance band or perform a Self-Sustained Natural Apophyseal Glide (SNAG) [5]. The strengthening option (using resistance bands) only works for flexion–extension and lateral flexion isometric strengthening, unless the patient holds the band in their teeth for rotation exercises [7]. Therefore, depending on the age, specific condition(s), and ability of a patient, these may not be viable rehabilitation options.

Between 1996 and 2004 in Ontario, almost 50% of all Workplace Safety and Insurance Board (WSIB) claims were Musculoskeletal (MSK) related [28]. The direct cost of this was over $3 billion over the eight year time period. The economic cost—or indirect cost, factoring in things such as loss of work and loss of productivity—to the province was closer to $12+ billion. In any given year, 20-40% of these WSIB MSK claims are neck related [28]. Nationally, upwards of two million insurance claims per year are from Whiplash Associated Disorder (WAD). In British Columbia alone, the economic costs associated with whiplash injuries are estimated to be $600 million per year [29].

These numbers above reflect workplace injuries in Ontario and whiplash injuries (usually from Motor Vehicle Accidents (MVAs)) in British Columbia, but these numbers do not include other causes of neck pain or disability, such as cervicogenic headaches, myofascial neck pain, and degenerative changes such as osteoarthritis and cervical spondylosis [11].

At the University of Western Ontario (UWO), the Collaboration for the Integration of Rehabilitation with Consumer Electronics (CIRCLE) group is looking at designing a fully integrated cervical spine telerehabilitation system that includes both a "tetherless" resistive strengthening therapy device and a suite of therapist-customizable Virtual Reality (VR) rehabilitation games for use in telerehabilitation applications [30, 31]. The ideal strengthing device for this application would be light and non-intrusive. It would also be able to provide adjustable resistance, both on a per-patient basis and while in use: adjusting in proportion to the user's range of motion and the velocity of neck rotation.

1.2 General Problem Statement

Neck pain can be debilitating, but research has shown that strength training can help mitigate the pain and the resulting disability [32]. Unfortunately, current technologies for strength training either require multiple visits a week to the clinic [33,34], or use at-home techniques that either do not strengthen the neck over the range of all neck motions and are unavailable to some demographics, or do not provide resistance beyond body weight exercises [35].

There is currently few options for take-home strength exercise technologies and a lack of take-home gamified rehabilitation technologies. This thesis aims to lay the groundwork to fill the gap between in-office options for rehabilitation and the current take home options and enhance expected outcomes by introducing gamification and/or a fully gamified suite of exergames for the Physical Therapist (PT) to add to their suite of interventions. In order to develop a device to meet this need, a proposed solution requires modelling to optimize for size, weight, and resistance, as well as modelling in order to produce an optimized control algorithm.

This work specifically explores the feasibility of using gyroscopes as stabilizers to fill this gap through modelling the dynamics of the head–neck–gyroscope system. The proposed method for calculating the dynamics and these dynamics equations themselves can be used for future iteration and optimization of the proposed device design.

1.3 Research Objectives

The overarching objective of this work is to develop a tetherless neck strengthening rehabilitation device that provides adjustable low resistances to small neck movements and that interfaces with a VR game.

To accomplish this goal, the feasibility of using gyroscopic stabilizers in such a capacity will be explored in this thesis. The specific objectives for this task were as follows:

- Create a biomechanical model of a PT–Patient interaction.
- Develop a method to model the dynamics of n-gyrostabilizers on a human head.
- Develop a dynamic model of a single gyrostabilizer on a human head.

- Create a list of specifications and requirements for such a device.
- Design and build an approximately anthropomorphic system to test the device.
- Validate the single gyrostabilizer dynamics by comparing the real-world torques to the model-predicted torques using the system angles measured on the real-world system.

For consistency, the term "gyroscope" will be used in the following chapters to refer to any use of gyroscopes, including in an actuator or stabilizer capacity, though these terms are considered to be interchangeable for the context of this work.

1.4 Outline

This thesis covers the development and testing of a novel use for gyroscopes: neck strengthening therapies.

Chapter 2 covers the state of the art for cervical spine rehabilitation therapies, the use of gyroscopic actuators in wearable robotic devices, and typical uses of gyroscopes as stabilizers.

Chapter 3 discusses the biomechanics modelling used in this thesis as well as the background mathematics used in the field of robotic manipulators and for gyroscopes.

Chapter 4 proposes a new method for modelling the dynamics of the interactions between a human head and n-gyroscopes.

Chapter 5 details the design and fabrication of both the gyroscope resistance device and the testing apparatus.

Chapter 6 covers the experiment protocols, analysis, results, and discussion of the validation of the mathematical model described in Chapter 4.

Chapter 7 summarizes the conclusions and future work, highlighting the contributions of this thesis and where research on this work could be continued.

The appendices include the MATLAB code used for data collection and validation in Appendix A and the data sheet for the motor used in Appendix B.

Chapter 2

Literature Review

The broader scope of this work touches on a number of fields. The intended use of the work presented in this thesis is to be used in a telerehabilitation context for patients with neck pain. The device is intended to offer resistance training and interact with a VR system, in order to gamify the rehabilitation experience. And finally, the resistance is to leverage the stabilization properties of gyroscopes.

This chapter gives a short overview on telerehabilitation, neck rehabilitation interventions, gamification, and gyroscope-based stabilization in non-wearable applications as well as in wearables.

2.1 Telerehabilitation

Telerehabilitation refers to emerging technologies and methods that are used to treat patients and walk them through rehabilitation exercises without the physical presence of a clinician. Other fields—such as surgery, diagnostics, and search and rescue—are looking at, and currently using, remote assistance and imaging for various applications, such as surgery or diagnosis [36–40]. This can reduce costs on the healthcare system and economy significantly, while decreasing the impact that participating in rehabilitation has on the patients' lives [41]. The ability to perform physical therapy at home should reduce wait lists, since the time required per patient is reduced [23]. A hospital in Ireland calculated that with the treatment plan at the time—three sessions a week at 40 minutes—resulted in approximately 10 hours per patient over 4–6 months; which is not only a lot of time for the patient, but the 350 new cases of WAD per year at their hospital would require they hire two additional full time PTs to handle demand. This study showed that

at-home exercises were just as effective at managing the pain as doing the therapy in the PT's office [23].

Using telerehabilitation, therapists will be able to track and monitor patient ability and progress remotely. It could even be the case that unless the PT wants to have a conversation with the patient, the patient does not need to make sure their schedule is clear to fit the therapist in, or vice versa. The patient can do the rehabilitation exercise regimen at their own convenience—for example, early in the morning before work, later at night after work, before a midnight shift—whereas the therapist can check in on progress and give feedback during the workday [41]. These systems have been designed, in some use cases, to give real-time feedback to the patient so they can adjust their movements as they perform them, increasing adherence to the exercise motions.

Depending on the specific design and function of the telerehabilitation system, the PT can check in at their convenience to track adherence of the patient to the regimen, see progression, and to confirm that the patient is performing the rehabilitation exercises in the correct manner [41]. The use of telerehabilitation software can greatly expand the availability, and with the right system, increase the outcomes for many more patients.

2.2 Current Methods of Neck Rehabilitation

There are a number of interventions that a physiotherapist can choose from when determining the appropriate care for a specific individual, based on a number of factors, including the specific condition(s) that the individual has, or the muscles affected by the condition(s). Due to the wide range of causes of neck pain and the number of muscles in the neck (a subsection of neck muscles are shown in Figure 2.1), there are a wide variety of interventions available to PTs. These include traditional interventions, such as manual therapy or passive interventions, exercise therapies, such as body weight exercises and resistance training, and immobilization or traction.

Passive physical therapy includes interventions such as ice packs, heat therapy, massage therapy, ultrasound, and electrotherapy [42]. The goal for passive therapies is, in general, to reduce pain and swelling enough that a patient can participate in more active interventions. Active therapy, in contrast, refers to when the patient moves their own body through exercises and stretches. Manual

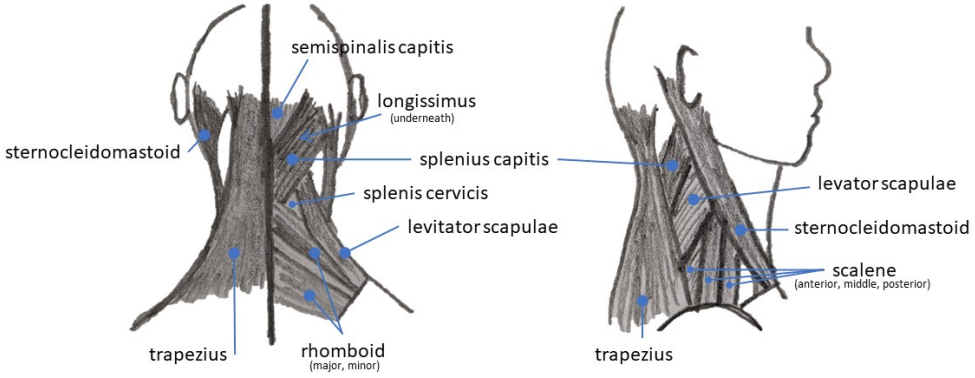

Figure 2.1: Drawing of the muscles of the neck, not to scale. L: Posterior view. R: Lateral view.

therapy includes manipulation or mobilization techniques performed by the PT on the patient [43].

A common form of active therapy is exercise therapy, and specifically resistance exercises. Strength training has been reported to have positive outcomes for the patients, though the quality of the studies were indicated to be of low-to-moderate quality in a Cochrane review on neck pain interventions [32]. Resistance exercises include body weight exercises, resistance bands, "low technology" exercises using dumbells and pulley systems, and exercise machines—akin to those found in a fitness gym—such as the MCU from BTE or the Four-Way Neck machine from MedX [44, 45].

A review of cervical traction (a passive intervention) outcomes by Peake and Harte in 2005 concluded that there was not enough data in the papers published to rule the intervention to be effective or ineffective [46]. Lluch et. al. compared passive mobilization by a therapist to body weight exercise therapies, and found that the exercise therapies had significantly better outcomes for the patients [47]. This aligns with other studies that show no long-term benefits to mobilization and manipulation or other passive interventions, such as transcutaneous electrical nerve stimulation [11, 19]. Improvements were also seen in cases of cervical spondylosis using resistance bands for the method of strength training [35].

One protocol for reducing the pain and disability experienced from neck pain that used a fitness machine—the Melbourne protocol—was reported to have provided an improvement in their Neck Disability Index (NDI) score by over 50% and an average of over 100% strength gain after nine sessions, approximately two per week. Six months after completion of the training program, over 90% of the patients retained the strength gains, and 89% retained their reduced NDI scores [33, 34]. Neck strength training has also been looked at as a preventative measure for injuries such as concussions and WAD, though the literature is still unclear on if there is a measurable impact from the training [48, 49].

The MCU has also been used in studies looking at cervical ROM and using that ROM motion data to inform diagnosis, prognosis, and/or evaluation of current intervention methods [47, 50].

These non-bodyweight strength training interventions can reach maximum resistances of around 50–60 lbs. According to collaborators at CIRCLE, they intend to use small forces (in the 0–5 lbs force range) to aid cases of severe neck pain.

2.3 Gamification

The concept of gamification is rooted in behavioural theory (psychology) and the psychology of rewards systems [51]. "Gamification" has been defined in the literature as an umbrella term to describe the use of video game elements in a non-gaming system [52]. These include things like high scores, streaks, and achievements or badges. These elements are used in a variety of applications, including language learning (Duolingo), social medias (see the screenshot of the Snapchat phone application in Figure 2.2), and even running (Nike Run Club; Zombies, Run!) [53–56]. In social media applications, Snapchat uses badges/awards for using the application in various ways, such as "sent a snap from a different timezone," and "sent a snap with the temperature below freezing," as well as having a "Snap streak," for opening the app and sending a snap to the same user each day. The productivity app Habitica takes a user's to-do list and "transforms [their] life into a role-playing game" [57]. The user sets tasks to complete—either a daily, weekly, or a traditional to-do item—and when these tasks are checked as completed, gains "gold." These in-game rewards can be used to purchase upgrades to their character—to be able to defeat monsters—or to "buy" real-world rewards, chosen by the user. For example, purchasing "Watch TV tonight," to reward

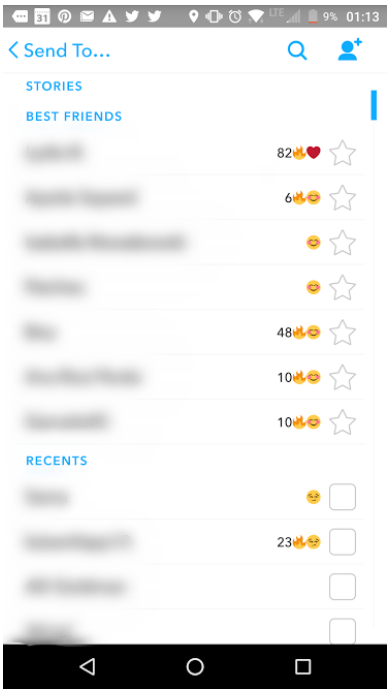

Figure 2.2: A screenshot of the phone application "Snapchat" by Snap Inc., showing the emojis used to gamify sending photos with the app. Adapted from [58].

oneself with relaxation time.

The term first appears in a Google scholar search as a pedagogical book on Serious Games published in 1970 [59], and since then, has grown to approximately 348,000 results (as of December 2023), with a five year growth of around 700% between 2015 and 2020. In 2014, Hamari et al. published a review paper on empirical-reviewed papers published between 2010 and 2013 (noting that there were no papers published before 2010 that matched the inclusion criteria). Of the 24 papers reviewed, all but 7 had at least part of the tests have positive experiences for the subjects (those 7 had only descriptive statistics). The papers looked at a wide range of motivational affordances, including points, leaderboards, achievements/badges, levels, story/theme, clear goals, feedback, rewards, progress, and challenges.

In physiotherapy, gamification has become a new trend in research, although not every paper written in the field used the keywords in Hamari et al.'s inclusion criteria. VR games are used in multiple forms for various conditions; for example, in walking or other Activity of Daily Living (ADL) based rehabilitation for Parkinson's Disease (PD) and other brain or MSK injuries, or as a means of pain mitigation [17, 60–64].

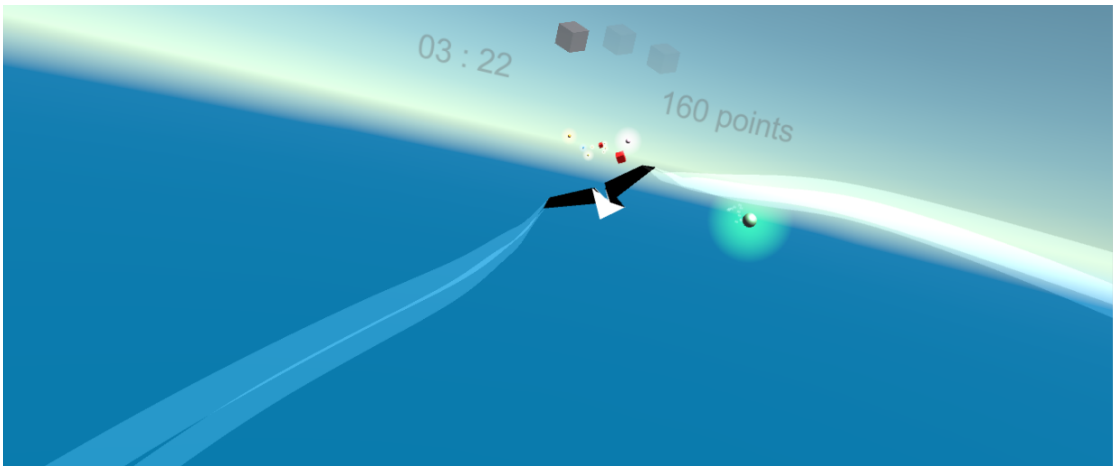

Figure 2.3: The infinite flyer "Paper Plane," developed by Selin Denise Acar at UWO. Adapted from [30]

For neck rehabilitation, the draw of gamification to attempt to increase adherence is strong. Traditional interventions can be considered boring and repetitive by the patient. At the time this thesis was being developed, collaborators at CIRCLE indicated that the most advanced gamification that they had seen for neck rehabilitation was attaching a Wii remote to a patient's head and using the neck to move the relevant game pieces in the desired trajectory. Wii technology is used by Saposnik et. al. in their 2010 work looking at the combination of VR technology and stroke rehabilitation versus the more traditional option of recreation therapy [65].

CIRCLE is aiming to take this a few steps further and use a VR game to both provide the rehabilitation movements—by moving your character through the game—and to track the progress of the patients. Currently, there is a game developed by the ECE Department at UWO that is an infinite flyer game (see Figure 2.3) where the patient has to collect objects by flying into them. The size, location, frequency, and distance of where and how these objects appear will be determined by the PT for each set of sessions.

The patients and physical therapists will be able to see the progress—the physical therapists with data collected of where and how often the patient can collect or misses the objects, the speed of movement, path taken, and other factors, and the patients will see statistics like how many days they have played in a row, their high scores, and potentially some achievements: could they play longer today? Did they collect more objects in the required time?

In order to enhance current options for gamified neck rehabilitation, there needs

to be a way to interface with a method for creating resistance while the system is being used. One proposed solution to this is using a gyroscope as an actuator to provide the desired resistance to motion.

2.4 Gyroscope Stabilization

Gyroscopes were first described in the 1850s [66], and have been used as an actuator as stabilizers since the early 1900s for use in applications such as boats, aircraft, warfare, monorailways, and some early motor vehicles [67–75]. In modern applications, they are still used in applications for aircraft [76], watercraft [77–80], and warfare [81], as well as in space systems [82–85] and two-wheel vehicles such as self-stabilizing bicycles and monorail cars [86–88].

The most basic form of "gyroscope" has no gimbals. These are not, by definition, gyroscopes, but they are governed by the same physics principles. These applications are either referred to as a reaction wheel or a momentum wheel, depending on their specific control. A momentum wheel is a flywheel mounted to the vehicle (or other system body) directly, with no gimbals. It is either heavy or operated at a high revolutions per minute, or both, in order to impart on the body a large amount of angular momentum. The system body does tend to precess around a second, perpendicular axis from the axis of rotation of the flywheel, so this prevents smaller disturbing forces from destabilizing the system along the third axis. A reaction wheel is controlled to spin up or down, and uses the precession motion of the system body as the stabilization motion.

The basic principle that governs the use of gyroscopes as stabilizing actuators is the precession force generated by the gyroscope. When a disturbing force is applied to an axis perpendicular to the axis of rotor rotation, the gyroscope precesses. In a three-gimbal gyroscope—the configuration most commonly associated with a gyroscope—the gyroscope would then nutate: rotate around its third axis, the nutation axis. If this third gimbal does not exist or is locked, the object the gyroscope is rigidly attached to would assume this forced caused by the precession of the gyroscope. In stabilizer applications, this is typically the vehicle body. Assuming the gimbals are set along the correct axes, a resulting torque acts opposite to the original disturbance, righting the vehicle [88].

In order to achieve a specific resulting torque, the angle of precession can be adjusted with a controlling motor on the gimbal. The literature varies in

what these applications are called; be it gyrostabilizer, CMG, or something else. "CMGs" are largely seen used in space applications [82,85,89]. By the early 2000s, CMGs had been used in large space stations (e.g., Skylab, MIR, and ISS), and in USSR spacecraft [82]. Using CMGs in satellites was first proposed in 2002 by Lappas et. al. [82]. Work is now currently being done on using these actuators in small satellites, and even CubeSat applications [89, 90].

In addition to large system bodies being stabilized with gyroscopic actuators, a number of applications have used stabilizers for specific parts or portions of a larger system. One example is the gyroscopically stabilized bed of a road vehicle for an anti-aircraft application, presented by Koruba et. al. in 2010 [81]. Another is the creation of a stabilization platform that stabilizes both roll and pitch, as described in Redwood's 2014 Ph.D. thesis [91].

Aircraft has had significantly less history with gyroscopes as stabilizers. Gyroscopes are currently used as sensors for knowing the orientation of the vehicle in space, and therefore as inputs to the stabilizing systems within the aircraft [92]. The original autopilot was a Sperry gyroscope, where deviation within the angles of the gimbals would indicate an orientation off the desired. Through a series of mechanical and pneumatic linkages, the stabilizing system within these early aeroplanes was adjusted without the aid of the pilot [68,92]. This first application of gyroscopes in aeronautics was half gyroscope-as-sensor and half gyroscope-as-actuator, so did not take advantage of the stabilizing properties that will be explored within this work. Gyroscope stabilizer applications now are occasionally found in drones and other small aircraft. In 2005, Chatys and Koruba proposed the use of gyroscopic stabilization in the use of mini-Unmanned Aerial Vehicles (UAVs) [76]. About a decade prior to this, mini-UAVs were largely only seen as model hobby planes, and the need to stabilize mini-UAVs for military operations was noted.

In boats, the gyroscopic stabilizer typically serves as an anti-roll solution, to minimize the rolling of the vessel due to ocean waves, though can be used to minimize pitching as well (pitching and rolling as defined in Figure 2.4). Large crafts, such as cruise ships, can have passive systems, like immobile fins to resist rolling motion in turbulent water, or use more active stabilization with a gyroscope–fin control system or moving masses [80]. Anti-roll gyrostabilizers are typically found in the smaller personal craft, though VEEM Gyro offers a model to work with "large super yachts and commercial work boats with displacement of 300–900 tonnes." [93] Multiple gyrostabilizers can be used in one vessel, allowing these

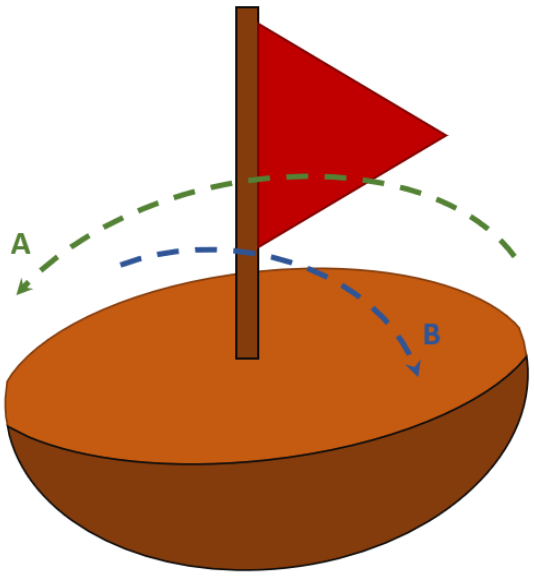

Figure 2.4: A boat, showing the directions of pitch (A) and roll (B).

gyrostabilizers to be used in ships up to 3,000 tonnes.

A new control algorithm from Song et. al. in 2023 was effective in suppressing the rolling motion of a ship with "a relatively low speed or light spinning wheel compared to passive gyrostabilizers" [80]. This work could have applications outside of the field of marine engineering, where weight is a consideration or where there are speed constraints exist within the system, such as wearable applications.

Since the early 1900s, the use of gyroscopes has been researched to stabilize two-wheeled vehicles, largely in the form of the monorail [72, 73, 91] In 2008, Spry and Girard modelled the dynamics of a gyroscopically stabilized two-wheeled cart riding a single track. The derivation of these dynamics via Lagrangian mechanics had yet to be undertaken. Since then, a number of applications using Lagrangian mechanics based on the Spry–Girard derivation method have been published [91, 94]. The anti-roll properties of gyroscopic stabilizers can be, and have been, applied to other vehicles. Research out of the Iran University of Science and Technology looked at applying this to a traditional road vehicle [94]. This application used a fuzzy controller to control the precession angle and resultant torque experienced from the paired gyroscopic stabilizer in order to prevent rollover during specific higher-risk turning manoeuvres. Another common application has been to stabilize unmanned bicycles, and more recently, unicycles and self-balancing scooters

and two-wheeled dicycle[1] robots [86, 87, 96, 97].

2.5 Gyroscopic Stabilization in the Context of Rehabilitation and Wearables

While not a wearable, a gyroscope-as-actuator device has been developed for occupational hand rehabilitation therapy purposes, called the GymBall [98]. The rehabilitation tool controls the rotor and the gimbal rotational velocity in order to produce various torques to be exerted on the user's wrist. The intention of the feasibility research was to see if the GymBall could cause motion of a relaxed wrist. Preliminary studies showed that a maximum displacement of four and seven degrees could be achieved using 0.5 N·m.

A device is still in development by GyroGear Ltd., called the GyroGlove, to help individuals with hand tremor, such as PD patients. Not much has been released on exactly how this is accomplished or the efficacy of the device, but the GyroGlove is described as designed to use gyroscopic actuators to provide a stabilizing force [99–102]. The patents owned by GyroGear Ltd. indicate either a double-gimbal Control Moment Gyroscope (CMG) or multiple gyroscopes would be used to apply the stabilizing force across multiple axes [101].

Two other previous patents, now expired, for hand tremor suppression exist that use gyroscopes [103, 104]. Both use one gyroscope to suppress tremor in one axis of motion. A literature search yielded no results on these devices specifically. Recently, Phan Van and Ngo (2021) approached the single-gyroscope stabilizer problem, and showed potential effectiveness up to approximately 93% [105]. Similarly, Bandsode and Thosar (2022) looked at the efficacy of one gyroscope to suppress tremor, and has shown promising initial results, suppressing up to 70% of the tremor [106].

A gryoscope based balance assistance device has also been proposed, comprising of multiple variable-speed CMGs in a backpack attached to a human [107–109]. Experiments have shown that the prototype device can significantly improve the balance of a healthy human adult, but more research is needed in non-healthy populations. However, preliminary results are promising for chronic stroke sub-

[1] A dicycle differs from a bicycle in that the two wheels are parallel instead of inline, relative to the direction of motion. A Scientific American article from 1928 defines it as "the two wheels hav[ing] a common axis." [95]

jects [108]. One conclusion drawn by D. Lemus et. al. in "Controller synthesis and clinical exploration of wearable gyroscopic actuators to support human balance," was that "subjects interact better with predictable controllers." The results showed that discontinuous and abrupt changes in the gyroscopic forces were followed in 70% of instances by a "loss of balance and task failure" [108]. This conclusion—that predictable and continuous application of forces perform better and are perceived better by users—should be taken into consideration for future wearable biomechatronics design.

2.6 Concluding Remarks

Telerehabilitation has a number of benefits for both the individual patients and the health care system as a whole. The literature shows that resistance training is one of the best methods for treating neck pain. Unfortunately, current options for neck pain interventions by PTs are largely for in-office use, or have lower expected outcomes. Gamification is a newer concept, using the motivational affordances that are seen in games in non-gaming situations. The field of rehabilitation has seen success using gamified therapy for conditions such as PD and MSK injuries, and for pain mitigation.

The gyroscope stabilizer applications discussed in this chapter are almost all intended to completely neutralize the rolling motion or disturbing force of the vehicle or application. Therefore, most applications require the use of a CMG or other control system to create the necessary corrective force to the system. In contrast, the intended use of the gyroscope actuator in this work is to simply create a resistance to the motion of a human head.

Chapter 3

Background Modelling

This chapter covers the background mathematics and modelling required for both the proposed method and the biomechanics modelling used in this thesis. The biomechanics models can be seen in Section 3.1, the background math for calculating the dynamics of a gyroscopically stabilized monorail cart using Lagrangian mechanics is provided in Section 3.2, and the Denavit–Hartenberg (DH) convention is explained in Section 3.3. Section 3.1.3 specifically contains novel work beyond the collation of anthropometric datasets.

For the purposes of this thesis—unless otherwise stated—the general coordinates and rotation directions for the body are as shown in Figure 3.1. The anatomical planes are shown in this figure as well; the (mid)sagittal plane is the x–z plane, the transverse plane is the x–y plane, and the coronal plane is the y–z plane.

3.1 Biomechanical Modelling

In order to calculate the dimensions and mechanical properties of an approximate 50^{th} percentile male's head and neck, a review of exiting literature and document sources was done. It was found that no singular document contained all of the measurements or landmarks necessary for the work that follows within this thesis.

NASA has a few Standards that compile data from a number of sources. Most of the data presented in this Section are cited directly from those individual works. The NASA-STD-3000 (1995) document has a clearer summary of the same data as the newer NASA-STD-3001 (2023) document for the specific data sets cited below [110, 111]. The older NASA-STD-3000 Standard also offers data for the

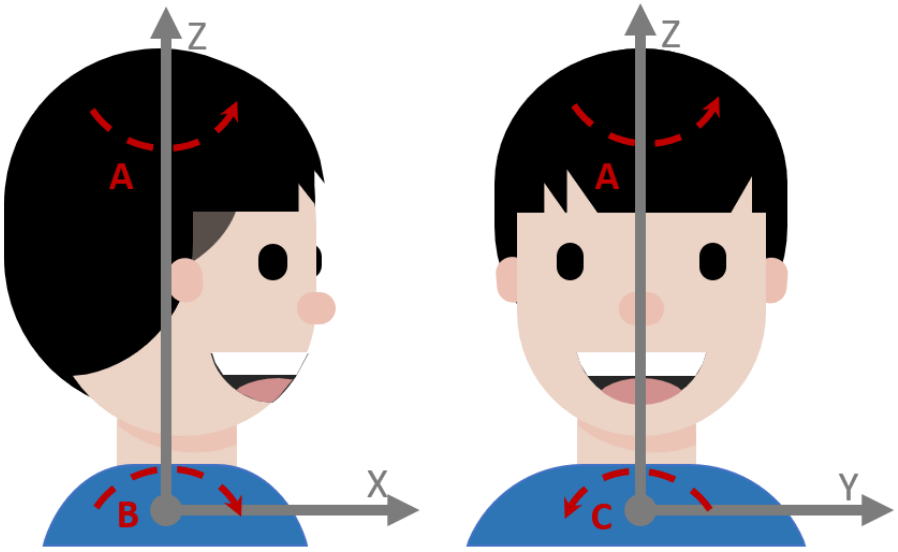

Figure 3.1: The general coordinate system and rotational directions for the purposes of this document. A: Rotation about the z axis. This is yaw and cervical rotation. B: Rotation about the y axis. This is pitch and cervical flexion–extension. C: Rotation about the x axis. This is roll and bilateral cervical flexion–extension.

50^{th} percentile, as opposed to simply listing the minimum and maximum values as done in the newer NASA-STD-3001.

This standard includes the approximate COM of the head of the 50^{th} percentile "American Male Crewmember," and is therefore not representative of the general population at large. As the application of these data is only to calculate the appropriate values for one hypothetical human, the 50^{th} percentile value was chosen at as many steps in the process as possible. When adjusting for a specific patient, or optimizing across a larger population, the specific measurements of a patient or the 5^{th} and 95^{th} percentile data will need to be substituted for the values discussed in this section as needed.

The biomechanics modelling within this Section has two purposes. The first is to calculate the equivalent torque experienced when a PT applies a "five pound force" against a patient's head, to have a torque to match to the dynamics output. The second is to model the head–neck system, as the coordinates of the COM and the mass moments of inertia are required for the model.

3.1.1 The Equivalent Torque Model

In discussions with collaborators at CIRCLE, the intention for the proposed device is to provide a small resistive force to neck motion, similar to when a PT used their hand to resist motion with approximately five lbf (pound-force). The specific range that CIRCLE is aiming for is in the 0–5 lbf range. In order to properly design a device to have the same torque experienced in the neck as this interaction, the approximate torque experienced in a patient's neck needs to be calculated to optimize a device to produce that output torque. A model created in this section is intended to calculate the approximate forces experienced by a 50^{th} percentile patient in the PT–patient interaction.

This section assumes that the PT locates their hand such that the force is approximately in line with the eyes, and is aligned with the neck in the x axis, so as not to create additional resistive force in the cervical rotational direction. This section also only models the motion in lateral flexion. This can be seen in Figure 3.2.

Using basic statics equations, the forces and moments experienced by the neck during early rehabilitation treatments can be calculated. Note that five lbf is

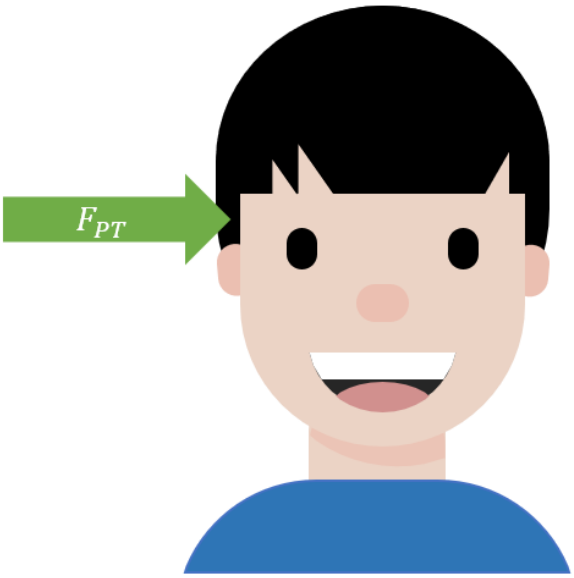

Figure 3.2: The approximate location in the z direction of the applied force.

approximately 22.24 Newtons.

$$\tau_{PT} = F_{PT} * d_{PT} \tag{3.1}$$

$$= 22.24N * d_{PT} \tag{3.2}$$

where d_{PT} is the vertical distance from the force to the desired point of interest. It can be calculated with the following equation:

$$d_{PT} = d_{m-s} - d_{m-n}, \tag{3.3}$$

and the variables d_{m-s} and d_{m-n} are the menton to sellion and the menton to subnasale distances, respectively. This equation gives the approximate torque at approximately the atlanto–occipital joint (C0–C1). If the approximate torque at the C7 is required, the equation for d_{PT} becomes as follows:

$$d_{PT} = (d_S - d_{m-v} + d_{m-s}) - d_C, \tag{3.4}$$

where the variables d_S, d_{m-v} and d_C are stature, the menton to vertex (top of head) length, and cervicale height. Stature is the vertical distance from the floor to the vertex (top of head), and cervicale height is the vertical distance from the

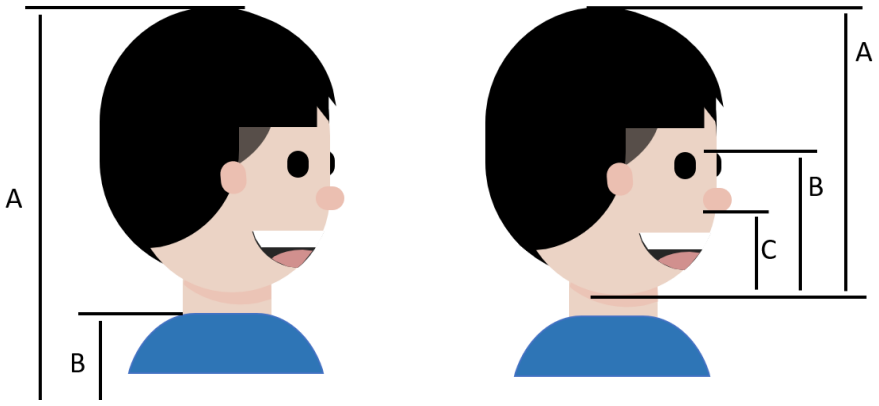

(a) The heights used in the calculations. A: Stature. B: Cervicale height.

(b) The face measurements. A: menton to vertex. B: menton to sellion. C: mention to subnasale.

Figure 3.3: The dimensions used to calculate the distances in the equivalent torque equations.

floor to the C7 bony landmark. The measurements used in these equations can be seen in Figure 3.3.

As an example, data from the The United States Department of Defense Human Factors Engineering Task Force Group (US DoD HFE TAG) can be used using the 50^{th} percentile male's dimensions. The measurement values can be seen in Table 3.1. Using this, the equivalent torque is as follows:

$$\begin{aligned} d_{PT} &= d_{m-s} - d_{m-n} \\ &= 12.2 - 7.3 \text{ cm} \\ &= 0.049 \text{ m} \end{aligned} \tag{3.5}$$

$$\begin{aligned} \tau_{PT} &= F_{PT} * d_{PT} \\ &= 22.24 \text{ N} * 0.049 \text{ m} \\ \tau_{PT} &= 1.090 \text{ N·m} , \end{aligned} \tag{3.6}$$

for the C0 case, and for the C7 case:

$$\begin{aligned} d_{PT} &= (175.5 - 23.2 + 7.3) - 151.8 \text{ cm} \\ &= 0.078 \text{ m} \end{aligned} \tag{3.7}$$

Table 3.1: Anthropometric values used in this thesis, Part 1

Measurement	Value	Unit	Source
Stature	175.5	cm	US DoD HFE TAG [112]
Cervicale height	151.8	cm	"
Menton to top of head	23.2	cm	"
Face length (menton–sellion)	12.2	cm	"
Menton–subnasale length	7.3	cm	"
Total Body Weight (TBW)	80	kg	ISO [113]

$$\begin{aligned} \tau_{PT} &= F_{PT} * d_{PT} \\ &= 22.24 \text{ N} * 0.078 \text{ m} \\ \tau_{PT} &= 1.73 \text{ N·m} \end{aligned} \tag{3.8}$$

Therefore, it can be said in this specific case that the required torque will need to match approximately 1.1 N·m at the base of the skull. To design such a device to do so, a mathematical model of a gyroscopic stabilizer system will be needed for size and weight optimization of the gyrostabilizer. This model is discussed in Chapter 4.

3.1.2 The Model Head–Neck System

Two pieces of information of the head–neck are needed for modelling the dynamics of the system: the location of the COM of the head and the mass moments of inertia. The COM location is described below in Equations 3.12–3.14. The mass moments of inertia for the 50^{th} percentile male head are given in NASA-STD-3000. The values are as follows:

$$I_x = 207.1 \tag{3.9}$$

$$I_y = 236.8 \tag{3.10}$$

$$I_z = 152.2, \tag{3.11}$$

measured in $g \cdot cm^2 \times 10^3$. The principal axes of inertia are in an unspecified direction, as shown in Figure 3.4. A more recent survey of the literature offers the principal moments of inertia for each direction across four different studies [114]. The resulting inertia values when averaging across the five studies is given in Table 3.2. The axes are the same as shown in Figure 3.1.

In order to calculate the location of the COM of the head, a ratio of the distance

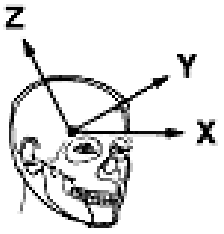

Figure 3.4: The principal axes of inertia for the human head. Adapted from [111].

Table 3.2: Anthropometric values used in this thesis, Part 2

Measurement	Distance (cm)	Source
From wall: x_{COM}	10.4	NASA-RP-1024 [115]
Horizontal from tragion: y_{COM}	7.2	"
Vertical from tragion: z_{COM}	2.3	"
Tragion to vertex	13.0	Burkhard and Sachs [116]
Bitragion breadth	14.2	"
Tragion to wall	10.2	"

Measurement	Average ($kg \cdot cm^2$)	Source
I_{xx}	169.9	Yoganandan et. al., 2009 [114]
I_{yy}	195.7	"
I_{zz}	168.0	"

to the COM along the measured length of the distance was used. These ratio equations were given in "Anthropometric Source Book: Volume 1: Anthropometry for Designers," published by NASA in 1978 [115]. The equations are as follows:

$$x_{COM} = \text{tragion to wall depth} \tag{3.12}$$

$$y_{COM} = 0.5 \cdot \text{bitragion breadth} \tag{3.13}$$

$$z_{COM} = 0.17 \cdot \text{tragion to vertex height} \tag{3.14}$$

These three measurements—tragion to wall depth, bitragion breadth, and tragion to vertex height—are shown in Figure 3.5. The tragion is the point directly above the tragus of the ear.

The data used to scale the model skull used in Chapters 4 through 6 can be seen in Table 3.2. These data were compiled in a paper by Burkhard and Sachs while developing a manikin for acoustic research [116]. This is the only paper found in the literature survey to include all three required measurements, except

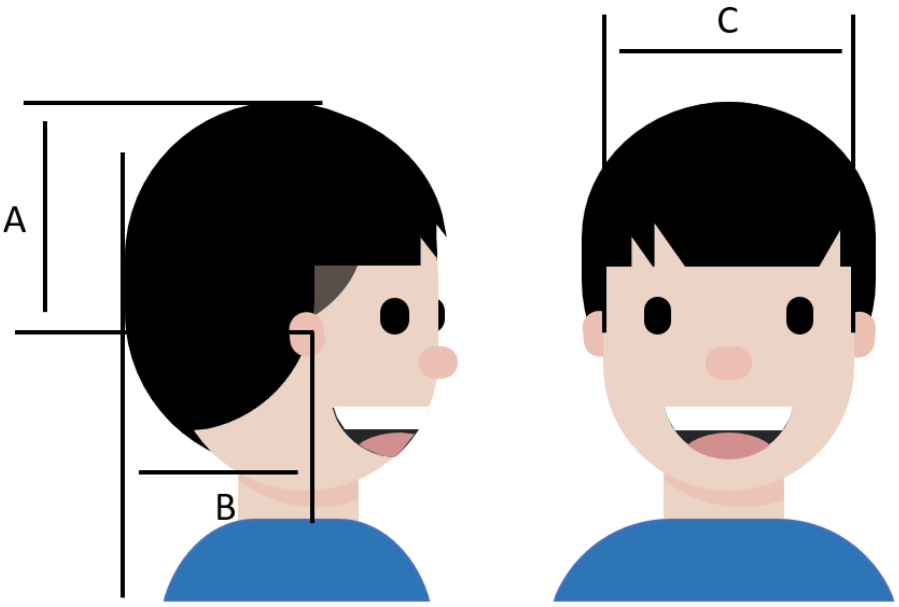

Figure 3.5: The measurements used to calculate the COM of the head. A: tragion to vertex. B: tragion to wall. C: bitragion breadth.

for the original NASA source for the equation. Since the NASA data are said to be representative only of a small subset of the American population, a more general source was preferred. The authors combined the data from multiple sources. The average measurement described in this paper was checked against the data from the NASA source book.

$$\begin{aligned} x_{COM} &= \textit{tragion to wall depth} \\ &= 10.2 \text{ cm} \end{aligned} \tag{3.15}$$

$$\begin{aligned} y_{COM} &= 0.5 \cdot \textit{bitragion breadth} \\ &= 0.5 \cdot (14.2 \text{ cm}) \\ &= 7.1 \text{ cm} \end{aligned} \tag{3.16}$$

$$\begin{aligned} z_{COM} &= 0.17 \cdot \textit{tragion to vertex height} \\ &= 0.17 \cdot (13.0 \text{ cm}) \\ &= 2.21 \text{ cm} \end{aligned} \tag{3.17}$$

As these are all within 0.2 cm (at minimum 96%) of the data for the American Crew Member (shown in Table 3.2), it seems reasonable to use the more general

data from the acoustic manikin work.

The NASA-RP-1024 book also provides an estimate for the mass in kg of a human head:

$$m_H = 0.0306 \cdot (TBW) + 2.46, \tag{3.18}$$

where TBW is total body weight in kg. Using this equation with the ISO Standard value for the 50$^{\text{th}}$ percentile male (80 kg [113]) results in an approximate weight for the 50$^{\text{th}}$ percentile male's head:

$$\begin{aligned} m_H &= 0.0306 \cdot (80 \text{ kg}) + 2.46 \\ &= 4.91 \text{ kg} \end{aligned} \tag{3.19}$$

Additionally, the approximate angle of the atlanto–occipital joint as compared to the horizontal world plane is required (specifically for the physical model created for this project). This angle is approximately 10 degrees [117–119].

3.1.3 Modelling Conclusions

Knowing the measurements of a specific person will allow for greater accuracy in the following equations. Unfortunately, the literature survey yielded no measurements or formulas to calculate the distance between the tragion (or the bone landmark porion) and the atlanto–occipital joint. Therefore, the following inaccurate assumptions are recommended at this stage: $COM_{H_x} = 0$, as the joint aligns closely to the location of the tragion; $COM_{H_y} = 0$, as both the cervical spine and the COM are aligned along the midsagittal plane; and the equation for COM_{H_Z} is as follows[†]:

$$COM_{H_z} = (\text{height to tragion} - \text{height to nose}) + 0.17 * \text{tragion to vertex} \tag{3.20}$$

The palatal plane is not quite parallel to the Frankfurt plane, with an average difference of one degree from horizontal. The palatal plane roughly aligns with the atlanto–occipital joint and has one of the landmarks for this plane located at the anterior nasal spine [120]. This allows a rough approximation of the vertical height of this joint as compared to the tragion.

[†]These are approximates made by the author.

3.2 Dynamics of Stabilized Monorail Carts Using Euler–Lagrange

The basic principle that governs the use of gyroscopes as stabilizing actuators is the precession forces generated by the gyroscope. When a disturbing force is applied to an axis perpendicular to the axis of rotor rotation, the gyroscope precesses. In a three-gimbal gyroscope—the configuration most commonly associated with a gyroscope—the gyroscope would then nutate: rotate around its third axis, the nutation axis. If this third gimbal does not exist, or is locked, the object to which the gyroscope is rigidly attached would have this force caused by the precession of the gyroscope act upon it. In stabilizer applications, this is typically the vehicle body. Assuming that the gimbals are set along the correct axes, the resulting torque acts opposite to the original disturbance, righting the vehicle.

The Spry–Girard derivation in 2008 was the first to derive the dynamics of a gyroscopically stabilized monorail cart using Lagrangian mechanics, as shown in Figure 3.6 [88]. This approach has since been applied to other gyroscopically stabilized systems to analyze the dynamics, such as a stabilized platform and road vehicles [91, 94]. This is the same approach that will be used in the proposed blended method.

The derivation for the system is quite short, and starts with the assignment of variables and body frames. From here, the linear and angular velocities are calculated by inspection. The work used Lagrange's equations of the form

$$\frac{\mathrm{d}}{\mathrm{d}t}\left(\frac{\partial \mathcal{K}}{\partial \dot{q}_i}\right) - \frac{\partial \mathcal{K}}{\partial q_i} = Q_i, \tag{3.21}$$

where q_i are the generalized coordinates for the the system, and Q_i is the sum of the potential energy ($\mathcal{P}$) and the torques acting on the system (including the disturbing force).

The generalized coordinates of the system are the head angle and the cage angle. The derivation takes into account the velocity with which the cart is moving along the track and the curvature of the track, in both the horizontal and vertical directions.

The work uses the derived equations, along with a paired double gyroscope model, to analyze the model. The system was linearized about the equilibrium point for the state vector $x = (q, \dot{q})$ and simulated for control parameters.

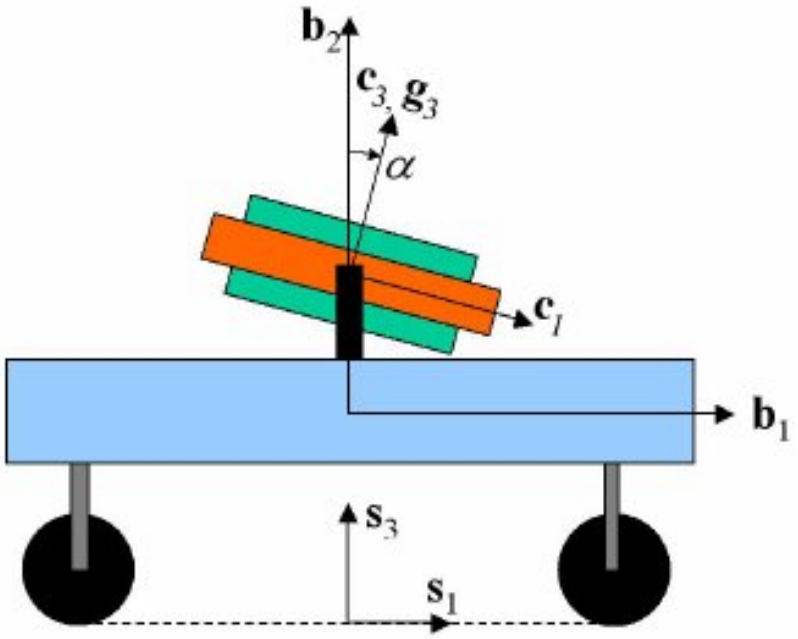

Figure 3.6: The gyroscopically stabilized cart, as proposed by Spry and Girard. Adapted from [88].

The method proposed in this thesis uses a similar approach to deriving the equations, though uses a different form for the Euler–Lagrange equation. The velocities are calculated with an alternative approach to inspection.

3.3 The Denavit–Hartenberg Convention

This convention was originally proposed in 1955 by J. Denavit and R. Hartenburg for mechanical linakges [121] [122]. It was popularized for the field of robotics by R. Paul in his 1981 book "Robotic Manipulators: Mathematics, Programming, and Control" [123]. The mathematics presented below is available in the book "Robot Modeling and Control" by Spong, Hutchinson, and Vidyasagar [124, 125].

To analyze a series of linkages using this method, each joint is identified and assigned a joint variable. Generalized coordinates for the joint variables—q_i—can be used, where the joint variable q_i is as follows:

$$q_i = \begin{cases} d_i, & \text{for a prismatic joint.} \\ \theta_i, & \text{for a revolute joint} \end{cases} \tag{3.22}$$

To set up the DH convention, the diagram and table must be completed. Once the joints have been identified, each joint then has its z_i axis identified and labelled. For revolute joints, the z axis is the axis of rotation. For prismatic joints, the z axis is the direction of motion of the joint. Typically, the positive direction of the axis is the one which is towards the next joint in the series. The base frame is then assigned using the Right Hand Rule (RHR). The origin (O_i) for each joint is located: in any convenient location along z_i for parallel z axes; at the intersection of the z axes for intersecting z axes; or at the intersection of the common normal with z_i for z axes that do not intersect and are not parallel. The x_i axes are assigned in a similar manner: any convenient direction for parallel z axes; normal to the plane created by intersecting z axes; or along the common normal from z_{i-1} to z_i for z axes that do not intersect and are not parallel. The direction of x is also constrained by two rules: "DH-1: the x_i axis must be perpendicular to z_{i-1}; [and] DH-2: the x_i axis must intersect z_{i-1}" [125]. The frames can then be completed using the RHR and a final tool frame, in any orientation, may be added if necessary for the application.

The DH Parameters Table is filled out based on the frame assignments given above. The table, seen in Table 3.3, contains the four variables related to the convention, a_i, d_i, α_i, and θ_i, where the joint variables are indicated with an asterisk. These variables are defined as follows:

$a_i =$ the distance along x_i from the intersection of x_i and z_{i-1} to O_i

$d_i =$ the distance along z_i from O_{i-1} to the intersection of x_i and z_{i-1}

$\alpha_i =$ the angle from z_{i-1} to z_i measured about x_i

$\theta_i =$ the angle from x_{i-1} to z_i measured about z_{i-1}

Table 3.3: DH Parameter Table example, with two joint variables filled in: the first joint being prismatic, and the last joint (n) being revolute, as indicated by the asterisk subscript.

	a	d	α	θ
1	a_1	d_1^*	α_i	θ_1
⋮	⋮	⋮	⋮	⋮
n	a_n	d_n	α_n	θ_n^*

The DH Parameters Table is used to populate the Homogenous Transformation

Matrices, $\mathbf{A}_i^{i-1}$.

$$\mathbf{A}_i^{i-1} = \begin{bmatrix} \cos\theta_i & -\sin\theta_i\cos\alpha_i & \sin\theta_i\sin\alpha_i & a_i\cos\theta_i \\ \sin\theta_i & \cos\theta_i\cos\alpha_i & -\cos\theta_i\sin\alpha_i & a_i\sin\theta_i \\ 0 & \sin\alpha_i & \cos\alpha_i & d_i \\ 0 & 0 & 0 & 1 \end{bmatrix} \tag{3.23}$$

Multiplying these $\mathbf{A}_i^{i-1}$ matrices will provide the Homogeneous Transformation Matrix for subsequent links; that is, a single matrix provides the transformation from the $i-1$ origin to the i origin.

$$\mathbf{T}_n^0 = \mathbf{A}_1^0\mathbf{A}_2^1 ... \mathbf{A}_n^{n-1} \tag{3.24}$$

To calculate the velocity of the linkages in the system, the Jacobian can be used. The general form of the geometric Jacobian is as follows:

$$\mathbf{J} = \begin{bmatrix} \mathbf{J}_v \\ \mathbf{J}_\omega \end{bmatrix}, \tag{3.25}$$

where $\mathbf{J}_v$ and $\mathbf{J}_\omega$ are concatenated vectors for each link in the system:

$$\mathbf{J}_v = \begin{bmatrix} \mathbf{J}_{v_1} & ... & \mathbf{J}_{v_n} \end{bmatrix} \text{ and} \tag{3.26}$$

$$\mathbf{J}_\omega = \begin{bmatrix} \mathbf{J}_{\omega_1} & ... & \mathbf{J}_{\omega_n} \end{bmatrix}, \tag{3.27}$$

and the values for each specific $\mathbf{J}_{v_i}$ and $\mathbf{J}_{\omega_i}$ are given by the following equations:

$$\mathbf{J}_{v_i} = \begin{cases} z_{i-1}, & \text{if joint } i \text{ is pismatic} \\ z_{i-1} \times (O_n - O_{i-1}), & \text{if joint i is revolute} \end{cases} \quad \text{and} \tag{3.28}$$

$$\mathbf{J}_{\omega_i} = \begin{cases} 0, & \text{if joint } i \text{ is prismatic} \\ z_{i-1}, & \text{if joint } i \text{ is revolute} \end{cases} \tag{3.29}$$

The values for z_i and O_i are found in the Homogeneous Transformation Matrix $\mathbf{T}_i^0$:

$$\mathbf{T}_i^0 = \begin{bmatrix} \mathbf{R}_i^0 & d_i^0 \\ \mathbf{0}_{1\times3} & 1 \end{bmatrix} \tag{3.30}$$

$$\mathbf{T}_i^0 = \begin{bmatrix} n_x & s_x & a_x & d_x \\ n_y & s_y & a_y & d_y \\ n_z & s_z & a_z & d_z \\ 0 & 0 & 0 & 1 \end{bmatrix}, \tag{3.31}$$

where z_i is the a vector and O_i is the d vector:

$$z_i = \begin{bmatrix} a_x \\ a_y \\ a_z \end{bmatrix} \tag{3.32}$$

$$O_i = \begin{bmatrix} d_x \\ d_y \\ d_z \end{bmatrix} \tag{3.33}$$

To attain the velocity vector ξ, the Jacobian $\mathbf{J}$ is multiplied by the generalized coordinate vector q:

$$\xi = \mathbf{J}q, \tag{3.34}$$

where the first three items in the ξ vector are the linear velocity vector, and the last three are the angular velocity vector. This ξ vector presents the velocities of the end effector in the base frame (ξ_e^0).

For a system that is rigidly attached, the equation for the tool velocity—when the end effector velocity is known—can be easily calculated using a matrix for transforming velocities in rigidly attached bodies. The general Velocity Transformation Matrix ($\boldsymbol{\mathcal{F}}$) is as follows:

$$\boldsymbol{\mathcal{F}}_a^b = \begin{bmatrix} \mathbf{R}_b^{aT} & -\mathbf{R}_b^{aT}\mathcal{S}(\vec{d}_b^a) \\ \mathbf{0}_{\times(3,3)} & \mathbf{R}_b^{aT} \end{bmatrix}, \tag{3.35}$$

where $\mathbf{R}_b^a$ and $\vec{d}_b^a$ are from the homogenous transformation matrix $\mathbf{H}_b^a$, and where S is the skew-symmetric matrix:

$$S(d_b^a) = \begin{bmatrix} 0 & -d_{b\,z}^a & d_{b\,y}^a \\ d_{b\,z}^a & 0 & -d_{b\,x}^a \\ -d_{b\,y}^a & d_{b\,x}^a & 0 \end{bmatrix} \tag{3.36}$$

The Velocity Transformation Matrix can be multiplied by a velocity vector ξ

in order to transform the frame of reference.

$$\xi_n^b = \boldsymbol{\mathcal{F}}_a^b \cdot \xi_n^a \tag{3.37}$$

$$= \begin{bmatrix} R_b^{aT} & R_b^{aT} S\left(d_b^a\right) \\ 0_{3\times 3} & R_b^{aT} \end{bmatrix} \xi_n^a \tag{3.38}$$

In the work that is presented in this thesis, frame a will be the base frame 0, and frame b will be the end-effector frame n. This results in transforming ξ_n^0 to ξ_n^n.

In general applications of the DH convention, the Euler–Lagrange method can be calculated directly from the configuration vector, the Jacobian matrices for each link, the inertia tensors of each link, the mass of each link, the positions of the COM of each link.

$$\sum_{j=1}^{n} d_{kj}(q)\ddot{q} + \sum_{j=1}^{n}\sum_{i=1}^{n} c_{ijk}(q)\dot{q}_i\dot{q}_j + g_k(q) = \tau_k, \tag{3.39}$$

where the c_{ijk} terms are the Christoffel symbols and the g_k terms are the effects of gravity on the k^{th} link:

$$c_{ijk} = \frac{1}{2}\left(\frac{\partial d_{kj}}{\partial q_i} + \frac{\partial d_{ki}}{\partial q_j} - \frac{\partial d_{ij}}{\partial q_k}\right) \tag{3.40}$$

$$g_k = \frac{\partial \mathcal{P}}{\partial q_k} \tag{3.41}$$

where $\mathcal{P}$ is the equation for potential energy from gravity:

$$\mathcal{P} = \sum_{i=1}^{n} m_i g^T r_c^i, \tag{3.42}$$

and where m_i is the mass of each link, g is the gravity vector in the inertial frame, and r_c^i is the COM of the link, given in the inertial frame.

A common form of the above equation is the matrix form:

$$D(q)\ddot{q} + C(q,\dot{q})\dot{q} + g(q) = \tau, \tag{3.43}$$

where the matrices used are defined as follows:

$$D = \sum_{i=1}^{n} \left\{ m_i J_{v_i}(q)^T J_{v_i}(q) + J_{\omega_i}(q)^T R_i(q) I_i R_i(q)^T J_{\omega_i}(q) \right\} \tag{3.44}$$

$$\text{item } c_{kj} = \sum_{i=1}^{n} c_{ijk}(q)\dot{q}_i, \text{ and} \tag{3.45}$$

$$g = \begin{bmatrix} g_1(q) & g_2(q) & \dots & g_n(q) \end{bmatrix}^T, \tag{3.46}$$

where I_i is the inertia tensor for the i^{th} link.

3.4 Concluding Statement

This chapter presented the necessary background information and derived equations to model both the torque experienced in a hypothetical head–neck system and the location of the COM of the same hypothetical head–neck system. Background information was also presented on the two approaches—the DH convention and the Spry–Girard derivation—that are blended in the proposed method in the following chapter.

Chapter 4

The Theoretical Model

The previous chapters presented the background information and mathematics required to model the biomechanical system, as well as understand the DH approach. This chapter covers the proposed method for calculating the resultant moment experienced by the user in a j-gyroscope system. The method is followed by an example section showing the equation for torque derived for a one-gyroscope system, as seen in Figure 4.1b. The last section of this chapter briefly covers how to use the methods and equations in this section to expand beyond a one-gyroscope device.

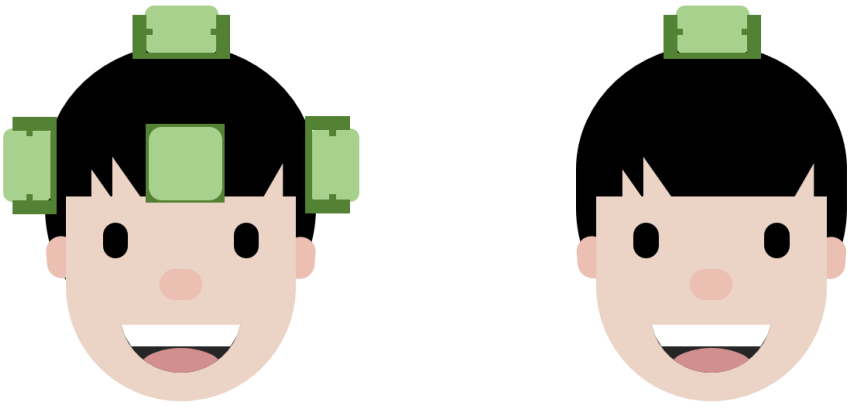

(a) Four visible gyroscopes from a five-gyroscope configuration, as would be required for balanced resistance to all rotational ROM.

(b) One gyroscope located parallel to the transverse plane of the body, with the axis of rotation aligned with the coronal plane.

Figure 4.1: The head–neck–gyroscope system, shown here with multiple gyroscopes (4.1a) as well as the one-gyroscope configuration (4.1b) used in Section 4.2.

4.1 Proposed Method

In order to develop the equations to model the interaction between a gyroscope as a stabilizer and a human head and neck, a new method for deriving the dynamics of such a system is proposed. A blended approach was implemented using both the Euler–Lagrange equation (from Lagrangian mechanics, a common approach for gyroscopes) and the method for using the DH convention to calculate the velocities of a given rigid link system (popular in the field of robotics). This approach allows for easy comparison of the addition or removal of gyroscopes to the system, as well as to analyze the dynamics experienced by the neck when factoring in any motion of the user's body that translates into a translational motion of the head. Looking at the dynamics with trunk motion of the user can be useful to ensure that the forces will not exceed a reasonable level, even with unexpected motion. A summary of the proposed method is outlined in Figure 4.2.

An overview of the method:

1. Describe the system frames for each body.
2. Calculate the velocities of each body (linear and angular):
   (a) Create DH representations for each body.
   (b) Calculate the linear velocity, convert to world system frame.
   (c) Calculate the angular velocity, convert to body frame using the velocity rotation matrix; convert from body frame to corresponding system frame.
3. Substitute the linear and angular velocities in the Lagrangian ($\mathcal{K}-\mathcal{P}$), then calculate the Q forces using the Euler–Lagrange equation:
   (a) Calculate each partial derivative with respect to q_i and $\dot{q}_i$, and the derivative with respect to time of the $\dot{q}_i$ terms.
   (b) Assemble the equation and simplify.

The resultant equations can be used to optimize the system. Additional gyroscopes can be added at this stage; simply add the time derivatives and subtract the partial derivatives for the additional bodies to the resultant equation.

Figure 4.2: Summary of the proposed method.

The Euler–Lagrange equation is used for optimization problems, which is the

intended use of the obtained dynamics of the system. This approach also works well for complex systems. The standard form is as follows:

$$\frac{\mathrm{d}}{\mathrm{d}t}\left(\frac{\partial \mathcal{L}}{\partial \dot{q}}\right) - \frac{\partial \mathcal{L}}{\partial q} = 0, \tag{4.1}$$

where the Lagrangian ($\mathcal{L}$) is the kinetic energy ($\mathcal{K}$) of a system minus the potential energy ($\mathcal{P}$) of a system:

$$\mathcal{L} = \mathcal{K}\left(\dot{q}_i, q_i\right) - \mathcal{P}\left(\dot{q}_i, q_i\right), \tag{4.2}$$

where $q\left(t\right)$ is the "generalized coordinate" vector of the system (for robotics, this is a vector of all of the joint variables θ_i and d_i^*).

Since the system under consideration contains non-conservative forces, a "generalized force" vector (Q) is added to the Right-Hand Side (RHS) of the equation:

$$\frac{\mathrm{d}}{\mathrm{d}t}\left(\frac{\partial \mathcal{L}}{\partial \dot{q}_i}\right) - \frac{\partial \mathcal{L}}{\partial q_i} = Q_i \tag{4.3}$$

In robotics, the Q vector is generally regarded as specifically representative of the torque or force relating to each coordinate in the generalized coordinate system $\vec{q}$. This method allows for the inclusion of dissipative loss for additional accuracy in the model (if the damping in the gyroscope mechanism(s) is known). Therefore, in order to account for these forces, the Rayleigh Dissipation Function ($\mathcal{R}$) can optionally be added to the RHS:

$$\frac{\mathrm{d}}{\mathrm{d}t}\left(\frac{\partial \mathcal{L}}{\partial \dot{q}_i}\right) - \frac{\partial \mathcal{L}}{\partial q_i} = Q_i + \frac{\partial \mathcal{R}}{\partial q_i} \tag{4.4}$$

Here $\mathcal{R}$ is the Rayleigh Dissipation Function and b_i is the damping coefficient for q_i:

$$\mathcal{R} = -\frac{1}{2}\sum_{i=1}^{n} b_i {\dot{q}_i}^2 \tag{4.5}$$

For the proposed system design (a human head with a number of single-gimballed gyroscopes attached), the kinetic energy is a function of both the linear ($\vec{v}$) and angular velocities ($\vec{\omega}$) of each body in the system. The potential energy is a function of the z-y'-x'' intrinsic Tait–Bryan angle set $[\psi\ \theta\ \phi]^T$ (yaw–pitch–roll) of the head. In the case that the COM of the gimbals and/or the rotor are not aligned with the precession axes, potential energy is also a function of the preces-

sion angles (α_j) of each gyroscope. The mapping of the roll–pitch–yaw angles to the human body is found in Section 3.1 (Figure 3.1).

The complexity of a system is magnified as the number of degrees of freedom is increased. Creating the equations of motion of each gyroscopic body by inspection is increasingly less feasible with the addition of degrees of freedom in the neck. Since the gyroscopes move independently of each other (that is, they are only kinematically dependent on the motion of the Head COM, and not serially linked), each gyroscope can be analyzed separately from the others. With this knowledge, the motion and velocities of the gimbals and rotors of each gyroscope can be represented as an individual serial kinematic chain, with the COM under consideration as the end-effector of the representative rigidly linked system.

To set up the system frames (the frames of reference for each body in the system), each moving part must be identified. This includes the world frame, head, and the number and locations of the gyroscopes. Each gyroscope has two frames associated with it, as there are two moving bodies (the gyroscope gimbals (cage) and the rotor (wheel)). The numbered order of the j gyroscopes does not matter, as long as the order remains constant throughout the analysis. The origin for each system frame should be located at the COM of the body in question. In this chapter, the first system frame (the Neck frame, or world frame) is represented as N (with N_x, N_y, N_z as the axes).

Using the system frames allows for less confusion when dealing with multiple manipulators. For example, when dealing with the body frames for multiple end-effectors with the same numerical notation. The system frames also allows for different base frames as needed.

In order to find the equations that describe the motion and velocity of each of these bodies, a representation for each COM as a serial kinematic chain using the DH convention should be created. For the head, a spherical wrist representation can be applied if using all rotational degrees of freedom for the neck. The head representation may have up to 6 Degrees of Freedom (DOF) (up to three revolute and three prismatic joints) if the translational motion of the user is to be considered, as well. If considering offsets in the system (i.e., not assuming symmetry, or for a COM that is not inline with axes of motion) an additional tool frame with no joint variable may need to be added to the system at the COM following the DH convention rules for assigning frame orientation. An example of this additional frame can be seen in the 1 DOF representation of the neck and head COM in Figure 4.3.

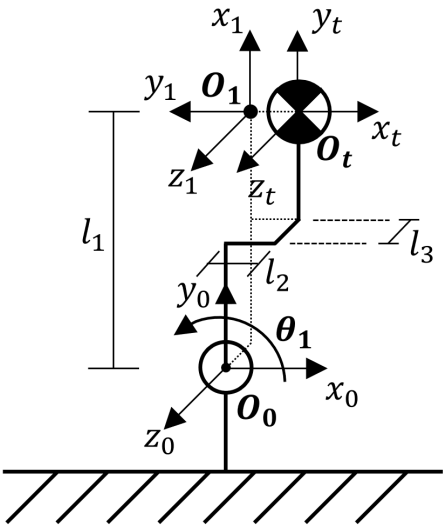

Figure 4.3: An example of a serial kinematic chain representation of the Head COM, using 1 DOF in the neck.

Ideally, the representations will be created in such a way that the x axes will align such that there is a one-to-one fashion with the angles from the system frames; for example, the system frame and the manipulator thetas are the same in direction and magnitude. When it is not possible to align the angles one-to-one, the conversion will be factored in when converting the velocities from the representation frame to the system frame. This conversion will likely be in a form similar to $\theta_i = \pm\phi + n$, where θ_i is the manipulator angle, ϕ is the same rotation in the system frames, and n is an angle offset.

Once each representation is created (for a resultant $k = 2j+1$ manipulators), a DH parameter table must be created for each. Note that the number of representations can be reduced if the COM of the gimbals and rotor are co-located, or are assumed to be so. After populating the $\mathbf{A}_i^{i-1}$ matrices with the corresponding DH parameters, all intermediate $\mathbf{A}_i^0$ matrices must be calculated, as they are needed to calculate the Jacobian of the manipulators, $\mathbf{J}_k$.

Multiplying the $\mathbf{J}_k$ Jacobian by $\dot{\vec{q}}_k$ (where each of the $\vec{q}_k$ vectors is a subset of the q generalized configuration coordinates used in the Lagrangian, introduced earlier in this section) gives $\xi_k^0 = [\vec{\omega}_k^0 \;\; \vec{v}_k^0]^T$, the angular and linear velocities of the end effector (the COM of the body) with respect to the manipulator representation base frame.

In order to use the principal axes ($I_{xx} \;\; I_{yy} \;\; I_{zz}$) for the kinetic energy equation $\mathcal{K} = \frac{1}{2} I \cdot \omega^2$, the angular velocity must be represented in the body frames (H,

Gj, and Wj). To achieve this frame change, a Velocity Transformation Matrix is applied to each of the velocities vectors ξ_k. When the final end-effector frame is the n^{th} frame, this equation is as follows:

$$\xi_n^b = \boldsymbol{\mathcal{F}}_a^b \cdot \xi_n^a, \tag{4.6}$$

where $\boldsymbol{\mathcal{F}}$ is the velocity transformation matrix, $\mathcal{S}$ is the skew symmetric representation, and $\mathbf{R}_b^a$ and $\vec{d}_b^a$ are from the Homogeneous Transformation Matrix $\mathbf{T}_b^a$. In this usage, Frame a will be the Base Frame 0, and Frame b will be the End-Effector Frame n, resulting in transforming ξ_n^0 to ξ_n^n:

$$\xi_n^n = \boldsymbol{\mathcal{F}}_0^n \cdot \xi_n^0 \tag{4.7}$$

and

$$\boldsymbol{\mathcal{F}}_0^n = \begin{bmatrix} \mathbf{R}_n^{0\,T} & -\mathbf{R}_n^{0\,T}\mathcal{S}(\vec{d}_n^0) \\ \mathbf{0}_{\times(3,3)} & \mathbf{R}_n^{0\,T} \end{bmatrix} \tag{4.8}$$

It is likely that an additional frame transformation will be required to align the End-Effector Frame n with the corresponding system frame. It is important when substituting in the true angles (for the yaw, pitch, and roll of the head: $[\psi \;\; \theta \;\; \phi]^T$, and for the precession, nutation, and spin of each gyroscope j: $[\alpha_j \;\; \beta_j{}^{\dagger} \;\; \gamma_j]^T$) that care is taken with the pitch of the head, as it is also θ, and that the representation angles may not directly map one-to-one with the angles as defined in the system frames. If this is the case, the conversion equation(s) calculated when creating the representations will be substituted for the θ angle(s).

Assuming the base frame(s) (the neck joint(s)) were prepared identically in each ($k = 2j + 1$) representation, each $\vec{v}_k^0$ can have the same rotation matrix applied to transform from the Base Frame 0 to the System Frame N. Otherwise, individual transformations must be applied to have all velocities in the common N frame.

To prepare the Euler–Lagrange, the q vector is set up as $[q_H \;\; q_1 \;\; ... \;\; q_j]^T$, where the head configuration is given by the corresponding degrees of freedom: $[d_x^* \; d_y^* \; d_z^* \; \psi \; \theta \; \phi]^T$, and q_j is the precession and spin angles for the j^{th} gyroscope: $[\alpha_j \; \gamma_j]^T$. If using any translational degrees of freedom with the expectation that they result from unintentional body movement, these can be discounted from the q_H vector.

[†]the gyrostabilizers are single-gimballed gyroscopes, and therefore have no nutation angle β_j

The linear and rotational velocities obtained from the representations are then substituted into the $\mathcal{K}$ and $\mathcal{P}$ equations for each body. Due to the Sum Rule in Differentiation, the generalized momentum conjugates to q_i ($\frac{\partial \mathcal{L}}{\partial \dot{q}_i}$) and the time derivative of the generalized momentum conjugates ($\frac{\partial \mathcal{L}}{\partial \dot{q}_i}$) can be split into smaller components: the partial derivative $\mathcal{K}$ and $\mathcal{P}$ terms for each body can be evaluated individually at $\dot{q}_i$ and q_i. These terms can then be collated into the Euler–Lagrange equation. If known, the damping or friction terms can be evaluated and added to the RHS of the collated Euler–Lagrange equation at this stage.

These equations can then be simplified to give the expressions for Q_i, where Q_1 through Q_n (where n is n degrees of rotational freedom in the neck) are the torques experienced in the neck of the user, and the following Q_{n+1} through Q_{n+2j} terms are the torques for each gimbal and wheel body in the previously-defined order of j-gyroscopes.

$$\vec{Q} = \begin{bmatrix} Q_1 \\ \vdots \\ Q_n \\ Q_{n+1} \\ Q_{n+2} \\ \vdots \\ Q_{n+2j-1} \\ Q_{n+2j} \end{bmatrix}, \vec{q} = \begin{bmatrix} q_1 \\ \vdots \\ q_n \\ q_{n+1} \\ q_{n+2} \\ \vdots \\ q_{n+2j-1} \\ q_{n+2j} \end{bmatrix} \tag{4.9}$$

Calculating all of these equations in the q set allows for optimization to take into account the material stresses in the axis of rotation for the gimbals, while the wheel torque is useful to note when designing the rotor, to check against the material properties of the chosen material.

The benefits of this method is that it allows for easier calculation of the linear and angular velocities of what may be a complex motion, if the head is allowed to translate and/or rotate along all three axes. By using the more general Euler–Lagrange equations instead of the standardized matrices and Christoffel symbols used in robotics, it allows for the inclusion of multiple gyroscopes not connected in series, as well as the ability to easily expand the system and see the effects to the dynamics of the system.

For verification purposes, a single-gyroscope system was tested on a 1 DOF head model (see Chapters 5 and 6 for the design and validation, respectively).

The following section is the application of the method for a single-gyroscope, 1 DOF model using this method and the resulting equations.

4.2 Single-Gyroscope System Dynamics

The equation for describing the moment experienced at approximately the atlanto–axial joint (C1–C2 joint) was calculated by analyzing the head–neck–gyroscope system with one degree of freedom in the neck (roll, or lateral cervical flexion) and one gyroscope ($j = 1$) located parallel to the transverse plane of the human body as seen in Figure 4.1b. For brevity, the following sections use the standard **s** and **c** notation to represent sin and cos, respectively.

First, the general relative motion equations of the system were developed, where the labelling convention outlined in Table 4.1 was used. A graphical representation of the system frames can be seen in Figure 4.4.

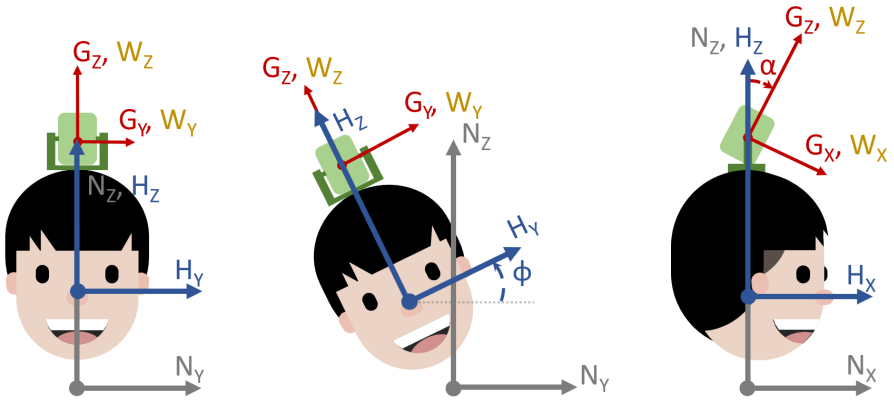

Figure 4.4: The system frames (coordinate frames) and angles used in the dynamics calculations for a single gyroscope application. Not to scale.

Table 4.1: The nomenclature used for the dynamics derivation.

N	Relating to Neck; the world frame
H	Relating to Head
G	Relating to Gimbals, or gyroscope "cage"
W	Relating to the gyroscope Wheel
ω	Angular velocity
v	Linear velocity

$\dot{\gamma}$	Rotational velocity of the gyroscope
ϕ	Angle between the y axes of the neck and head; lateral neck flexion angle
α	Angle between the z axes of the head and the gyroscope wheel; precession angle
m	Mass
I	Mass moment of inertia
$x_{\_}$	Distance between neck rotation point and COM of the subscript along the Neck Frame x axis
$y_{\_}$	Distance between neck rotation point and COM of the subscript along the Neck Frame y axis
$z_{\_}$	Distance between neck rotation point and COM of the subscript along the Neck Frame z axis

By inspection, it was possible to develop the equations of rotational velocity for each system body with respect to the individual frame of each body. The linear (tangential) velocities of these bodies—which are in the world frame—are more complex. By representing the system as rigid link system—similar to a robotic manipulator—these equations were calculated using standard methods in the field of robotics. The velocities calculated using the above method were checked against the angular velocities obtained by inspection.

4.2.1 Calculating Velocities Using a Rigid Link Model

Modelling this system as if it were a 1 DOF, 2 DOF, and a 3 DOF robotic manipulator allowed for a geometric approach for calculating the angular and linear velocities of each body, utilizing the Jacobian matrix. The model representations can be seen in Figure 4.5. The DH convention has been applied to the models, with O_t in Figure 4.5a located at the COM of the head. The $x_{\_}$, $y_{\_}$, and $z_{\_}$ values shown in the representations are vector values, relative to the Neck frame. O_t acts as the Tool Frame in the first model and O_2 and O_3 act as the End-Effector Frame for the second and third models, respectively. Both O_2 and O_3 are located at the axis of rotation of the cage (Figures 4.5b and 4.5c).

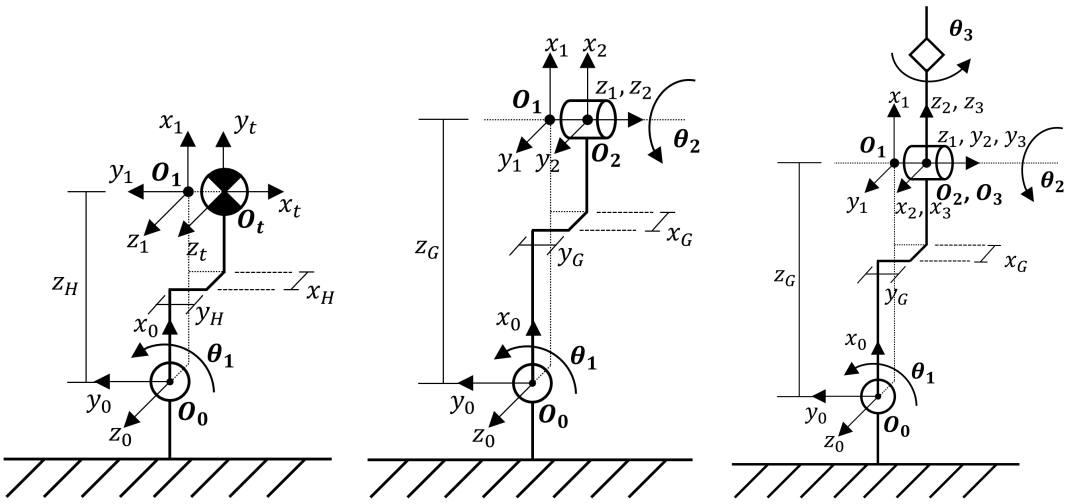

(a) 1 DOF Model of the Head–Neck joint, where O_t is located at the COM of the head.

(b) 2 DOF Model of the Head–Neck–Gyro system, where O_2 is located at the axis of rotation of the cage.

(c) 3 DOF Model of the Head–Neck–Gyro system, where O_2 and O_3 are co-located at the axis of rotation of the cage.

Figure 4.5: Model representations of the Head–Neck–Gyroscope system as a robotic manipulator, where $x_{\_}$, $y_{\_}$, and $z_{\_}$ are vectors.

4.2.1.1 Velocity of the COM of the Head

The angular and linear velocities of the Head were analyzed first. From the 1 DOF model, the DH parameters table (Table 4.2) was created and substituted into Homogeneous Transformation Matrices ($\mathbf{A}_i^{i-1}$).

	a	d	α	θ
1	$z_{_H}$	$x_{_H}$	0	θ_1^*
2[†]	$y_{_H}$	0	0	$-\pi/2$

Table 4.2: DH Table for the 1 DOF representation.

"Joint 2" in the DH table was used to populate the end-effector-to-tool-frame Transformation matrix (also a Homogeneous Transformation Matrix, $\mathbf{A}_1^t$), since the transforms required fit within the DH requirements.

[†]Frame 2 is equivalent to Frame t in this instance

$$\mathbf{A}_i^{i-1} = \begin{bmatrix} \mathbf{c}\theta_i & -\mathbf{s}\theta_i\,\mathbf{c}\alpha_i & \mathbf{s}\theta_i\,\mathbf{s}\alpha_i & a_i\,\mathbf{c}\theta_i \\ \mathbf{s}\theta_i & \mathbf{c}\theta_i\,\mathbf{c}\alpha_i & -\mathbf{c}\theta_i\,\mathbf{s}\alpha_i & a_i\,\mathbf{s}\theta_i \\ 0 & \mathbf{s}\alpha_i & \mathbf{c}\alpha_i & d_i \\ 0 & 0 & 0 & 1 \end{bmatrix} \tag{4.10}$$

$$\begin{aligned} \mathbf{A}_1^0 &= \begin{bmatrix} \mathbf{c}\theta_1 & -\mathbf{s}\theta_1\,\cancelto{1}{\mathbf{c}(0)} & \mathbf{s}\theta_1\,\cancelto{0}{\mathbf{s}(0)} & z_{_H}\,\mathbf{c}\theta_1 \\ \mathbf{s}\theta_1 & \mathbf{c}\theta_1\,\cancelto{1}{\mathbf{c}(0)} & -\mathbf{c}\theta_1\,\cancelto{0}{\mathbf{s}(0)} & z_{_H}\,\mathbf{s}\theta_1 \\ 0 & \cancelto{0}{\mathbf{s}(0)} & \cancelto{1}{\mathbf{c}(0)} & x_{_H} \\ 0 & 0 & 0 & 1 \end{bmatrix} \\ &= \begin{bmatrix} \mathbf{c}\theta_1 & -\mathbf{s}\theta_1 & 0 & z_{_H}\,\mathbf{c}\theta_1 \\ \mathbf{s}\theta_1 & \mathbf{c}\theta_1 & 0 & z_{_H}\,\mathbf{s}\theta_1 \\ 0 & 0 & 1 & x_{_H} \\ 0 & 0 & 0 & 1 \end{bmatrix} \end{aligned} \tag{4.11}$$

$$\begin{aligned} \mathbf{A}_t^1 &= \begin{bmatrix} \cancelto{0}{\mathbf{c}\tfrac{-\pi}{2}} & -\mathbf{s}\cancelto{-1}{\tfrac{-\pi}{2}}\,\cancelto{1}{\mathbf{c}(0)} & \mathbf{s}\cancelto{-1}{\tfrac{-\pi}{2}}\,\cancelto{0}{\mathbf{s}(0)} & y_{_H}\,\cancelto{0}{\mathbf{c}\tfrac{-\pi}{2}} \\ \cancelto{-1}{\mathbf{s}\tfrac{-\pi}{2}} & \mathbf{c}\cancelto{0}{\tfrac{-\pi}{2}}\,\cancelto{1}{\mathbf{c}(0)} & -\mathbf{c}\cancelto{0}{\tfrac{-\pi}{2}}\,\cancelto{0}{\mathbf{s}(0)} & y_{_H}\,\cancelto{-1}{\mathbf{s}\tfrac{-\pi}{2}} \\ 0 & \cancelto{0}{\mathbf{s}(0)} & \cancelto{1}{\mathbf{c}(0)} & 0 \\ 0 & 0 & 0 & 1 \end{bmatrix} \\ &= \begin{bmatrix} 0 & 1 & 0 & 0 \\ -1 & 0 & 0 & -y_{_H} \\ 0 & 0 & 1 & 0 \\ 0 & 0 & 0 & 1 \end{bmatrix} \end{aligned} \tag{4.12}$$

The final homogeneous transformation matrix ($\mathbf{T}_t^0$) was obtained by multiplying $\mathbf{A}_1^0$ and $\mathbf{A}_t^1$.

$$\begin{aligned} \mathbf{T}_t^0 &= \mathbf{A}_1^0\mathbf{A}_t^1 \\ &= \begin{bmatrix} \mathbf{c}\theta_1 & -\mathbf{s}\theta_1 & 0 & z_{_H}\,\mathbf{c}\theta_1 \\ \mathbf{s}\theta_1 & \mathbf{c}\theta_1 & 0 & z_{_H}\,\mathbf{s}\theta_1 \\ 0 & 0 & 1 & x_{_H} \\ 0 & 0 & 0 & 1 \end{bmatrix} \begin{bmatrix} 0 & 1 & 0 & 0 \\ -1 & 0 & 0 & -y_{_H} \\ 0 & 0 & 1 & 0 \\ 0 & 0 & 0 & 1 \end{bmatrix} \end{aligned}$$

$$= \begin{bmatrix} \mathbf{s}\theta_1 & \mathbf{c}\theta_1 & 0 & z_{_H}\,\mathbf{c}\theta_1 + y_{_H}\,\mathbf{s}\theta_1 \\ -\,\mathbf{c}\theta_1 & \mathbf{s}\theta_1 & 0 & z_{_H}\,\mathbf{s}\theta_1 - y_{_H}\,\mathbf{c}\theta_1 \\ 0 & 0 & 1 & x_{_H} \\ 0 & 0 & 0 & 1 \end{bmatrix} \tag{4.13}$$

Using the above matrices, the Jacobian matrix (**J**) was calculated. For the 1 DOF representation, with one revolute joint:

$$\begin{aligned} \mathbf{J}_1 &= \begin{bmatrix} J_{v_1} \\ J_{\omega_1} \end{bmatrix} \\ &= \begin{bmatrix} z_0 \times (O_2 - O_0) \\ z_0 \end{bmatrix} \\ &= \begin{bmatrix} \begin{bmatrix} 0 \\ 0 \\ 1 \end{bmatrix} \times \left(\begin{bmatrix} z_{_H}\,\mathbf{c}\theta_1 + y_{_H}\,\mathbf{s}\theta_1 \\ z_{_H}\,\mathbf{s}\theta_1 - y_{_H}\,\mathbf{c}\theta_1 \\ x_{_H} \end{bmatrix} - \begin{bmatrix} 0 \\ 0 \\ 0 \end{bmatrix} \right) \\ 0 \\ 0 \\ 1 \end{bmatrix} \end{aligned} \tag{4.14}$$

$$\mathbf{J}_1 = \begin{bmatrix} -z_{_H}\,\mathbf{s}\theta_1 + y_{_H}\,\mathbf{c}\theta_1 \\ z_{_H}\,\mathbf{c}\theta_1 + y_{_H}\,\mathbf{s}\theta_1 \\ 0 \\ 0 \\ 0 \\ 1 \end{bmatrix} \tag{4.15}$$

To calculate the velocities (ξ_1), the Jacobian $\mathbf{J}_1$ was multiplied by the velocity vector $\dot{q}_{jm}$:

$$\xi_1 = \mathbf{J}_1 \dot{q}_{11} \tag{4.16}$$

$$= \begin{bmatrix} -z_{_H}\,\mathbf{s}\theta_1 + y_{_H}\,\mathbf{c}\theta_1 \\ z_{_H}\,\mathbf{c}\theta_1 + y_{_H}\,\mathbf{s}\theta_1 \\ 0 \\ 0 \\ 0 \\ 1 \end{bmatrix} \dot{\theta}_1$$

$$\xi_1 = \begin{bmatrix} (-z_{_H}\,\mathbf{s}\theta_1 + y_{_H}\,\mathbf{c}\theta_1)\,\dot{\theta}_1 \\ (z_{_H}\,\mathbf{c}\theta_1 + y_{_H}\,\mathbf{s}\theta_1)\,\dot{\theta}_1 \\ 0 \\ 0 \\ 0 \\ \dot{\theta}_1 \end{bmatrix} \tag{4.17}$$

where m is the m^{th} representation for the j^{th} gyroscope.

For this use, the linear velocities are needed with respect to the world frame, and the angular velocities are needed with respect to the body frame. To convert the velocities from the robotic manipulator representation frames to the general world frame N (as seen in Figure 4.1) a simple rotation matrix was applied to the linear velocity $\vec{v}_1$. A graphical representation of this frame rotation can be seen in Figure 4.6.

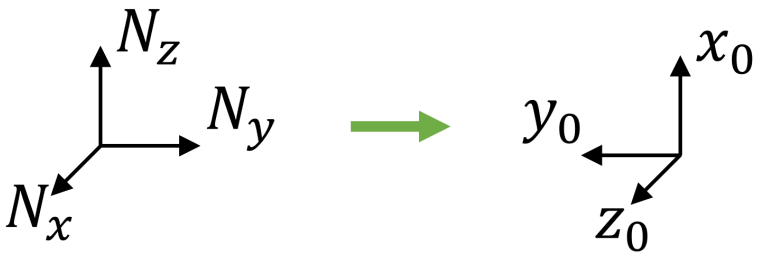

Figure 4.6: Frame rotations from the Robotic Manipulator 1 DOF End-Effector Frame to the Neck/Global Frame.

$$\mathbf{R}_0^N = \text{Rot}_{y,\pi/2} \cdot \text{Rot}_{z,\pi} \tag{4.18}$$

$$
\begin{aligned}
&= \begin{bmatrix} \mathbf{c}\pi/2 & 0 & \mathbf{s}\pi/2 \\ 0 & 1 & 0 \\ -\mathbf{s}\pi/2 & 0 & \mathbf{c}\pi/2 \end{bmatrix} \cdot \begin{bmatrix} \mathbf{c}\pi & -\mathbf{s}\pi & 0 \\ \mathbf{s}\pi & \mathbf{c}\pi & 0 \\ 0 & 0 & 1 \end{bmatrix} \\
&= \begin{bmatrix} 0 & 0 & 1 \\ 0 & 1 & 0 \\ -1 & 0 & 0 \end{bmatrix} \cdot \begin{bmatrix} -1 & 0 & 0 \\ 0 & -1 & 0 \\ 0 & 0 & 1 \end{bmatrix} \\
&= \begin{bmatrix} 0 & 0 & 1 \\ 0 & -1 & 0 \\ 1 & 0 & 0 \end{bmatrix}
\end{aligned} \tag{4.19}
$$

The generic θ_1 was replaced at this stage with the head angle, ϕ, noting that the angle θ_1 is in the same direction and has the same zero position as ϕ.

$$
\vec{v}_H^N = \mathbf{R}_0^N \vec{v}_1 \tag{4.20}
$$

$$
\begin{aligned}
&= \begin{bmatrix} 0 & 0 & 1 \\ 0 & -1 & 0 \\ 1 & 0 & 0 \end{bmatrix} \begin{bmatrix} (-z_{_H}\,\mathbf{s}\phi + y_{_H}\,\mathbf{c}\phi)\;\dot{\phi} \\ (z_{_H}\,\mathbf{c}\phi + y_{_H}\,\mathbf{s}\phi)\;\dot{\phi} \\ 0 \end{bmatrix} \\
\vec{v}_H^N &= \begin{bmatrix} 0 \\ -\left(z_{_H}\,\mathbf{c}\phi + y_{_H}\,\mathbf{s}\phi\right)\;\dot{\phi} \\ (-z_{_H}\,\mathbf{s}\phi + y_{_H}\,\mathbf{c}\phi)\;\dot{\phi} \end{bmatrix}
\end{aligned} \tag{4.21}
$$

To calculate the angular velocity with respect to the body frame, the velocity transform matrix $\boldsymbol{\mathcal{F}}$ was applied, where $\mathbf{R}_t^0$ and $\vec{d}_t^0$ come from the matrix $\mathbf{T}_t^0$ (Equation 4.13). The velocity vector ξ_1, the velocity of the end effector with respect to the manipulator base frame, can also be written as ξ_t^0. The variable θ_1 was replaced by ϕ at the stage, as with the linear velocities:

$$
\xi_t^t = \boldsymbol{\mathcal{F}}_0^t \cdot \xi_t^0 \tag{4.22}
$$

$$
= \begin{bmatrix} \mathbf{R}_t^{0^T} & -\mathbf{R}_t^{0^T} \cdot \mathcal{S}(\vec{d}_t^0) \\ \mathbf{0}_{3\times 3} & \mathbf{R}_t^{0^T} \end{bmatrix} \cdot \begin{bmatrix} (-z_{_H}\,\mathbf{s}\theta_1)\,\dot{\theta}_1 \\ (z_{_H}\,\mathbf{c}\theta_1)\,\dot{\theta}_1 \\ 0 \\ 0 \\ 0 \\ \dot{\theta}_1 \end{bmatrix}
$$

$$= \begin{bmatrix} -\left(z_{_H}\,\mathbf{s}\phi + y_{_H}\,\mathbf{c}\phi + z_{_H}\right)\dot{\phi} \\ \left(-z_{_H}\,\mathbf{c}\phi + y_{_H}\,\mathbf{s}\phi + y_{_H}\right)\dot{\phi} \\ 0 \\ 0 \\ 0 \\ \dot{\phi} \end{bmatrix} \tag{4.23}$$

Therefore:

$$\vec{\omega}_t^t = \begin{bmatrix} 0 \\ 0 \\ \dot{\phi} \end{bmatrix} \tag{4.24}$$

A rotation matrix $\mathbf{R}_t^H$ was created to transform the body angular velocities into the system frame for the body under consideration, as shown in Figure 4.7:

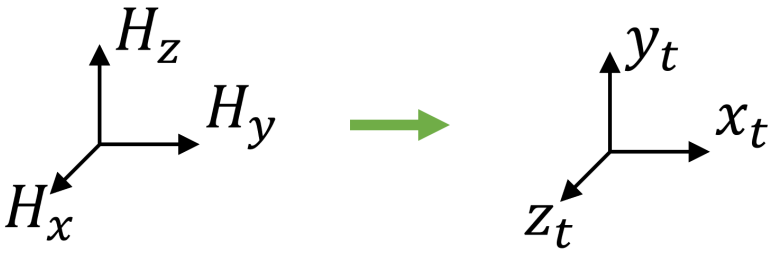

Figure 4.7: Frame rotations from the Robotic Manipulator 1 DOF Tool Frame (t) to the Head Frame.

$$\begin{aligned} \mathbf{R}_t^H &= \mathrm{Rot}_{x,\pi/2} \cdot \mathrm{Rot}_{y,\pi/2} \\ &= \begin{bmatrix} 1 & 0 & 0 \\ 0 & \mathbf{c}\pi/2 & -\mathbf{s}\pi/2 \\ 0 & \mathbf{s}\pi/2 & \mathbf{c}\pi/2 \end{bmatrix} \cdot \begin{bmatrix} \mathbf{c}\pi/2 & 0 & \mathbf{s}\pi/2 \\ 0 & 1 & 0 \\ -\mathbf{s}\pi/2 & 0 & \mathbf{c}\pi/2 \end{bmatrix} \\ &= \begin{bmatrix} 1 & 0 & 0 \\ 0 & 0 & -1 \\ 0 & 1 & 0 \end{bmatrix} \cdot \begin{bmatrix} 0 & 0 & 1 \\ 0 & 1 & 0 \\ -1 & 0 & 0 \end{bmatrix} \end{aligned} \tag{4.25}$$

$$= \begin{bmatrix} 0 & 0 & 1 \\ 1 & 0 & 0 \\ 0 & 1 & 0 \end{bmatrix} \tag{4.26}$$

The Rotation matrix was then applied, noting that the body under consideration is the head, H:

$$\vec{\omega}_H^H = \mathbf{R}_t^H \vec{\omega}_t^t \tag{4.27}$$

$$= \begin{bmatrix} 0 & 1 & 0 \\ 0 & 0 & 1 \\ 1 & 0 & 0 \end{bmatrix} \begin{bmatrix} \dot{\phi}\,\mathbf{s}\alpha \\ \dot{\phi}\,\mathbf{c}\alpha \\ \dot{\alpha} \end{bmatrix}$$

$$\vec{\omega}_H^H = \begin{bmatrix} \dot{\phi} \\ 0 \\ 0 \end{bmatrix} \tag{4.28}$$

Which aligns with the results calculated by inspection.

4.2.1.2 Velocity of the COM of the Cage

This process was repeated for the two joint representation shown in Figure 4.5b, to calculate the cage angular and linear velocities. First, the DH parameters table (Table 4.3) was created and substituted into the two Homogeneous Transformation Matrices ($\mathbf{A}_i^{i-1}$) (one per joint):

	a	d	α	θ
1	z_G	x_G	$\pi/2$	θ_1^*
2	0	y_G	0	θ_2^*

Table 4.3: DH Table for the 2 DOF representation.

$$\mathbf{A}_i^{i-1} = \begin{bmatrix} \mathbf{c}\theta_i & -\mathbf{s}\theta_i\,\mathbf{c}\alpha_i & \mathbf{s}\theta_i\,\mathbf{s}\alpha_i & a_i\,\mathbf{c}\theta_i \\ \mathbf{s}\theta_i & \mathbf{c}\theta_i\,\mathbf{c}\alpha_i & -\mathbf{c}\theta_i\,\mathbf{s}\alpha_i & a_i\,\mathbf{s}\theta_i \\ 0 & \mathbf{s}\alpha_i & \mathbf{c}\alpha_i & d_i \\ 0 & 0 & 0 & 1 \end{bmatrix}$$

$$\mathbf{A}_1^0 = \begin{bmatrix} \mathbf{c}\theta_1 & -\mathbf{s}\theta_1 \cancelto{0}{\mathbf{c}\pi/2} & \mathbf{s}\theta_1 \cancelto{1}{\mathbf{s}\pi/2} & z_{_G}\,\mathbf{c}\theta_1 \\ \mathbf{s}\theta_1 & \mathbf{c}\theta_1 \cancelto{0}{\mathbf{c}\pi/2} & -\mathbf{c}\theta_1 \cancelto{1}{\mathbf{s}\pi/2} & z_{_G}\,\mathbf{s}\theta_1 \\ 0 & \cancelto{1}{\mathbf{s}\pi/2} & \cancelto{0}{\mathbf{c}\pi/2} & x_{_G} \\ 0 & 0 & 0 & 1 \end{bmatrix}$$
$$= \begin{bmatrix} \mathbf{c}\theta_1 & 0 & \mathbf{s}\theta_1 & z_{_G}\,\mathbf{c}\theta_1 \\ \mathbf{s}\theta_1 & 0 & -\mathbf{c}\theta_1 & z_{_G}\,\mathbf{s}\theta_1 \\ 0 & 1 & 0 & x_{_G} \\ 0 & 0 & 0 & 1 \end{bmatrix} \tag{4.29}$$

$$\mathbf{A}_2^1 = \begin{bmatrix} \mathbf{c}\theta_2 & -\mathbf{s}\theta_2 \cancelto{1}{\mathbf{c}\,(0)} & \mathbf{s}\theta_2 \cancelto{0}{\mathbf{s}\,(0)} & \cancelto{0}{a_2}\mathbf{c}\theta_2 \\ \mathbf{s}\theta_2 & \mathbf{c}\theta_2 \cancelto{1}{\mathbf{c}\,(0)} & -\mathbf{c}\theta_2 \cancelto{0}{\mathbf{s}\,(0)} & \cancelto{0}{a_2}\mathbf{s}\theta_2 \\ 0 & \cancelto{0}{\mathbf{s}\,(0)} & \cancelto{1}{\mathbf{c}\,(0)} & y_{_G} \\ 0 & 0 & 0 & 1 \end{bmatrix}$$
$$= \begin{bmatrix} \mathbf{c}\theta_2 & -\mathbf{s}\theta_2 & 0 & 0 \\ \mathbf{s}\theta_2 & \mathbf{c}\theta_2 & 0 & 0 \\ 0 & 0 & 1 & y_{_G} \\ 0 & 0 & 0 & 1 \end{bmatrix} \tag{4.30}$$

The final homogeneous transformation matrix ($\mathbf{T}_2^0$) was obtained by multiplying $\mathbf{A}_1^0$ and $\mathbf{A}_2^1$. Note that these are the generic notation used for the DH convention, and are different within this section than for previous or subsequent sections.

$$\mathbf{T}_2^0 = \mathbf{A}_1^0\mathbf{A}_2^1$$
$$= \begin{bmatrix} \mathbf{c}\theta_1 & 0 & \mathbf{s}\theta_1 & z_{_G}\,\mathbf{c}\theta_1 \\ \mathbf{s}\theta_1 & 0 & -\mathbf{c}\theta_1 & z_{_G}\,\mathbf{s}\theta_1 \\ 0 & 1 & 0 & x_{_G} \\ 0 & 0 & 0 & 1 \end{bmatrix} \begin{bmatrix} \mathbf{c}\theta_2 & -\mathbf{s}\theta_2 & 0 & 0 \\ \mathbf{s}\theta_2 & \mathbf{c}\theta_2 & 0 & 0 \\ 0 & 0 & 1 & y_{_G} \\ 0 & 0 & 0 & 1 \end{bmatrix}$$
$$= \begin{bmatrix} \mathbf{c}\theta_1\,\mathbf{c}\theta_2 & -\mathbf{c}\theta_1\,\mathbf{s}\theta_2 & \mathbf{s}\theta_1 & z_{_G}\,\mathbf{c}\theta_1 + y_{_G}\,\mathbf{s}\theta_1 \\ \mathbf{s}\theta_1\,\mathbf{c}\theta_2 & -\mathbf{s}\theta_1\,\mathbf{s}\theta_2 & -\mathbf{c}\theta_1 & z_{_G}\,\mathbf{s}\theta_1 - y_{_G}\,\mathbf{c}\theta_1 \\ \mathbf{s}\theta_2 & \mathbf{c}\theta_2 & 0 & x_{_G} \\ 0 & 0 & 0 & 1 \end{bmatrix} \tag{4.31}$$

Using the above matrices, the Jacobian matrix ($\mathbf{J}$) was calculated. For the 2 DOF representation, with two revolute joints:

$$\mathbf{J}_2 = \begin{bmatrix} J_{v_2} \\ J_{\omega_2} \end{bmatrix} \tag{4.32}$$

$$= \begin{bmatrix} z_0 \times (O_2 - O_0) & z_1 \times (O_2 - O_1) \\ z_0 & z_1 \end{bmatrix}, \tag{4.33}$$

where the first and second columns in the Jacobian are calculated as:

$$\text{column 1} = \begin{bmatrix} \begin{bmatrix} 0 \\ 0 \\ 1 \end{bmatrix} \times \left(\begin{bmatrix} z_{_G}\, \mathbf{c}\theta_1 + y_{_G}\, \mathbf{s}\theta_1 \\ z_{_G}\, \mathbf{s}\theta_1 - y_{_G}\, \mathbf{c}\theta_1 \\ x_{_G} \end{bmatrix} - \begin{bmatrix} 0 \\ 0 \\ 0 \end{bmatrix} \right) \\ 0 \\ 0 \\ 1 \end{bmatrix}, \text{ and} \tag{4.34}$$

$$\text{column 2} = \begin{bmatrix} \begin{bmatrix} \mathbf{s}\theta_1 \\ -\,\mathbf{c}\theta_1 \\ 0 \end{bmatrix} \times \left(\begin{bmatrix} z_{_G}\, \mathbf{c}\theta_1 + y_{_G}\, \mathbf{s}\theta_1 \\ z_{_G}\, \mathbf{s}\theta_1 - y_{_G}\, \mathbf{c}\theta_1 \\ x_{_G} \end{bmatrix} - \begin{bmatrix} z_{_G}\, \mathbf{c}\theta_1 \\ z_{_G}\, \mathbf{s}\theta_1 \\ -x_{_G} \end{bmatrix} \right) \\ \mathbf{s}\theta_1 \\ -\,\mathbf{c}\theta_1 \\ 0 \end{bmatrix} \tag{4.35}$$

Resulting in the following matrix for the Jacobian:

$$\mathbf{J}_2 = \begin{bmatrix} -z_{_G}\, \mathbf{s}\theta_1 + y_{_G}\, \mathbf{c}\theta_1 & 0 \\ z_{_G}\, \mathbf{c}\theta_1 + y_{_G}\, \mathbf{s}\theta_1 & 0 \\ 0 & 0 \\ 0 & \mathbf{s}\theta_1 \\ 0 & -\,\mathbf{c}\theta_1 \\ 1 & 0 \end{bmatrix} \tag{4.36}$$

To calculate the velocities of the body (ξ_k), the Jacobian (J_k) was multiplied by the velocity vector $\dot{\vec{q}}_{jm}$.

$$\xi_2 = \mathbf{J}_2 \dot{q_{12}} \tag{4.37}$$

$$= \begin{bmatrix} -z_{_G}\,\mathbf{s}\theta_1 + y_{_G}\,\mathbf{c}\theta_1 & 0 \\ z_{_G}\,\mathbf{c}\theta_1 + y_{_G}\,\mathbf{s}\theta_1 & 0 \\ 0 & 0 \\ 0 & \mathbf{s}\theta_1 \\ 0 & -\,\mathbf{c}\theta_1 \\ 1 & 0 \end{bmatrix} \begin{bmatrix} \dot{\theta_1} \\ \dot{\theta_2} \end{bmatrix}$$

$$= \begin{bmatrix} \left(-z_{_G}\,\mathbf{s}\theta_1 + y_{_G}\,\mathbf{c}\theta_1\right)\dot{\theta_1} \\ \left(z_{_G}\,\mathbf{c}\theta_1 + y_{_G}\,\mathbf{s}\theta_1\right)\dot{\theta_1} \\ 0 \\ -\,\mathbf{s}\theta_1\dot{\theta_2} \\ \mathbf{c}\theta_1\dot{\theta_2} \\ \dot{\theta_1} \end{bmatrix} \tag{4.38}$$

Where m is the m^{th} representation for the j^{th} gyroscope.

For this use, the linear velocities are needed with respect to the world frame, and the angular velocities are needed with respect to the body frame. To convert the velocities from the robotic manipulator representation frames to the general frames used, a simple rotation matrix (see Equation 4.19) was applied to the linear velocity $\vec{v}_2$. The generic θ_1 and θ_2 were replaced with the head angle, ϕ, and the cage angle, α. Both of these θ angles map directly to the system frame angles.

$$\vec{v}_G^{\,N} = \mathbf{R}_0^N \vec{v}_2$$

$$= \begin{bmatrix} 0 & 0 & 1 \\ 0 & -1 & 0 \\ 1 & 0 & 0 \end{bmatrix} \begin{bmatrix} \left(-z_{_G}\,\mathbf{s}\phi + y_{_G}\,\mathbf{c}\phi\right)\dot{\phi} \\ \left(z_{_G}\,\mathbf{c}\phi + y_{_G}\,\mathbf{s}\phi\right)\dot{\phi} \\ 0 \end{bmatrix}$$

$$\vec{v}_G^{\,N} = \begin{bmatrix} 0 \\ -\left(z_{_G}\,\mathbf{c}\phi + y_{_G}\,\mathbf{s}\phi\right)\ \dot{\phi} \\ \left(-z_{_G}\,\mathbf{s}\phi + y_{_G}\,\mathbf{c}\phi\right)\ \dot{\phi} \end{bmatrix} \tag{4.39}$$

To calculate the angular velocity with respect to the body frame, the velocity transform matrix $\boldsymbol{\mathcal{F}}$ was applied, where $\mathbf{R}_2^0$ and $\vec{d}_2^0$ come from the matrix $\mathbf{T}_2^0$

(Equation 4.31), and replacing θ_1 and θ_2 with ϕ and α, as with the linear velocities:

$$\xi_2^2 = \boldsymbol{\mathcal{F}}_0^2 \cdot \xi_2^0 \tag{4.40}$$

$$= \begin{bmatrix} \mathbf{R}_2^{0T} & -\mathbf{R}_2^{0T} \cdot \mathcal{S}(\vec{d}_2^0) \\ \mathbf{0}_{3\times 3} & \mathbf{R}_2^{0T} \end{bmatrix} \begin{bmatrix} -\left(z_G\, \mathbf{s}\phi + y_G\, \mathbf{c}\phi\right)\dot{\phi} \\ \left(z_G\, \mathbf{c}\phi - y_G\, \mathbf{s}\phi\right)\dot{\phi} \\ 0 \\ -\,\mathbf{s}\phi\dot{\alpha} \\ \mathbf{c}\phi\dot{\alpha} \\ \dot{\phi} \end{bmatrix}$$

$$= \begin{bmatrix} v_{2_x}^2 \\ v_{2_y}^2 \\ v_{2_z}^2 \\ \dot{\phi}\,\mathbf{s}\alpha \\ \dot{\phi}\,\mathbf{c}\alpha \\ \dot{\alpha} \end{bmatrix} \tag{4.41}$$

Therefore:

$$\vec{\omega}_2^2 = \begin{bmatrix} \dot{\phi}\,\mathbf{s}\alpha \\ \dot{\phi}\,\mathbf{c}\alpha \\ \dot{\alpha} \end{bmatrix} \tag{4.42}$$

A rotation matrix $\mathbf{R}_2^G$ was created to transform the body angular velocities into the system frame for the body under consideration, as shown in Figure 4.8:

Figure 4.8: Frame rotations from the Robotic Manipulator 2 DOF End-Effector Frame (2) to the Gimbal/cage frame.

$$\mathbf{R}_2^G = \mathrm{Rot}_{y,-\pi/2} \cdot \mathrm{Rot}_{x,-\pi/2} \tag{4.43}$$

$$= \begin{bmatrix} \mathbf{c}_{-\pi/2} & 0 & \mathbf{s}_{-\pi/2} \\ 0 & 1 & 0 \\ -\mathbf{s}_{-\pi/2} & 0 & \mathbf{c}_{-\pi/2} \end{bmatrix} \cdot \begin{bmatrix} 1 & 0 & 0 \\ 0 & \mathbf{c}_{-\pi/2} & -\mathbf{s}_{-\pi/2} \\ 0 & \mathbf{s}_{-\pi/2} & \mathbf{c}_{-\pi/2} \end{bmatrix}$$

$$= \begin{bmatrix} 0 & 0 & -1 \\ 0 & 1 & 0 \\ 1 & 0 & 0 \end{bmatrix} \cdot \begin{bmatrix} 1 & 0 & 0 \\ 0 & 0 & 1 \\ 0 & -1 & 0 \end{bmatrix}$$

$$= \begin{bmatrix} 0 & 1 & 0 \\ 0 & 0 & 1 \\ 1 & 0 & 0 \end{bmatrix} \tag{4.44}$$

The Rotation matrix was applied, noting that the body under consideration is the gimbal, G:

$$\vec{\omega}_G^G = \mathbf{R}_2^G \omega_2^2 \tag{4.45}$$

$$= \begin{bmatrix} 0 & 1 & 0 \\ 0 & 0 & 1 \\ 1 & 0 & 0 \end{bmatrix} \begin{bmatrix} \dot{\phi}\,\mathbf{s}\alpha \\ \dot{\phi}\,\mathbf{c}\alpha \\ \dot{\alpha} \end{bmatrix}$$

$$\vec{\omega}_G^G = \begin{bmatrix} \dot{\phi}\,\mathbf{c}\alpha \\ \dot{\alpha} \\ \dot{\phi}\,\mathbf{s}\alpha \end{bmatrix} \tag{4.46}$$

Which aligns with the results calculated by inspection.

4.2.1.3 Velocity of the COM of the Wheel

This process was repeated for the three joint representation shown in Figure 4.5c, to calculate the angular and linear velocities of the gyroscope wheel. This representation assumed the COM of the wheel was co-located with the COM of the cage. First, the DH parameters table (Table 4.4) was created and substituted into the three Homogeneous Transformation Matrices ($\mathbf{A}_i^{i-1}$) (one per joint):

	a	d	α	θ
1	$z_{_G}$	$x_{_G}$	$\pi/2$	θ_1^*
2	0	$y_{_G}$	$\pi/2$	$\theta_2^{*\dagger}$
3	0	0	0	θ_3^*

Table 4.4: DH Table for the 3 DOF representation.

$$\mathbf{A}_i^{i-1} = \begin{bmatrix} \mathbf{c}\theta_i & -\mathbf{s}\theta_i\,\mathbf{c}\alpha_i & \mathbf{s}\theta_i\,\mathbf{s}\alpha_i & a_i\,\mathbf{c}\theta_i \\ \mathbf{s}\theta_i & \mathbf{c}\theta_i\,\mathbf{c}\alpha_i & -\mathbf{c}\theta_i\,\mathbf{s}\alpha_i & a_i\,\mathbf{s}\theta_i \\ 0 & \mathbf{s}\alpha_i & \mathbf{c}\alpha_i & d_i \\ 0 & 0 & 0 & 1 \end{bmatrix}$$

$$\mathbf{A}_1^0 = \begin{bmatrix} \mathbf{c}\theta_1 & -\mathbf{s}\theta_1\,\cancelto{0}{\mathbf{c}\pi/2} & \mathbf{s}\theta_1\,\cancelto{1}{\mathbf{s}\pi/2} & z_{_G}\,\mathbf{c}\theta_1 \\ \mathbf{s}\theta_1 & \mathbf{c}\theta_1\,\cancelto{0}{\mathbf{c}\pi/2} & -\mathbf{c}\theta_1\,\cancelto{1}{\mathbf{s}\pi/2} & z_{_G}\,\mathbf{s}\theta_1 \\ 0 & \cancelto{1}{\mathbf{s}\pi/2} & \cancelto{0}{\mathbf{c}\pi/2} & x_{_G} \\ 0 & 0 & 0 & 1 \end{bmatrix}$$

$$= \begin{bmatrix} \mathbf{c}\theta_1 & 0 & \mathbf{s}\theta_1 & z_{_G}\,\mathbf{c}\theta_1 \\ \mathbf{s}\theta_1 & 0 & -\mathbf{c}\theta_1 & z_{_G}\,\mathbf{s}\theta_1 \\ 0 & 1 & 0 & x_{_G} \\ 0 & 0 & 0 & 1 \end{bmatrix} \tag{4.47}$$

$$\mathbf{A}_2^1 = \begin{bmatrix} \mathbf{c}\theta_2 & -\mathbf{s}\theta_2\,\cancelto{0}{\mathbf{c}\pi/2} & \mathbf{s}\theta_2\,\cancelto{1}{\mathbf{s}\pi/2} & \cancelto{0}{a_2}\,\mathbf{c}\theta_2 \\ \mathbf{s}\theta_2 & \mathbf{c}\theta_2\,\cancelto{0}{\mathbf{c}\pi/2} & -\mathbf{c}\theta_2\,\cancelto{1}{\mathbf{s}\pi/2} & \cancelto{0}{a_2}\,\mathbf{s}\theta_2 \\ 0 & \cancelto{1}{\mathbf{s}\pi/2} & \cancelto{0}{\mathbf{c}\pi/2} & y_{_G} \\ 0 & 0 & 0 & 1 \end{bmatrix}$$

$$= \begin{bmatrix} \mathbf{c}\theta_2 & 0 & \mathbf{s}\theta_2 & 0 \\ \mathbf{s}\theta_2 & 0 & -\mathbf{c}\theta_2 & 0 \\ 0 & 1 & 0 & y_{_G} \\ 0 & 0 & 0 & 1 \end{bmatrix} \tag{4.48}$$

[†]Due to DH orientation constraints, $\theta_2 = \alpha + \pi/2$, where α is the cage angle in the system frame.

$$\mathbf{A}_3^2 = \begin{bmatrix} \mathbf{c}\theta_3 & -\mathbf{s}\theta_3 \cancel{\mathbf{c}(0)}^{1} & \mathbf{s}\theta_3 \cancel{\mathbf{s}(0)}^{0} & \cancel{a_3}^{0}\mathbf{c}\theta_3 \\ \mathbf{s}\theta_3 & \mathbf{c}\theta_3 \cancel{\mathbf{c}(0)}^{1} & -\mathbf{c}\theta_3 \cancel{\mathbf{s}(0)}^{0} & \cancel{a_3}^{0}\mathbf{s}\theta_3 \\ 0 & \cancel{\mathbf{s}(0)}^{0} & \cancel{\mathbf{c}(0)}^{1} & \cancel{d_3}^{0} \\ 0 & 0 & 0 & 1 \end{bmatrix}$$
$$= \begin{bmatrix} \mathbf{c}\theta_3 & -\mathbf{s}\theta_3 & 0 & 0 \\ \mathbf{s}\theta_3 & \mathbf{c}\theta_3 & 0 & 0 \\ 0 & 0 & 1 & 0 \\ 0 & 0 & 0 & 1 \end{bmatrix} \tag{4.49}$$

In order to obtain the final homogeneous transformation matrix ($\mathbf{T}_3^0$) the above $\mathbf{A}$ matrices were multiplied together: $\mathbf{A}_1^0\mathbf{A}_2^1\mathbf{A}_3^2$. An intermediate homogeneous transformation matrix was required ($\mathbf{T}_2^0$) to locate the second z axis and origin for the Jacobian ($\mathbf{J}$), and was calculated at this stage as well.

$$\begin{aligned} \mathbf{T}_2^0 &= \mathbf{A}_1^0\mathbf{A}_2^1 \\ &= \begin{bmatrix} \mathbf{c}\theta_1 & 0 & \mathbf{s}\theta_1 & z_{_G}\,\mathbf{c}\theta_1 \\ \mathbf{s}\theta_1 & 0 & -\mathbf{c}\theta_1 & z_{_G}\,\mathbf{s}\theta_1 \\ 0 & 1 & 0 & -x_{_G} \\ 0 & 0 & 0 & 1 \end{bmatrix} \begin{bmatrix} \mathbf{c}\theta_2 & 0 & \mathbf{s}\theta_2 & 0 \\ \mathbf{s}\theta_2 & 0 & -\mathbf{c}\theta_2 & 0 \\ 0 & 1 & 0 & y_{_G} \\ 0 & 0 & 0 & 1 \end{bmatrix} \\ &= \begin{bmatrix} \mathbf{c}\theta_1\,\mathbf{c}\theta_2 & \mathbf{s}\theta_1 & \mathbf{c}\theta_1\,\mathbf{s}\theta_2 & z_{_G}\,\mathbf{c}\theta_1 + y_{_G}\,\mathbf{s}\theta_1 \\ \mathbf{s}\theta_1\,\mathbf{c}\theta_2 & -\mathbf{c}\theta_1 & \mathbf{s}\theta_1\,\mathbf{s}\theta_2 & z_{_G}\,\mathbf{s}\theta_1 - y_{_G}\,\mathbf{c}\theta_1 \\ \mathbf{s}\theta_2 & 0 & -\mathbf{c}\theta_2 & -x_{_G} \\ 0 & 0 & 0 & 1 \end{bmatrix} \end{aligned} \tag{4.50}$$

$$\begin{aligned} \mathbf{T}_3^0 &= \mathbf{T}_2^0\mathbf{A}_3^2 \\ &= \begin{bmatrix} \mathbf{c}\theta_1\,\mathbf{c}\theta_2 & \mathbf{s}\theta_1 & \mathbf{c}\theta_1\,\mathbf{s}\theta_2 & z_{_G}\,\mathbf{c}\theta_1 + y_{_G}\,\mathbf{s}\theta_1 \\ \mathbf{s}\theta_1\,\mathbf{c}\theta_2 & -\mathbf{c}\theta_1 & \mathbf{s}\theta_1\,\mathbf{s}\theta_2 & z_{_G}\,\mathbf{s}\theta_1 - y_{_G}\,\mathbf{c}\theta_1 \\ \mathbf{s}\theta_2 & 0 & -\mathbf{c}\theta_2 & x_{_G} \\ 0 & 0 & 0 & 1 \end{bmatrix} \begin{bmatrix} \mathbf{c}\theta_3 & -\mathbf{s}\theta_3 & 0 & 0 \\ \mathbf{s}\theta_3 & \mathbf{c}\theta_3 & 0 & 0 \\ 0 & 0 & 1 & 0 \\ 0 & 0 & 0 & 1 \end{bmatrix} \end{aligned}$$

$$= \begin{bmatrix} \mathbf{s}\theta_1\,\mathbf{s}\theta_3 + \mathbf{c}\theta_1\,\mathbf{c}\theta_2\,\mathbf{c}\theta_3 & \mathbf{s}\theta_1\,\mathbf{c}\theta_3 - \mathbf{c}\theta_1\,\mathbf{c}\theta_2\,\mathbf{s}\theta_3 & \mathbf{c}\theta_1\,\mathbf{s}\theta_2 & z_{_G}\,\mathbf{c}\theta_1 + y_{_G}\,\mathbf{s}\theta_1 \\ \mathbf{s}\theta_1\,\mathbf{c}\theta_2\,\mathbf{c}\theta_3 - \mathbf{c}\theta_1\,\mathbf{s}\theta_3 & -\mathbf{c}\theta_1\,\mathbf{c}\theta_3 - \mathbf{s}\theta_1\,\mathbf{c}\theta_2\,\mathbf{s}\theta_3 & \mathbf{s}\theta_1\,\mathbf{s}\theta_2 & z_{_G}\,\mathbf{s}\theta_1 - y_{_G}\,\mathbf{c}\theta_1 \\ \mathbf{s}\theta_2\,\mathbf{c}\theta_3 & -\mathbf{s}\theta_2\,\mathbf{s}\theta_3 & -\mathbf{c}\theta_2 & x_{_G} \\ 0 & 0 & 0 & 1 \end{bmatrix} \tag{4.51}$$

Using the above matrices, the Jacobian matrix ($\mathbf{J}$) was calculated. For the 3 DOF representation, with three revolute joints:

$$\mathbf{J}_3 = \begin{bmatrix} J_{v_3} \\ J_{\omega_3} \end{bmatrix} \tag{4.52}$$

$$= \begin{bmatrix} z_0 \times (O_3 - O_0) & z_1 \times (O_3 - O_1) & z_2 \times (O_3 - O_2) \\ z_0 & z_1 & z_2 \end{bmatrix}$$

$$\mathbf{J}_3 = \begin{bmatrix} -z_{_G}\,\mathbf{s}\theta_1 + y_{_G}\,\mathbf{c}\theta_1 & 0 & 0 \\ z_{_G}\,\mathbf{c}\theta_1 + y_{_G}\,\mathbf{s}\theta_1 & 0 & 0 \\ 0 & 0 & 0 \\ 0 & \mathbf{s}\theta_1 & \mathbf{c}\theta_1\,\mathbf{s}\theta_2 \\ 0 & -\mathbf{c}\theta_1 & \mathbf{s}\theta_1\,\mathbf{s}\theta_2 \\ 1 & 0 & -\mathbf{c}\theta_2 \end{bmatrix} \tag{4.53}$$

Where:

$$O_0 = \begin{bmatrix} 0 \\ 0 \\ 0 \end{bmatrix} \qquad z_0 = \begin{bmatrix} 0 \\ 0 \\ 1 \end{bmatrix}$$

$$O_1 = \begin{bmatrix} z_{_G}\,\mathbf{c}\theta_1 \\ z_{_G}\,\mathbf{s}\theta_1 \\ x_{_G} \end{bmatrix} \qquad z_1 = \begin{bmatrix} \mathbf{s}\theta_1 \\ -\mathbf{c}\theta_1 \\ 0 \end{bmatrix}$$

$$O_2 = \begin{bmatrix} z_{_G}\,\mathbf{c}\theta_1 + y_{_G}\,\mathbf{s}\theta_1 \\ z_{_G}\,\mathbf{s}\theta_1 - y_{_G}\,\mathbf{c}\theta_1 \\ x_{_G} \end{bmatrix} \qquad z_2 = \begin{bmatrix} \mathbf{c}\theta_1\,\mathbf{s}\theta_2 \\ \mathbf{s}\theta_1\,\mathbf{s}\theta_2 \\ -\mathbf{c}\theta_2 \end{bmatrix}$$

$$O_3 = \begin{bmatrix} z_{_G}\,\mathbf{c}\theta_1 + y_{_G}\,\mathbf{s}\theta_1 \\ z_{_G}\,\mathbf{s}\theta_1 - y_{_G}\,\mathbf{c}\theta_1 \\ x_{_G} \end{bmatrix} \tag{4.54}$$

To calculate the velocities of the body (ξ_k), the Jacobian ($\mathbf{J}_k$) was multiplied by the velocity vector $\vec{\dot{q}}_{jm}$.

$$\begin{aligned}\xi_3 &= \mathbf{J}_3 \dot{q_{13}} \qquad (4.55)\\ &= \begin{bmatrix} -z_{_G}\,\mathbf{s}\theta_1 + y_{_G}\,\mathbf{c}\theta_1 & 0 & 0 \\ z_{_G}\,\mathbf{c}\theta_1 + y_{_G}\,\mathbf{s}\theta_1 & 0 & 0 \\ 0 & 0 & 0 \\ 0 & \mathbf{s}\theta_1 & \mathbf{c}\theta_1\,\mathbf{s}\theta_2 \\ 0 & -\,\mathbf{c}\theta_1 & \mathbf{s}\theta_1\,\mathbf{s}\theta_2 \\ 1 & 0 & -\,\mathbf{c}\theta_2 \end{bmatrix} \begin{bmatrix} \dot{\theta}_1 \\ \dot{\theta}_2 \\ \dot{\theta}_3 \end{bmatrix} \\ &= \begin{bmatrix} (-z_{_G}\,\mathbf{s}\theta_1 + y_{_G}\,\mathbf{c}\theta_1)\,\dot{\theta}_1 \\ (z_{_G}\,\mathbf{c}\theta_1 + y_{_G}\,\mathbf{s}\theta_1)\,\dot{\theta}_1 \\ 0 \\ \mathbf{s}\theta_1\dot{\theta}_2 + \mathbf{c}\theta_1\,\mathbf{s}\theta_2\dot{\theta}_3 \\ -\,\mathbf{c}\theta_1\dot{\theta}_2 + \mathbf{s}\theta_1\,\mathbf{s}\theta_2\dot{\theta}_3 \\ \dot{\theta}_1 - \mathbf{c}\theta_2\dot{\theta}_3 \end{bmatrix} \qquad (4.56)\end{aligned}$$

where m is the m^{th} representation for the j^{th} gyroscope.

To convert the velocities from the robotic manipulator representation frames to the system frames used, a simple rotation matrix (see Equation 4.19) was applied to the linear velocity $\vec{v_2}$. The generic angles θ_1 and θ_3 were replaced with the head angle, ϕ, and the wheel rotation angle (γ from the angular velocity of the wheel, $\dot{\gamma}$). These two angles map directly to the system frame angles. At this point, the equation for mapping the cage angle from the representation to the system frame ($\theta_2 = \alpha + \pi/2$), was included.

$$\begin{aligned}\vec{v}_W^N &= \mathbf{R}_0^N v_3 \\ &= \begin{bmatrix} 0 & 0 & 1 \\ 0 & -1 & 0 \\ 1 & 0 & 0 \end{bmatrix} \begin{bmatrix} (-z_{_G}\,\mathbf{s}\phi + y_{_G}\,\mathbf{c}\phi)\,\dot{\phi} \\ (z_{_G}\,\mathbf{c}\phi + y_{_G}\,\mathbf{s}\phi)\,\dot{\phi} \\ 0 \end{bmatrix} \\ \vec{v}_W^N &= \begin{bmatrix} 0 \\ -\,(z_{_G}\,\mathbf{c}\phi + y_{_G}\,\mathbf{s}\phi)\;\dot{\phi} \\ (-z_{_G}\,\mathbf{s}\phi + y_{_G}\,\mathbf{c}\phi)\;\dot{\phi} \end{bmatrix} \qquad (4.57)\end{aligned}$$

To calculate the angular velocity with respect to the body frame, the velocity transform matrix $\boldsymbol{\mathcal{F}}$ was applied, where $\mathbf{R}_3^0$ and $\vec{d}_3^0$ come from the matrix $\mathbf{T}_3^0$ (Equation 4.51).

$$\xi_3^3 = \boldsymbol{\mathcal{F}}_0^3 \cdot \xi_3^0 \tag{4.58}$$

$$= \begin{bmatrix} \mathbf{R}_3^{0T} & -\mathbf{R}_3^{0T} \cdot \mathcal{S}\left(\vec{d}_3^0\right) \\ 0_{3\times 3} & \mathbf{R}_3^{0T} \end{bmatrix} \cdot \begin{bmatrix} \left(-z_{_G}\,\mathbf{s}\theta_1 + y_{_G}\,\mathbf{c}\theta_1\right)\dot{\theta}_1 \\ \left(z_{_G}\,\mathbf{c}\theta_1 + y_{_G}\,\mathbf{s}\theta_1\right)\dot{\theta}_1 \\ 0 \\ \mathbf{s}\theta_1\dot{\theta}_2 + \mathbf{c}\theta_1\,\mathbf{s}\theta_2\dot{\theta}_3 \\ -\mathbf{c}\theta_1\dot{\theta}_2 + \mathbf{s}\theta_1\,\mathbf{s}\theta_2\dot{\theta}_3 \\ \dot{\theta}_1 - \mathbf{c}\theta_2\dot{\theta}_3 \end{bmatrix}$$

$$= \begin{bmatrix} v_{3_x} \\ v_{3_y} \\ v_{3_z} \\ \mathbf{s}\theta_2\,\mathbf{c}\theta_3\dot{\theta}_1 + \mathbf{s}\theta_3\dot{\theta}_2 \\ -\mathbf{s}\theta_2\,\mathbf{s}\theta_3\dot{\theta}_1 + \mathbf{c}\theta_3\dot{\theta}_2 \\ -\mathbf{c}\theta_2\dot{\theta}_1 + \dot{\theta}_3 \end{bmatrix} \tag{4.59}$$

Due to the design of the wheel (specifically, the symmetry in cross section), the application of these velocities is agnostic to the angle of the wheel, θ_3. Because of this, the value of θ_3 was set to 0 instead of the wheel angle γ. The head angle, ϕ, and the cage angle, $(\alpha + \pi/2)$, were substituted in for θ_1 and θ_2, respectively. Therefore, the rotational velocity of the wheel was:

$$\omega_3^3 = \begin{bmatrix} \dot{\phi}\,\mathbf{c}\alpha \\ \dot{\alpha} \\ \dot{\phi}\,\mathbf{s}\alpha + \dot{\gamma} \end{bmatrix} \tag{4.60}$$

As the System Frame W and Frame 3 have the same orientation, no rotational transformation was needed to transform the angular velocities into the system Frame. The body under consideration is the wheel, and the Frame W was set up such that it aligned with the Gimbal Frame G, as shown in Figure 4.9:

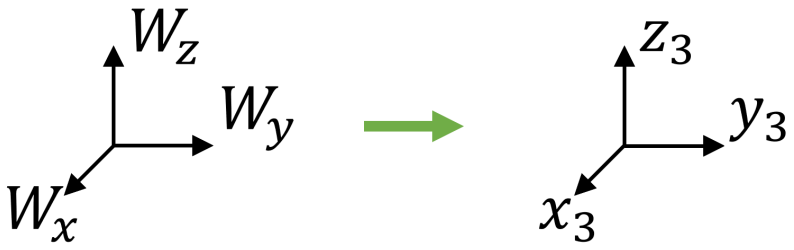

Figure 4.9: Frame rotations from the Robotic Manipulator 2 DOF End-Effector Frame (3) to the Wheel Frame.

$$\omega_W^G = \begin{bmatrix} \dot{\phi}\,\mathbf{c}\alpha \\ \dot{\alpha} \\ \dot{\phi}\,\mathbf{s}\alpha + \dot{\gamma} \end{bmatrix} \tag{4.61}$$

$$\omega_W^G = \omega_G^G + \dot{\gamma}\hat{\mathbf{g}}_z \tag{4.62}$$

which aligns with the value obtained by inspection.

4.2.1.4 Summary

Rotational velocities, as explained in 4.2, were developed by inspection, and validated using the more intensive calculations above. In summary, the relevant velocities of the bodies in this system are as follows:

$$
\begin{aligned}
\vec{\omega}_H^H &= \begin{bmatrix} \omega_1 \\ \omega_2 \\ \omega_3 \end{bmatrix} & \vec{v}_H^N &= \begin{bmatrix} v_1 \\ v_2 \\ v_3 \end{bmatrix} \\
&= \begin{bmatrix} \dot{\phi} \\ 0 \\ 0 \end{bmatrix} & &= \begin{bmatrix} 0 \\ -\left(z_{_H}\,\mathbf{c}\phi + y_{_H}\,\mathbf{s}\phi\right)\dot{\phi} \\ \left(-z_{_H}\,\mathbf{s}\phi + y_{_H}\,\mathbf{c}\phi\right)\dot{\phi} \end{bmatrix} \\
\vec{\omega}_G^G &= \begin{bmatrix} \omega_4 \\ \omega_5 \\ \omega_6 \end{bmatrix} & \vec{v}_G^N &= \begin{bmatrix} v_4 \\ v_5 \\ v_6 \end{bmatrix} \\
&= \begin{bmatrix} \dot{\phi}\,\mathbf{c}\alpha \\ \dot{\alpha} \\ \dot{\phi}\,\mathbf{s}\alpha \end{bmatrix} & &= \begin{bmatrix} 0 \\ -\left(z_{_G}\,\mathbf{c}\phi + y_{_G}\,\mathbf{s}\phi\right)\dot{\phi} \\ \left(-z_{_G}\,\mathbf{s}\phi + y_{_G}\,\mathbf{c}\phi\right)\dot{\phi} \end{bmatrix} \\
\vec{\omega}_W^W &= \vec{\omega}_G^G + \dot{\gamma}\hat{\mathbf{g}}_{\mathbf{z}} & \vec{v}_W^N &= \vec{v}_G^N \\
&= \begin{bmatrix} \omega_4 \\ \omega_5 \\ \omega_6 + \dot{\gamma} \end{bmatrix} & & \\
&= \begin{bmatrix} \dot{\phi}\,\mathbf{c}\alpha \\ \dot{\alpha} \\ \dot{\phi}\,\mathbf{s}\alpha + \dot{\gamma} \end{bmatrix} & &
\end{aligned}
\tag{4.63}
$$

4.2.2 Initial Euler–Lagrangian Calculations

To solve using Lagrangian mechanics, the kinetic and potential energies of the system must be calculated. The general form of the kinetic energy equation is as follows:

$$\mathcal{K} = \sum_{i=1}^{n} \left[\frac{1}{2} m_i v_i^2 + \frac{1}{2} I_i \omega_i^2\right] \tag{4.64}$$

The velocities from Equation 4.63 were substituted into the kinetic energy equation for each body in the system, where $v_i = \sqrt{v_{i_x}^2 + v_{i_y}^2 + v_{i_z}^2}$:

$$\mathcal{K}_H = \frac{1}{2} m_H \left(v_1^2 + v_2^2 + v_3^2\right) + \frac{1}{2}\left(I_{H_{xx}}\omega_1^2 + I_{H_{yy}}\omega_2^2 + I_{H_{zz}}\omega_3^2\right) \tag{4.65}$$

$$\mathcal{K}_G = \frac{1}{2} m_G \left(v_4^2 + v_5^2 + v_6^2\right) + \frac{1}{2}\left(I_{G_{xx}}\omega_4^2 + I_{G_{yy}}\omega_5^2 + I_{G_{zz}}\omega_6^2\right) \tag{4.66}$$

$$\mathcal{K}_W = \frac{1}{2} m_W \left(v_4^2 + v_5^2 + v_6^2\right) + \frac{1}{2}\left(I_{W_{xx}}\omega_4^2 + I_{W_{yy}}\omega_5^2 + I_{W_{zz}}\left(\omega_6 + \dot{\gamma}\hat{\mathbf{g}}_z\right)^2\right) \tag{4.67}$$

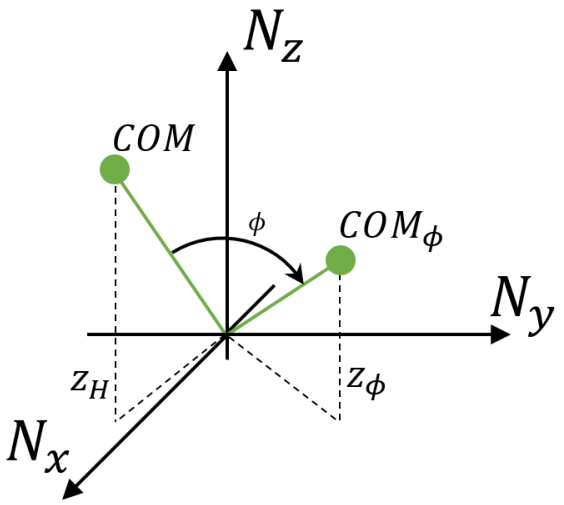

Figure 4.10: z displacement change of the COM with a rotation about x of ϕ.

The moment of inertia in the x and y directions of the gyroscope wheel are identical: $I_{W_{xx}} = I_{W_{yy}}$. This was substituted into equation 4.67:

$$\mathcal{K}_W = \frac{1}{2} m_W \left(v_4^2 + v_5^2 + v_6^2\right) + \frac{1}{2}\left(I_{W_{xx}}\left(\omega_4^2 + \omega_5^2\right) + I_{W_{zz}}\left(\omega_6 + \dot{\gamma}\right)^2\right) \tag{4.68}$$

The general form for Potential Energy (from gravity) is as follows:

$$\mathcal{P} = \sum_{i=1}^{n} m_i g h_i \tag{4.69}$$

The base of the system (the rotation point) was used as the zero level. The change in height of the COM, h, was obtained by using a rotation matrix of ϕ about x to calculate the $z_{H,\phi}$ height, as shown in Figure 4.10. $z_{H,\phi}$ represents the vertical distance of the centre of mass at rotation ϕ.

$$\mathbf{R} = \mathrm{Rot}_{x,\phi} \tag{4.70}$$

$$= \begin{bmatrix} 1 & 0 & 0 \\ 0 & \mathbf{c}\phi & -\mathbf{s}\phi \\ 0 & \mathbf{s}\phi & \mathbf{c}\phi \end{bmatrix} \tag{4.71}$$

$$\vec{d}_{H,\phi} = \mathrm{Rot}_{x,\phi}\vec{d}_H \tag{4.72}$$

$$
\begin{aligned}
&= \begin{bmatrix} 1 & 0 & 0 \\ 0 & \mathbf{c}\phi & -\mathbf{s}\phi \\ 0 & \mathbf{s}\phi & \mathbf{c}\phi \end{bmatrix} \begin{bmatrix} x_{_H} \\ y_{_H} \\ z_{_H} \end{bmatrix} \\
&= \begin{bmatrix} x_{_H} \\ \mathbf{c}\phi y_{_H} - \mathbf{s}\phi z_{_H} \\ \mathbf{c}\phi z_{_H} + \mathbf{s}\phi y_{_H} \end{bmatrix} \qquad (4.73)
\end{aligned}
$$

Therefore, h_i for the head COM is defined as follows:

$$
\begin{aligned}
h_{_H} &= z_{_{H,\phi}} && (4.74) \\
&= \mathbf{c}\phi z_{_H} + \mathbf{s}\phi y_{_H} && (4.75)
\end{aligned}
$$

The above derivation was repeated for h_i with $\vec{d}_{_G}$ and $\vec{d}_{_W}$. These h_i values were substituted into the general form for Potential Energy (Equation 4.69), for each body:

$$
\begin{aligned}
\mathcal{P}_H &= m_{_H} g \left[z_{_H}\, \mathbf{c}\phi + y_{_H}\, \mathbf{s}\phi \right] && (4.76) \\
\mathcal{P}_G &= m_{_G} g \left[z_{_G}\, \mathbf{c}\phi + y_{_G}\, \mathbf{s}\phi \right] && (4.77) \\
\mathcal{P}_W &= m_{_W} g \left[z_{_W}\, \mathbf{c}\phi + y_{_W}\, \mathbf{s}\phi \right] && (4.78)
\end{aligned}
$$

The $\mathcal{K}$ and $\mathcal{P}$ terms were summed to give the total energy in the system:

$$
\begin{aligned}
\mathcal{K}_{_{TOT}} &= \sum_{k=1}^{n} \mathcal{K}_k = \mathcal{K}_H + \mathcal{K}_G + \mathcal{K}_W && (4.79) \\
\mathcal{P}_{_{TOT}} &= \sum_{k=1}^{n} \mathcal{P}_k = \mathcal{P}_H + \mathcal{P}_G + \mathcal{P}_W && (4.80)
\end{aligned}
$$

The Euler–Lagrange equation was introduced at this stage, assuming no dissipation from friction or other sources ($\mathcal{R} = 0$), so that the Euler–Lagrange equation as described in Equation 4.4 became the following:

$$
\frac{\mathrm{d}}{\mathrm{d}t} \left(\frac{\partial \mathcal{L}}{\partial \dot{q}_i} \right) - \frac{\partial \mathcal{L}}{\partial q_i} = Q_i, \qquad (4.81)
$$

where $\mathcal{L}$ is the Lagrangian, $\mathcal{L} = \mathcal{K} - \mathcal{P}$, and q_i is the i^{th} item in the variable vector $\vec{q} = \begin{bmatrix} \phi & \alpha & \gamma \end{bmatrix}^T$, and Q_i is item i in the forces vector $\vec{Q} = \begin{bmatrix} \tau_H & \tau_G & \tau_W \end{bmatrix}^T$.

4.2.3 The Derivatives and Partial Derivatives of $\mathcal{L}$

The partial derivatives of $\mathcal{L}$ with respect to $\dot{q}_i$ and with respect to q_i were calculated. The sum rule in differentiation allowed the partial derivatives to be broken down into smaller, more manageable parts:

$$\begin{aligned}\frac{\partial \mathcal{L}}{\partial \dot{q}_i} &= \frac{\partial (\mathcal{K} - \mathcal{P})}{\partial \dot{q}_i} \\ &= \frac{\partial \mathcal{K}}{\partial \dot{q}_i} - \frac{\partial \mathcal{P}}{\partial \dot{q}_i}\end{aligned} \tag{4.82}$$

$$\begin{aligned}\frac{\partial \mathcal{L}}{\partial q_i} &= \frac{\partial (\mathcal{K} - \mathcal{P})}{\partial q_i} \\ &= \frac{\partial \mathcal{K}}{\partial q_i} - \frac{\partial \mathcal{P}}{\partial q_i}\end{aligned} \tag{4.83}$$

Equations 4.79 and 4.80 were substituted into 4.82 and 4.83, and using the sum rule in differentiation again, Equations 4.82 and 4.83 were split into three components:

$$\frac{\partial \mathcal{K}}{\partial \dot{q}_i} = \frac{\partial \mathcal{K}_H}{\partial \dot{q}_i} + \frac{\partial \mathcal{K}_G}{\partial \dot{q}_i} + \frac{\partial \mathcal{K}_W}{\partial \dot{q}_i} \tag{4.84}$$

$$\frac{\partial \mathcal{P}}{\partial \dot{q}_i} = \frac{\partial \mathcal{P}_H}{\partial \dot{q}_i} + \frac{\partial \mathcal{P}_G}{\partial \dot{q}_i} + \frac{\partial \mathcal{P}_W}{\partial \dot{q}_i} \tag{4.85}$$

$$\frac{\partial \mathcal{K}}{\partial q_i} = \frac{\partial \mathcal{K}_H}{\partial q_i} + \frac{\partial \mathcal{K}_G}{\partial q_i} + \frac{\partial \mathcal{K}_W}{\partial q_i} \tag{4.86}$$

$$\frac{\partial \mathcal{P}}{\partial q_i} = \frac{\partial \mathcal{P}_H}{\partial q_i} + \frac{\partial \mathcal{P}_G}{\partial q_i} + \frac{\partial \mathcal{P}_W}{\partial q_i} \tag{4.87}$$

In the following sections, these four partial derivatives (Equations 4.84–4.87) were evaluated at each q_i.

4.2.3.1 Kinetic Energy of the Head

The equation for $\mathcal{K}_H$ (Equation 4.65) and the values in Equation 4.63 for v_1, v_2, v_3, ω_1, ω_2, and ω_3 were substituted into the first partial derivative in Equation 4.84, and simplified:

$$\begin{aligned}\frac{\partial \mathcal{K}_H}{\partial \dot{q}_i} &= \frac{\partial}{\partial \dot{q}_i}\left[\frac{1}{2} m_{_H}\left(v_1^2 + v_2^2 + v_3^2\right) + \frac{1}{2}\left(I_{H_{xx}}\omega_1^2 + I_{H_{yy}}\omega_2^2 + I_{H_{zz}}\omega_3^2\right)\right] \\ &= \frac{\partial}{\partial \dot{q}_i}\left[\frac{1}{2} m_{_H}\left(\cancelto{0}{v_1^2} + \left[-\left(z_{_H}\,\mathbf{c}\phi + y_{_H}\,\mathbf{s}\phi\right)\dot{\phi}\right]^2 + \left[\left(-z_{_H}\,\mathbf{s}\phi + y_{_H}\,\mathbf{c}\phi\right)\dot{\phi}\right]^2\right)\right.\end{aligned} \tag{4.88}$$

$$
\begin{aligned}
&+\frac{1}{2}\left(I_{H_{xx}}\dot{\phi}^2+I_{H_{yy}}\cancelto{0}{\omega_2^2}+I_{H_{zz}}\cancelto{0}{\omega_3^2}\right)\Bigg]\\
&=\frac{\partial}{\partial\dot{q}_i}\left[\frac{1}{2}m_{_H}\left(\left(z_{_H}\,\mathbf{c}\phi+y_{_H}\,\mathbf{s}\phi\right)^2\dot{\phi}^2+\left(-z_{_H}\,\mathbf{s}\phi+y_{_H}\,\mathbf{c}\phi\right)^2\dot{\phi}^2\right)+\frac{1}{2}I_{H_{xx}}\dot{\phi}^2\right]\\
&=\frac{\partial}{\partial\dot{q}_i}\Bigg[\frac{1}{2}\big(m_{_H}\big[y_{_H}^2\,\mathbf{s}^2\phi+y_{_H}z_{_H}\,\mathbf{s}2\phi+z_{_H}^2\,\mathbf{c}^2\phi+y_{_H}^2\,\mathbf{c}^2\phi+y_{_H}z_{_H}\,\mathbf{s}2\phi\\
&\quad+z_{_H}^2\,\mathbf{s}^2\phi\big]+I_{H_{xx}}\big)\dot{\phi}^2\Bigg]\\
&=\frac{\partial}{\partial\dot{q}_i}\Bigg[\frac{1}{2}\Bigg(m_{_H}\Bigg[y_{_H}^2\cancelto{1}{\left(\mathbf{s}^2\phi+\mathbf{c}^2\phi\right)}+y_{_H}z_{_H}\,\mathbf{s}2\phi-y_{_H}z_{_H}\,\mathbf{s}2\phi\\
&\quad+z_{_H}^2\cancelto{1}{\left(\mathbf{c}^2\phi+\mathbf{s}^2\phi\right)}\Bigg]+I_{H_{xx}}\big)\dot{\phi}^2\Bigg]\\
&=\frac{\partial}{\partial\dot{q}_i}\left[\frac{1}{2}\left(m_{_H}\left(z_{_H}^2+y_{_H}^2\right)+I_{H_{xx}}\right)\dot{\phi}^2\right]
\end{aligned}
\tag{4.89}
$$

Equation 4.89 was evaluated at $\dot{\phi}$:

$$
\begin{aligned}
\frac{\partial\mathcal{K}_H}{\partial\dot{\phi}}&=\frac{1}{\cancel{2}}\cancelto{1}{\left[2\left(m_{_H}\left(z_{_H}^2+y_{_H}^2\right)+I_{H_{xx}}\right)\dot{\phi}\right]}\\
&=\left(m_{_H}\left(z_{_H}^2+y_{_H}^2\right)+I_{H_{xx}}\right)\dot{\phi}
\end{aligned}
\tag{4.90}
$$

And evaluated at $\dot{\alpha}$ and $\dot{\gamma}$:

$$
\begin{aligned}
\frac{\partial\mathcal{K}_H}{\partial\dot{\alpha}}&=\frac{\partial}{\partial\dot{\alpha}}\left[\frac{1}{2}\left(m_{_H}\left(z_{_H}^2+y_{_H}^2\right)+I_{H_{xx}}\right)\cancelto{0}{\dot{\phi}^2}\right]\\
&=0
\end{aligned}
\tag{4.91}
$$

$$
\begin{aligned}
\frac{\partial\mathcal{K}_H}{\partial\dot{\gamma}}&=\frac{\partial}{\partial\dot{\gamma}}\left[\frac{1}{2}\left(m_{_H}\left(z_{_H}^2+y_{_H}^2\right)+I_{H_{xx}}\right)\cancelto{0}{\dot{\phi}^2}\right]\\
&=0
\end{aligned}
\tag{4.92}
$$

Using the same method as above, $\frac{\partial \mathcal{K}_H}{\partial q}$ was evaluated at ϕ:

$$\begin{aligned}\frac{\partial \mathcal{K}_H}{\partial \phi} &= \frac{\partial}{\partial \phi}\left[\frac{1}{2}\left(m_{_H}\left(z_{_H}^2 + y_{_H}^2\right) + I_{H_{xx}}\right)\cancelto{0}{\dot{\phi}^2}\right] \\ &= 0 \end{aligned} \tag{4.93}$$

And evaluated at α and γ:

$$\begin{aligned}\frac{\partial \mathcal{K}_H}{\partial \alpha} &= \frac{\partial}{\partial \alpha}\left[\frac{1}{2}\left(m_{_H}\left(z_{_H}^2 + y_{_H}^2\right) + I_{H_{xx}}\right)\cancelto{0}{\dot{\phi}^2}\right] \\ &= 0 \end{aligned} \tag{4.94}$$

$$\begin{aligned}\frac{\partial \mathcal{K}_H}{\partial \gamma} &= \frac{\partial}{\partial \gamma}\left[\frac{1}{2}\left(m_{_H}\left(z_{_H}^2 + y_{_H}^2\right) + I_{H_{xx}}\right)\cancelto{0}{\dot{\phi}^2}\right] \\ &= 0 \end{aligned} \tag{4.95}$$

4.2.3.2 Kinetic Energy of the Gimbals

Similar to the process in Section 4.2.3.1, substitutions were made for the Equation $\mathcal{K}_G$ (Equation 4.66) and the values in Equation 4.63 for $v_4, v_5, v_6, \omega_4, \omega_5$, and ω_6. As the linear velocities differ only in the y and z distance values, the same algebra was performed:

$$\frac{\partial \mathcal{K}_G}{\partial \dot{q}_i} = \frac{\partial}{\partial \dot{q}_i}\left[\frac{1}{2} m_{_G}\left(v_4^2 + v_5^2 + v_6^2\right) + \frac{1}{2}\left(I_{G_{xx}}\omega_4^2 + I_{G_{yy}}\omega_5^2 + I_{G_{zz}}\omega_6^2\right)\right] \tag{4.96}$$

$$\begin{aligned} &= \frac{\partial}{\partial \dot{q}_i}\left[\frac{1}{2} m_{_G}\left(\cancelto{0}{y_4^2} + \left[-\left(z_{_G}\,\mathbf{c}\phi + y_{_G}\,\mathbf{s}\phi\right)\dot{\phi}\right]^2 + \left[\left(-z_{_G}\,\mathbf{s}\phi + y_{_G}\,\mathbf{c}\phi\right)\dot{\phi}\right]^2\right) + \right. \\ &\left. \frac{1}{2}\left(I_{G_{xx}}\left[\dot{\phi}\,\mathbf{c}\alpha\right]^2 + I_{G_{yy}}\dot{\alpha}^2 + I_{G_{zz}}\left[\dot{\phi}\,\mathbf{s}\alpha\right]^2\right)\right] \\ &= \frac{\partial}{\partial \dot{q}_i}\left[\frac{1}{2} m_{_G}\left(z_{_G}^2 + y_{_G}^2\right)\dot{\phi}^2 + \frac{1}{2}\left(\left[I_{G_{xx}}\,\mathbf{c}^2\alpha + I_{G_{zz}}\,\mathbf{s}^2\alpha\right]\dot{\phi}^2 + I_{G_{yy}}\dot{\alpha}^2\right)\right] \\ &= \frac{\partial}{\partial \dot{q}_i}\left[\frac{1}{2}\left(m_{_G}\left[z_{_G}^2 + y_{_G}^2\right]\dot{\phi}^2 + \left[I_{G_{xx}}\,\mathbf{c}^2\alpha + I_{G_{zz}}\,\mathbf{s}^2\alpha\right]\dot{\phi}^2 + I_{G_{yy}}\dot{\alpha}^2\right)\right] \end{aligned} \tag{4.97}$$

Equation 4.97 was evaluated at $\dot{\phi}$, $\dot{\alpha}$, and $\dot{\gamma}$:

$$\begin{aligned}\frac{\partial \mathcal{K}_G}{\partial \dot{\phi}} &= \frac{1}{2}\Big(2\left[\left(m_G\left[z_G^2+y_G^2\right]\right)\dot{\phi}+\left(I_{G_{xx}}\,\mathbf{c}^2\alpha+I_{G_{zz}}\,\mathbf{s}^2\alpha\right)\dot{\phi}\right]+I_{G_{yy}}\dot{\alpha}^2\Big)\\ &= m_G\left(z_G^2+y_G^2\right)\dot{\phi}+\left(I_{G_{xx}}\,\mathbf{c}^2\alpha+I_{G_{zz}}\,\mathbf{s}^2\alpha\right)\dot{\phi}\end{aligned} \tag{4.98}$$

$$\begin{aligned}\frac{\partial \mathcal{K}_G}{\partial \dot{\alpha}} &= \frac{1}{2}\left[2I_{G_{yy}}\dot{\alpha}+\left(m_G\left[z_G^2+y_G^2\right]\right)\dot{\phi}^2+\left(I_{G_{xx}}\,\mathbf{c}^2\alpha+I_{G_{zz}}\,\mathbf{s}^2\alpha\right)\dot{\phi}^2\right]\\ &= I_{G_{yy}}\dot{\alpha}\end{aligned} \tag{4.99}$$

$$\begin{aligned}\frac{\partial \mathcal{K}_G}{\partial \dot{\gamma}} &= \frac{\partial}{\partial \dot{\gamma}}\left[\frac{1}{2}\left(m_G\left[z_G^2+y_G^2\right]\right)\dot{\phi}^2+\left(I_{G_{xx}}\,\mathbf{c}^2\alpha+I_{G_{zz}}\,\mathbf{s}^2\alpha\right)\dot{\phi}^2+I_{G_{yy}}\dot{\alpha}^2+\right]\\ &= 0\end{aligned} \tag{4.100}$$

Using the same method as above, $\frac{\partial \mathcal{K}_G}{\partial q}$ was evaluated at ϕ, α, and γ:

$$\begin{aligned}\frac{\partial \mathcal{K}_G}{\partial \phi} &= \frac{1}{2}\left[\left(m_G\left[z_G^2+y_G^2\right]\right)\dot{\phi}^2+\left(I_{G_{xx}}\,\mathbf{c}^2\alpha+I_{G_{zz}}\,\mathbf{s}^2\alpha\right)\dot{\phi}^2+I_{G_{yy}}\dot{\alpha}^2\right]\\ &= 0\end{aligned} \tag{4.101}$$

$$\begin{aligned}\frac{\partial \mathcal{K}_G}{\partial \alpha} &= \frac{1}{2}\left[\left(m_G\left[z_G^2+y_G^2\right]\right)\dot{\phi}^2+\frac{\partial}{\partial \alpha}\left[\left(I_{G_{xx}}\,\mathbf{c}^2\alpha+I_{G_{zz}}\,\mathbf{s}^2\alpha\right)\dot{\phi}^2\right]+I_{G_{yy}}\dot{\alpha}^2\right]\\ &= \frac{1}{2}\left[2\left(I_{G_{zz}}-I_{G_{xx}}\right)\,\mathbf{s}\alpha\,\mathbf{c}\alpha\dot{\phi}^2\right]\\ &= \left(I_{G_{zz}}-I_{G_{xx}}\right)\,\mathbf{s}\alpha\,\mathbf{c}\alpha\dot{\phi}^2\end{aligned} \tag{4.102}$$

$$\frac{\partial \mathcal{K}_G}{\partial \gamma} = \frac{1}{2}\left[\left(m_G\left[z_G^2+y_G^2\right]\right)\dot{\phi}^2+\left(I_{G_{xx}}\,\mathbf{c}^2\alpha+I_{G_{zz}}\,\mathbf{s}^2\alpha\right)\dot{\phi}^2+I_{G_{yy}}\dot{\alpha}^2\right]$$

$$= 0 \tag{4.103}$$

4.2.3.3 Kinetic Energy of the Wheel

Substitutions were made for the Equation $\mathcal{K}_W$ (Equation 4.68) and the values in Equation 4.63 for $v_4, v_5, v_6, \omega_4, \omega_5$, and ω_6, and the $\dot{\gamma}$ terms were expanded:

$$\frac{\partial \mathcal{K}_W}{\partial \dot{q}_i} = \frac{\partial}{\partial \dot{q}_i}\left[\frac{1}{2} m_W \left(v_4^2 + v_5^2 + v_6^2\right) + \frac{1}{2}\left(I_{W_{xx}}\left[\omega_4^2 + \omega_5^2\right] + I_{W_{zz}}\left[\omega_6 + \dot{\gamma}\right]^2\right)\right] \tag{4.104}$$

$$\begin{aligned}
&= \frac{\partial}{\partial \dot{q}_i}\left[\frac{1}{2}\Bigg(m_W \left[\cancelto{0}{v_4^2} + \left(-\left[z_G\,\mathbf{c}\phi + y_G\,\mathbf{s}\phi\right]\dot{\phi}\right)^2 + \left(-\left[z_G\,\mathbf{s}\phi + y_G\,\mathbf{c}\phi\right]\dot{\phi}\right)^2\right] \right.\\
&\quad \left. + I_{W_{xx}}\left[\left(\dot{\phi}\,\mathbf{c}\alpha\right)^2 + \dot{\alpha}^2\right] + I_{W_{zz}}\left[\dot{\phi}\,\mathbf{s}\alpha + \dot{\gamma}\right]^2\Bigg)\right]\\
&= \frac{\partial}{\partial \dot{q}_i}\left[\frac{1}{2}\Big(m_W\left[z_G^2 + y_G^2\right]\dot{\phi}^2 + I_{W_{xx}}\left[\dot{\phi}^2\,\mathbf{c}^2\alpha + \dot{\alpha}^2\right]\right.\\
&\quad \left. + I_{W_{zz}}\left[\dot{\phi}^2\,\mathbf{s}^2\alpha + 2\dot{\phi}\dot{\gamma}\,\mathbf{s}\alpha + \dot{\gamma}^2\right]\Big)\right]\\
&= \frac{\partial}{\partial \dot{q}_i}\left[\frac{1}{2}\Big(m_W\left[z_G^2 + y_G^2\right]\dot{\phi}^2 + \left[I_{W_{xx}}\,\mathbf{c}^2\alpha + I_{W_{zz}}\,\mathbf{s}^2\alpha\right]\dot{\phi}^2 + I_{W_{xx}}\dot{\alpha}^2\right.\\
&\quad \left. + 2I_{W_{zz}}\dot{\gamma}\dot{\phi}\,\mathbf{s}\alpha + I_{W_{zz}}\dot{\gamma}^2\Big)\right]
\end{aligned} \tag{4.105}$$

Equation 4.105 was evaluated at $\dot{\phi}$, $\dot{\alpha}$, and $\dot{\gamma}$:

$$\begin{aligned}
\frac{\partial \mathcal{K}_W}{\partial \dot{\phi}} &= \frac{1}{\cancel{2}}\cancelto{1}{2}\Bigg[\Bigg(m_W\left[z_G^2 + y_G^2\right]\dot{\phi} + \left[I_{W_{xx}}\,\mathbf{c}^2\alpha + I_{W_{zz}}\,\mathbf{s}^2\alpha\right]\dot{\phi} + I_{W_{xx}}\cancelto{0}{\dot{\alpha}^2}\\
&\quad + I_{W_{zz}}\dot{\gamma}\cancelto{1}{\dot{\phi}}\,\mathbf{s}\alpha + I_{W_{zz}}\cancelto{0}{\dot{\gamma}^2}\Bigg)\Bigg]\\
&= m_W\left(z_G^2 + y_G^2\right)\dot{\phi} + \left(I_{W_{xx}}\,\mathbf{c}^2\alpha + I_{W_{zz}}\,\mathbf{s}^2\alpha\right)\dot{\phi} + I_{W_{xx}}\dot{\gamma}\,\mathbf{s}\alpha
\end{aligned} \tag{4.106}$$

$$\frac{\partial \mathcal{K}_W}{\partial \dot{\alpha}} = \frac{1}{\cancel{2}}\cancelto{1}{2}\Bigg[\Bigg(m_W\left[z_G^2 + y_G^2\right]\cancelto{0}{\dot{\phi}^2} + \left[I_{W_{xx}}\,\mathbf{c}^2\alpha + I_{W_{zz}}\,\mathbf{s}^2\alpha\right]\cancelto{0}{\dot{\phi}^2} + I_{W_{xx}}\dot{\alpha}$$

$$+ 2I_{W_{zz}}\dot{\gamma}\dot{\phi}\,\mathbf{s}\cancel{\alpha}^{0} + I_{W_{zz}}\cancel{\dot{\gamma}^{2}}^{0}\Big)\Big]$$
$$= I_{W_{xx}}\dot{\alpha} \tag{4.107}$$

$$\frac{\partial \mathcal{K}_W}{\partial \dot{\gamma}} = \frac{1}{\cancel{2}^{1}}\Big[\cancel{2}^{1}\Big(m_W\left[z_G^2 + y_G^2\right]\cancel{\dot{\phi}^{2}}^{0} + \left[I_{W_{xx}}\,\mathbf{c}^2\alpha + I_{W_{zz}}\,\mathbf{s}^2\alpha\right]\cancel{\dot{\phi}^{2}}^{0} + I_{W_{xx}}\cancel{\dot{\alpha}^{2}}^{0}$$
$$+ I_{W_{zz}}\dot{\phi}\,\mathbf{s}\alpha + I_{W_{zz}}\dot{\gamma}\Big)\Big]$$
$$= I_{W_{zz}}\dot{\gamma} + I_{W_{zz}}\dot{\phi}\,\mathbf{s}\alpha \tag{4.108}$$

Using the same method as above, $\frac{\partial \mathcal{K}_W}{\partial q}$ was evaluated at ϕ, α, and γ:

$$\frac{\partial \mathcal{K}_W}{\partial \phi} = \frac{1}{2}\Big[m_W\left[z_G^2 + y_G^2\right]\cancel{\dot{\phi}^{2}}^{0} + \left[I_{W_{xx}}\,\mathbf{c}^2\alpha + I_{W_{zz}}\,\mathbf{s}^2\alpha\right]\cancel{\dot{\phi}^{2}}^{0} + I_{W_{xx}}\cancel{\dot{\alpha}^{2}}^{0}$$
$$+ 2I_{W_{zz}}\dot{\gamma}\dot{\phi}\,\mathbf{s}\cancel{\alpha}^{0} + I_{W_{zz}}\cancel{\dot{\gamma}^{2}}^{0}\Big]$$
$$= 0 \tag{4.109}$$

$$\frac{\partial \mathcal{K}_W}{\partial \alpha} = \frac{1}{2}\Big[m_W\left[z_G^2 + y_G^2\right]\cancel{\dot{\phi}^{2}}^{0} + \frac{\partial}{\partial\alpha}\left[I_{W_{xx}}\,\mathbf{c}^2\alpha + I_{W_{zz}}\,\mathbf{s}^2\alpha\right]\dot{\phi}^2 + I_{W_{xx}}\cancel{\dot{\alpha}^{2}}^{0}$$
$$+ \frac{\partial}{\partial\alpha}2I_{W_{zz}}\dot{\gamma}\dot{\phi}\,\mathbf{s}\alpha + I_{W_{zz}}\cancel{\ddot{\gamma}^{2}}^{0}\Big]$$
$$= \frac{1}{\cancel{2}^{1}}\Big[\cancel{2}^{1}\Big(\left[I_{W_{zz}} - I_{W_{xx}}\right]\,\mathbf{s}\alpha\,\mathbf{c}\alpha\dot{\phi}^2 + I_{W_{zz}}\dot{\gamma}\dot{\phi}\,\mathbf{c}\alpha\Big)\Big]$$
$$= \left(I_{W_{zz}} - I\_W_{xx}\right)\,\mathbf{s}\alpha\,\mathbf{c}\alpha\dot{\phi}^2 + I_{W_{zz}}\dot{\gamma}\dot{\phi}\,\mathbf{c}\alpha \tag{4.110}$$

$$\frac{\partial \mathcal{K}_W}{\partial \gamma} = \frac{1}{2}\Big[m_W\left[z_G^2 + y_G^2\right]\cancel{\dot{\phi}^{2}}^{0} + \left[I_{W_{xx}}\,\mathbf{c}^2\alpha + I_{W_{zz}}\,\mathbf{s}^2\alpha\right]\cancel{\dot{\phi}^{2}}^{0} + I_{W_{xx}}\cancel{\dot{\alpha}^{2}}^{0}$$

$$+ 2I_{W_{zz}}\dot{\gamma}\dot{\phi}\,\mathbf{s}\cancelto{0}{\alpha} + I_{W_{zz}}\cancelto{0}{\dot{\gamma}^2}\Big]$$

$$= 0 \tag{4.111}$$

4.2.3.4 Potential Energy of the Head

The general equation for $\mathcal{P}_H$ (Equation 4.76):

$$\frac{\partial \mathcal{P}_H}{\partial \dot{q}_i} = \frac{\partial}{\partial \dot{q}_i}\left(m_H g\left[z_H\,\mathbf{c}\phi + y_H\,\mathbf{s}\phi\right]\right) \tag{4.112}$$

This equation was evaluated at $\dot{q}_i = \dot{\phi}$, $\dot{\alpha}$, and $\dot{\gamma}$, and $q_i = \alpha$ and γ by inspection:

$$\frac{\partial \mathcal{P}_H}{\partial \dot{\phi}} = 0 \tag{4.113}$$

$$\frac{\partial \mathcal{P}_H}{\partial \dot{\alpha}} = 0 \tag{4.114}$$

$$\frac{\partial \mathcal{P}_H}{\partial \dot{\gamma}} = 0 \tag{4.115}$$

$$\frac{\partial \mathcal{P}_H}{\partial \alpha} = 0 \tag{4.116}$$

$$\frac{\partial \mathcal{P}_H}{\partial \gamma} = 0 \tag{4.117}$$

Evaluated at $q_i = \phi$:

$$\frac{\partial \mathcal{P}_H}{\partial \phi} = m_H g\left(-z_H\,\mathbf{s}\phi + y_H\,\mathbf{c}\phi\right) \tag{4.118}$$

4.2.3.5 Potential Energy of the Gimbals

The general equation for $\mathcal{P}_G$ (Equation 4.77):

$$\frac{\partial \mathcal{P}_G}{\partial \dot{q}_i} = \frac{\partial}{\partial \dot{q}_i}\left(m_G g\left[z_G\,\mathbf{c}\phi + y_G\,\mathbf{s}\phi\right]\right) \tag{4.119}$$

As before, this equation was evaluated at $\dot{q}_i = \dot{\phi}$, $\dot{\alpha}$, and $\dot{\gamma}$, and $q_i = \alpha$ and γ by inspection:

$$\frac{\partial \mathcal{P}_G}{\partial \dot{\phi}} = 0 \tag{4.120}$$

$$\frac{\partial \mathcal{P}_G}{\partial \dot{\alpha}} = 0 \tag{4.121}$$

$$\frac{\partial \mathcal{P}_G}{\partial \dot{\gamma}} = 0 \tag{4.122}$$

$$\frac{\partial \mathcal{P}_G}{\partial \alpha} = 0 \tag{4.123}$$

$$\frac{\partial \mathcal{P}_G}{\partial \gamma} = 0 \tag{4.124}$$

Evaluated at $q_i = \phi$:

$$\frac{\partial \mathcal{P}_G}{\partial \phi} = m_{_G} g \left(-z_{_G}\, \mathbf{s}\phi + y_{_G}\, \mathbf{c}\phi\right) \tag{4.125}$$

4.2.3.6 Potential Energy of the Wheel

The general equation for $\mathcal{P}_W$ (Equation 4.78), after substituting $z_{_G}$ and $y_{_G}$ for $z_{_W}$ and $y_{_W}$, as the centre of masses are assumed to be co-located:

$$\begin{aligned}\frac{\partial \mathcal{P}_W}{\partial \dot{q}_i} &= \frac{\partial}{\partial \dot{q}_i} \left(m_{_W} g \left[z_{_W}\, \mathbf{c}\phi + y_{_W}\, \mathbf{s}\phi\right]\right) \\ &= \frac{\partial}{\partial \dot{q}_i} \left(m_{_W} g \left[z_{_G}\, \mathbf{c}\phi + y_{_G}\, \mathbf{s}\phi\right]\right)\end{aligned} \tag{4.126}$$

This equation was evaluated at $\dot{q}_i = \dot{\phi}$, $\dot{\alpha}$, and $\dot{\gamma}$, and $q_i = \alpha$ and γ by inspection:

$$\frac{\partial \mathcal{P}_W}{\partial \dot{\phi}} = 0 \tag{4.127}$$

$$\frac{\partial \mathcal{P}_W}{\partial \dot{\alpha}} = 0 \tag{4.128}$$

$$\frac{\partial \mathcal{P}_W}{\partial \dot{\gamma}} = 0 \tag{4.129}$$

$$\frac{\partial \mathcal{P}_W}{\partial \alpha} = 0 \tag{4.130}$$

$$\frac{\partial \mathcal{P}_W}{\partial \gamma} = 0 \tag{4.131}$$

Evaluated at $q_i = \phi$ results in the following:

$$\frac{\partial \mathcal{P}_W}{\partial \phi} = m_{_W} g \left(-z_{_G}\, \mathbf{s}\phi + y_{_G}\, \mathbf{c}\phi\right) \tag{4.132}$$

4.2.4 Euler–Lagrangian

The above components were summed into the partial derivatives presented in Equations 4.82 and 4.83, and then simplified for $q_i = \phi$, α, and γ.

4.2.4.1 Evaluating for Head Position

The Euler–Lagrangian was evaluated for the $q_i = \phi$ case. The evaluated partial derivatives were simplified and had the state space variables (q, $\dot{q}$, and $\ddot{q}$) isolated when possible. The resulting partial derivatives for $\dot{\phi}$ and ϕ, respectively, are as follows:

$$\begin{aligned}
\frac{\partial \mathcal{L}}{\partial \dot{\phi}} &= \sum \frac{\partial \mathcal{K}}{\partial \dot{\phi}} - \sum \frac{\partial \mathcal{P}}{\partial \dot{\phi}} \\
&= \left(m_{_H}\left(z_{_H}^2 + y_{_H}^2\right) + I_{H_{xx}}\right)\dot{\phi} + m_{_G}\left(z_{_G}^2 + y_{_G}^2\right)\dot{\phi} + \left(I_{G_{xx}}\,\mathbf{c}^2\alpha I_{G_{zz}}\,\mathbf{s}^2\alpha\right)\dot{\phi} + \\
&\quad m_{_W}\left(z_{_G}^2 + y_{_G}^2\right)\dot{\phi} + \left(I_{W_{xx}}\,\mathbf{c}^2\alpha + I_{W_{zz}}\,\mathbf{s}^2\alpha\right)\dot{\phi} + I_{W_{xx}}\dot{\gamma}\,\mathbf{s}\alpha - 0 \\
&= \left[m_{_H}\left(z_{_H}^2 + y_{_H}^2\right) + (m_{_G} + m_{_W})\left(z_{_G}^2 + y_{_G}^2\right) + I_{H_{xx}}\right]\dot{\phi} + (I_{G_{xx}} + I_{W_{xx}})\,\mathbf{c}^2\alpha\dot{\phi} + \\
&\quad (I_{G_{zz}} + I_{W_{zz}})\,\mathbf{s}^2\alpha\dot{\phi} + I_{W_{xx}}\dot{\gamma}\,\mathbf{s}\alpha,
\end{aligned} \tag{4.133}$$

and

$$\begin{aligned}
\frac{\partial \mathcal{L}}{\partial \phi} &= \sum \frac{\partial \mathcal{K}}{\partial \phi} - \sum \frac{\partial \mathcal{P}}{\partial \phi} \\
&= 0 - \left[m_{_H} g\left(-z_{_H}\,\mathbf{s}\phi + y_{_H}\,\mathbf{c}\phi\right) + m_{_G} g\left(-z_{_G}\,\mathbf{s}\phi + y_{_G}\,\mathbf{c}\phi\right)\right. \\
&\quad \left. + m_{_W} g\left(-z_{_G}\,\mathbf{s}\phi + y_{_G}\,\mathbf{c}\phi\right)\right] \\
&= m_{_H} g\left(z_{_H}\,\mathbf{s}\phi - y_{_H}\,\mathbf{c}\phi\right) + m_{_G} g\left(z_{_G}\,\mathbf{s}\phi - y_{_G}\,\mathbf{c}\phi\right) + m_{_W} g\left(z_{_G}\,\mathbf{s}\phi - y_{_G}\,\mathbf{c}\phi\right) \\
&= g\left(m_{_H} z_{_H}\,\mathbf{s}\phi - m_{_H} y_{_H}\,\mathbf{c}\phi + m_{_G} z_{_G}\,\mathbf{s}\phi - m_{_G} y_{_G}\,\mathbf{c}\phi + m_{_W} z_{_G}\,\mathbf{s}\phi - m_{_W} y_{_G}\,\mathbf{c}\phi\right) \\
&= g\left(\left[m_{_H} z_{_H} + m_{_G} z_{_G} + m_{_W} z_{_G}\right]\,\mathbf{s}\phi - \left[m_{_H} y_{_H} + m_{_G} y_{_G} + m_{_W} z_{_G}\right]\,\mathbf{c}\phi\right) \\
&= g\left[m_{_H} z_{_H} + (m_{_G} + m_{_W})\,z_{_G}\right]\,\mathbf{s}\phi - g\left[m_{_H} y_{_H} + (m_{_G} + m_{_W})\,y_{_G}\right]\,\mathbf{c}\phi
\end{aligned} \tag{4.134}$$

The derivative of Equation 4.133 with respect to t was calculated, noting that ϕ, α, and γ are all functions of time. The equation was then arranged to create constants. The wheel spins at a constant velocity $\dot{\gamma}$, which means that the acceleration of the wheel, $\ddot{\gamma}$ is zero.

$$\begin{aligned}
\frac{\mathrm{d}}{\mathrm{d}t}\left(\frac{\partial \mathcal{L}}{\partial \dot{\phi}}\right) &= \frac{\mathrm{d}}{\mathrm{d}t}\Big(\left[m_{_H}\left(z_{_H}^2 + y_{_H}^2\right) + (m_{_G} + m_{_W})\left(z_{_G}^2 + y_{_G}^2\right) + I_{H_{xx}}\right]\dot{\phi} \\
&\qquad + (I_{G_{xx}} + I_{W_{xx}})\,\mathbf{c}^2\alpha\dot{\phi} + (I_{G_{zz}} + I_{W_{zz}})\,\mathbf{s}^2\alpha\dot{\phi} + I_{W_{xx}}\dot{\gamma}\,\mathbf{s}\alpha\Big) \\
&= a_1\ddot{\phi} + a_2\,\mathbf{c}^2\alpha\ddot{\phi} + a_3\,\mathbf{s}^2\alpha\ddot{\phi} - a_2 2\,\mathbf{s}\alpha\,\mathbf{c}\alpha\dot{\alpha}\dot{\phi} + a_3 2\,\mathbf{s}\alpha\,\mathbf{c}\alpha\dot{\alpha}\dot{\phi} + I_{W_{xx}}\dot{\gamma}\,\mathbf{c}\alpha\dot{\alpha} \\
&\qquad + I_{W_{xx}}\,\mathbf{s}\alpha\cancelto{0}{\ddot{\gamma}} \\
&= a_1\ddot{\phi} + a_2\left(1 - \mathbf{s}^2\alpha\right)\ddot{\phi} + a_3\,\mathbf{s}^2\alpha\ddot{\phi} - a_2\,\mathbf{s}2\alpha\dot{\alpha}\dot{\phi} + a_3\,\mathbf{s}2\alpha\dot{\alpha}\dot{\phi} + I_{W_{xx}}\dot{\gamma}\,\mathbf{c}\alpha\dot{\alpha}
\end{aligned}$$

$$= (a_1 + a_2)\,\ddot{\phi} + (a_3 - a_2)\;\mathbf{s}^2\alpha\ddot{\phi} + (a_3 - a_2)\;\mathbf{s}2\alpha\dot{\alpha}\dot{\phi} + I_{W_{xx}}\dot{\gamma}\,\mathbf{c}\alpha\dot{\alpha} \tag{4.135}$$

where the constants a_1 through a_3 are defined as follows:

$$\begin{aligned} a_1 &= m_{_H}\left(z_{_H}^2 + y_{_H}^2\right) + \left(m_{_G} + m_{_W}\right)\left(z_{_G}^2 + y_{_G}^2\right) + I_{H_{xx}} \\ a_2 &= I_{G_{xx}} + I_{W_{xx}} \\ a_3 &= I_{G_{zz}} + I_{W_{zz}} \end{aligned}$$

The general form of the Euler–Lagrangian equation (4.81) was completed by substituting Equations 4.135 and 4.134—the time derivative of the $\dot{\phi}$ partial derivative of Lagrangian, and the partial derivative with respect to ϕ:

$$\frac{\mathrm{d}}{\mathrm{d}t}\left(\frac{\partial\mathcal{L}}{\partial\dot{\phi}}\right) - \frac{\partial\mathcal{L}}{\partial\phi} \tag{4.136}$$

$$\begin{aligned} &= (a_1 + a_2)\,\ddot{\phi} + (a_3 - a_2)\;\mathbf{s}^2\alpha\ddot{\phi} + (a_3 - a_2)\;\mathbf{s}2\alpha\dot{\alpha}\dot{\phi} + I_{W_{xx}}\dot{\gamma}\,\mathbf{c}\alpha\dot{\alpha} \\ &\quad - \left[g\left[m_{_H}z_{_H} + \left(m_{_G} + m_{_W}\right)z_{_G}\right]\,\mathbf{s}\phi - g\left[m_{_H}y_{_H} + \left(m_{_G} + m_{_W}\right)y_{_G}\right]\,\mathbf{c}\phi\right. \\ \tau_H &= (a_1 + a_2)\,\ddot{\phi} + (a_3 - a_2)\;\mathbf{s}^2\alpha\ddot{\phi} + (a_3 - a_2)\;\mathbf{s}2\alpha\dot{\alpha}\dot{\phi} + I_{W_{xx}}\dot{\gamma}\,\mathbf{c}\alpha\dot{\alpha} \\ &\quad - a_4\,\mathbf{s}\phi + a_5\,\mathbf{c}\phi \end{aligned} \tag{4.137}$$

where the constants a_4 and a_5 are defined as follows:

$$\begin{aligned} a_4 &= g\left(m_{_H}z_{_H} + \left(m_{_G} + m_{_W}\right)z_{_G}\right) \\ a_5 &= g\left(m_{_H}y_{_H} + \left(m_{_G} + m_{_W}\right)y_{_G}\right) \end{aligned}$$

4.2.4.2 Evaluating for Cage Position

The Euler–Lagrangian was evaluated for the $q_i = \alpha$ case. The evaluated partial derivatives were simplified and had the state space variables isolated when possible. The resulting partial derivatives for $\dot{\alpha}$ and α, respectively, are as follows:

$$\begin{aligned} \frac{\partial\mathcal{L}}{\partial\dot{\alpha}} &= \sum\frac{\partial\mathcal{K}}{\partial\dot{\alpha}} - \sum\frac{\partial\mathcal{P}}{\partial\dot{\alpha}} \\ &= 0 + I_{G_{yy}}\dot{\alpha} + I_{W_{xx}}\dot{\alpha} - 0 \\ &= \left(I_{G_{yy}} + I_{W_{xx}}\right)\dot{\alpha}, \end{aligned} \tag{4.138}$$

and

$$\begin{aligned}\frac{\partial \mathcal{L}}{\partial \alpha} &= \sum \frac{\partial \mathcal{K}}{\partial \alpha} - \sum \frac{\partial \mathcal{P}}{\partial \alpha} \\ &= 0 + \left(I_{G_{zz}} - I_{G_{xx}}\right)\, \mathrm{s}\alpha\, \mathrm{c}\alpha \dot{\phi}^2 + \left(I_{W_{zz}} - I_{W_{xx}}\right)\, \mathrm{s}\alpha\, \mathrm{c}\alpha \dot{\phi}^2 + I_{W_{zz}} \dot{\gamma}\, \mathrm{c}\alpha \dot{\phi} - 0 \\ &= \left[\left(I_{G_{zz}} - I_{G_{xx}}\right) + \left(I_{W_{zz}} - I_{W_{xx}}\right)\right]\, \mathrm{s}\alpha\, \mathrm{c}\alpha \dot{\phi}^2 + I_{W_{zz}} \dot{\gamma}\, \mathrm{c}\alpha \dot{\phi} \\ &= \left(a_3 - a_2\right)\, \mathrm{s}\alpha\, \mathrm{c}\alpha \dot{\phi}^2 + I_{W_{zz}} \dot{\gamma}\, \mathrm{c}\alpha \dot{\phi} \end{aligned} \tag{4.139}$$

As in Section 4.2.4.1, the derivative of Equation 4.138 with respect to t was calculated, noting that the derivative of $\dot{\gamma}$ is zero:

$$\begin{aligned}\frac{\mathrm{d}}{\mathrm{d}t}\left(\frac{\partial \mathcal{L}}{\partial \dot{\alpha}}\right) &= \frac{\mathrm{d}}{\mathrm{d}t}\Big[\left(I_{G_{yy}} + I_{W_{xx}}\right)\dot{\alpha}\Big] \\ &= a_6 \ddot{\alpha} \end{aligned} \tag{4.140}$$

where the constant a_6 is defined as follows:

$$a_6 = I_{G_{yy}} + I_{W_{xx}}$$

The general form of the Euler–Lagrange equation (4.81) was completed by substituting Equations 4.140 and 4.139—the time derivative of the $\dot{\alpha}$ partial derivative of the Lagrangian, and the partial derivative with respect to α:

$$\begin{aligned}\frac{\mathrm{d}}{\mathrm{d}t}\left(\frac{\partial \mathcal{L}}{\partial \dot{\alpha}}\right) - \frac{\partial \mathcal{L}}{\partial \alpha} &= a_6 \ddot{\alpha} - \Big[\left(a_3 - a_2\right)\, \mathrm{s}\alpha\, \mathrm{c}\alpha \dot{\phi}^2 + I_{W_{zz}} \dot{\gamma}\, \mathrm{c}\alpha \dot{\phi}\Big] \\ \tau_G &= a_6 \ddot{\alpha} - \left(a_3 - a_2\right)\, \mathrm{s}\alpha\, \mathrm{c}\alpha \dot{\phi}^2 - I_{W_{zz}} \dot{\gamma}\, \mathrm{c}\alpha \dot{\phi} \end{aligned} \tag{4.141}$$

4.2.4.3 Evaluating for Wheel Position

The Euler–Lagrangian was evaluated for the $q_i = \gamma$ case. The evaluated partial derivatives were simplified and had the state space variables isolated when possible. The resulting partial derivatives for $\dot{\gamma}$ and γ, respectively, are as follows:

$$\begin{aligned}\frac{\partial \mathcal{L}}{\partial \dot{\gamma}} &= \sum \frac{\partial \mathcal{K}}{\partial \dot{\gamma}} - \sum \frac{\partial \mathcal{P}}{\partial \dot{\gamma}} \\ &= 0 + 0 + I_{W_{zz}} \dot{\gamma} + I_{W_{zz}} \dot{\phi}\, \mathrm{s}\alpha - 0 \\ &= I_{W_{zz}} \dot{\gamma} + I_{W_{zz}} \dot{\phi}\, \mathrm{s}\alpha, \end{aligned} \tag{4.142}$$

and

$$\begin{aligned}\frac{\partial \mathcal{L}}{\partial \gamma} &= \sum \frac{\partial \mathcal{K}}{\partial \gamma} - \sum \frac{\partial \mathcal{P}}{\partial \gamma} \\ &= 0 - 0 \\ &= 0 \end{aligned} \tag{4.143}$$

As in Section 4.2.4.1, the derivative of Equation 4.142 with respect to t was calculated, noting that the derivative of $\dot{\gamma}$ is zero:

$$\begin{aligned}\frac{\mathrm{d}}{\mathrm{d}t}\left(\frac{\partial \mathcal{L}}{\partial \dot{\alpha}}\right) &= \frac{\mathrm{d}}{\mathrm{d}t}\Big[I_{W_{zz}}\dot{\gamma} + I_{W_{zz}}\dot{\phi}\,\mathbf{s}\alpha\Big] \\ &= I_{W_{zz}}\,\mathbf{c}\alpha\dot{\phi}\dot{\alpha} + I_{W_{zz}}\,\mathbf{s}\alpha\ddot{\phi} + \cancelto{0}{\ddot{\gamma}} \\ &= I_{W_{zz}}\,\mathbf{s}\alpha\ddot{\phi} + I_{W_{zz}}\,\mathbf{c}\alpha\dot{\phi}\dot{\alpha} \end{aligned} \tag{4.144}$$

The general form of the Euler–Lagrange equation (4.81) was completed by substituting Equations 4.140 and 4.139—the time derivative of the $\dot{\gamma}$ partial derivative of the Lagrangian, and the partial derivative with respect to γ:

$$\begin{aligned}\frac{\mathrm{d}}{\mathrm{d}t}\left(\frac{\partial \mathcal{L}}{\partial \dot{\alpha}}\right) - \frac{\partial \mathcal{L}}{\partial \alpha} &= I_{W_{zz}}\,\mathbf{s}\alpha\ddot{\phi} + I_{W_{zz}}\,\mathbf{c}\alpha\dot{\phi}\dot{\alpha} - 0 \\ \tau_W &= I_{W_{zz}}\,\mathbf{s}\alpha\ddot{\phi} + I_{W_{zz}}\,\mathbf{c}\alpha\dot{\phi}\dot{\alpha} \end{aligned} \tag{4.145}$$

4.2.5 Summary of Dynamics Equations and Constants

In summary, the equations that describe the torque experienced by the three bodies in the single gyroscope system are as follows:

$$\begin{aligned}\tau_H &= (a_1 + a_2)\,\ddot{\phi} + (a_3 - a_2)\,\mathbf{s}^2\alpha\ddot{\phi} + (a_3 - a_2)\,\mathbf{s}2\alpha\dot{\alpha}\dot{\phi} \\ &\quad + I_{W_{xx}}\dot{\gamma}\,\mathbf{c}\alpha\dot{\alpha} - a_4\,\mathbf{s}\phi + a_5\,\mathbf{c}\phi \\ \tau_G &= a_6\ddot{\alpha} - (a_3 - a_2)\,\mathbf{s}\alpha\,\mathbf{c}\alpha\dot{\phi}^2 - I_{W_{zz}}\dot{\gamma}\,\mathbf{c}\alpha\dot{\phi} \\ \tau_W &= I_{W_{zz}}\,\mathbf{s}\alpha\ddot{\phi} + I_{W_{zz}}\,\mathbf{c}\alpha\dot{\phi}\dot{\alpha} \end{aligned} \tag{4.146}$$

where the constants a_1 through a_6 are defined as follows:

$$\begin{aligned} a_1 &= m_{_H}\left(z_{_H}^2 + y_{_H}^2\right) + \left(m_{_G} + m_{_W}\right)\left(z_{_G}^2 + y_{_G}^2\right) + I_{H_{xx}} \\ a_2 &= I_{G_{xx}} + I_{W_{xx}} \end{aligned}$$

$$a_3 = I_{G_{zz}} + I_{W_{zz}}$$
$$a_4 = g\left(m_{_H} z_{_H} + \left(m_{_G} + m_{_W}\right) z_{_G}\right)$$
$$a_5 = g\left(m_{_H} y_{_H} + \left(m_{_G} + m_{_W}\right) y_{_G}\right)$$
$$a_6 = I_{G_{yy}} + I_{W_{xx}}$$

4.3 Concluding Statement

In order to easily account for the addition of gyroscopes, two additional angles can be vertically concatenated to the generalized coordinate vector, q: $[\alpha_j \ \gamma_j]^T$. To modify the final equations, the time derviative of the partial derivative of the Lagrangian with respect to the velocities of the generalized coordinate vector for the j^{th} gimbal and wheel ($\mathcal{K}_{G_j}$ and $\mathcal{K}_{W_j}$, similarly for $\mathcal{P}$) can be added to the final equations:

$$\frac{\mathrm{d}}{\mathrm{d}t}\left(\frac{\partial \mathcal{L}\left(v,\omega\right)}{\partial \dot{q}_i}\right), \tag{4.147}$$

and the partial derivative of the Lagrangian with respect to the generalized coordinate vector of the system is subtracted from the final equations:

$$\frac{\partial \mathcal{L}\left(v,\omega\right)}{\partial q_i}, \tag{4.148}$$

where the linear velocity (v) and rotational velocity (ω) of the gimbals and wheel of the j^{th} gyroscope are obtained using the modified DH convention as outlined previously.

This chapter presented a method to calculate the dynamics of the human head and neck with the addition of one or more gyroscopes as stabilizers, as well as the specific dynamics for such a system using one gyroscope located at the crown of the head, parallel to the transverse plane. The next chapter presents the design and fabrication of the experimental device with one gyroscope, in order to validate the theoretical torque as calculated in Section 4.2.

Chapter 5

Design of the Experimental Setup and Gyroscope System

In order to use the dynamics as described in the previous chapter to optimize a design for a resistive device, the dynamics must first be validated. Since there are a number of unknown variables in the equations in the one-gyroscope system proposed in the previous chapter (Equations 4.137, 4.141, and 4.145), a reasonably-sized gyroscope was designed (as described within this chapter). If the method is proven to be representative of the real-world dynamics, these equations can then be optimized to create the required wheel size for a specified resistance value.

The dynamics equations for each body were calculated to be

$$\begin{aligned}
\tau_H &= (a_1 + a_2)\,\ddot{\phi} + (a_3 - a_2)\ \mathbf{s}^2\alpha\ddot{\phi} + (a_3 - a_2)\ \mathbf{s}2\alpha\dot{\alpha}\dot{\phi} \\
&\quad + I_{W_{xx}}\dot{\gamma}\,\mathbf{c}\alpha\dot{\alpha} - a_4\,\mathbf{s}\phi + a_5\,\mathbf{c}\phi \\
\tau_G &= a_6\ddot{\alpha} - (a_3 - a_2)\ \mathbf{s}\alpha\,\mathbf{c}\alpha\dot{\phi}^2 - I_{W_{zz}}\dot{\gamma}\,\mathbf{c}\alpha\dot{\phi} \\
\tau_W &= I_{W_{zz}}\,\mathbf{s}\alpha\ddot{\phi} + I_{W_{zz}}\,\mathbf{c}\alpha\dot{\phi}\dot{\alpha},
\end{aligned} \tag{5.1}$$

with the a constants calculated as follows:

$$\begin{aligned}
a_1 &= m_{_H}\left(z_{_H}^2 + y_{_H}^2\right) + \left(m_{_G} + m_{_W}\right)\left(z_{_G}^2 + y_{_G}^2\right) + I_{H_{xx}} \\
a_2 &= I_{G_{xx}} + I_{W_{xx}} \\
a_3 &= I_{G_{zz}} + I_{W_{zz}} \\
a_4 &= g\left(m_{_H} z_{_H} + \left(m_{_G} + m_{_W}\right) z_{_G}\right) \\
a_5 &= g\left(m_{_H} y_{_H} + \left(m_{_G} + m_{_W}\right) y_{_G}\right)
\end{aligned}$$

$$a_6 = I_{G_{yy}} + I_{W_{xx}}$$

5.1 Specifications and Requirements

A number of specifications and requirements exist for this proposed device. At minimum, it must not interfere with normal head motion, which is said to be approximately 80–90 degrees in flexion, 70 degrees in extension, 20–45 degrees in both directions for lateral flexion, and 90 degrees in both directions for rotation. At this stage, the device should be able to provide approximately the equivalent of 0–5 lbf of resistance to the side of the head. The device should be as compact as possible, and as light as possible, with an even weight distribution across the head. The device must also have a safety switch and a physical limit in the form of mechanical stops for the precession angle (as limiting the precession angle limits torque).

As the device will be used in the home environment, it should be both tetherless and plug-and-play. As a medical device, the design and use will need to be in accordance with Health Canada standards and the ISO Standard ISO 13485. The device should be made from materials that are sanitizable, non-reactive, and hypo-allergenic. The end users of this device are both the PTs and the patients. For PTs, it will be important to be easy to learn how to use, and have no programming required. For patients, the device should be able to be used autonomously by otherwise-healthy individuals. Ideally, this device will interface solely with the user's head, though if required, a battery stored in a backpack-type holder could be possible.

As the human head has much variation within populations, the device will need to be adjustable or come with different sized parts. Typical adult heads range between 52–60 cm in circumference (a range of 5^{th} percentile female to 95^{th} percentile male, as described in the US population data in the ISO Standard ISO/TR 7250-2:2010(E)) [113]).

Competition Benchmarking

- Traditional manual therapy
  - Estimation of forces by physiotherapist (by "feel")
  - Requires patient to be in person at a physiotherapist's office

- The Multi-Cervical Unit (MCU) from BTE
  - Allows for strength measurements and baseline testing
  - Allows for head tracking
  - Large: 31" x 47" x 77", as well as the computer cart: 20" x 30" x 59"
  - Requires the patient to go to a PT's office
- At-home Cervical traction devices
  - A passive stretch for pain relief, no strength training
  - Includes devices such as blow-up neck collars, over-the-door head harnesses, and sand bags or plate weights with head harnesses
- At-home resistance band training
  - Using basic resistance bands or over-the-door options
  - Only works for two of the three types of neck motion

5.2 Concept Generation

One of the biggest considerations at the beginning of this project was simplicity in design—the less complex the system, the fewer mechanisms of failure for a system designed to be used on the head–neck system of a human being.

The first design considered only used a momentum wheel: a flywheel with a large inertia that is used to store angular momentum, designed to be robust and resist movement using this "stored" angular momentum. The proposed design would use multiple wheels to affect each axis of rotation, and a mock up of this design can be seen in Figure 5.1. By design, these momentum wheels can be physically large, heavy, or both. A typical use for momentum wheels is spacecraft applications. After considering the equations of motion and dynamics for such an application, it was found that the head motion with respect to the neck would act as the gimbals for the wheel(s)—as if it were a gyroscope—and would produce reactionary forces in non-intuitive directions for the users, especially in cases with lower numbers of gyroscopes. That is, the resistance would be felt around a different axis from the one around which the user is moving their head. For example, in a one-gyroscope system if the patient were to move their head along the coronal plane—lateral neck flexion—the resulting force would have a torque

Figure 5.1: A mock up of a first concept for the reaction wheel set up. The initial five wheel design was maintained into the final design. Shown here with the forehead wheel suppressed for a cleaner image.

that would be experienced as a rotation or a flexion–extension, as shown in Figure 5.2. While it would theoretically be possible to imbue the momentum wheel(s) with enough energy to resist all neck movement, rendering this a non-issue, the end use of this device does require the patient to have resultant movement in order to perform the exercises prescribed by their physical therapist. Momentum wheels were therefore declared unsuitable for this application.

The second iteration looked at using a control system with a five momentum wheel system—an application referred to as a "reaction wheel." These are also used in spacecraft applications, typically for attitude control of satellites [83]. This method would sense the direction and speed of the neck motion, and would activate the necessary reaction wheels at a required angular velocity to produce the desired stabilization force—or in this application, the required resistance. This option requires a control system, which adds computer failure to the list of potential hazards to the end user.

When considering the reaction wheel, it was ultimately decided it would be best for both the ability of the patient to use the device—and their safety—to have the resulting torques be acting passively (without a control algorithm), and to act in an opposite and intuitive direction to the head motion. This ruled out the reaction wheel, due to requiring a control algorithm, as a possible actuator.

The third iteration looked at using a "gyrostabilizer", or a gyroscope acting as an actuator. The previous two iterations were looking at spinning wheels, where

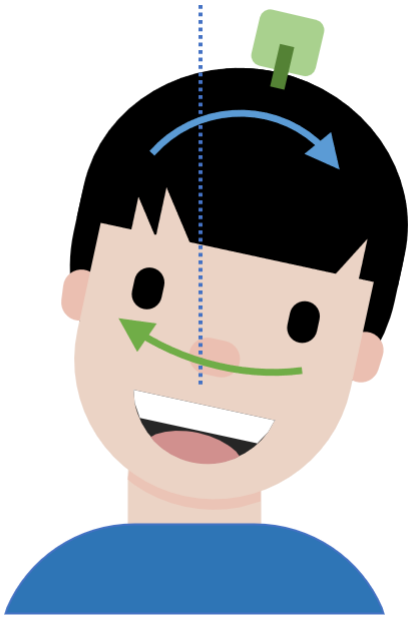

Figure 5.2: The head is shown here moving in lateral flexion (blue), with a resultant moment experienced as a rotation (green).

the head–neck joint acted as the gimbals of the gyroscope. While some gyroscopes have control systems controlling the precession angle or angular velocity, a gyroscope can be used passively for this application and would exert a resistive torque in the intuitive opposite direction of the movement. That is, the resistive torque would be experienced around the same axis that the user is moving their head; the same that would be felt when using a resistance band or pressing their head against a hand. Due to this, the gyroscope was chosen for the scope of this work.

5.3 Prototype Construction

This section covers the design and construction of the device prototype and the experimental setup used to test the dynamics in Chapter 4. All Three Dimension (3D) printed parts were designed in SolidWorks and printed using the Vero® material from Stratasys.

The device was designed to be one gyroscope attached to the head with a harness. The head motion was tested by using a skull model attached to a C1 model mounted to a rotating board that would allow for either simulating lateral flexion or flexion–extension. Two sensors were used to collect the data: one position

sensor to collect the position data of the head and the gyroscope cage, and one Force/Torque (F/T) sensor to collect the force and torque data experienced in the neck during the motions.

Section 5.3.1 covers the device prototype, and Section 5.3.2 covers the experimental setup.

5.3.1 Device Prototype

The device was designed to be worn on the head, held on with an adjustable-strap elastic harness. The prototype version of this—with a gimbal mount and four printed placeholders—can be seen in Figure 5.3. The size of the gyroscope mount plate was based on the size of the base for a head-mounted camera. In a multi-gyroscope application, additional gyroscopes would replace the blank placeholder mounts. Each of the four blank sides had three sides with an oval slit to allow for the hook-and-loop and elastic harness to be attached.

The gimbal mount was designed with a base the same size as the blank mounts, with each of the four sides having the oval slit for the harness attachment. A simple slot for the pegs of the gimbal to be seated in acted as the rotation joint for the gimbals. The height of the arms for this mount was calculated to be short enough that the gyroscope could not attain more than a 30 degree angle, as the cage bottom would connect with the mount plate. The intention behind this mechanical limit was that the resultant torque of a gyroscope increases with an increase in precession angle, and this is a method to limit the torque experienced by the user. This 30 degree angle was created as an arbitrary limit that can be further optimized with the equations presented and developed in Chapters 3 and 4 after validation.

The gyroscope gimbal was designed to be a symmetric cage along two of the three Cartesian planes. Two pegs were included on the cage bars to sit in the slots in the mount. The motor was mounted to the bottom of the cage with flat top M3 mounting screws. The symmetry was retained when adding two sensor arms. The arms are thin rectangular posts with a notch in order to sit flush to the top of the cage. The cage and the mounted motor can be seen in Figure 5.4. More on the cage design can be found in Section 5.3.1.1, and more on the sensor arms can be found in Section 5.3.1.3.

The motor was chosen to be an outrunner brushless Direct Current (DC) motor, which is commonly used in drone and model plane applications. These motors can

(a) The oval slits and the elastic attachment.

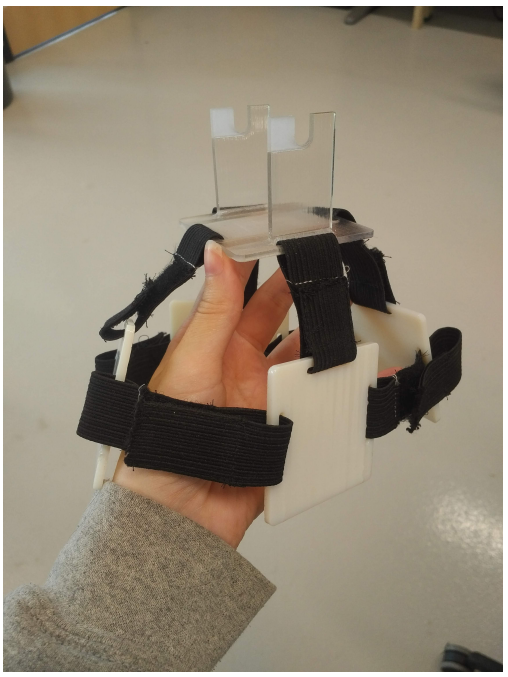

(b) The white squares shown are placeholders for where future gyroscopes could be placed.

(c) The harness being worn on a human head.

Figure 5.3: The sewn harness prototype, with eight hook-and-loop fastener-elastic straps.

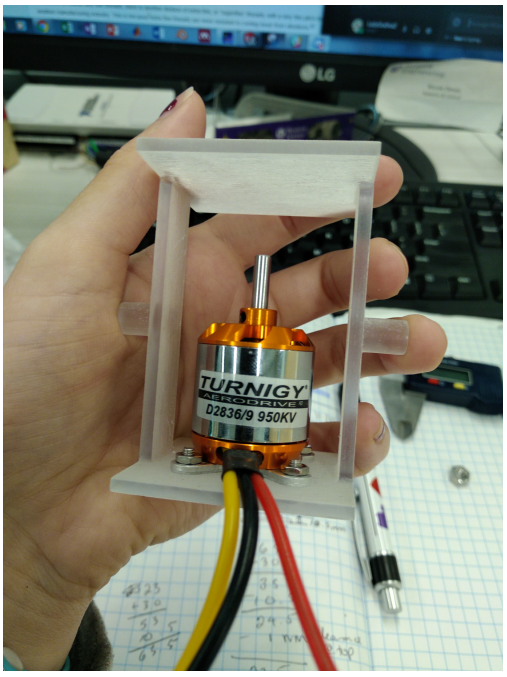

(a) The gyroscope cage and motor, showing the pegs on both sides of the cage.

(b) The gyroscope cage seated in the gimbal mount on the harness.

Figure 5.4: The gyroscope cage and motor.

typically provide high RPM with minimal weight and size. The specific motor is the Turnigy D2836/9 950 KV Brushless Outrunner Motor, and the data sheet for this can be found in Appendix B.1. The motor is taller than would typically be used in a gyroscope at this scale, so the cage for the prototype is also taller than would be reasonable for this application. The size is another factor that can be optimized with the validated dynamics for future use. The model used in SolidWorks was created by G'llaume RBL, available on GrabCAD [126]. More information on the issues encountered with the motor and the interference from it can be found in Section 5.3.1.3.

The wheel was designed to fit over the motor, since the motor was already tall, and the wheel fitting over the motor kept the design the most compact. In order to keep the gyroscope motor and wheel design to be within the constraints of the base size, the wheel was constrained to a fairly thin thickness, reducing the amount of angular momentum that would be available from this first iteration. The wheel was also 3D printed. The wheel was designed with a hexagon-shaped indent to have a pressfit mate with a nut, which could then be attached to the motor shaft, as well as a through hole for the motor shaft. The mate was too loose for a pressfit, so the wheel had some additional motion during testing. The mass properties for this part can be found in Section 5.3.1.2.

The motor was controlled within the Arduino Integrated Development Environment (IDE) and connected to the motor via an Electronic Speed Controller (ESC) for the motor. The ESC was connected to an external power source running at 12 V giving the motor a speed of 11,400 RPM. This system can be seen in Figure 5.5.

5.3.1.1 Gyroscope Cage

The cage and wheel were initially modelled in SolidWorks. The cage needed additional sensor arms because of the motor interference, which is discussed more in Section 5.3.1.3. The arms were mounted on the centering lines on the cage, as seen in Figure 5.6. The arms can be seen in the SolidWorks assembly in Figure 5.7.

In order to know the position of the COM in the real-world system, a "landmark" was chosen on the cage assembly that could be measured with respect to the position sensor. Measuring from the landmark to the COM in the SolidWorks model would allow the use of vector subtraction to find the position of the COM

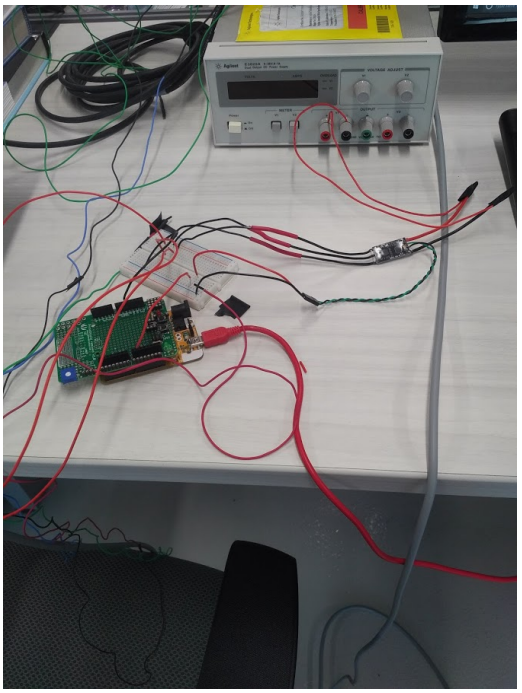

Figure 5.5: The microcontroller (left hand side) and the ESC (right hand side), connected to the external power source (top).

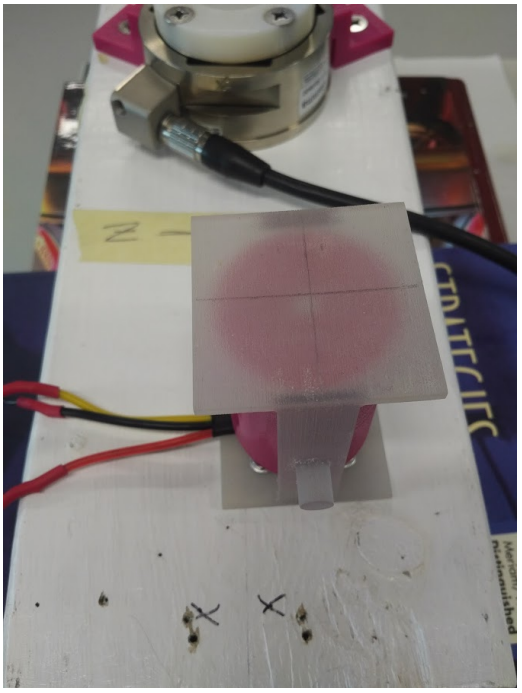

Figure 5.6: Gyroscope cage showing centering lines, used to mount the sensor arms.

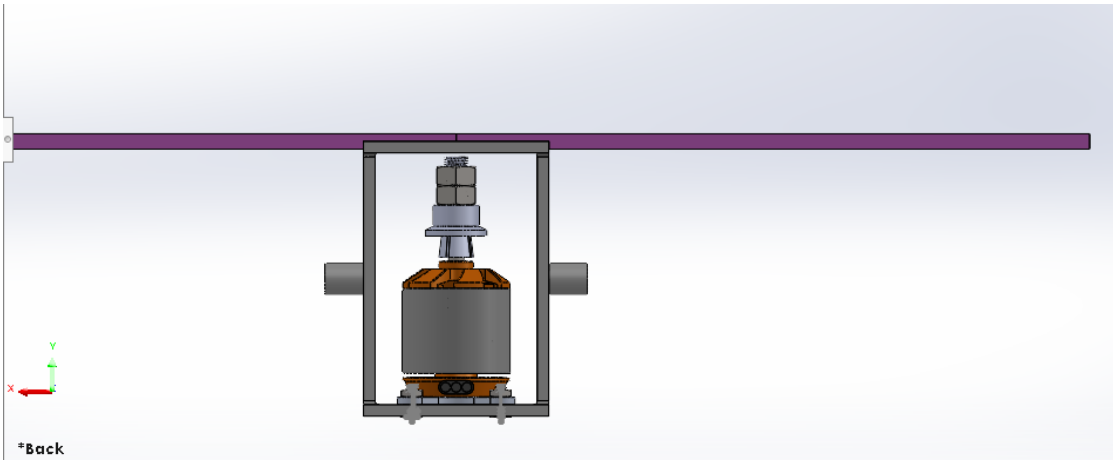

Figure 5.7: The cage, motor, and wheel assembly in SolidWorks. Showing the Back of the assembly. Motor model adapted from [126].

with respect to the position sensor. The location of the sensor for the experiment, on the sensor arm, was chosen to be the landmark. The location of this can be seen in Figure 5.8.

The assembly was intentionally oriented to have the same orientation as the skull model (described later in Section 5.3.2.2), in order to use the same rotation matrix for each of the SolidWorks model transformations for the Mass Properties.

The top of the cage assembly was aligned such that it would be parallel to the x–z plane in the SolidWorks coordinate frame. The front–back of the cage and wheel objects are symmetrical along the coronal plane, so this part was rotated to have this coronal plane be parallel to same plane as the coronal plane of the skull: the SolidWorks x–y plane, rotated such that the front of the skull is facing the positive direction for the z axis. While the cage and the wheel are symmetric, the motor has a difference (due to the wiring connections). The wheel–cage assembly was aligned with the motor wiring connections facing the negative z direction. The flat sides of the cage were aligned such that they were parallel with the SolidWorks planes.

The assembly was positioned such that the landmark was co-located with the origin of the assembly. The mass and moments of inertia data were then pulled from the Mass Properties of the model, using the Vero material used in the printer as the applied material for the 3D printed parts. The mass calculated for the cage—which included the cage mount, the mounting screws and nuts, the sensor arms, the motor, and the wheel mounting hardware—was calculated to be 113.60 grams.

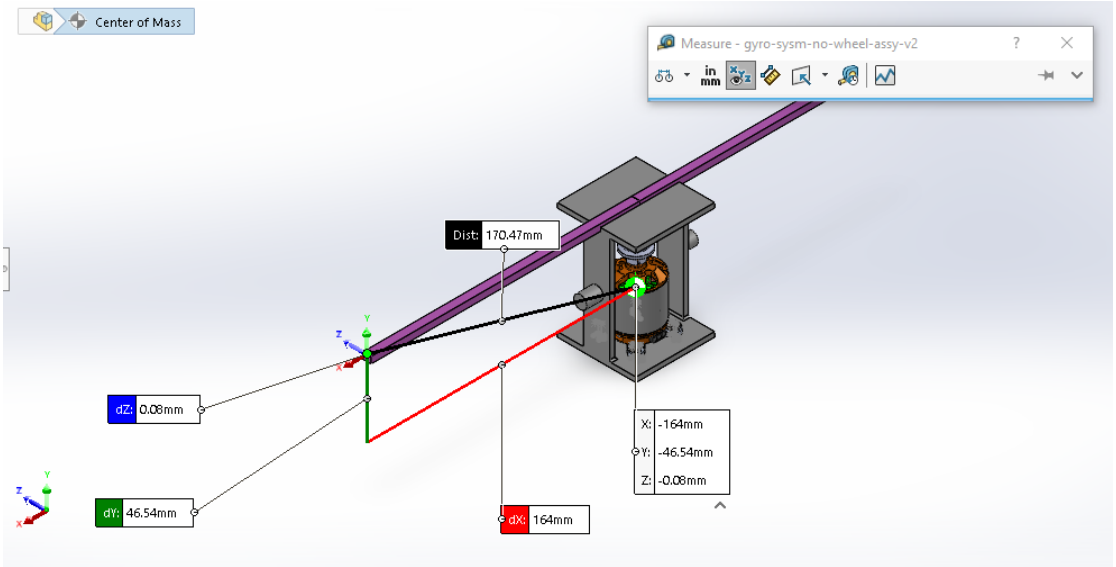

Figure 5.8: The location of *sensor*2/the cage landmark in the assembly. Showing the measurement from the landmark to the COM.

The motor had its mass properties overwritten, as the weight calculated by the Mass Properties in SolidWorks differed significantly from the data provided by the manufacturer. The weight of the motor was given as 70 grams.

The principal axes of inertia for the cage assembly, with respect to the SolidWorks orientation, were calculated to be

$$\hat{\mathbf{i}_G} = \begin{bmatrix} 1.00 \\ 0.00 \\ 0.00 \end{bmatrix} \hat{\mathbf{j}_G} = \begin{bmatrix} 0.00 \\ 1.00 \\ 0.00 \end{bmatrix} \hat{\mathbf{k}_G} = \begin{bmatrix} 0.00 \\ 0.00 \\ 1.00 \end{bmatrix}, \tag{5.2}$$

with the values for the principal moments of inertia for the cage (P_G), in $g * mm^2$, calculated as

$$\begin{aligned} P_{G_x} &= 68,809.34\ \hat{\mathbf{i}_G} \\ P_{G_y} &= 87,013.14\ \hat{\mathbf{j}_G} \\ P_{G_z} &= 142,392.58\ \hat{\mathbf{k}_G} \end{aligned} \tag{5.3}$$

The inertia tensor for this assembly was calculated by SolidWorks and ex-

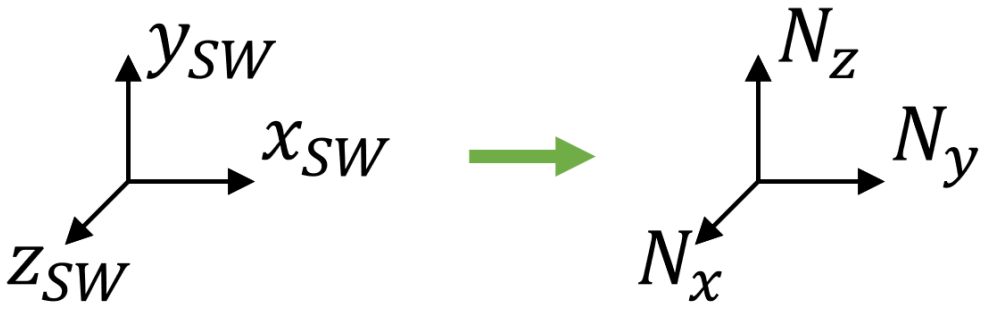

Figure 5.9: The SolidWorks frame of reference as compared to the Neck frame from Chapter 4.

pressed in the SolidWorks coordinate frame:

$$\mathbf{I_G} = \begin{bmatrix} 68,809.35 & 0.49 & 8.15 \\ 0.49 & 87,013.16 & 37.95 \\ 8.15 & 37.95 & 142,392.55 \end{bmatrix} \tag{5.4}$$

Since the principal axes align with the SolidWorks frame of reference (i.e., $\hat{\mathbf{i}}_\mathbf{G} = [1.00; 0; 0]^T$), the principal moments of inertia were used as the I_{xx}, I_{yy}, and I_{zz} values.

$$I_G^{SW} = \begin{bmatrix} P_{G_x} \\ P_{G_y} \\ P_{G_z} \end{bmatrix} \tag{5.5}$$

In order to represent the P_G terms in the Base Frame (as used in Chapter 4), a rotational transformation matrix was used, as shown in Figure 5.9.

$$\begin{aligned} \mathbf{R_B^{SW}} &= \mathbf{R_{z,-\pi/2}} \cdot \mathbf{R_{y,-\pi/2}} \\ &= \begin{bmatrix} \mathbf{c}(-\pi/2) & -\mathbf{s}(-\pi/2) & 0 \\ \mathbf{s}(-\pi/2) & \mathbf{c}(-\pi/2) & 0 \\ 0 & 0 & 1 \end{bmatrix} \cdot \begin{bmatrix} \mathbf{c}(-\pi/2) & 0 & \mathbf{s}(-\pi/2) \\ 0 & 1 & 0 \\ -\mathbf{s}(-\pi/2) & 0 & \mathbf{c}(-\pi/2) \end{bmatrix} \end{aligned} \tag{5.6}$$

$$= \begin{bmatrix} 0 & 1 & 0 \\ -1 & 0 & 0 \\ 0 & 0 & 1 \end{bmatrix} \cdot \begin{bmatrix} 0 & 0 & -1 \\ 0 & 1 & 0 \\ 1 & 0 & 0 \end{bmatrix}$$

$$\mathbf{R_B^{SW}} = \begin{bmatrix} 0 & 1 & 0 \\ 0 & 0 & 1 \\ 1 & 0 & 0 \end{bmatrix} \tag{5.7}$$

This rotation matrix was then applied to the principal moments of inertia:

$$I_G = \mathbf{R_B^{SW}}^T \cdot I_G^{SW} \tag{5.8}$$

$$= \begin{bmatrix} 0 & 1 & 0 \\ 0 & 0 & 1 \\ 1 & 0 & 0 \end{bmatrix}^T \cdot \begin{bmatrix} P_{G_x} \\ P_{G_y} \\ P_{G_z} \end{bmatrix}$$

$$= \begin{bmatrix} P_{G_z} \\ P_{G_x} \\ P_{G_y} \end{bmatrix} \tag{5.9}$$

The Mass Properties and Measure tool within SolidWorks calculated the location of the COM in the SolidWorks coordinate frame (in mm), as measured from the origin (the left sensor arm) to the COM:

$$\vec{d_G^{SW}}_{COM} = \begin{bmatrix} -164.00 \\ -46.54 \\ -0.08 \end{bmatrix} \tag{5.10}$$

The same rotation matrix as above was used to transform this landmark–COM distance to be expressed in the Base Frame coordinates:

$$\vec{d_{G_{COM}}^B} = \mathbf{R_B^{SW}}^T \cdot \vec{d_G^{SW}}_{COM} \tag{5.11}$$

$$= \begin{bmatrix} 0 & 1 & 0 \\ 0 & 0 & 1 \\ 1 & 0 & 0 \end{bmatrix}^T \cdot \begin{bmatrix} -164.00 \\ -46.54 \\ -0.08 \end{bmatrix}$$

$$\vec{d_{G_{COM}}^B} = \begin{bmatrix} -0.08 \\ -164.00 \\ -46.54 \end{bmatrix} \tag{5.12}$$

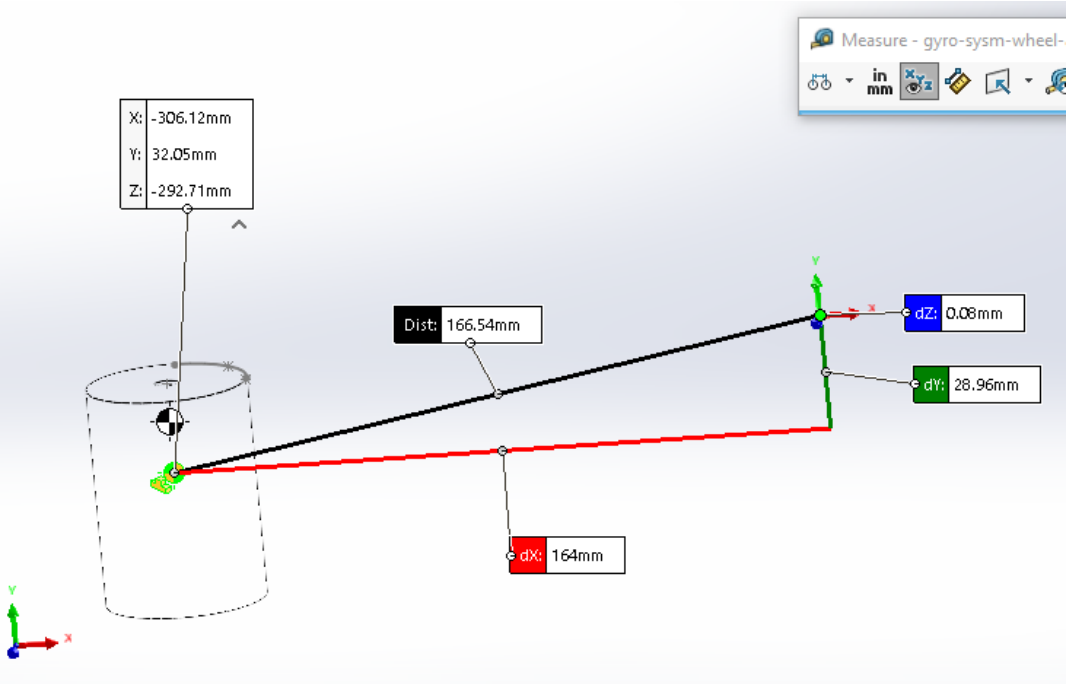

Figure 5.10: The wheel model in the SolidWorks assembly. All the other models have been suppressed so the distance is measured from *sensor*2/the cage landmark location to the COM of the wheel only. The landmark is shown on the right hand side where the frame of reference orientation object is.

5.3.1.2 Gyroscope Wheel

As mentioned previously, the wheel was modelled in SolidWorks. The wheel was designed to be symmetrical and have planes that would align with the principal axes of inertia of the parts. In order to simplify calculations, the location of the COM and the mass of the wheel were calculated in SolidWorks within the cage-wheel assembly. By suppressing all non-wheel parts, the calculations would only take into consideration the wheel. This allowed the use of the same landmark—the *sensor*2—to be used for both the wheel as well as the cage. The distance between the landmark point and the wheel can be seen in Figure 5.10.

In order to calculate the principal moments of inertia, the wheel had the Vero material properties applied. The mass calculated for the wheel was 55.47 grams, which is within 2% of the weight measured of the printed part (56.06 grams). The weight as calculated by SolidWorks was used in subsequent calculations, but this does provide more confidence in the calculated values for this part and the other parts in the system. The Mass Properties tool within SolidWorks was then used to calculate the principal axes of inertia, with respect to the SolidWorks frame of

reference.

$$\hat{\mathbf{i_W}} = \begin{bmatrix} 0.00 \\ 1.00 \\ 0.00 \end{bmatrix} , \hat{\mathbf{j_W}} = \begin{bmatrix} 0.00 \\ 0.00 \\ 1.00 \end{bmatrix} , \hat{\mathbf{k_W}} = \begin{bmatrix} 1.00 \\ 0.00 \\ 0.00 \end{bmatrix} , \tag{5.13}$$

where the values for the principal moments of inertia for the wheel (P_W), in $g{*}mm^2$ in the above principal axes directions, were calculated as

$$\begin{aligned} P_{W_x} &= 13,835.29\hat{\mathbf{i_W}} \\ P_{W_y} &= 19,582.42\hat{\mathbf{j_W}} \\ P_{W_z} &= 19,582.42\hat{\mathbf{k_W}} \end{aligned} \tag{5.14}$$

The inertia tensor—as calculated by SolidWorks—adjusted to be in line with the SolidWorks coordinate frame and located at the COM was

$$\mathbf{I_W} = \begin{bmatrix} 19,582.42 & 0.00 & 0.00 \\ 0.00 & 13,835.29 & 0.00 \\ 0.00 & 0.00 & 19,582.42 \end{bmatrix} \tag{5.15}$$

Transforming the principal moments of inertia from the principal axes to the SolidWorks frame yields the same as the diagonal:

$$\hat{\mathbf{u_W}} = \left[\hat{\mathbf{i_W}}, \hat{\mathbf{j_W}}, \hat{\mathbf{k_W}}\right] \tag{5.16}$$

$$\begin{aligned} I_W^{SW} &= \hat{\mathbf{u_W}} \cdot P_W \\ &= \begin{bmatrix} 0 & 0 & 1 \\ 1 & 0 & 0 \\ 0 & 1 & 0 \end{bmatrix} \cdot \begin{bmatrix} P_{W_x} \\ P_{W_y} \\ P_{W_z} \end{bmatrix} \end{aligned} \tag{5.17}$$

$$I_W^{SW} = \begin{bmatrix} P_{W_z} \\ P_{W_x} \\ P_{W_y} \end{bmatrix} \tag{5.18}$$

In order to represent the P_W terms in the Base Frame (as used in Chapter 4), the same rotational transformation matrix was used as the above section, Equation

5.7:

$$I_W = \mathbf{R_B^{SW}}^T \cdot I_H^{SW} \tag{5.19}$$
$$= \begin{bmatrix} 0 & 1 & 0 \\ 0 & 0 & 1 \\ 1 & 0 & 0 \end{bmatrix}^T \cdot \begin{bmatrix} P_{W_z} \\ P_{W_x} \\ P_{W_y} \end{bmatrix}$$
$$I_W = \begin{bmatrix} P_{H_y} \\ P_{H_z} \\ P_{H_x} \end{bmatrix} \tag{5.20}$$

The Mass Properties and Measure tool within SolidWorks calculated the location of the COM in the SolidWorks coordinates frame (in mm), as measured from the origin (the landmark on the left sensor arm) to the COM:

$$\vec{d_W^{SW}}_{COM} = \begin{bmatrix} -164.00 \\ -28.96 \\ -0.08 \end{bmatrix} \tag{5.21}$$

The same rotation matrix was used to transform this landmark–COM distance to be expressed in the Base Frame coordinates:

$$\vec{d_W^B}_{COM} = \mathbf{R_B^{SW}}^T \cdot \vec{d_W^{SW}}_{COM} \tag{5.22}$$
$$= \begin{bmatrix} 0 & 1 & 0 \\ 0 & 0 & 1 \\ 1 & 0 & 0 \end{bmatrix}^T \cdot \begin{bmatrix} -164.00 \\ -28.96 \\ -0.08 \end{bmatrix}$$
$$\vec{d_W^B}_{COM} = \begin{bmatrix} -0.08 \\ -164.00 \\ -28.96 \end{bmatrix} \tag{5.23}$$

5.3.1.3 Motor Interference

While testing the experiential setup during the developmental stage, it was noted that the position sensor (the "Aurora") was collecting a lot of erroneous data. This was ultimately attributed to Electromagnetic Interference (EMI) from the motor, as the position sensor system uses magnetic fields to track the position of the sensors. This initial position can be seen in Figure 5.11.

Therefore, the motor needed to be shielded from interfering with the data

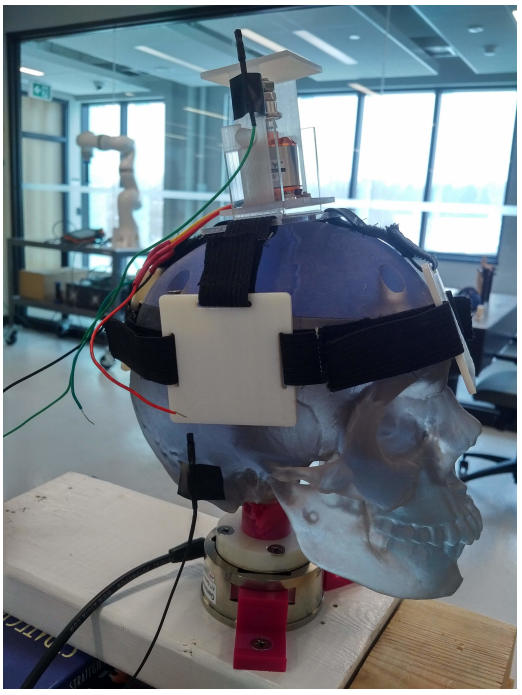

Figure 5.11: The initial position of the cage sensor.

collection. An EMI-Shielding Nickel Alloy film was used to wrap the wheel to shield the sensor setup from the motor. This can be seen in Figure 5.12. This shielded some of the interference, but not enough to use the sensors in the originally planned positions.

The shielding caused the cage sensor to not be picked up by the Aurora when placed directly above the motor, even without the motor turned on or running. When the motor was not running, the sensor was able to be identified by the position sensor when it was placed on the edge of the cage, even when rotating the system.

Once the motor was turned on, the motor interference affected both the sensors, even with modified positions. Shielding was added to the top of the wheel as well, but this affected the sensor on the skull more than in previous iterations.

In order to gain some distance from the interference for the position sensors, two sensor arms were developed. One was a fairly short, thin cylindrical tube (as seen in Figure 5.13), used for the skull sensor. The other was designed to be a long, flat, thin arm. Two were used in order to retain symmetry in the parts. They can be seen in Figures 5.8 and 5.13. The sensor arms worked well to prevent some interference, but did have some residual issues when rotation of the system caused the displacement from the field generator to the sensor to be closer in magnitude

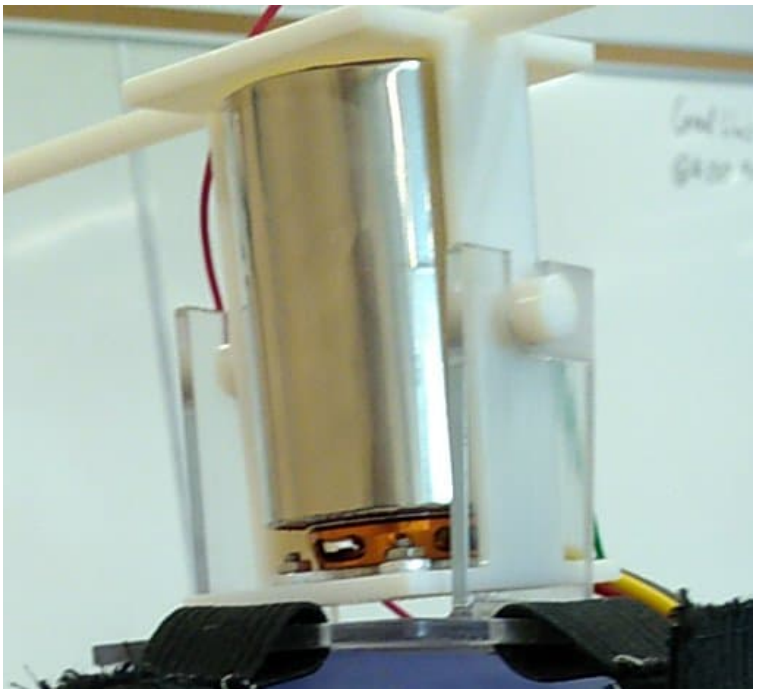

Figure 5.12: The shielded gyroscope wheel. The wheel was 3D printed in magenta Vero, and the silver is the EMI-shielding film.

to the displacement to the motor.

5.3.2 Experiment Setup

The device was tested on a cervical spine–skull model, which was mounted on a F/T sensor on a board which would allow for rotation, simulating either lateral flexion or flexion–extension of a human neck. An electromagnetic tracking sensor—the Aurora—was used to track two sensors placed on the skull and the gyroscope cage.

The rotation board was designed by Lidka (2017) to simulate wrist motion [127]. The wooden board, as seen in Figure 5.14, had a handle pressfit to allow for rotation. The base for the rotation board was clamped to a desk.

The F/T sensor from ATI was mounted to this wooden board, as shown in Figure 5.15. The sensor was mounted with 3D printed clips screwed into the board. An attachment was created to hold the C1 model as a pressfit connection. The clips, mount, and C1 were all 3D printed parts.

The C1 model was created from a Computed Tomography (CT) scan, to be pressfit into a mount created to sit on the F/T sensor. The C1 pressfit part sits

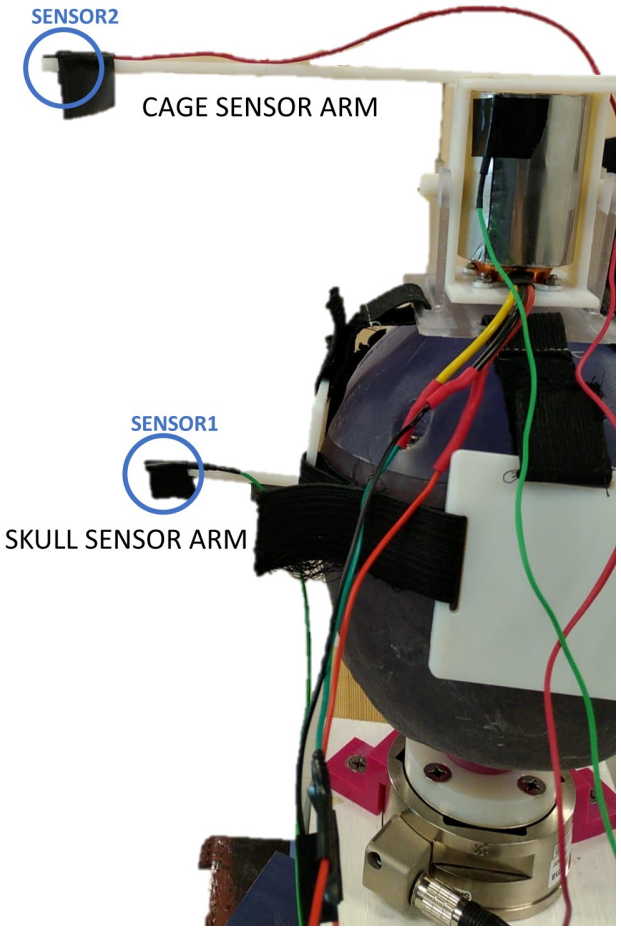

Figure 5.13: The two sensor arms. The skull arm can be seen attached to the parietal bone, and one the two cage arms can be seen extending in the left–right direction from the top of the cage.

(a) The base for the rotation board, clamped to a desk.

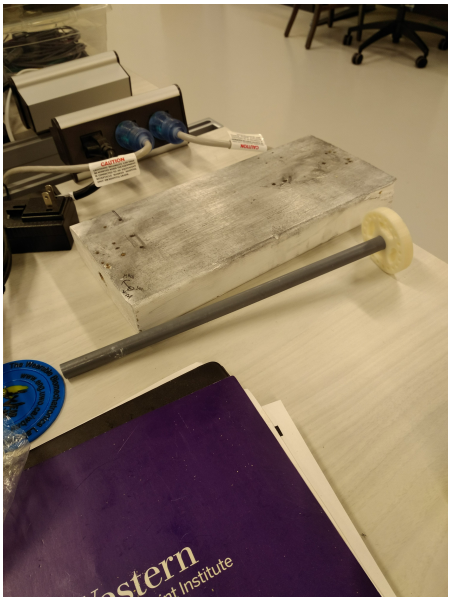

(b) The rotation board (white) and the rotation handle.

(c) The rotation board assembled, the handle pressfit into the board through the mount.

Figure 5.14: The wooden rotation board setup.

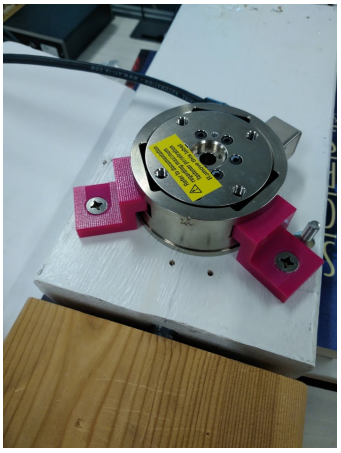

(a) The ATI F/T sensor mounted to the wooden rotation board with 3D printed clamps (magenta).

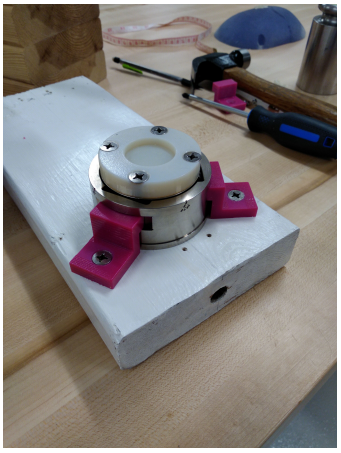

(b) The C1 mount (white) attached to the F/T sensor with screws.

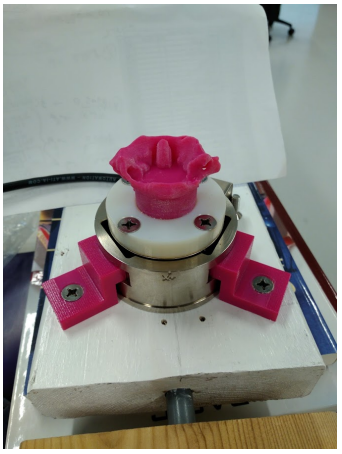

(c) The C1 model (magenta) pressfit into the mount (white).

Figure 5.15: The sensor–mount–C1 assembly.

in such a way that the atlanto–occipital joint holds the head at a 10 degree angle from the transverse plane, a natural angle for a human to hold their head. More information on the modelling of the cervical spine can be found in Section 5.3.2.1.

A 3D anatomic model of a human skull was slightly hollowed out around the COM and had a cap created that would be held on with screws. The skull and the cap were then 3D printed. The skull was attached with Hot Melt Adhesive (HMA) to the C1 model and pressfit into the sensor mount. Additionally, a cylindrical sensor arm was attached using hot melt adhesive near the junction of the frontal, parietal, and temporal skull bones. More information on the skull design can be found in Section 5.3.2.2.

The Aurora field generator was set up a distance from the rotation board, parallel to the axis of rotation of the board. The two sensors, as described previously, were attached to two sensor arms: one on the skull model, and one on an arm attached to the top of the gyroscope cage. The sensor arms are described in more detail in the earlier Section 5.3.1.3. Below is a more in-depth look at the key parts of the experiment setup: the model neck and the skull model.

5.3.2.1 Model Neck

The intention was to test the device using a fairly accurate biomechanical model. This was to be accomplished using a 3D printed cervical spine and skull, created

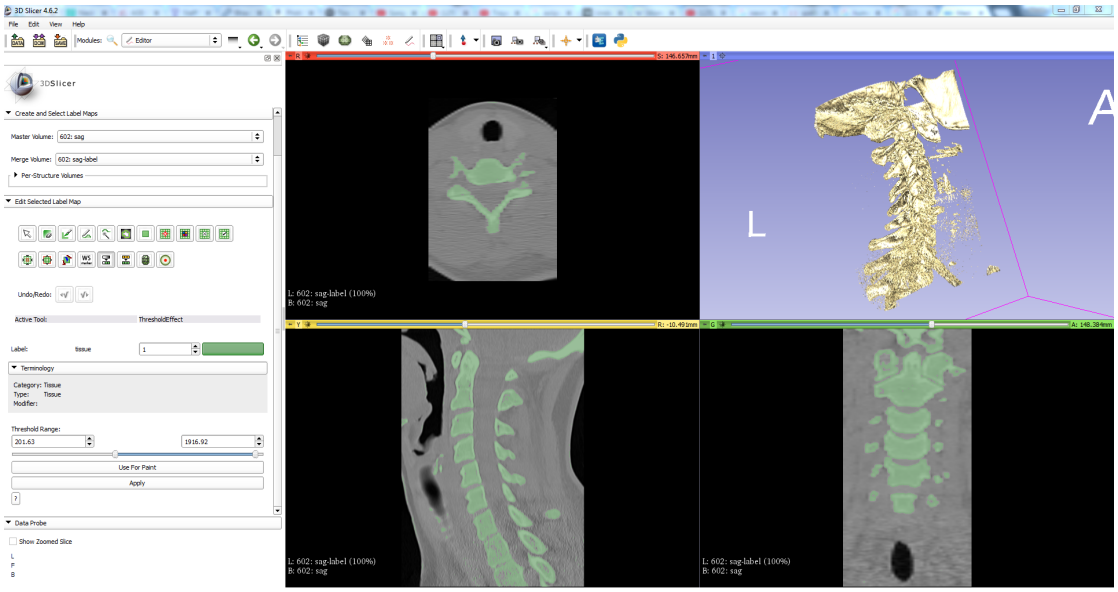

Figure 5.16: A screenshot of Slicer 3D, applying a threshold to the images to pull out the bone data as an STL file. Showing the mineralized tissues.

from scans of a real human being. This section will describe the steps taken to design the cervical spine and the issues that were encountered while attempting to do this. As stated in the summary of the experimental setup, the cervical spine ultimately was replaced by a single vertebra.

The preliminary design was designed such that the neck would be straight, as opposed to being shaped like a real spine: a metal or plastic rod, at calculated length from Chapter 3. This was quickly replaced with the decision that a biologically accurate neck would be a better option.

Due to the number and complexity of the muscles in a human neck, the muscle connections were to be ignored for this experiment: to aim for a model that would be a cross between an anatomically correct neck and the straight rod in the previous design option. By focusing on the cervical column itself, a CT scan of a neck could be converted to a STL file and printed. This would include soft discs in the design by using a multi material 3D printer.

An anonymized CT scan was used to create the 3D spine model. The open-source program Slicer 3D was used to convert the DICOM data to an STL file. Threshold values were chosen such that the bone in the CT scan was isolated. The program thresholds were unable to reliably pull out the soft tissues of the intervertebral discs as compared to the other soft tissues in the neck, so the 3D model was isolated to the cervical bones only. Figure 5.16 shows the mineralized

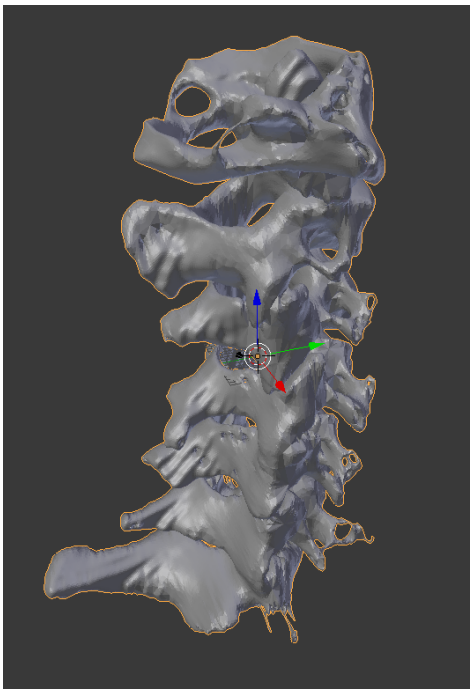

Figure 5.17: The cleaned version of the neck STL produced by Slicer 3D. The base is not yet modified.

tissue isolated into a 3D model.

Blender, another open source 3D modelling software, was used to clean up the exported STL file and to further reduce the computational size via optimization. The cleaned version of the STL can be seen in Figure 5.17.

After the optimization in Blender, the file was appropriately small enough to be imported into SolidWorks. The file was imported to SolidWorks to add a base to the bottom of C7 in order to be press-fit into a mount on a F/T sensor. Before each print, the final STL file from SolidWorks was then checked in Autodesk MeshMixer to correct any build errors before printing.

A number of iterations of the spine were created from this point. Issues encountered included the scaling being too large for the average male, the assembly with spine and head (discussion on the head model can be found in Section 5.3.2.2) being too large for SolidWorks to process, and brittle connections between the vertebra causing the spine to snap during the press-fit mounting. One of the failed iterations can be seen in Figure 5.18.

These figures show the attempt that had the cervical column snap between C6 and C7 while press fitting into neck mount. To test the strength of the rest of the 3Dprinted joints before printing another prototype, C6 was adhered back onto C7

(a) C7 through C3, shown here pressfit into the mount.

(b) C2 (Axis), having snapped out of the column at both the C1–C2 and C2–C3 joints.

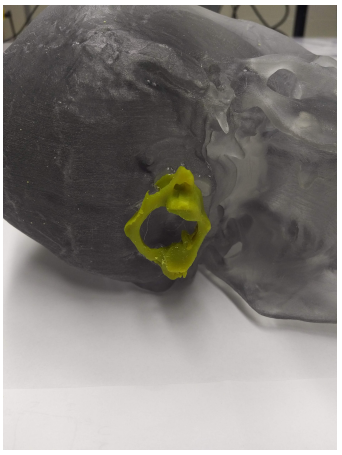

(c) C1 (Atlas), shown here attached to C0 on the skull.

Figure 5.18: One of the spinal column iteration failures. The atlas snapped out of the column due to the weight of the skull.

using HMA. The skull (described in Section 5.3.2.2) was connected to the cervical spine by using HMA at the atlanto–axial joint. When stood upright, the weight of the head caused too much of a moment for the plastic connections between the joints without the support from musculature. The part failed at both the C1–C2 and C2–C3 joints. The glued C6–C7 held fine.

A new mount was printed, using just the C1 vertebra: to measure the forces at the top of the cervical spine, instead of at the base of the spine. This allows for biomechanics modelling to calculate the anticipated forces over the entire neck. It also allows for a more accurate connection to the skull and removes the problem of supporting the fragile bone structure without the soft tissues.

In order to avoid the weak points, the C1 vertebra was modified to sit in the mount directly, cutting out C2–C7, on an angle such that the angle between C0 and C1 was approximately 10°, so that the head would sit at a typical angle with respect to the floor plane. The final iteration can be seen in the mount in Figure 5.19.

5.3.2.2 Skull Model

A scan of an anatomical model skull was available from Embodi3d, and originally posted by Dr. Marco Vettorello on Thingiverse [128]. The file was first imported

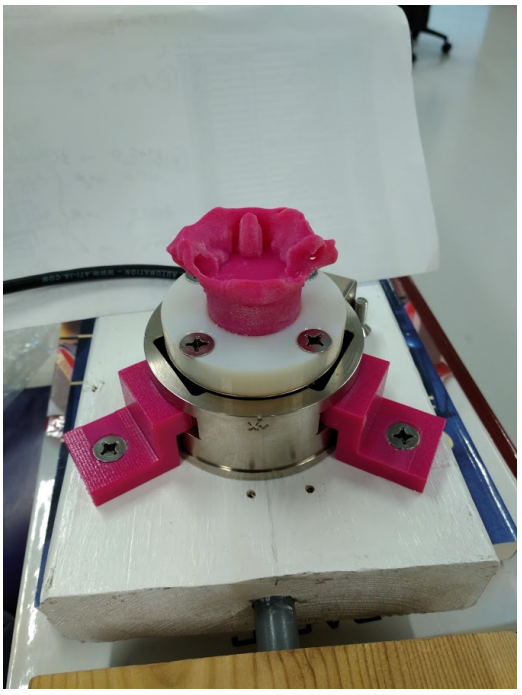

Figure 5.19: The final iteration of the neck mount for the experimental setup—a modified cervical CT scan with only the C1 vertebra (atlas), printed on a pressfit mount to connect to the F/T sensor.

to Blender to clean and optimize the size, as was done with the cervical spine in the previous section. After this optimization, the STL file was imported into SolidWorks so a cylinder could be carved out at the approximate location of the COM of the average male head. The intention of this was both to reduce the amount of material the 3D print would require, and to allow for the possibility of adding weight to the skull before the experiments, to be closer to the weight of the 50^{th} percentile human male head—approximately 4.91 kg.

In order to do this, the model was cut into eight sections parallel to the three anatomical planes—along the transverse, coronal, and sagittal planes, through the COM point. Most anthropomorphic measurement landmarks (as seen in Chapter 3) for the head are a fleshy landmark, so a best attempt was made at finding those landmarks on the skull bones. On the skull, the tragion is approximately located at the porion (the superior margin of the external auditory meatus). A best estimate was used for both the location of the head against a wall and the vertex. The skull measurements from these landmarks were fed into the equations for the COM given in Chapter 3, Equations 3.12–3.14, giving the approximate location of the COM of a human head on the skull model.

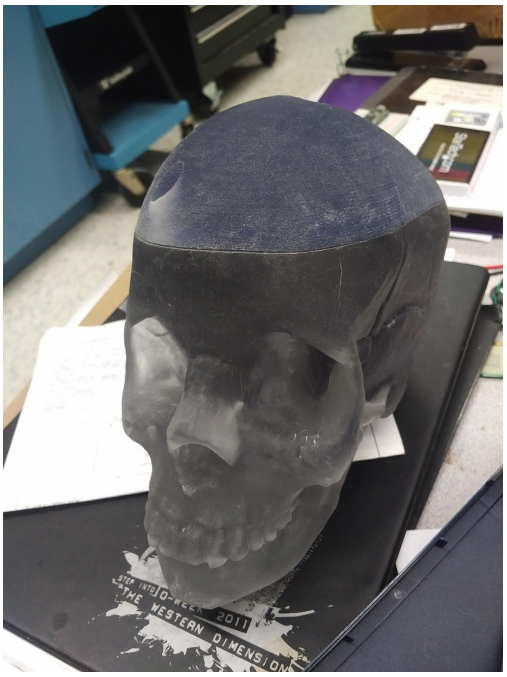

(a) The 3D printed skull with the cap on. One of the screw holes can be see on the left-hand side of the cap.

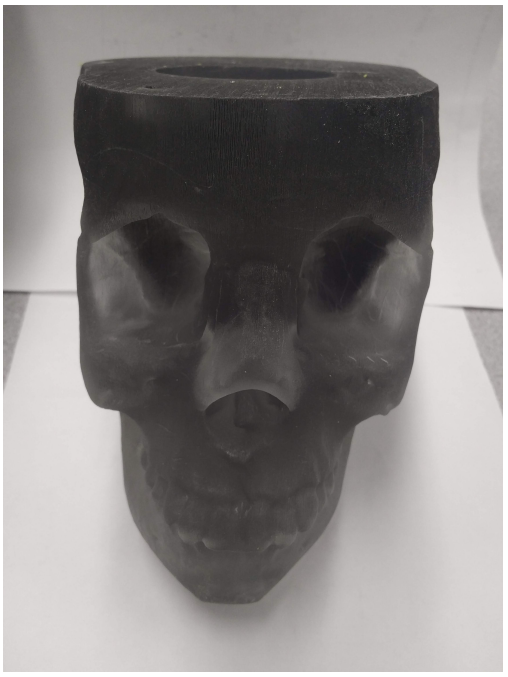

(b) The 3D printed skull with the cap off. The hollowed COM cylinder can be seen on the top flat.

Figure 5.20: The 3D printed skull.

These eight parts were then used to hollow out the cylinder around the COM. The inner corner of each piece being the location of the COM, so the extruded cut was made at a constant radius across each piece from that centre point along the transverse plane, and extended the same amount into the piece perpendicular to the transverse plane.

The head was then re-assembled in SolidWorks as an assembly, and a cap was cut off at the same vertical height that the COM extruded cut ended. The skull was re-scaled to be approximately the same size as the model described in Chapter 3. Two measurements were looked at: tragion to wall and tragion to crown. The scaling factor for these were 1.064 and 1.079, so a scaling factor of 1.08 was applied to the entire assembly. The printed skull with and without the cap in place can be seen in Figure 5.20. Three screw holes (for flat head M6 screws) were added to the cap and threaded holes to the skull in order to hold the cap on while using the skull for testing. These threaded holes were included in the STL print file, but the print quality was lower for the skull than the other threaded parts in the system and the screws to hold the cap on could not be fully tightened.

After printing, the head weighed about 2.4 kg. Because the screws were unable

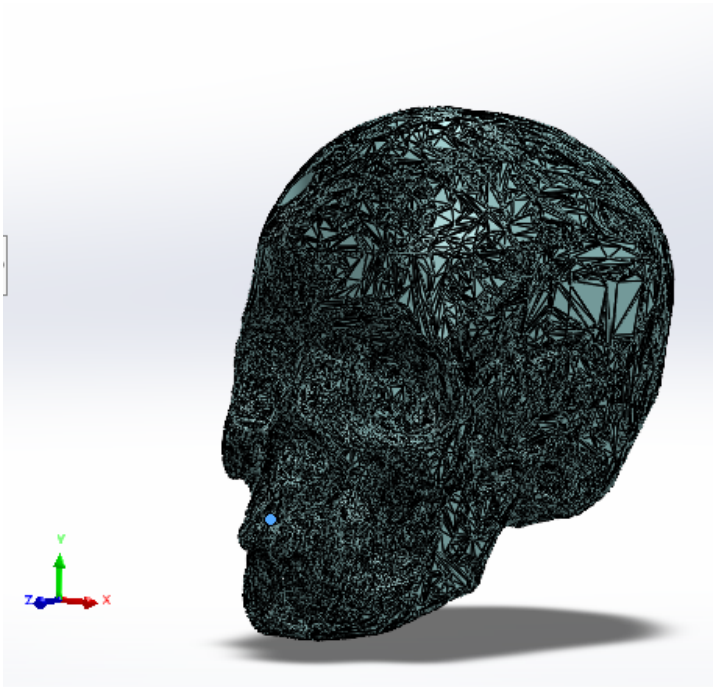

Figure 5.21: The skull model in SolidWorks, re-assembled from the eight pieces and cap. The landmark on the anterior nasal spine can be seen on the lower left of the model, indicated with a pale blue dot. The orientation of the model can also be seen on the bottom left corner, showing the x-, y-, and z-axes. Skull model adapted from [128].

to be fully tightened and the use of added weight could complicate the principal axes and moments of inertia and the inertia tensor, it was decided that it would be better to not fill the printed skull to a proper weight. The weight measured and the SolidWorks-calculated model moments of inertia would be used instead to validate the dynamics model.

In order to know the position of the COM in the real-world system, a "landmark" was chosen on the skull that could be measured with respect to the position sensor. Measuring from this landmark to the COM in the SolidWorks model would allow the use of vector subtraction to find the position of the COM with respect to the position sensor. A bony protuberance exists on the maxilla between the nasal aperture and the teeth, called the anterior nasal spine. This point can be seen as the pale dot in Figure 5.21

The faces of the anatomical plane cuts in the assembly were used to re-orient the skull along the output coordinate system of SolidWorks (mated with the front/right/top planes). The skull assembly was positioned such that the landmark was co-located with the origin of the assembly. The mass and moments of iner-

tia data were then pulled from the Mass Properties of the model, using the Vero material used in the printer as the applied material for the skull model pieces. The mass of the head assembly, including the three screws, was calculated to be 2,384.53 grams. The principal axes of inertia, with respect to the SolidWorks orientation, were calculated to be

$$\hat{\mathbf{i}}_{\mathbf{H}} = \begin{bmatrix} 0.00 \\ -0.29 \\ 0.96 \end{bmatrix} \quad \hat{\mathbf{j}}_{\mathbf{H}} = \begin{bmatrix} -0.05 \\ -0.95 \\ -0.29 \end{bmatrix} \quad \hat{\mathbf{k}}_{\mathbf{H}} = \begin{bmatrix} 1.00 \\ -0.05 \\ -0.02 \end{bmatrix} \tag{5.24}$$

where the values of the principal moments of inertia (P_H), in $g \cdot mm^2$ were calculated to be as follows:

$$\begin{aligned} P_{H_x} &= 6,146,383.34\ \hat{\mathbf{i}}_{\mathbf{H}} \\ P_{H_y} &= 8,123,580.47\ \hat{\mathbf{j}}_{\mathbf{H}} \\ P_{H_z} &= 9,719,428.66\ \hat{\mathbf{k}}_{\mathbf{H}} \end{aligned} \tag{5.25}$$

SolidWorks also calculated the values of the Inertia tensor at the COM of the assembly using the SolidWorks orientation (the coordinate frame can be seen in Figure 5.21):

$$\mathbf{I_H} = \begin{bmatrix} 9,714,668.16 & 79,861.41 & 35,447.40 \\ 79,861.41 & 7,956,821.32 & -557,194.48 \\ 35,447.40 & -557,194.48 & 6,317,902.99 \end{bmatrix} \tag{5.26}$$

Seeing as the principal axes for the skull are closely aligned with the SolidWorks orientation, the principal axes were rounded to the nearest one.

Rounded unit vectors:

$$\hat{\mathbf{i}}_{\mathbf{H}} = \begin{bmatrix} 0 \\ 0 \\ 1 \end{bmatrix} \quad \hat{\mathbf{j}}_{\mathbf{H}} = \begin{bmatrix} 0 \\ -1 \\ 0 \end{bmatrix} \quad \hat{\mathbf{k}}_{\mathbf{H}} = \begin{bmatrix} 1 \\ 0 \\ 0 \end{bmatrix} \tag{5.27}$$

$$\hat{\mathbf{u}}_{\mathbf{H}} = \left[\hat{\mathbf{i}}_{\mathbf{H}}, \hat{\mathbf{j}}_{\mathbf{H}}, \hat{\mathbf{k}}_{\mathbf{H}}\right] \tag{5.28}$$

Since principal moments of inertia are always a positive value, the unit vector was applied to the inertia tensor and had the absolute value taken:

$$I_H^{SW} = \hat{\mathbf{u_H}} \cdot P_H \tag{5.29}$$
$$= \begin{bmatrix} 0 & 0 & 1 \\ 0 & -1 & 0 \\ 1 & 0 & 0 \end{bmatrix} \cdot \begin{bmatrix} P_{H_x} \\ P_{H_y} \\ P_{H_z} \end{bmatrix}$$
$$I_H^{SW} = \begin{bmatrix} P_{H_z} \\ P_{H_y} \\ P_{H_x} \end{bmatrix} \tag{5.30}$$

As with the cage and wheel, the P_{H_i} terms needed to be represented in the Base Frame (as used in Chapter 4), the same rotational transformation matrix was used (Equation 5.7). This rotation matrix was applied to the principal moments of inertia:

$$I_H = \mathbf{R_B^{SW}}^T \cdot I_H^{SW} \tag{5.31}$$
$$= \begin{bmatrix} 0 & 1 & 0 \\ 0 & 0 & 1 \\ 1 & 0 & 0 \end{bmatrix}^T \cdot \begin{bmatrix} P_{H_z} \\ P_{H_y} \\ P_{H_x} \end{bmatrix}$$
$$I_H = \begin{bmatrix} P_{H_x} \\ P_{H_z} \\ P_{H_y} \end{bmatrix} \tag{5.32}$$

The Mass Properties and Measure tool within SolidWorks calculated location of the COM in the SolidWorks coordinate frame (in mm), as measured from the origin (the anterior nasal spine landmark) to the COM, as shown in Figure 5.22:

$$\vec{d}_{H_{COM}}^{SW} = \begin{bmatrix} 1.33 \\ 48.24 \\ -106.04 \end{bmatrix} \tag{5.33}$$

The same rotation matrix as above was used to transform this landmark–COM distance to be expressed in the Base Frame coordinates:

$$\vec{d}_{H_{COM}}^{B} = \mathbf{R_B^{SW}}^T \cdot \vec{d}_H^{SW}{}_{COM} \tag{5.34}$$

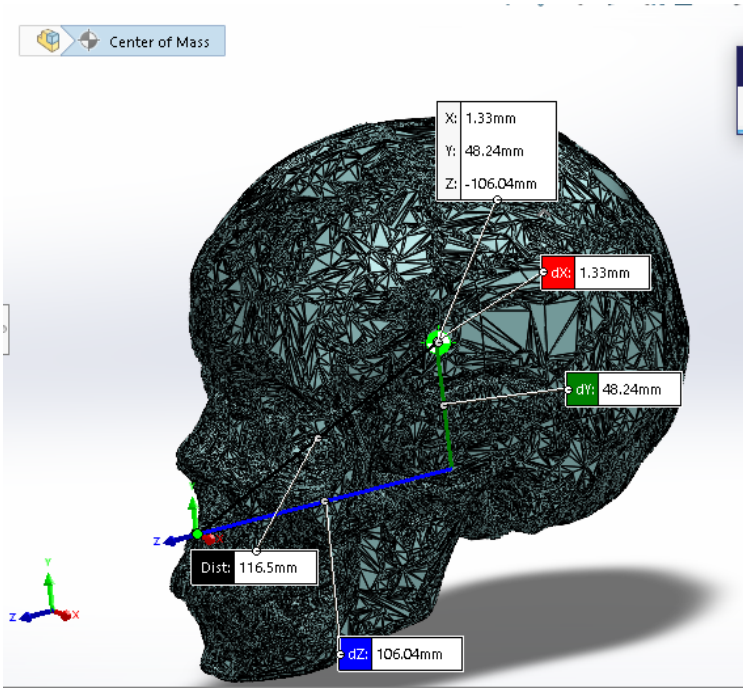

Figure 5.22: The location of the skull COM in SolidWorks, as measured in mm from the landmark on the anterior nasal spine.

$$= \begin{bmatrix} 0 & 1 & 0 \\ 0 & 0 & 1 \\ 1 & 0 & 0 \end{bmatrix}^T \cdot \begin{bmatrix} 1.33 \\ 48.24 \\ -106.04 \end{bmatrix}$$

$$\vec{d^B_{H_{COM}}} = \begin{bmatrix} -106.04 \\ 1.33 \\ 48.24 \end{bmatrix} \tag{5.35}$$

5.4 Concluding Statement

This chapter presented the initial prototype design for a gyroscope based stabilizer for a human head. The proposed design still needs to be optimized, but that first requires a validated dynamics model for the system. To this end, this chapter also presented the setup for an experiment designed to validate the dynamics equations presented in Chapter 4.

Chapter 6

Validating the Theoretical Model

The previous chapter described the experimental setup to test the validity of the theoretical model proposed in Chapter 4. It also covered the design and fabrication of both the prototype gyroscopic resistive device and the device for the validation experiment. This chapter outlines the experimental protocol and the data collection, processing, analysis, and results of these experiments. The results are presented in Section 6.4, followed by the results discussion.

6.1 Experimental Protocol

6.1.1 Objective

The objective of this experiment was to validate the theoretical system model calculated in Section 4.2 against a real-world system.

6.1.2 Hypothesis

It was hypothesized that the theoretical equations would match reality, with the predicted torques (calculated using the measured position, velocity, and acceleration data) from the model falling within 10% of the torque measured in the system during the experiments.

6.1.3 Experimental Setup

An in-depth look at the system design and experimental setup before the start of the experiment can be found in Section 5.3.2 in the previous chapter. The

Figure 6.1: The rotation apparatus.

ATI sensor was mounted using two plastic mounts to the wooden board of the rotation apparatus (Figures 6.1 and 6.2a), and the base mount was screwed into the sensor (Figure 6.2b). The skull–C1 assembly (Figure 6.2c) was then press-fit into the mount (an image of C1 in the mount without the skull attached can be seen in Figure 6.2d). A stack of books was placed underneath the wooden rotation apparatus to prevent the system from tilting when not actively collecting data, as this would cause parts of the assembly to fall from the system. The resulting setup can be seen in Figure 6.2e.

6.1.4 Methods

The method to calibrate the system and collect data included the following steps:

1. The hook-and-loop fastener on the prototype harness was taken apart and re-strapped to the skull (see Figure 5.3 in the previous chapter for the prototype harness).

2. The Aurora system (shown in Figure 6.4) was set up as follows:

   (a) The *Aurora Sensor1* was attached to the skull sensor arm, shown in Figure 6.3b

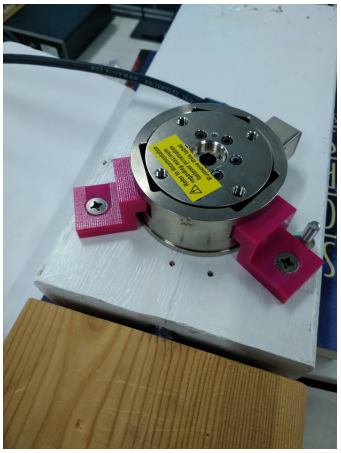

(a) ATI F/T sensor mounted to the rotation board.

(b) Base mount attached to the F/T sensor.

(c) C1 attached to the skull.

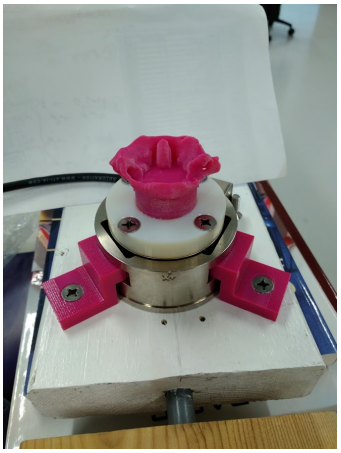

(d) C1 press fit into the base mount.

(e) The full experimental setup.

Figure 6.2: Experimental setup.

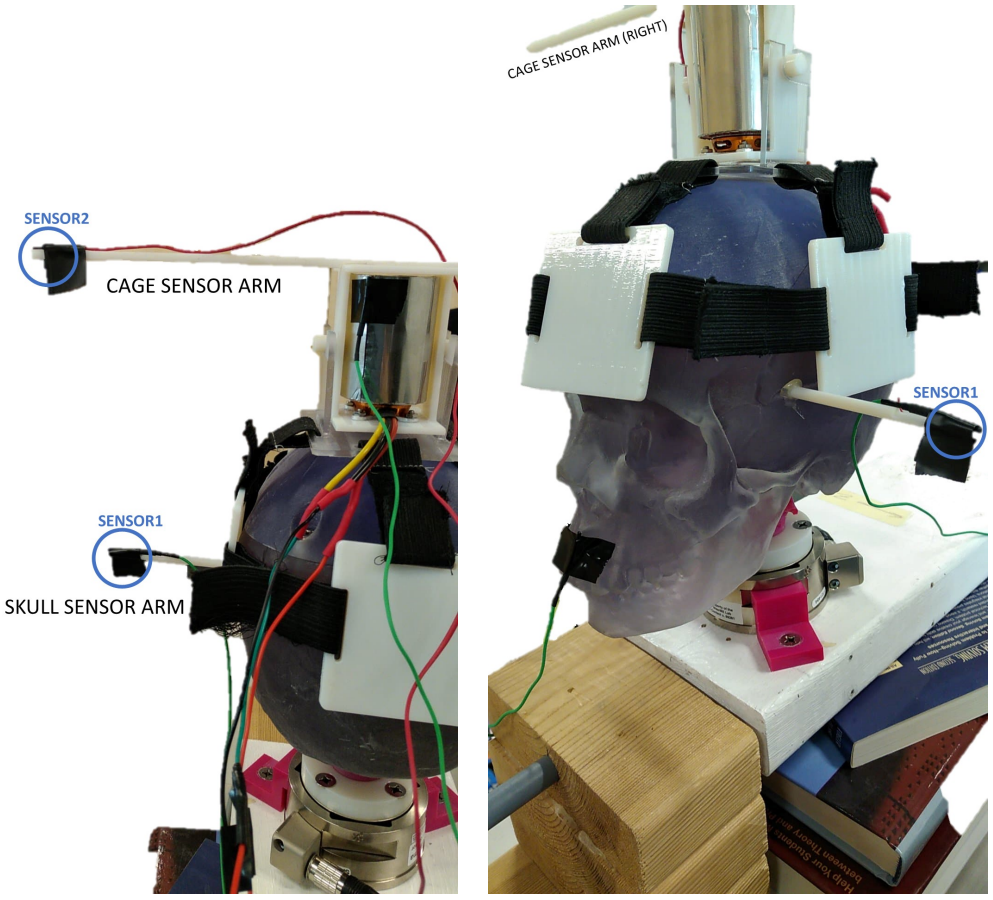

(a) Cage and skull sensor arms can be seen to the left of the system. The cage sensor arm is attached to the top of the gyroscope cage, and the skull sensor arm is attached to the skull.

(b) Skull sensor arm attached on the parietal bone near the junction of the frontal, parietal, and temporal bones.

Figure 6.3: Sensor arm placement.

(b) The *Aurora Sensor2* was attached to the cage sensor arm, as seen in Figure 6.3a.

(c) Both Aurora sensors were plugged into the Aurora Sensor Unit (Figure 6.4b).

(d) the Aurora system (Figure 6.4) was connected as instructed by the manufacturer.

(e) The Aurora tracking software ("NDI Track") was started on the PC.

(f) Set NDI Track to record "Euler Angles".

3. Measurements required for calibration and analysis were obtained using a

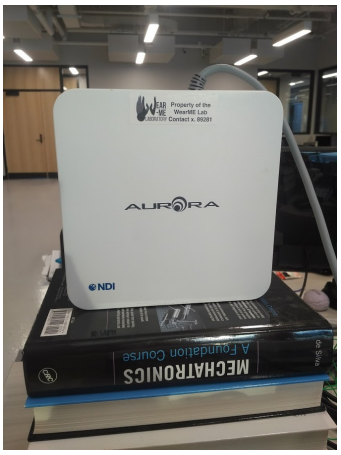

(a) The Aurora Field Generator.

(b) The Aurora Sensor Unit. The sensor cables are connected at the front, as shown.

(c) Aurora Control System Unit. This connects to the PC, wall outlet, sensor control unit, and the field generator.

Figure 6.4: The Aurora system: the Field Generator (6.4a) and the Sensor Unit (6.4b) are connected to the Control System Unit (6.4c). The Control System Unit is connected to the PC and a wall outlet.

third Aurora sensor:

(a) The sensor used was taped to a number of specific locations on the system, as described below in Step 3e.

(b) NDI Track was set to record with the following settings: Frame Rate: 40 Hz.

(c) Position data from the Aurora were collected from the static system for at least 4 seconds for each of the measurements described below in Step 3e.

(d) To ensure the data recorded in the output file were correct, the experimenter recorded, in a separate text file, the approximate x, y, and z translation data as displayed by the NDI Track program GUI for each measurement described below in Step 3e.

(e) The following landmarks and other measurements were recorded:

   i. The Skull Landmark (as described in Section 5.3.2.2 and shown in Figure 6.5). The tip of the sensor was taped against the landmark to record translation in all three directions.

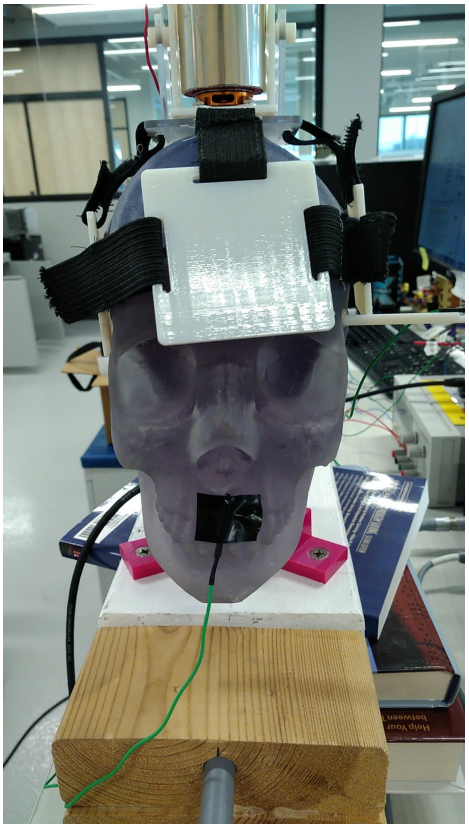

(a) Skull landmark on the experimental setup.

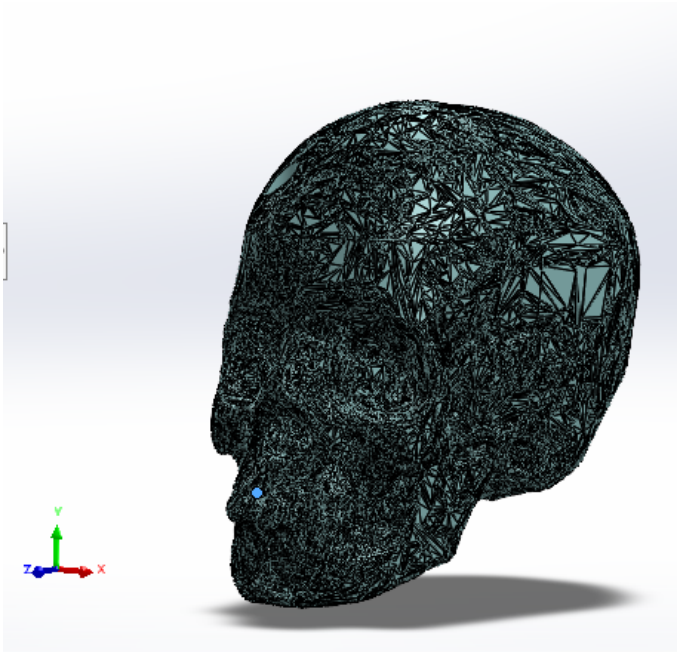

(b) Skull landmark on the SolidWorks model. Indicated with a pale dot.

Figure 6.5: Location of skull landmark on the experimental setup and on the 3D model. Located at the anterior nasal spine.

ii. The Cage Landmark (as described in Section 5.3.1.1 and shown in Figure 6.6). Since the landmark for the cage is the same position as the position of *Aurora Sensor2* (Step 2b), the initial position of this sensor was used instead to record translation in all three directions.

iii. The Wheel Landmark (as described in Section 5.3.1.2 and shown in Figure 6.7). This was recorded to be the location of *sensor*2, as shown in the Figure 5.10.

iv. A non-Landmark Wheel location was also recorded. The tip of the sensor was taped against the wheel at the seam of the EMI-shielding film, to record translation in all three directions.

v. The base. To measure this position, data were collected in two locations, which can be seen in Figure 6.8:

A. *Aurora Sensor3* was taped at the midpoint of the rotation board (opposite to the rotation handle), which was marked with centering lines. The Aurora x and z translations were recorded at this position.

B. *Aurora Sensor3* was taped in line with the "x" label on the ATI sensor (The label for the x axis for the internal ATI frame of reference). The Aurora y translation was recorded at this position.

vi. The x translation at the axis of rotation of Joint2 (the gyro cage). The tip of the sensor was taped at the axis of rotation of the gyro cage, which can be seen in Figure 6.9.

4. The ATI system (shown in Figure 6.10) was set up as follows:

(a) The ATI Gamma F/T sensor (Figure 6.10a) was connected to the Data Acquisition (DAQ)Interface Power Supply (Figure 6.10b).

(b) The Power Supply was plugged into both an outlet and the NI DAQ (Figure 6.10c). All wires in the Power Supply-to-DAQ cable were checked to ensure that they were all still properly connected to the screw terminals.

(c) The NI DAQ was plugged into the computer.

(d) The ATI NI DAQ software ("ATI DAQ F/T .NET") was loaded on the PC.

(a) Cage landmark on the experimental setup; the same location as *sensor*2 for data collection.

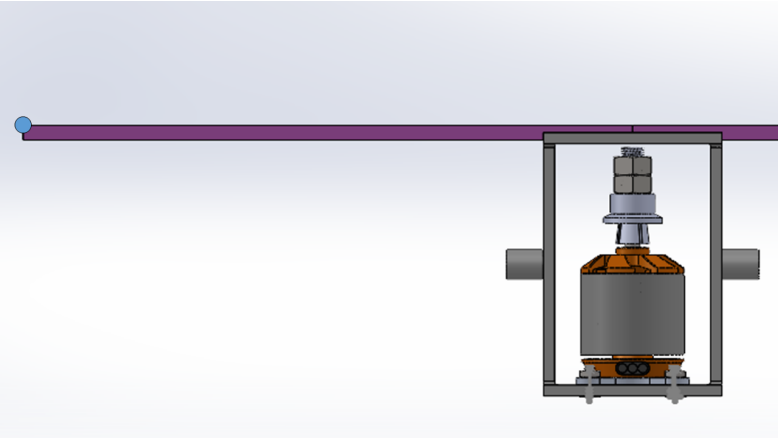

(b) Cage landmark on the SolidWorks model. Indicated on the left hand side by a pale dot.

Figure 6.6: Location of cage landmark on the experimental setup and on the 3D model.

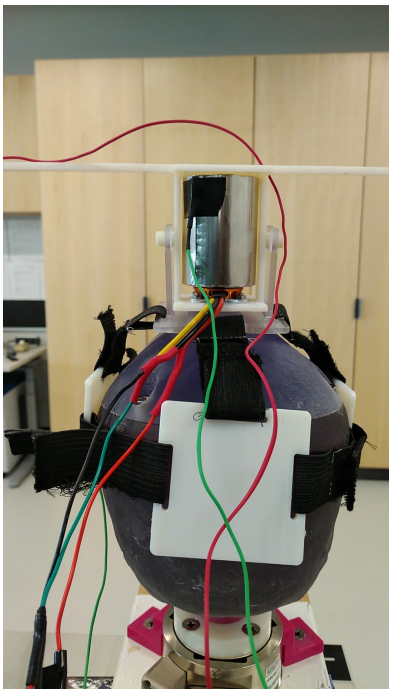

Figure 6.7: Location of additional wheel landmark on the experimental setup; at the seam of the EMI-shielding film.

(e) The program option "Bias" was then used to zero the sensor.

5. The Arduino system (shown in Figure 6.11) was set up as follows:

   (a) The ESC board for the gyroscope wheel was connected to the Arduino (via a breadboard, as seen in Figure 6.11). The three ESC-to-motor wires, being interchangeable (as they control direction), had the direction they were wired for recorded.

   (b) Connections on the breadboard were checked for proper placement and connection for the following connections:

      i. Pin 13 and Ground on the Arduino were connected to the ESC input.

      ii. The external variable DC Power Supply connected directly to the ESC power input wires.

      iii. The ESC output wires connected to the three input wires for the motor.

   (c) Plugged the Arduino into the PC via USB.

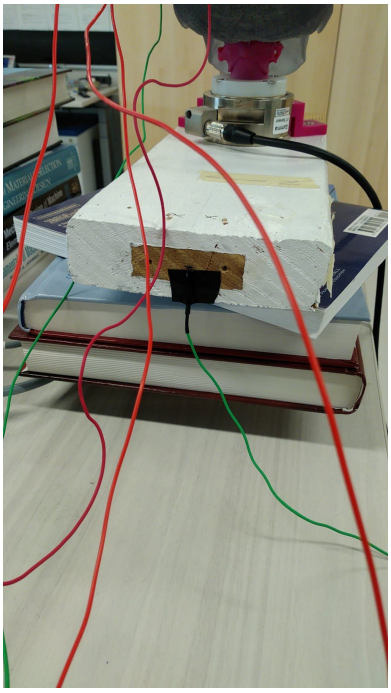

(a) Location of the sensor to measure the x and z distances for the base, where x is distance top-to-bottom and z is distance right-to-left in this image.

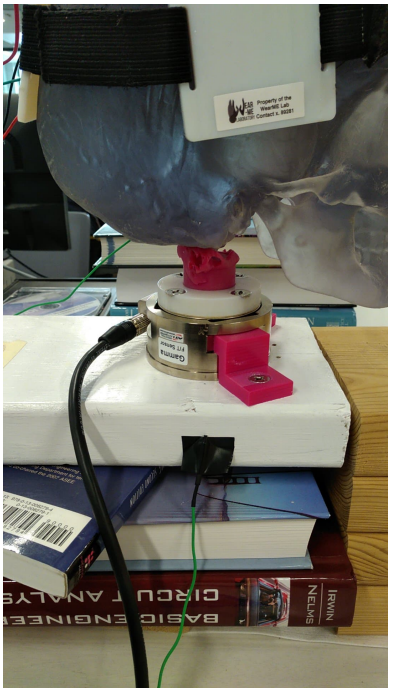

(b) Location of the sensor to measure the y distance of the base, where y is distance right-to-left in this image.

Figure 6.8: Location of measurements for the base x, y, and z positions.

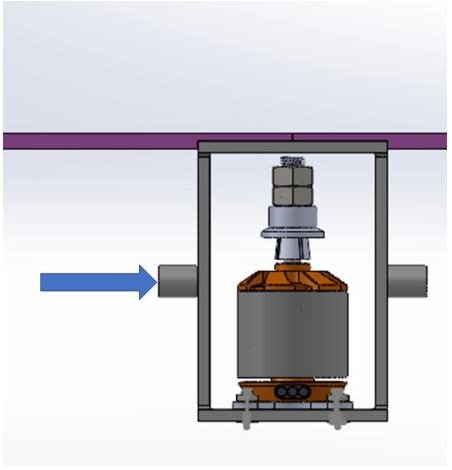

Figure 6.9: SolidWorks model showing where the Aurora sensor was placed for the Joint2 x measurement.

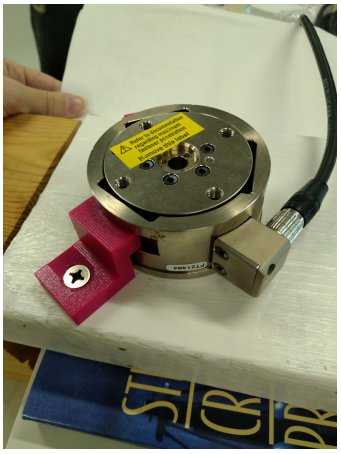

(a) The ATI Gamma F/T sensor. Cable connects to the Power Supply.

(b) The DAQ Interface Power Supply. Connects to the ATI sensor (left), and the NI DAQ (right) and wall outlet.

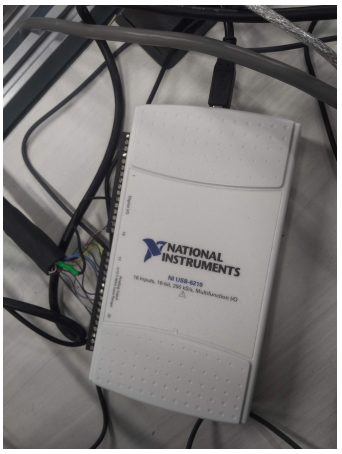

(c) The NI DAQ. Cables wired by experimenter. Connects to the Power Supply (left) and PC (top).

Figure 6.10: The ATI system: the ATI F/T Gamma Sensor (6.10a) is connected to the DAQ Interface Power Supply (6.10b). The Power Supply is connected to the DAQ and a wall outlet. The NI DAQ (6.10c) accepts signals from the DAQ Interface Power Supply via screw terminal connections and is connected to the PC.

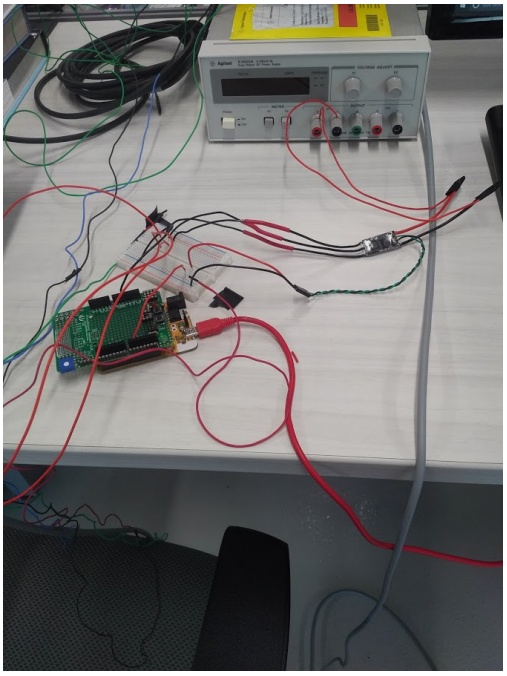

(a) The Arduino–PC and –breadboard connections, breadboard–ESC board connections, and ESC–power supply connections.

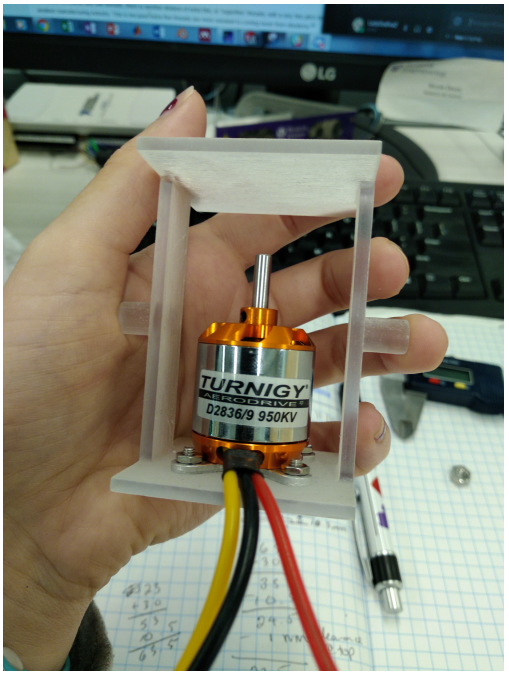

(b) Motor (mounted here to the cage) connected to the Arduino system via the three wires at the bottom of the image.

Figure 6.11: Arduino system and wiring connections, including the motor and ESC.

(d) The Arduino IDE ("Arduino") was loaded on the PC and the Arduino Serial Monitor was opened.

(e) The variable DC Power Supply was turned on and set to 12 V.

(f) To program the ESC, the following set of commands were sent via the Serial Monitor: (0, 1, 800, 2000, 1500)

(g) After this initialization, "2000" was sent over Serial to start the motor.

6. The Aurora and ATI sensor DAQ were set to record.

   (a) The settings for the Aurora were as follows: Delay before start: 2 seconds, Frame Rate: 40 Hz.

   (b) The settings for the ATI were as follows: Sampling rate: 1000 Hz, Delay Before Start: None, Stop Condition: Stop Button Pressed.

7. The top book holding the system level was removed.

8. The test was conducted by turning the rotation platform approximately 10–15 degrees off perpendicular to the ground, and back to approximately perpendicular to ground. During each trial, the platform was rotated three times towards the Aurora Field Generator (Left Lateral Flexion, counter clockwise motion), and then three times away from the Field Generator (Right Lateral Flexion, clockwise motion).

9. Data collection was stopped.

10. This method (Steps 5g–9) was run three times with the motor running before the start of the trial (as described in Step 5g), and three times with Step 5g performed after data collection had started—immediately after Step 6, resulting in six sets of data, each with three sets of six motions recorded.

6.2 Data Validation and Calculation

To validate and calibrate the data from the two sensors—the Aurora electromagnetic tracking system (position data) and the ATI force/torque sensor (force/-torque data)—the raw datasets were validated, interpolated, and filtered (Section 6.2.1) and then used to calculate the position, velocity, and acceleration of the

system bodies, and synchronized across the two sampling frequencies (Sections 6.2.2 and 6.2.3). The MATLAB scripts used can be found in a GitHub repository, linked in Appendix A.

6.2.1 Position Data Validation

All codes used for preprocessing the position (Aurora) data can be found in the linked GitHub repository in Appendix A, and the main script for the validation of the Aurora datasets is `auroraPreProcess.m`. The script was run for each set of experiment data. The datasets were imported from the original CSV output files to MATLAB using the `timetable` table format. The `Rz`, `Ry`, `Rz`, `Tx`, `Ty`, `Tz` measurements for both sensors were imported using the Aurora frequency of 40 Hz, resulting in the `clean` version where the superfluous data deleted and each data column labelled with its respective sensor (s_1 and s_2).

Preliminary verification of the datasets occurred next. Each set was checked to ensure that the correct number of sensors was detected; for the experiment sets, this was two. An error occurred with the Aurora system during data collection, affecting the cage sensor *sensor2*. The sensor was not recognized for a number of trials, and therefore no data were collected. This issue affected the third set in the second trial (exp2-3), and the entire third and fourth trials (exp3-1 through exp4-3). These datasets were subsequently removed from the pool of available experimental data. The raw datasets were graphed and an example set can be seen in Figure 6.12. The data from the Aurora were plotted showing each channel for both sensors using the `plotAurora` function (available on GitHub).

Each dataset was then checked for errors. The Aurora system records the value as `-3.70E+20` when the individual data point was not recorded properly, which produces the vertical lines seen in the raw data graphs in Figure 6.12. These errors were located and replaced by linear interpolation using the `fixerrors.m` function (available on GitHub). An example of the interpolated data can be seen in Figure 6.13. The interpolated datasets was then filtered, using the `filterTT.m` function (available on GitHub), which uses a low-pass sixth-order Butterworth filter. The filtering process used the `butter` and `filtfilt` functions available in the Signal Processing Toolbox; the process to use this specific filter followed the process by Trejos in 2012 [129]. The filter was designed to use 0.5 Hz as the cutoff frequency. One set of filtered data can be seen plotted in Figure 6.14.

In order to separate and isolate the datasets in each experiment set—that is,

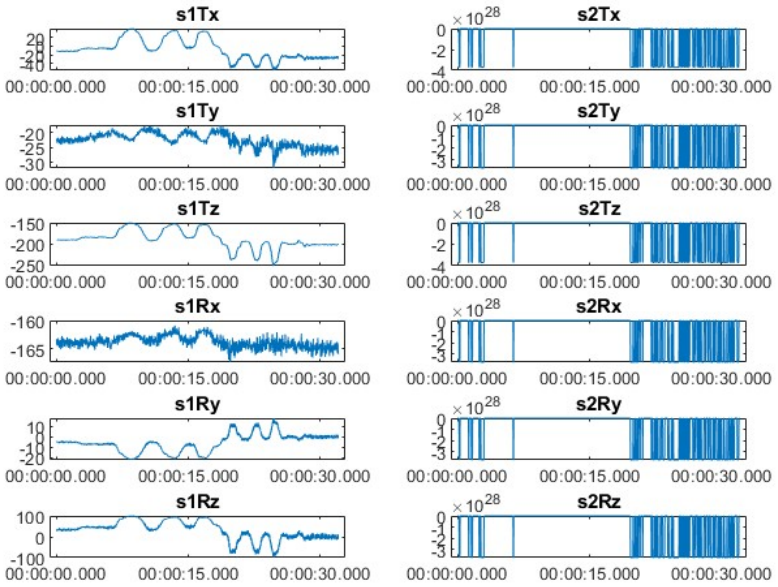

(a) Experiment set 1-3.

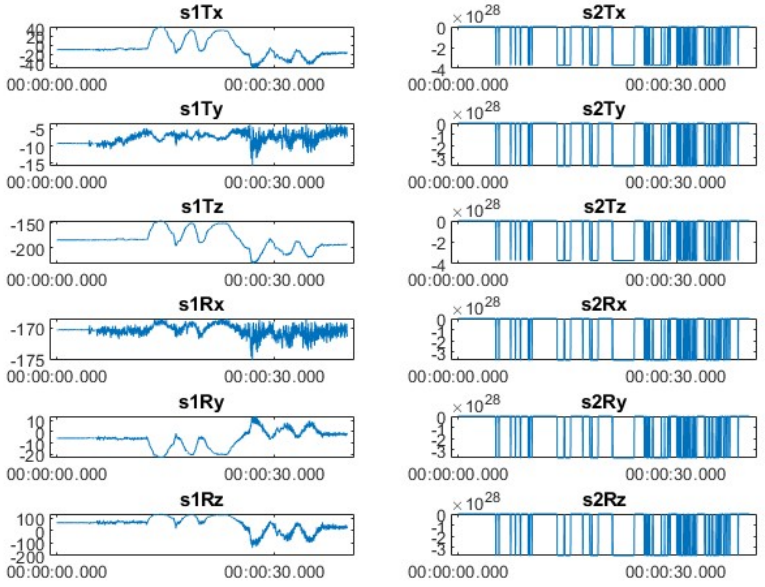

(b) Experiment set 2-1.

Figure 6.12: Two example sets of the raw data displayed in each translation and orientation direction. The vertical lines in the right column plots indicate "error" data points due to magnetic interference from the gyroscope motor. Each dataset was similar in the second half of 6.12a, and the excessive error in 6.12b invalidated the entire exp2-1 set.

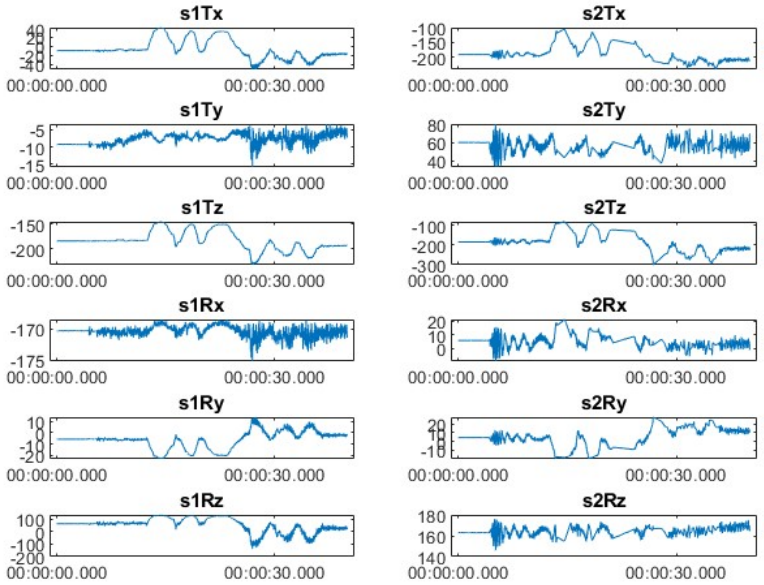

Figure 6.13: The interpolated results for Exp2-1 (a dataset with significant interpolation in both the A and B sets). The raw data for this set can be seen in Figure 6.12b.

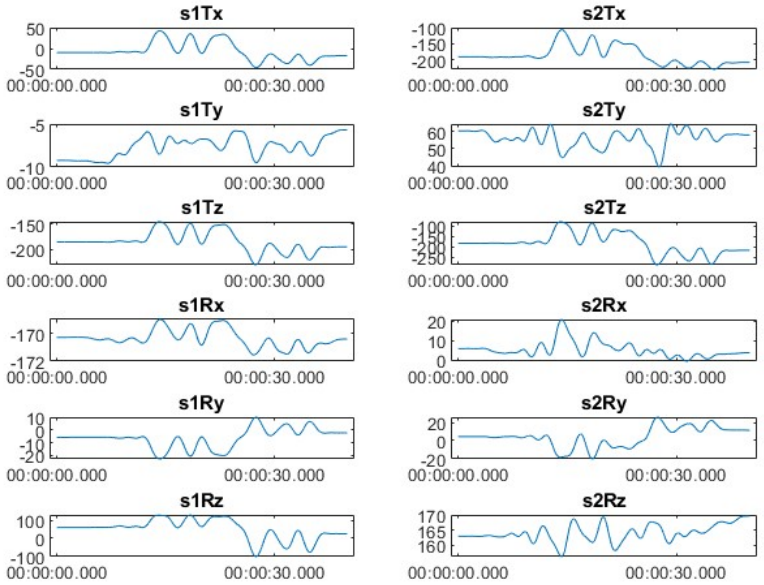

Figure 6.14: The filtered results for Exp2-1 (a dataset with significant interpolation in both the A and B sets).

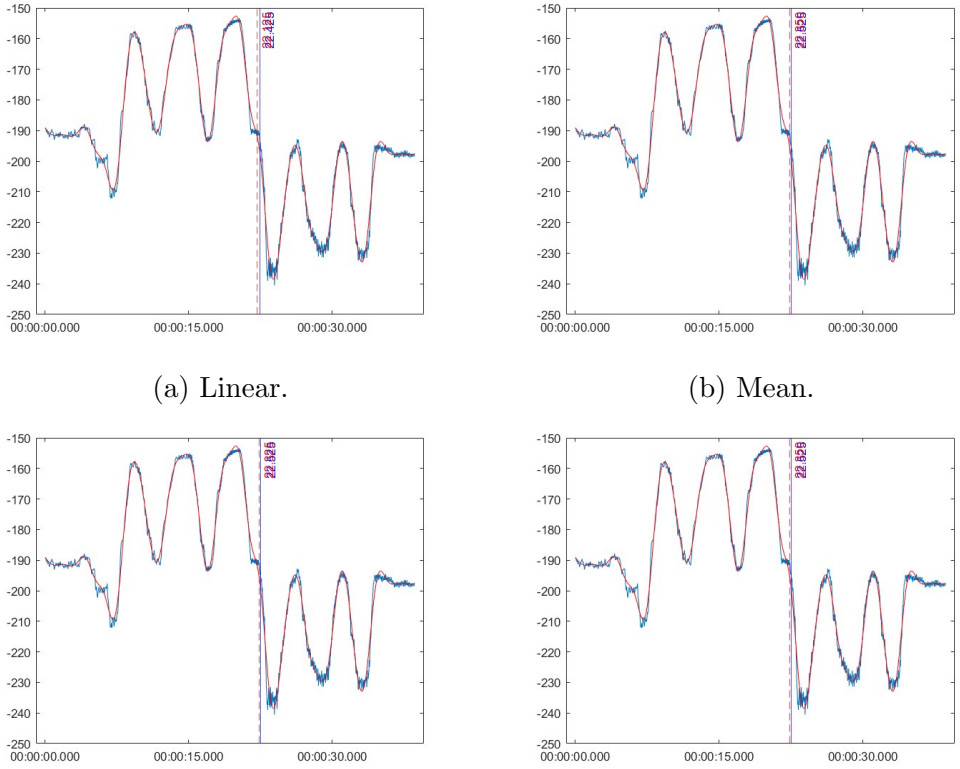

(a) Linear.

(b) Mean.

(c) RMS.

(d) STD.

Figure 6.15: Comparing the raw (blue) and filtered (red) results of `findchagepts` for each statistic available for analysis, on the Exp 1-1 dataset.

extracting the 'A' set (motion in the right lateral direction) and 'B' set (motion in the left lateral direction)—the MATLAB function `findchangepts` from the Signal Processing Toolbox was used to locate the inflection point, or the point at which the data changed direction. This function provided the point in the data where the mean had the least error residual for each section of the data. Functionally, this function gives the index at which the mean of the input changes most significantly. For completeness, all four function options were tested (`linear`, `std` (Standard deviation (STD)), `mean`, and `rms`), on both the raw and the filtered data. A comparison of the four options can be see in Figure 6.15. The option to use the change in mean (`mean`) was chosen for each set. An example of the output plots from this can be seen in Figure 6.16 for Exp1-1.

The chosen statistic (`mean`) was applied to each channel in the dataset and graphed; an example graph of the results for each channel can be seen in Figures 6.17 and 6.18, for `mean` and `std`, respectively. The locations of the inflection points

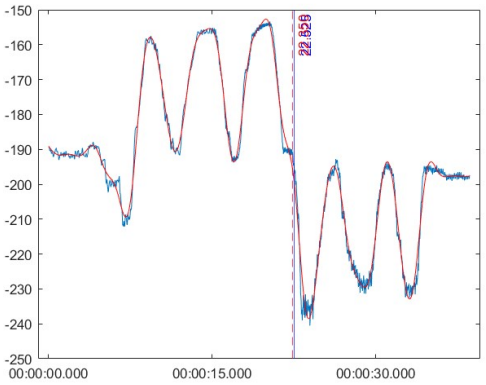

(a) The change point for both the raw (blue) and filtered (red) data overlaid on the same plot.

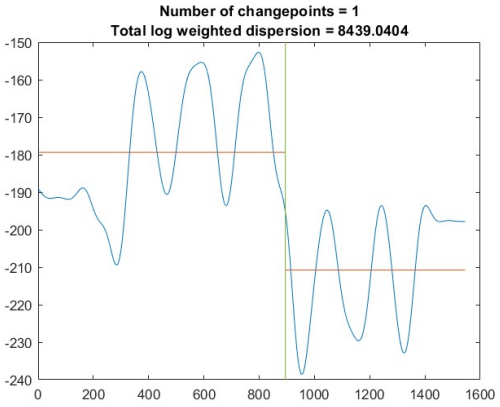

(b) The `findchangepts` plot result for the filtered data.

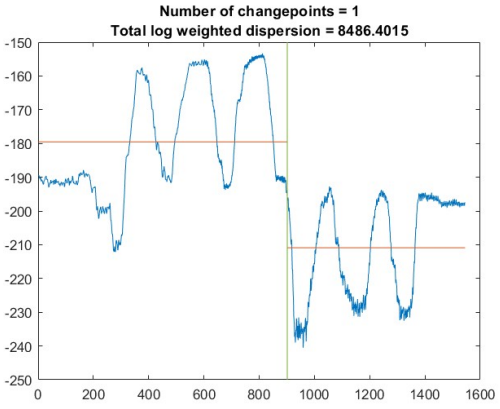

(c) The `findchangepts` plot result for the raw data.

Figure 6.16: Graphs showing the points with the largest change in standard deviation (`std`) in the Exp 1-1 dataset, using the `s1Tz` data.

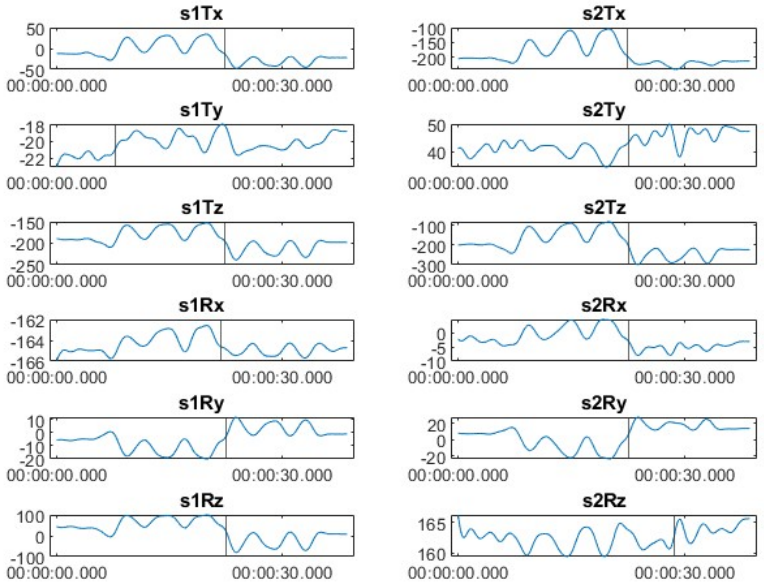

Figure 6.17: The `findchangepts` results for each channel using `mean` for each channel in the Exp1-1 dataset.

were averaged across the channels that were expected to see the most movement: `Tx`, `Tz`, `Ry`, and `Rz` for *sensor1*. This average was used as the point in the data where dataset 'A' turns into dataset 'B'. Both the raw and filtered signals for each dataset was then split at this point, giving two `timetables`: `initial ... position-set A` and `set B-final position`. The change point itself was included in the first portion (set A). An example of this can be seen in Figure 6.19 of Exp1-1, showing the `s1Tz` channel (translation in the z direction of the Aurora sensor).

The datasets are split into "front" and "back" sections, for both the raw and filtered. The result of the splitting can be seen for Exp1-1 in 6.20. The "front" and "back" sections include the initial data points collected before the motion started and after the motion ended.

At this point, a preliminary check for percent error was done on each half using the `checkError.m` function (available on GitHub), which returns the percent error for each channel as compared to the total number of data points in the given set. As expected from looking at original raw data, the second half of each experiment set had significant error from the interference from the motor, even with the shielding and additional distance provided to the sensors by the sensor

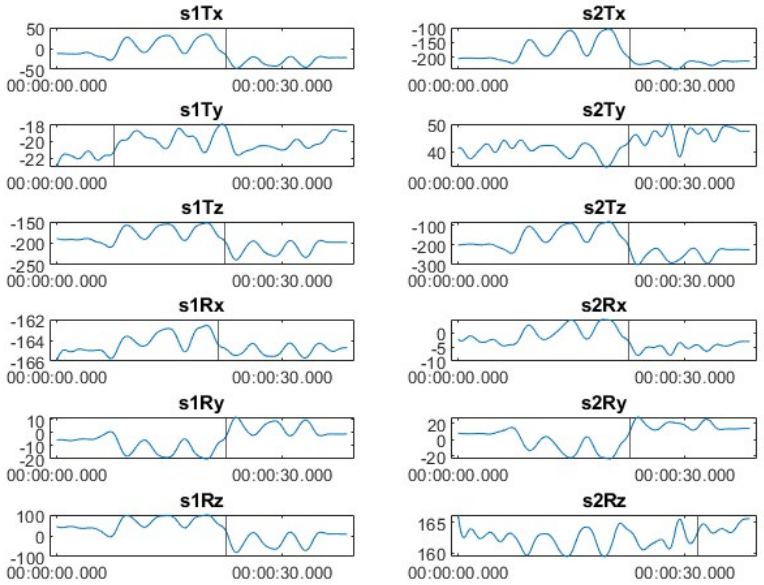

Figure 6.18: The change point, using standard deviation, for each of the directions that motion was measured in (translation and rotation along the x, y, and z axes). The graph shows dataset Exp1-1.

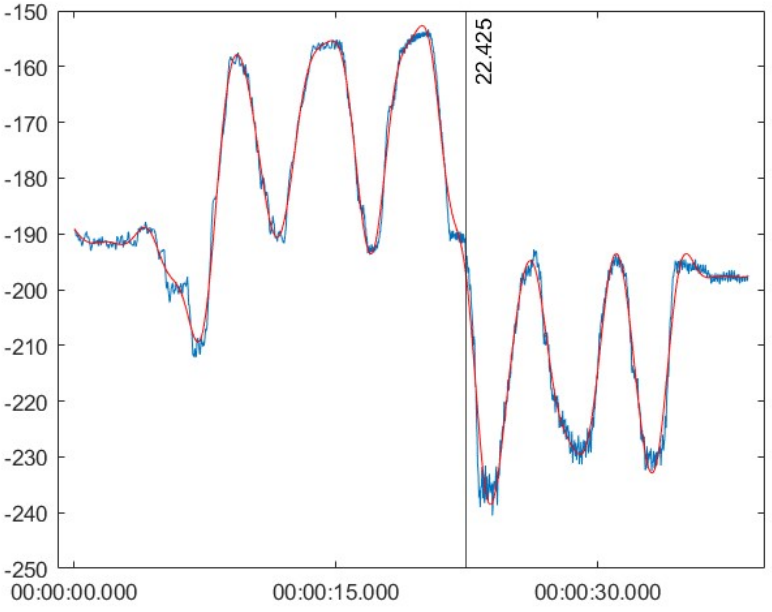

Figure 6.19: The averaged point across relevant channels at which the data switches from set A to set B, for Exp1-1, shown on the `s1Tz` channel.

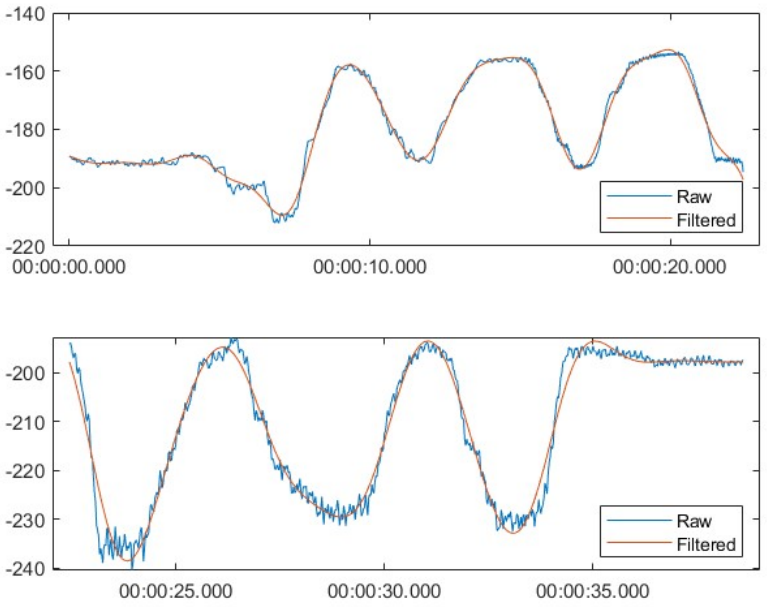

Figure 6.20: The results from separating the data at the averaged change point. The top plot is the first half of motion, and the bottom plot is the second half of motion.

arms. This can also be observed in the interpolated data. An example can be seen in Figure 6.21, showing the back half of the first experiment set (Exp1-1). In this case, the percent of the data points that were erroneous was 58.11% for the `s2Rx` channel.

In order to isolate the three motions that comprise both of the 'A' and 'B' sets, the datasets were reviewed with the `multiPT` function (available on GitHub). This code returns the value and location for all peaks and troughs in the input data, working for both the Aurora sensor data and the ATI force/torque data, as well as graphing the peaks and troughs in a subplot. This code makes use of the MATLAB function `findpeaks` (from the Signal Processing Toolbox) which locates the indices of local peaks. Using Exp1-1 as an example set again, the graph showing the local peaks and troughs can be seen in Figure 6.22. The data were split, again, at the peak or trough the most closely resembled the start (or end, for set B) of the experimental motion. The initial data—the data preceding set A—were retained as the "initial position" of the sensors. Since each channel has different local minima and maxima, the locations of the local extrema of note for both `s1Tx` and `s1Tz` had the indices averaged. The graph showing the local

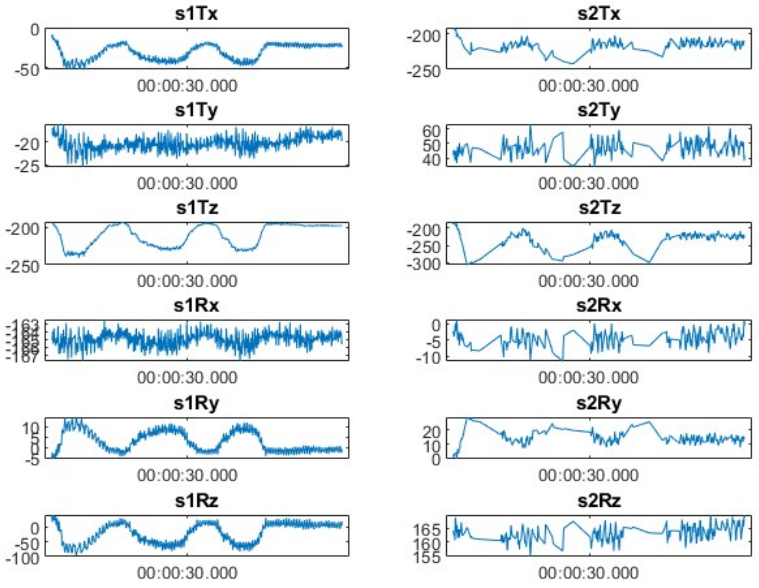

Figure 6.21: The interpolated results from the second half of Exp1-1. Note the straight sections where there was significant interpolation due to error.

extrema for each channel in the front portion of Exp1-1 can be seen in Figure 6.23.

The error in motion sets A and B was re-checked at this stage. Any set at or over 2% error was rejected due to inaccuracy. A summary table of the percent error in each experimental set can be seen in Table 6.1. The median[1] percent error of *sensor2* for the A sets was 0%, and the mean for the B sets was 35.38%. Using the 2% criteria, one A set (Exp2-1), and every B set was rejected. In order to verify that this model is accurate in both directions of rotation, the B sets with a percent error below 10% (Exp5-2 and Exp5-3, with an error of 6.10% and 8.09%, respectively) are also included in the Results and Discussion sections. The amount of interpolated points is shown graphically in three sets in Figures 6.24 through 6.26.

For data validation and preprocessing of the ATI force/torque data, see Section 6.2.3. The next section covers the calculations done to the preprocessed Aurora data to calculate the position and motion data of the system parts.

[1]Median was used for the percent error for the A datasets as there were two outliers, based on the 1.5 times the Interquartile Range (IQR) fences

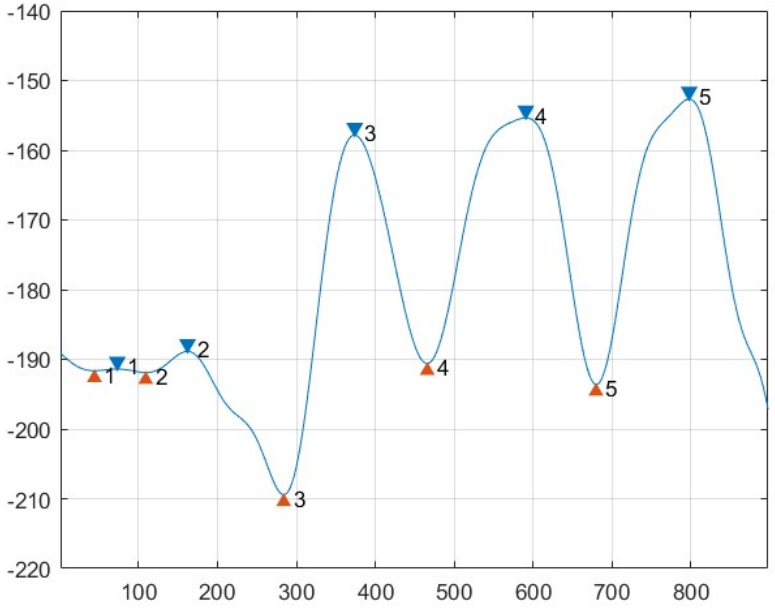

(a) The locations of each peak and trough in the front portion of the Exp1-1 dataset.

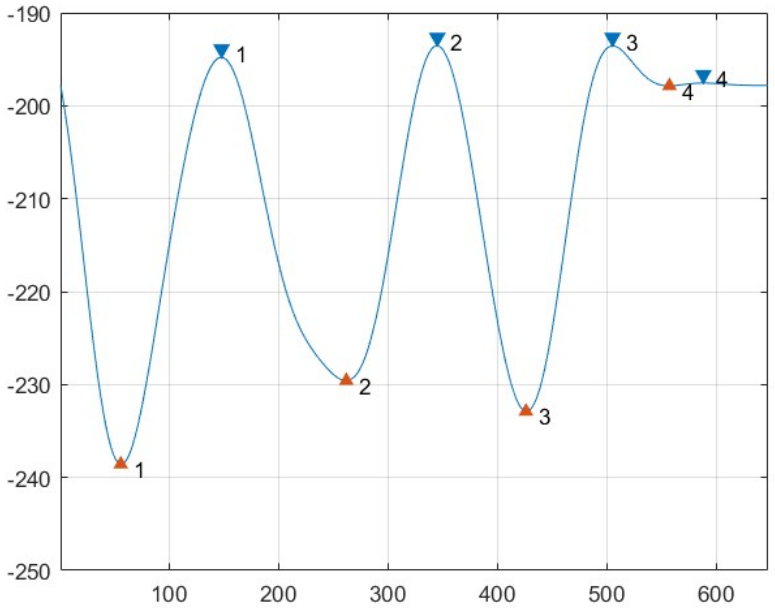

(b) The locations of each peak and trough in the back portion of the Exp1-1 dataset.

Figure 6.22: Each experiment set had a peak or trough number associated with the A and B datasets. For Exp1-1 looking specifically at the `s1Tz` channel, set A began at Trough 3 and set B ended at Peak 3.

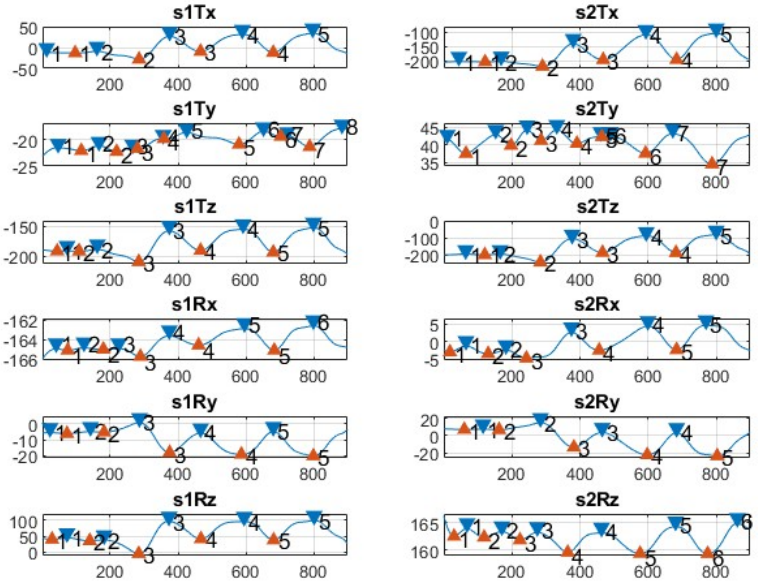

Figure 6.23: The results from the `multiPT` function across all channels for the front portion of Exp1-1. Note the different "start" locations for the motion in `s1Tx` and `s1Tz`.

Table 6.1: Amount of error data points in each set, measured as a percent of the total number of data points within the set.

Experiment	Dataset A		Dataset B*	
	s1	s2	s1	s2
exp1-1	0%	1.63%	0%	67.86%
exp1-2	0%	0.76%	0%	56.51%
exp1-3	0%	0.39%	0%	47.47%
exp2-1‡	0%	43.12%	0%	59.65%
exp2-2	0%	0.36%	0%	50.47%
exp5-1	0%	0%	0%	16.71%
exp5-2†	0%	0%	0%	6.10%
exp5-3†	0%	0%	0%	8.09%
exp6-1	0%	0%	0%	19.24%
exp6-2	0%	0%	0%	24.18%
exp6-3	0%	0%	0%	32.86%

* Every set in Dataset B was rejected
‡ Both set A and B were rejected
† Set B was used to validate the right lateral flexion, despite meeting the rejection criteria

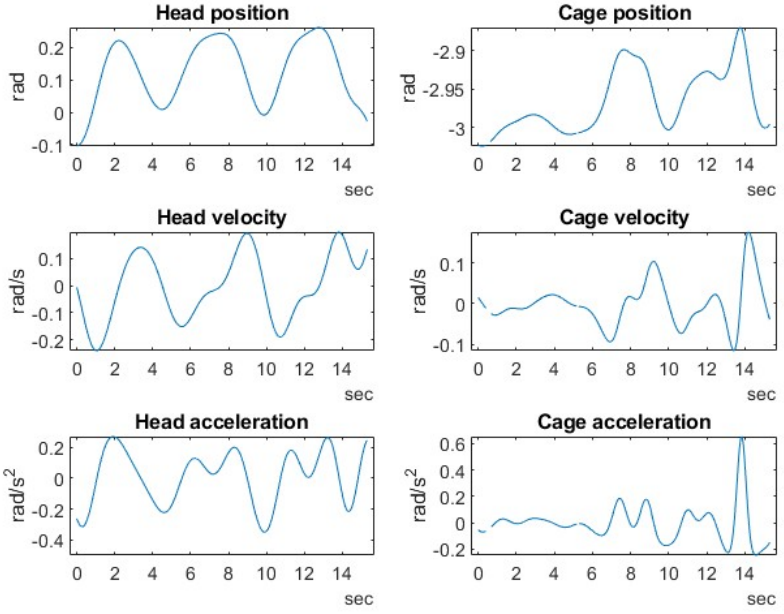

(a) Exp1-1 Set A. 1.63% in cage data.

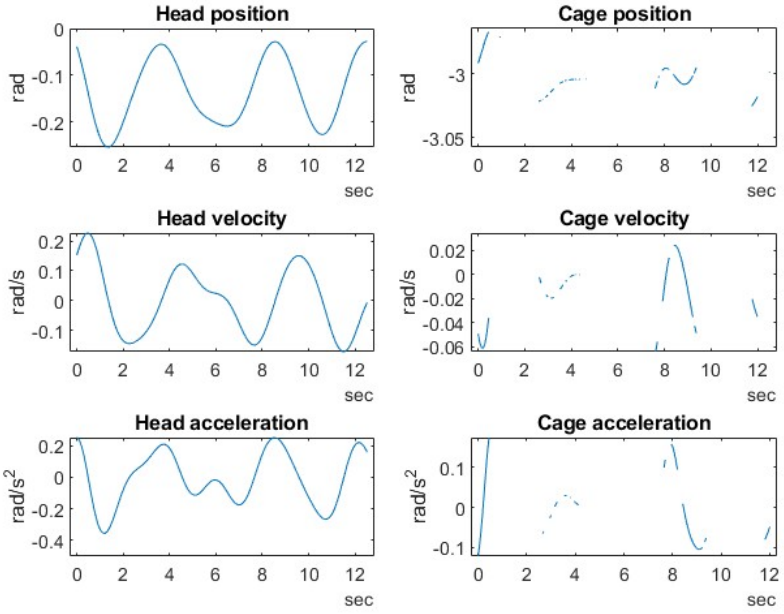

(b) Exp1-1 Set B. 67.86% in cage data.

Figure 6.24: Part 1. A selection of experiment motion data depicting the amount of error data points in the set. All head angle datasets have 0% interpolation.

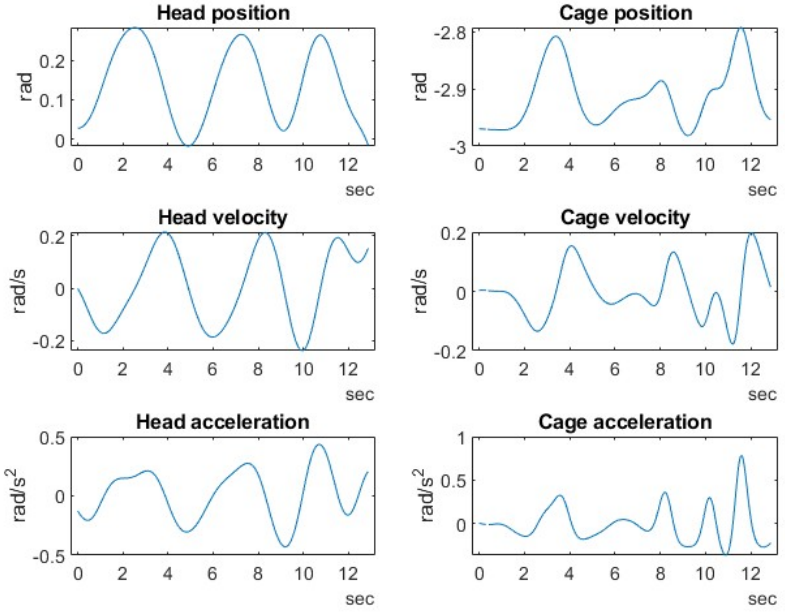

(a) Exp1-3 Set A. 0.39% in cage data.

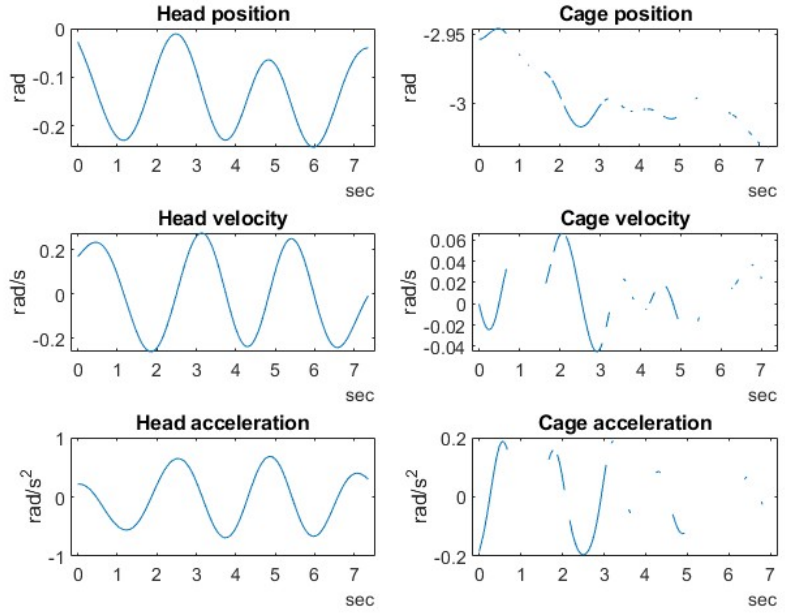

(b) Exp1-3 Set B. 47.47% in cage data.

Figure 6.25: Part 2. A selection of experiment motion data depicting the amount of error data points in the set. All head angle datasets have 0% interpolation.

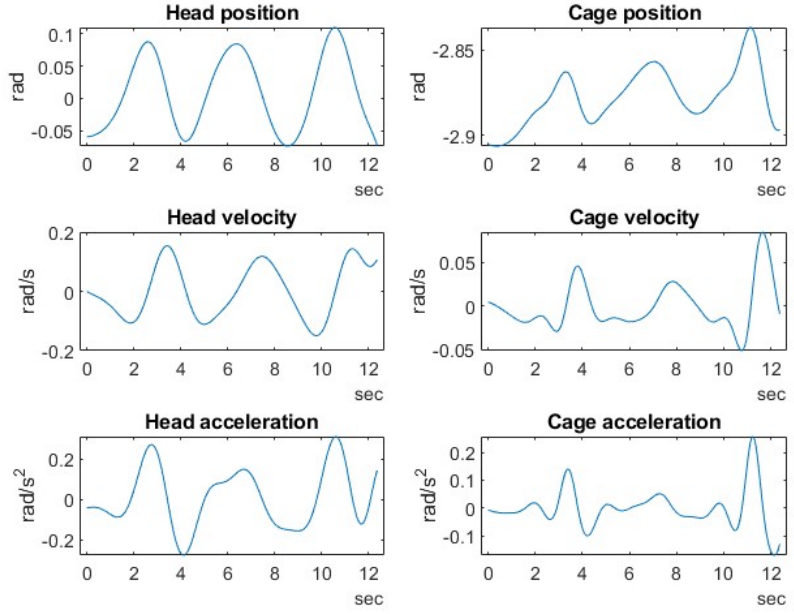

(a) Exp5-1 Set A. 0% in cage data.

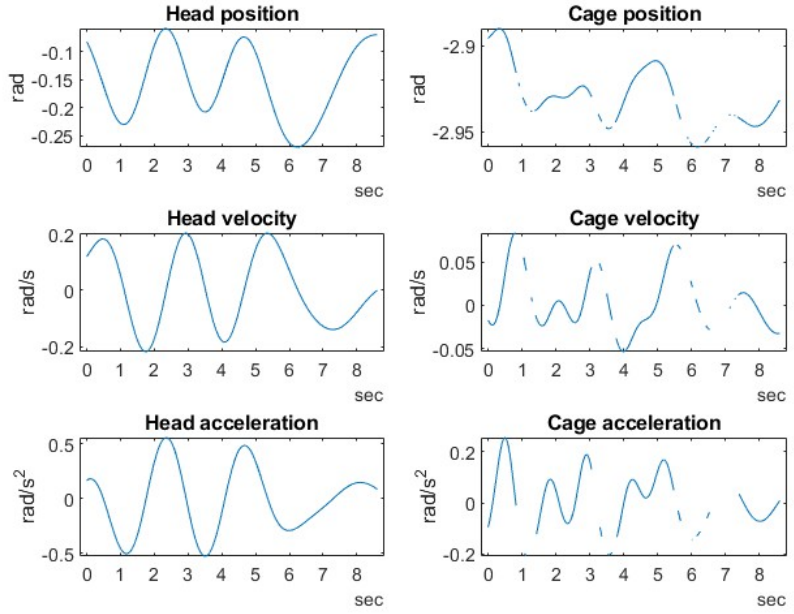

(b) Exp5-1 Set B. 16.71% in cage data.

Figure 6.26: Part 3. A selection of experiment motion data depicting the amount of error data points in the set. All head angle datasets have 0% interpolation.

6.2.2 Position Data

To calculate the angle of both the head and the gyroscope cage, the system was treated similarly to a one-joint and a two-joint robotic manipulator; the rigid link system had a modified DH convention applied to it. This approach is similar to the rigid-link representation approach in Chapter 4 in the proposed method. An electromagnetic tracking system—the Aurora System—was used to track the position of the head and the cage during the experiments. This system is described in Section 6.1 and Figure 6.4. In order to relate the sensor data from the above preprocessing section ($\mathbf{T}^{\mathbf{Aurora}}_{\mathbf{sensor1,2}}$) to the position of the head and the cage (with respect to the neck world frame), the sensor frame was treated as the end effector or tool of the rigid link system. The algebraic approach for inverse kinematics was used, as described below in Sections 6.2.2.1 Head Angle and 6.2.2.2 Cage Angle. The notation used in this section can be seen in Table 6.2. A sketch of the real-world system can be found in Figure 6.27, and a sketch of the rigid link system representations can be seen in Figure 6.28.

Table 6.2: Notation used in Section 6.2.2 (typically when used as a subscript or superscript).

0	Relating to the Base/Base Frame of the rigid link system representation
$\hat{\mathbf{0}}$	Coordinates expressed in the Base Frame of the rigid link system representation
A	(As superscript or subscript), relating to the Aurora/Aurora frame
$\mathbf{A}$	(As a matrix), a homogeneous transformation matrix using the DH convention
$\hat{\mathbf{a}}$	Coordinates expressed in the Aurora reference frame
B	Relating to the base/base frame
$\hat{\mathbf{b}}$	Coordinates expressed in the base reference frame
C	Relating to the cage/cage frame
$\mathbf{H}$	(As a matrix), a homogeneous transformation matrix not using the DH convention
JT_1	Relating to Joint 1/the frame of Joint 1 (the neck)
JT_2	Relating to Joint 2/the frame of Joint 2 (the cage)
L	(As an addition to a subscript or superscript), relating to a landmark (as measured in step 3e of the experimental protocol)

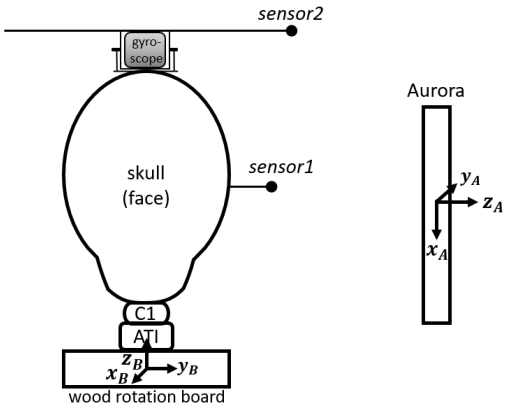

Figure 6.27: The experimental setup, showing the head, C1, and gyroscope assembly, the ATI and Aurora sensors and field generator, and the wood rotation board. The Base and Aurora frames are labelled.

s_1 Relating to sensor 1/the frame of sensor 1 (the sensor for the head/the end effector of joint 1)

s_2 Relating to sensor 2/the frame of sensor 2 (the sensor for the cage/the end effector of joint 2)

$\mathbf{T}$ (As a matrix), a resulting homogeneous transformation matrix using the DH convention

The rigid link representations for the head angle (ϕ from Chapter 4) and the cage angle (α from Chapter 4) can be seen in Figures 6.28a and 6.28b, respectively.

Where l_1, l_3, and l_2 are the x, y, and z components, respectively, of the O_0 to *sensor*1 vector; this vector is shown in Figure 6.29a. l_4 and l_5 are the x and z components of the O_0 to cage vector; this vector is shown in Figure 6.29b. l_6 and l_7 are the x component minus l_4 and y component of the O_0 to *sensor*2 vector, respectively; this vector is shown in 6.29c.

To calculate the distances l_i for the rigid link representations, the measurements taken in Step 3e of the experimental protocol were processed by using a number of vector additions and subtractions, and then had the $\mathbf{R}_0^A$ rotation matrix (derivation for this can be seen in Equation 6.34 on page 143) applied.

$$\vec{d}_{s_1}^{B}\hat{\mathbf{a}} = \vec{d}_{s_1}^{A}\hat{\mathbf{a}} - \vec{d}_{B}^{A}\hat{\mathbf{a}} \tag{6.1}$$

$$\vec{d}_{c_x}^{B}\hat{\mathbf{a}} = \vec{d}_{c_x}^{A}\hat{\mathbf{a}} - \vec{d}_{B}^{A}\hat{\mathbf{a}} \tag{6.2}$$

$$\vec{d}_{s_2}^{B}\hat{\mathbf{a}} = \vec{d}_{s_2}^{A}\hat{\mathbf{a}} - \vec{d}_{B}^{A}\hat{\mathbf{a}} \tag{6.3}$$

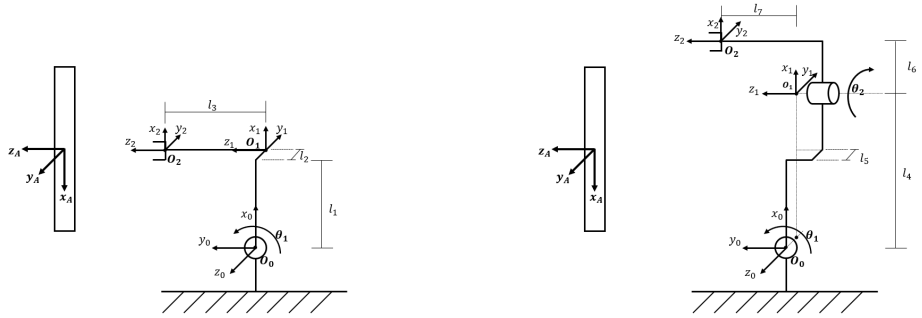

(a) Rigid link representation of sensor 1.

(b) Rigid link representation of sensor 2.

Figure 6.28: Representing the head–sensor1 system and the head–cage–sensor2 systems as rigid link systems.

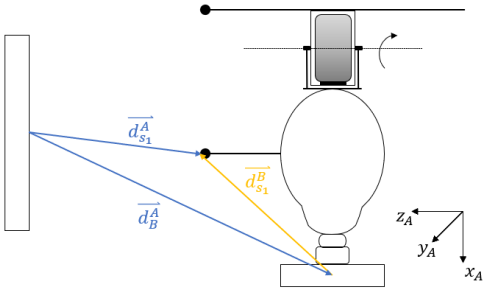

(a) Base to *sensor*1 distance.

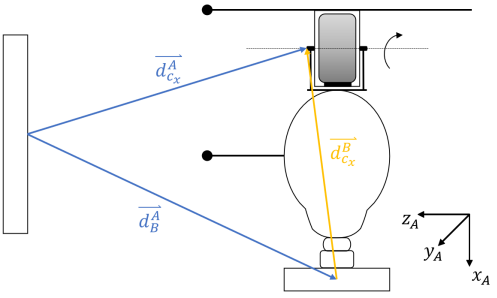

(b) Base to the centre of the cage's rotation joint distance.

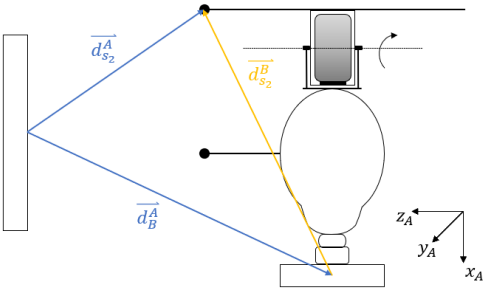

(c) Base to *sensor*2 distance.

Figure 6.29: Graphic representations of the vector subtractions used. All vectors are in Aurora-frame coordinates (shown on the right).

Where c_x denotes the axis of rotation for the cage (measured in step 3(e)vi). After applying the rotation matrix 6.34 to convert Equations 6.1–6.3 from the Aurora Frame ($\hat{\mathbf{a}}$) to the Base Frame (O_0), the resulting displacements became

$$\begin{aligned}
\vec{d}^{\,0}_{s_1} &= \mathbf{R}_0^{A^T} \cdot \vec{d}^{\,B}_{s_1}\hat{\mathbf{a}} \\
&= \mathbf{R}_0^{A^T} \cdot \left(\vec{d}^{\,A}_{s_1}\hat{\mathbf{a}} - \vec{d}^{\,A}_{B}\hat{\mathbf{a}}\right) && (6.4)\\
\vec{d}^{\,0}_{c_x} &= \mathbf{R}_{\mathbf{0}}^{\mathbf{A}^T} \cdot \vec{d}^{\,B}_{c_x}\hat{\mathbf{a}} \\
&= \mathbf{R}_{\mathbf{0}}^{\mathbf{A}^T} \cdot \left(d^{A}_{c_x} - \vec{d}^{\,\mathbf{A}}_{B}\hat{\mathbf{a}}\right) && (6.5)\\
\vec{d}^{\,0}_{s_2} &= \mathbf{R}_{\mathbf{0}}^{\mathbf{A}^T} \cdot \vec{d}^{\,B}_{s_2}\hat{\mathbf{a}} \\
&= \mathbf{R}_{\mathbf{0}}^{\mathbf{A}^T} \cdot \left(\vec{d}^{\,A}_{s_2}\hat{\mathbf{a}} - \vec{d}^{\,A}_{B}\hat{\mathbf{a}}\right) && (6.6)
\end{aligned}$$

The relationship between Equations 6.4–6.6 and each l_i term is as follows:

$$\vec{d}^{\,0}_{s_1} = \begin{bmatrix} l_1 \\ l_3 \\ l_2 \end{bmatrix} \tag{6.7}$$

$$\vec{d}^{\,0}_{c} = \begin{bmatrix} l_4 \\ d^0_{c_y} \\ d^0_{c_z} \end{bmatrix} \tag{6.8}$$

$$\vec{d}^{\,0}_{s_2} = \begin{bmatrix} l_4 + l_6 \\ l_7 \\ l_5 \end{bmatrix} \tag{6.9}$$

$$l_6 = d^0_{s_{2_x}} - l_4 \tag{6.10}$$

$$\begin{aligned}
l_1 &= d^0_{s_{1_x}} \\
l_2 &= d^0_{s_{1_z}} \\
l_3 &= d^0_{s_{1_y}} \\
l_4 &= d^0_{c_x} \\
l_5 &= d^0_{s_{2_z}}
\end{aligned}$$

$$l_6 = d^0_{s_{2x}} - d^0_{c_x}$$
$$l_7 = d^0_{s_{2y}} \tag{6.11}$$

6.2.2.1 Head Angle

To calculate the value of the first joint angle, θ_1 (the angle of the head, ϕ), the one-joint rigid link representation, as seen in Figure 6.28a, was used. The sensor frame location and orientation were retained in order to simplify the data processing required to calculate the joint angle. The representation was created using the DH convention, so there is an additional frame (O_2) to account for the required location of the end-effector frame. The tool frame, t, is the adjustment for the orientation; though for this application the additional tool frame transformation does not affect the inverse kinematics. The DH parameters table can be seen in Table 6.3. For brevity, the following sections use the standard compact notation of $\mathbf{c}$ and $\mathbf{s}$ to represent cos and sin, respectively, where a subscript i indicates θ_i is the argument for the function.

	a_i	d_i	α_i	θ_i
1	l_1	$-l_2$	$-\pi/2$	θ_1^*
2	0	l_3	0	0
t	0	0	0	π

Table 6.3: DH Parameters, One Joint.

Using this model, the joint angle (θ_1) can be calculated using an algebraic approach to inverse kinematics. The homogeneous transformation matrix for the final frame in a manipulator representation ($\mathbf{T}^0_t$) includes the position of the final frame with respect to the base frame as the $\vec{d}$ vector (shown in Equation 6.12). When given a known position and orientation of the end effector, this vector can be equated to the known (or desired) position to calculate the joint angle(s) required to result in this position. To compute the final homogeneous transformation matrix $\mathbf{T}^0_n$, the homogeneous transformation matrix for each joint ($\mathbf{A}^{i-1}_i$) is required. The

one joint representation in Figure 6.28a has an $n = 2$:

$$\mathbf{T}_n^0 = \begin{bmatrix} n_x & s_x & a_x & d_x \\ n_y & s_y & a_y & d_y \\ n_z & s_z & a_z & d_z \\ 0 & 0 & 0 & 1 \end{bmatrix} \tag{6.12}$$

$$= \mathbf{A}_1^0 \cdot \mathbf{A}_2^1 \cdot \ldots \cdot \mathbf{A}_n^{n-1} \tag{6.13}$$

when $n = 2$, $\mathbf{T}_2^0$ is calculated as follows:

$$\mathbf{T_2^0} = \mathbf{A_1^0} \cdot \mathbf{A_2^1} \tag{6.14}$$

The parameters in Table 6.3 were used to populate the **A** (homogeneous transform) matrices:

$$\mathbf{A}_i^{i-1} = \begin{bmatrix} \mathbf{c}\theta_i & -\mathbf{s}\theta_i\,\mathbf{c}\alpha_i & \mathbf{s}\theta_i\,\mathbf{s}\alpha_i & a_i\,\mathbf{c}\theta_i \\ \mathbf{s}\theta_i & \mathbf{c}\theta_i\,\mathbf{c}\alpha_i & -\mathbf{c}\theta_i\,\mathbf{s}\alpha_i & a_i\,\mathbf{s}\theta_i \\ 0 & \mathbf{s}\alpha_i & \mathbf{c}\alpha_i & d_i \\ 0 & 0 & 0 & 1 \end{bmatrix} \tag{6.15}$$

$$\mathbf{A}_1^0 = \begin{bmatrix} \mathbf{c}_1 & -\mathbf{s}_1\,\cancelto{0}{\mathbf{c}_{-\pi/2}} & \mathbf{s}_1\,\cancelto{-1}{\mathbf{s}_{-\pi/2}} & l_1\,\mathbf{c}_1 \\ \mathbf{s}_1 & \mathbf{c}_1\,\cancelto{0}{\mathbf{c}_{-\pi/2}} & -\mathbf{c}_1\,\cancelto{-1}{\mathbf{s}_{-\pi/2}} & l_1\,\mathbf{s}_1 \\ 0 & \cancelto{-1}{\mathbf{s}_{-\pi/2}} & \cancelto{0}{\mathbf{c}_{-\pi/2}} & -l_2 \\ 0 & 0 & 0 & 1 \end{bmatrix}$$

$$= \begin{bmatrix} \mathbf{c}_1 & 0 & -\mathbf{s}_1 & l_1\,\mathbf{c}_1 \\ \mathbf{s}_1 & 0 & \mathbf{c}_1 & l_1\,\mathbf{s}_1 \\ 0 & -1 & 0 & -l_2 \\ 0 & 0 & 0 & 1 \end{bmatrix} \tag{6.16}$$

$$\mathbf{A}_2^1 = \begin{bmatrix} \mathbf{c}(0) & -\mathbf{s}(0)\,\mathbf{c}(0) & \mathbf{s}(0)\,\mathbf{s}(0) & 0\cdot\,\mathbf{c}(0) \\ \mathbf{s}(0) & \mathbf{c}(0)\,\mathbf{c}(0) & -\mathbf{c}(0)\,\mathbf{s}(0) & 0\cdot\,\mathbf{s}(0) \\ 0 & \mathbf{s}(0) & \mathbf{c}(0) & l_3 \\ 0 & 0 & 0 & 1 \end{bmatrix}$$

$$= \begin{bmatrix} 1 & 0 & 0 & 0 \\ 0 & 1 & 0 & 0 \\ 0 & 0 & 1 & l_3 \\ 0 & 0 & 0 & 1 \end{bmatrix} \tag{6.17}$$

The value for $\mathbf{T}_2^0$ was calculated by substituting Equations 6.16 and 6.17 into Equation 6.14:

$$\begin{aligned} \mathbf{T}_2^0 &= \mathbf{A}_1^0 \cdot \mathbf{A}_2^1 \\ &= \begin{bmatrix} \mathbf{c}_1 & 0 & -\mathbf{s}_1 & l_1\,\mathbf{c}_1 \\ \mathbf{s}_1 & 0 & \mathbf{c}_1 & l_1\,\mathbf{s}_1 \\ 0 & -1 & 0 & -l_2 \\ 0 & 0 & 0 & 1 \end{bmatrix} \cdot \begin{bmatrix} 1 & 0 & 0 & 0 \\ 0 & 1 & 0 & 0 \\ 0 & 0 & 1 & l_3 \\ 0 & 0 & 0 & 1 \end{bmatrix} \\ &= \begin{bmatrix} \mathbf{c}_1 & 0 & -\mathbf{s}_1 & l_1\,\mathbf{c}_1 - l_3\,\mathbf{s}_1 \\ \mathbf{s}_1 & 0 & \mathbf{c}_1 & l_1\,\mathbf{s}_1 + l_3\,\mathbf{c}_1 \\ 0 & -1 & 0 & -l_2 \\ 0 & 0 & 0 & 1 \end{bmatrix} \end{aligned} \tag{6.18}$$

The tool frame t was then applied by multiplying $\mathbf{T}_2^0$ by $\mathbf{A}_t^2$:

$$\begin{aligned} \mathbf{A}_t^2 &= \begin{bmatrix} \mathbf{c}(\pi) & -\mathbf{s}(\pi)\,\mathbf{c}(0) & \mathbf{s}(\pi)\,\mathbf{s}(0) & 0 \cdot\ \mathbf{c}(\pi) \\ \mathbf{s}(\pi) & \mathbf{c}(\pi)\,\mathbf{c}(0) & -\mathbf{c}(\pi)\,\mathbf{s}(0) & 0 \cdot\ \mathbf{s}(\pi) \\ 0 & \mathbf{s}(0) & \mathbf{c}(0) & 0 \\ 0 & 0 & 0 & 1 \end{bmatrix} \\ &= \begin{bmatrix} -1 & 0 & 0 & 0 \\ 0 & -1 & 0 & 0 \\ 0 & 0 & 1 & 0 \\ 0 & 0 & 0 & 1 \end{bmatrix} \end{aligned} \tag{6.19}$$

$$\begin{aligned} \mathbf{T}_t^0 &= \mathbf{A}_2^0 \cdot \mathbf{A}_t^2 \\ &= \begin{bmatrix} \mathbf{c}_1 & 0 & -\mathbf{s}_1 & l_1\,\mathbf{c}_1 - l_3\,\mathbf{s}_1 \\ \mathbf{s}_1 & 0 & \mathbf{c}_1 & l_1\,\mathbf{s}_1 + l_3\,\mathbf{c}_1 \\ 0 & -1 & 0 & -l_2 \\ 0 & 0 & 0 & 1 \end{bmatrix} \cdot \begin{bmatrix} -1 & 0 & 0 & 0 \\ 0 & -1 & 0 & 0 \\ 0 & 0 & 1 & 0 \\ 0 & 0 & 0 & 1 \end{bmatrix} \end{aligned} \tag{6.20}$$

$$= \begin{bmatrix} -\mathbf{c}_1 & 0 & -\mathbf{s}_1 & l_1\,\mathbf{c}_1 - l_3\,\mathbf{s}_1 \\ -\mathbf{s}_1 & 0 & \mathbf{c}_1 & l_1\,\mathbf{s}_1 + l_3\,\mathbf{c}_1 \\ 0 & 1 & 0 & -l_2 \\ 0 & 0 & 0 & 1 \end{bmatrix} \tag{6.21}$$

As stated previously, when the position of the end effector is known, the position coordinates are the values found in the $\vec{d}$ vector in the final transformation matrix ($\mathbf{T}_t^0$):

$$\begin{aligned} \vec{d}_t^0 &= \begin{bmatrix} l_1\,\mathbf{c}_1 - l_3\,\mathbf{s}_1 \\ l_1\,\mathbf{s}_1 + l_3\,\mathbf{c}_1 \\ -l_2 \end{bmatrix} \\ \begin{bmatrix} x_t^0 \\ y_t^0 \\ z_t^0 \end{bmatrix} &= \begin{bmatrix} l_1\,\mathbf{c}_1 - l_3\,\mathbf{s}_1 \\ l_1\,\mathbf{s}_1 + l_3\,\mathbf{c}_1 \\ -l_2 \end{bmatrix} \end{aligned} \tag{6.22}$$

This resulted in three equations with one unknown (θ_1).

$$x_t^0 = l_1\,\mathbf{c}_1 - l_3\,\mathbf{s}_1 \tag{6.23}$$

$$y_t^0 = l_1\,\mathbf{s}_1 + l_3\,\mathbf{c}_1 \tag{6.24}$$

$$z_t^0 = -l_2 \tag{6.25}$$

Isolating for $\mathbf{s}_1$ in Equation 6.24, substituting $\mathbf{s}_1$ into Equation 6.23, and solving for $\mathbf{c}_1$ yielded the following equations for $\mathbf{s}_1$ and $\mathbf{c}_1$:

$$\begin{aligned} y_t^0 &= l_1\,\mathbf{s}_1 + l_3\,\mathbf{c}_1 \\ y_t^0 - l_3\,\mathbf{c}_1 &= l_1\,\mathbf{s}_1 \\ l_1\,\mathbf{s}_1 &= y_t^0 - l_3\,\mathbf{c}_1 \\ \mathbf{s}_1 &= \frac{y_t^0 - l_3\,\mathbf{c}_1}{l_1} \end{aligned} \tag{6.26}$$

$$\begin{aligned} x_t^0 &= l_1\,\mathbf{c}_1 - l_3\,\mathbf{s}_1 \\ x_t^0 - l_1\,\mathbf{c}_1 &= -l_3\frac{y_t^0 - l_3\,\mathbf{c}_1}{l_1} \\ l_1\left(x_t^0 - l_1\,\mathbf{c}_1\right) &= -l_3\left(y_t^0 - l_3\,\mathbf{c}_1\right) \end{aligned}$$

$$\begin{aligned} x_t^0 l_1 - l_1^2\,\mathbf{c}_1 &= -y_t^0 l_3 + l_3^2\,\mathbf{c}_1 \\ x_2^0 l_1 + y_t^0 l_3 &= l_1^2\,\mathbf{c}_1 + l_3^2\,\mathbf{c}_1 \\ \mathbf{c}_1\left(l_1^2 + l_3^2\right) &= x_t^0 l_1 + y_t^0 l_3 \\ \mathbf{c}_1 &= \frac{x_t^0 l_1 + y_t^0 l_3}{(l_1^2 + l_3^2)} \end{aligned} \tag{6.27}$$

Therefore, the values for $\mathbf{c}_1$ and $\mathbf{s}_1$ were as follows:

$$\begin{aligned} \mathbf{c}_1 &= \frac{x_t^0 l_1 + y_t^0 l_3}{(l_1^2 + l_3^2)} \\ \mathbf{s}_1 &= \frac{y_t^0 - l_3\,\mathbf{c}_1}{l_1} \end{aligned} \tag{6.28}$$

The isolated $\mathbf{s}_1$ and $\mathbf{c}_1$ equations (Equations 6.28 and 6.27) are the arguments for the MATLAB function `atan2(Y,X)`—this function gives the four-quadrant inverse tangent (θ_1 is within the range $(-\pi, \pi]$), as opposed to the result that a standard arctangent computation would give: $(-\pi/2, \pi/2)$.

$$\theta_1 = \texttt{atan2}\left(\frac{y_t^0 - l_3\,\mathbf{c}_1}{l_1}, \frac{x_t^0 l_1 + y_t^0 l_3}{(l_1^2 + l_3^2)}\right) \tag{6.29}$$

In order to express the known position ($\mathbf{T}_t^0$) of the end effector—*sensor*1—in the base frame, the known position in the Aurora frame had a homogeneous transformation matrix applied (the "raw" data that is collected by the Aurora system: $\mathbf{T}_{s_1}^A$). Applying the known "base with respect to the Aurora" transformation matrix resulted in the following equation:

$$\begin{aligned} \mathbf{T}_t^0 &= \mathbf{T}_{s_1}^0 \\ &= \mathbf{H}_A^0 \cdot \mathbf{T}_{s_1}^A \end{aligned} \tag{6.30}$$

To calculate $\mathbf{H}_A^0$ (the position of the Aurora Frame with respect to the Base Frame) the inverse of the homogeneous transformation matrix of the Base Frame with respect to the Aurora Frame ($\mathbf{H}_0^{A^{-1}}$) was used:

$$\begin{aligned} \mathbf{H_A^0} &= \mathbf{A_0^A}^{-1} \\ &= \begin{bmatrix} \mathbf{R_0^A} & \vec{d_0^A} \\ \vec{0} & 1 \end{bmatrix}^{-1} \end{aligned}$$

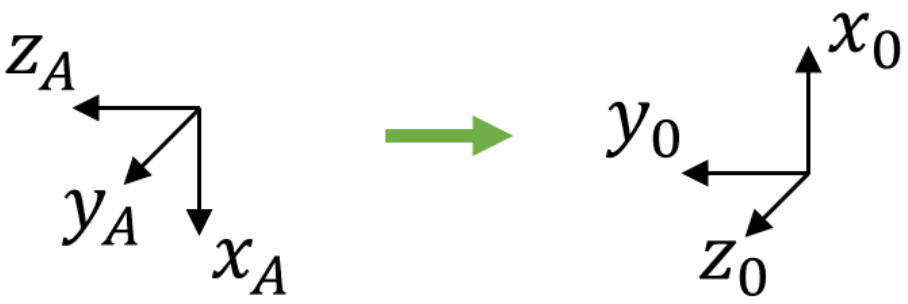

Figure 6.30: Graphic representation of the Aurora Frame and the Base Frame.

$$= \begin{bmatrix} \mathbf{R_0^A}^T & -\mathbf{R_0^A}^T \cdot \vec{d_0^A} \\ \vec{0} & 1 \end{bmatrix}, \tag{6.31}$$

where $\mathbf{R}_0^A$ is the rotation matrix between the Aurora and the Base Frames, and $\vec{d_B^A}$ is a position vector. This vector is the distance from the Aurora to the base, which was measured in step 3(e)v of the Experimental Protocol (Section 6.1).

$$\vec{d_0^A} = \begin{bmatrix} d_{0_x}^A \\ d_{0_y}^A \\ d_{0_z}^A \end{bmatrix} \tag{6.32}$$

To rotate from the Aurora Frame to the Base Frame, a rotation of $\pi/2$ about x, followed by a rotation of π about y was needed, as seen in Figure 6.30:

$$\begin{aligned} \mathbf{R}_0^A &= \mathbf{R}_{z,\pi} \cdot \mathbf{R}_{x,\pi/2} \\ &= \begin{bmatrix} \mathbf{c}(\pi) & -\mathbf{s}(\pi) & 0 \\ \mathbf{s}(\pi) & \mathbf{c}(\pi) & 0 \\ 0 & 0 & 1 \end{bmatrix} \cdot \begin{bmatrix} 1 & 0 & 0 \\ 0 & \mathbf{c}(\pi/2) & -\mathbf{s}(\pi/2) \\ 0 & \mathbf{s}(\pi/2) & \mathbf{c}(\pi/2) \end{bmatrix} \\ &= \begin{bmatrix} 1 & 0 & 0 \\ 0 & 0 & -1 \\ 0 & 1 & 0 \end{bmatrix} \cdot \begin{bmatrix} -1 & 0 & 0 \\ 0 & 1 & 0 \\ 0 & 0 & -1 \end{bmatrix} \end{aligned} \tag{6.33}$$

$$\mathbf{R}_0^A = \begin{bmatrix} -1 & 0 & 0 \\ 0 & 0 & 1 \\ 0 & 1 & 0 \end{bmatrix} \tag{6.34}$$

Equations 6.32 and 6.34 could then be substituted into Equation 6.31 to calculate the Homogeneous Transformation Matrix:

$$\begin{aligned}
\mathbf{H}_A^0 &= \begin{bmatrix} \mathbf{R}_0^{A^T} & -\mathbf{R}_0^{A^T} \cdot \vec{d}_0^A \\ \vec{0} & 1 \end{bmatrix} \\
&= \begin{bmatrix} \begin{bmatrix} -1 & 0 & 0 \\ 0 & 0 & 1 \\ 0 & 1 & 0 \end{bmatrix}^T & - \begin{bmatrix} -1 & 0 & 0 \\ 0 & 0 & 1 \\ 0 & 1 & 0 \end{bmatrix}^T \begin{bmatrix} d_{0_x}^A \\ d_{0_y}^A \\ d_{0_z}^A \end{bmatrix} \\ \vec{0} & 1 \end{bmatrix} \\
&= \begin{bmatrix} \begin{bmatrix} -1 & 0 & 0 \\ 0 & 0 & 1 \\ 0 & 1 & 0 \end{bmatrix} & - \begin{bmatrix} -1 & 0 & 0 \\ 0 & 0 & 1 \\ 0 & 1 & 0 \end{bmatrix} \begin{bmatrix} d_{0_x}^A \\ d_{0_y}^A \\ d_{0_z}^A \end{bmatrix} \\ \vec{0} & 1 \end{bmatrix} \\
&= \begin{bmatrix} \begin{bmatrix} -1 & 0 & 0 \\ 0 & 0 & 1 \\ 0 & 1 & 0 \end{bmatrix} & \begin{bmatrix} d_{0_x}^A \\ -d_{0_z}^A \\ -d_{0_y}^A \end{bmatrix} \\ \vec{0} & 1 \end{bmatrix} \\
&= \begin{bmatrix} -1 & 0 & 0 & d_{0_x}^A \\ 0 & 0 & 1 & -d_{0_z}^A \\ 0 & 1 & 0 & -d_{0_y}^A \\ 0 & 0 & 0 & 1 \end{bmatrix}
\end{aligned} \tag{6.35}$$

To calculate the homogeneous transformation matrix for the end effector from the collected data, the raw data were converted from the Aurora-measured Euler angles to a rotation matrix, $\mathbf{R}_{s_1}^A$. The translation data (T_x, T_y, and T_z) was unchanged from the raw state and added to the transformation matrix $\mathbf{T}_{s_1}^A$. The following formula to convert from Euler angles to a rotation matrix was provided in the User Manual for the Aurora System:

$\mathbf{R}_{S_1}^A =$

$$\begin{bmatrix} \mathbf{c}\alpha \cdot \mathbf{c}\beta & \mathbf{c}\alpha \cdot \mathbf{s}\beta \cdot \mathbf{s}\gamma - \mathbf{s}\alpha \cdot \mathbf{c}\gamma & \mathbf{c}\alpha \cdot \mathbf{s}\beta \cdot \mathbf{c}\gamma + \mathbf{s}\alpha \cdot \mathbf{s}\gamma \\ \mathbf{s}\alpha \cdot \mathbf{c}\beta & \mathbf{s}\alpha \cdot \mathbf{s}\beta \cdot \mathbf{s}\gamma + \mathbf{c}\alpha \cdot \mathbf{c}\gamma & \mathbf{s}\alpha \cdot \mathbf{s}\beta \cdot \mathbf{c}\gamma - \mathbf{c}\alpha \cdot \mathbf{s}\gamma \\ -\mathbf{s}\beta & \mathbf{c}\beta \cdot \mathbf{s}\gamma & \mathbf{c}\beta \cdot \mathbf{c}\gamma \end{bmatrix}, \quad (6.36)$$

where the vector for each data point in the raw data output is given as [α, β, γ, T_x, T_y, T_z].

This rotation matrix was used with the transposed translation data from the Aurora ($d^{\vec{A}}_{S_1} = [T_x \;\; T_y \;\; T_z]^T$), the homogeneous transformation matrix for each data point was as follows:

$$\mathbf{T}^A_{S_1} = \begin{bmatrix} \mathbf{R}^A_{S_1} & d^{\vec{A}}_{s_1} \\ \vec{0} & 1 \end{bmatrix} \quad (6.37)$$

In summary, θ_1 (head angle, ϕ) was derived using Equation 6.29, where x^0_t and y^0_t are matrix elements t_{14} and t_{24} from the transformation matrix calculated after substituting Equations 6.35 and 6.37 into Equation 6.30:

$$\theta_1 = \texttt{atan2}\left(\frac{y^0_t - l_3\,\mathbf{c}_1}{l_1}, \frac{x^0_t l_1 + y^0_t l_3}{(l^2_1 + l^2_3)}\right) \quad (6.38)$$

where x^0_t and y^0_t are elements t_{14} and t_{24} of the resulting matrix:

$$\begin{aligned} \mathbf{T}^0_2 &= \mathbf{H}^0_A \cdot \mathbf{T}^A_{s_1} \\ &= \begin{bmatrix} \begin{bmatrix} -1 & 0 & 0 \\ 0 & 0 & 1 \\ 0 & 1 & 0 \end{bmatrix} & \begin{bmatrix} d^A_{0_x} \\ -d^A_{0_z} \\ -d^A_{0_y} \end{bmatrix} \\ \vec{0} & 1 \end{bmatrix} \cdot \begin{bmatrix} \mathbf{R}^A_{S_1} & d^{\vec{A}}_{s_1} \\ \vec{0} & 1 \end{bmatrix} \\ &= \begin{bmatrix} -1 & 0 & 0 & d^A_{0_x} \\ 0 & 0 & 1 & -d^A_{0_z} \\ 0 & 1 & 0 & -d^A_{0_y} \\ 0 & 0 & 0 & 1 \end{bmatrix} \cdot \begin{bmatrix} \mathbf{R}^A_{S_1} & d^{\vec{A}}_{s_1} \\ \vec{0} & 1 \end{bmatrix} \\ \mathbf{T}^0_2 &= \begin{bmatrix} t_{11} & t_{12} & t_{13} & t_{14} \\ t_{21} & t_{22} & t_{23} & t_{24} \\ t_{31} & t_{32} & t_{33} & t_{34} \\ t_{41} & t_{42} & t_{43} & t_{44} \end{bmatrix} \end{aligned} \quad (6.39)$$

6.2.2.2 Cage Angle

To calculate the value of the second joint angle, θ_2 (the precession angle of the gyroscope, α), the two-joint rigid link representation, as seen in Figure 6.28b, was used. As in section 6.2.2.1, the sensor frame location and was retained as the end-effector frame in order to simplify the data processing required to calculate the joint angle. Similarly, the addition of the final tool frame (t, to align with the Aurora orientation) does not affect the inverse kinematics of the end effector, and was not applied to this second representation to slightly simplify the calculations in this section. This had the added benefit of clarifying which x, y, and z distances are being referred to in the final inverse kinematics calculations. The DH parameters table can be seen in Table 6.4. As in the previous section, $\mathbf{c}$ and $\mathbf{s}$ are used to represent cos and sin, where a subscript i indicates θ_i is the argument for the function.

	a_i	d_i	α_i	θ_i
1	l_4	l_5	α_1	θ_1^*
2	l_6	l_7	0	θ_2^*

Table 6.4: DH Parameters, Two Joints.

Where $\alpha_1 = -\pi/2 + \beta$, and β is the angle between the y_0 axis and the z_1 axis, as measured about x_1. In an ideal system, $\beta = 0$, as the axis of rotation of the gimbal of the gyroscope would be orthogonal to the axis of rotation of the user. The computations in this section assume $\beta \approx 0$ radians.

Using this model, the joint angle (θ_2) can be calculated using an algebraic approach to inverse kinematics, as explained in Section 6.2.2.1.

The parameters in Table 6.4 were used to populate the $\mathbf{A}$ (homogeneous transform) matrices:

$$\mathbf{A}_i^{i-1} = \begin{bmatrix} \mathbf{c}\theta_i & -\mathbf{s}\theta_i\,\mathbf{c}\alpha_i & \mathbf{s}\theta_i\,\mathbf{s}\alpha_i & a_i\,\mathbf{c}\theta_i \\ \mathbf{s}\theta_i & \mathbf{c}\theta_i\,\mathbf{c}\alpha_i & -\mathbf{c}\theta_i\,\mathbf{s}\alpha_i & a_i\,\mathbf{s}\theta_i \\ 0 & \mathbf{s}\alpha_i & \mathbf{c}\alpha_i & d_i \\ 0 & 0 & 0 & 1 \end{bmatrix} \tag{6.40}$$

$$\mathbf{A_1^0} = \begin{bmatrix} \mathbf{c}_1 & -\mathbf{s}_1\,\mathbf{c}\,(-\pi/2+\beta) & \mathbf{s}_1\,\mathbf{s}\,(-\pi/2+\beta) & l_4\,\mathbf{c}_1 \\ \mathbf{s}_1 & \mathbf{c}_1\,\mathbf{c}\,(-\pi/2+\beta) & -\mathbf{c}_1\,\mathbf{s}\,(-\pi/2+\beta) & l_4\,\mathbf{s}_1 \\ 0 & \mathbf{s}\,(-\pi/2+\beta) & \mathbf{c}\,(-\pi/2+\beta) & l_5 \\ 0 & 0 & 0 & 1 \end{bmatrix} \tag{6.41}$$

$$\begin{aligned} \mathbf{A_2^1} &= \begin{bmatrix} \mathbf{c}_2 & -\mathbf{s}_2\,\mathbf{c}(0) & \mathbf{s}_2\,\mathbf{s}(0) & l_6\,\mathbf{c}_2 \\ \mathbf{s}_2 & \mathbf{c}_2\,\mathbf{c}(0) & -\mathbf{c}_2\,\mathbf{s}(0) & l_6\,\mathbf{s}_2 \\ 0 & \mathbf{s}(0) & \mathbf{c}(0) & l_7 \\ 0 & 0 & 0 & 1 \end{bmatrix} \\ &= \begin{bmatrix} \mathbf{c}_2 & -\mathbf{s}_2 & 0 & l_6\,\mathbf{c}_2 \\ \mathbf{s}_2 & \mathbf{c}_2 & 0 & l_6\,\mathbf{s}_2 \\ 0 & 0 & 1 & l_7 \\ 0 & 0 & 0 & 1 \end{bmatrix} \end{aligned} \tag{6.42}$$

The value for $\mathbf{T}_2^0$ was calculated by substituting Equations 6.41 and 6.42 Equation 6.14:

$$\begin{aligned} \mathbf{T}_2^0 &= \mathbf{A}_1^0 \cdot \mathbf{A}_2^1 \\ &= \begin{bmatrix} \mathbf{c}_1 & -\mathbf{s}_1\,\mathbf{c}\,(-\pi/2+\beta) & \mathbf{s}_1\,\mathbf{s}\,(-\pi/2+\beta) & l_4\,\mathbf{c}_1 \\ \mathbf{s}_1 & \mathbf{c}_1\,\mathbf{c}\,(-\pi/2+\beta) & -\mathbf{c}_1\,\mathbf{s}\,(-\pi/2+\beta) & l_4\,\mathbf{s}_1 \\ 0 & \mathbf{s}\,(-\pi/2+\beta) & \mathbf{c}\,(-\pi/2+\beta) & l_5 \\ 0 & 0 & 0 & 1 \end{bmatrix} \cdot \begin{bmatrix} \mathbf{c}_2 & -\mathbf{s}_2 & 0 & l_6\,\mathbf{c}_2 \\ \mathbf{s}_2 & \mathbf{c}_2 & 0 & l_6\,\mathbf{s}_2 \\ 0 & 0 & 1 & l_7 \\ 0 & 0 & 0 & 1 \end{bmatrix} \end{aligned}$$

$$\mathbf{T}_2^0 = \begin{bmatrix} \mathbf{c}_1\,\mathbf{c}_2 - \mathbf{s}_1\,\mathbf{s}_2\,\mathbf{c}\,(-\pi/2+\beta) & -\mathbf{c}_1\,\mathbf{s}_2 - \mathbf{s}_1\,\mathbf{c}_2\,\mathbf{c}\,(-\pi/2+\beta) & \mathbf{s}_1\,\mathbf{s}\,(-\pi/2+\beta) \\ \mathbf{s}_1\,\mathbf{c}_2 + \mathbf{c}_1\,\mathbf{s}_2\,\mathbf{c}\,(-\pi/2+\beta) & -\mathbf{s}_1\,\mathbf{s}_2 + \mathbf{c}_1\,\mathbf{c}_2\,\mathbf{c}\,(-\pi/2+\beta) & -\mathbf{c}_1\,\mathbf{s}\,(-\pi/2+\beta) \\ \mathbf{s}_2\,\mathbf{s}\,(-\pi/2+\beta) & \mathbf{c}_2\,\mathbf{s}\,(-\pi/2+\beta) & \mathbf{c}\,(-\pi/2+\beta) \\ 0 & 0 & 0 \end{bmatrix}$$

$$\begin{bmatrix} l_4\,\mathbf{c}_1 + l_6\,\mathbf{c}_1\,\mathbf{c}_2 - l_6\,\mathbf{s}_1\,\mathbf{s}_2\,\mathbf{c}\,(-\pi/2+\beta) + l_7\,\mathbf{s}_1\,\mathbf{s}\,(-\pi/2+\beta) \\ l_4\,\mathbf{s}_1 + l_6\,\mathbf{s}_1\,\mathbf{c}_2 + l_6\,\mathbf{c}_1\,\mathbf{s}_2\,\mathbf{c}\,(-\pi/2+\beta) - l_7\,\mathbf{c}_1\,\mathbf{s}\,(-\pi/2+\beta) \\ l_5 + l_6\,\mathbf{s}_2\,\mathbf{s}\,(-\pi/2+\beta) + l_7\,\mathbf{c}\,(-\pi/2+\beta) \\ 1 \end{bmatrix} \tag{6.43}$$

After applying the $\beta \approx 0$ assumption, $\mathbf{T_2^0}$ was simplified to become

$$\mathbf{T_2^0} = \begin{bmatrix} \mathbf{c}_1\,\mathbf{c}_2 - \mathbf{s}_1\,\mathbf{s}_2\,\mathbf{c}\,(-\pi/2) & -\mathbf{c}_1\,\mathbf{s}_2 - \mathbf{s}_1\,\mathbf{c}_2\,\mathbf{c}\,(-\pi/2) & \mathbf{s}_1\,\mathbf{s}\,(-\pi/2) \\ \mathbf{s}_1\,\mathbf{c}_2 + \mathbf{c}_1\,\mathbf{s}_2\,\mathbf{c}\,(-\pi/2) & -\mathbf{s}_1\,\mathbf{s}_2 + \mathbf{c}_1\,\mathbf{c}_2\,\mathbf{c}\,(-\pi/2) & -\mathbf{c}_1\,\mathbf{s}\,(-\pi/2) \\ \mathbf{s}_2\,\mathbf{s}\,(-\pi/2) & \mathbf{c}_2\,\mathbf{s}\,(-\pi/2) & \mathbf{c}\,(-\pi/2) \\ 0 & 0 & 0 \end{bmatrix}$$
$$\begin{bmatrix} l_4\,\mathbf{c}_1 + l_6\,\mathbf{c}_1\,\mathbf{c}_2 - l_6\,\mathbf{s}_1\,\mathbf{s}_2\,\mathbf{c}\,(-\pi/2) + l_7\,\mathbf{s}_1\,\mathbf{s}\,(-\pi/2) \\ l_4\,\mathbf{s}_1 + l_6\,\mathbf{s}_1\,\mathbf{c}_2 + l_6\,\mathbf{c}_1\,\mathbf{s}_2\,\mathbf{c}\,(-\pi/2) - l_7\,\mathbf{c}_1\,\mathbf{s}\,(-\pi/2) \\ l_5 + l_6\,\mathbf{s}_2\,\mathbf{s}\,(-\pi/2) + l_7\,\mathbf{c}\,(-\pi/2) \\ 1 \end{bmatrix}$$

$$= \begin{bmatrix} \mathbf{c}_1\,\mathbf{c}_2 & -\mathbf{c}_1\,\mathbf{s}_2 & -\mathbf{s}_1 & l_4\,\mathbf{c}_1 + l_6\,\mathbf{c}_1\,\mathbf{c}_2 - l_7\,\mathbf{s}_1 \\ \mathbf{s}_1\,\mathbf{c}_2 & -\mathbf{s}_1\,\mathbf{s}_2 & \mathbf{c}_1 & l_4\,\mathbf{s}_1 + l_6\,\mathbf{s}_1\,\mathbf{c}_2 + l_7\,\mathbf{c}_1 \\ -\mathbf{s}_2 & -\mathbf{c}_2 & 0 & l_5 - l_6\,\mathbf{s}_2 \\ 0 & 0 & 0 & 1 \end{bmatrix} \tag{6.44}$$

As stated previously, the fourth column ($\vec{d}$) in the final transformation matrix ($\mathbf{T}_n^0$) of a robotic manipulator are the coordinates of the position of the end effector. This can be seen in Equation 6.12).

$$\vec{d_2^0} = \begin{bmatrix} l_4\,\mathbf{c}_1 + l_6\,\mathbf{c}_1\,\mathbf{c}_2 - l_7\,\mathbf{s}_1 \\ l_4\,\mathbf{s}_1 + l_6\,\mathbf{s}_1\,\mathbf{c}_2 + l_7\,\mathbf{c}_1 \\ l_5 - l_6\,\mathbf{s}_2 \end{bmatrix}$$
$$\begin{bmatrix} x_2^0 \\ y_2^0 \\ z_2^0 \end{bmatrix} = \begin{bmatrix} l_4\,\mathbf{c}_1 + l_6\,\mathbf{c}_1\,\mathbf{c}_2 - l_7\,\mathbf{s}_1 \\ l_4\,\mathbf{s}_1 + l_6\,\mathbf{s}_1\,\mathbf{c}_2 + l_7\,\mathbf{c}_1 \\ l_5 - l_6\,\mathbf{s}_2 \end{bmatrix} \tag{6.45}$$

This resulted in three equations with two unknowns, though these equations were only needed to calculate one unknown: θ_2.

$$x_2^0 = l_4\,\mathbf{c}_1 + l_6\,\mathbf{c}_1\,\mathbf{c}_2 - l_7\,\mathbf{s}_1 \tag{6.46}$$
$$y_2^0 = l_4\,\mathbf{s}_1 + l_6\,\mathbf{s}_1\,\mathbf{c}_2 + l_7\,\mathbf{c}_1 \tag{6.47}$$
$$z_2^0 = l_5 - l_6\,\mathbf{s}_2 \tag{6.48}$$

Isolating for $\mathbf{s}_2$ in Equation 6.48 yielded the following:

$$\begin{aligned} z_2^0 &= l_5 - l_6\,\mathbf{s}_2 \\ z_2^0 - l_5 &= -l_6\,\mathbf{s}_2 \\ \mathbf{s}_2 &= \frac{l_5 - z_2^0}{l_6} \end{aligned} \tag{6.49}$$

To isolate for $\mathbf{c}_2$, Equations 6.46–6.48 were squared and summed. Substituting 6.49 for $\mathbf{s}_2$ (as isolated above), yielded the following equation for $\mathbf{c}_2$:

$$\begin{aligned} x_2^{0^2} + y_2^{0^2} + z_2^{0^2} &= (l_4\,\mathbf{c}_1 + l_6\,\mathbf{c}_1\,\mathbf{c}_2 - l_7\,\mathbf{s}_1)^2 + (l_4\,\mathbf{s}_1 + l_6\,\mathbf{s}_1\,\mathbf{c}_2 + l_7\,\mathbf{c}_1)^2 + (l_5 - l_6\,\mathbf{s}_2)^2 \\ x_2^{0^2} + y_2^{0^2} + z_2^{0^2} &= l_4^2\,\mathbf{c}_1^2 + 2l_4l_6\,\mathbf{c}_1^2\,\mathbf{c}_2 - 2l_4l_7\,\mathbf{c}_1\,\mathbf{s}_1 + l_6^2\,\mathbf{c}_1^2\,\mathbf{c}_2^2 - 2l_6l_7\,\mathbf{c}_1\,\mathbf{s}_1\,\mathbf{c}_2 + l_7^2\,\mathbf{s}_1^2 \\ &\quad + l_4^2\,\mathbf{s}_1^2 + 2l_4l_6\,\mathbf{s}_1^2\,\mathbf{c}_2 + 2l_4l_7\,\mathbf{s}_1\,\mathbf{c}_1 + l_6^2\,\mathbf{s}_1^2\,\mathbf{c}_2^2 + 2l_6l_7\,\mathbf{s}_1\,\mathbf{c}_1\,\mathbf{c}_2 + l_7^2\,\mathbf{c}_1^2 \\ &\quad + l_5^2 - 2l_5l_6\,\mathbf{s}_2 + l_6^2 s_2^2 \\ x_2^{0^2} + y_2^{0^2} + z_2^{0^2} &= l_4^2\left(s_1^2 + \mathbf{c}_1^2\right) + l_6\,\mathbf{c}_2^2\left(s_1^2 + \mathbf{c}_1^2\right) + l_7^2\left(\mathbf{s}_1^2 + \mathbf{c}^2\right) + 2l_4l_6\,\mathbf{c}_2\left(s_1^2 + \mathbf{c}_1^2\right) \\ &\quad + 2l_4l_7\,\mathbf{s}_1\,\mathbf{c}_1 - 2l_4l_7\,\mathbf{s}_1\,\mathbf{c}_1 + 2l_6l_7\,\mathbf{s}_1\,\mathbf{c}_1\,\mathbf{c}_2 - 2l_6l_7\,\mathbf{s}_1\,\mathbf{c}_1\,\mathbf{c}_2 \\ &\quad + l_5^2 + l_6^2\,\mathbf{s}_2^2 - 2l_5l_6\,\mathbf{s}_2 \\ x_2^{0^2} + y_2^{0^2} + z_2^{0^2} &= l_4^2 + l_5^2 + l_6^2\left(\mathbf{s}_1^2 + \mathbf{c}_1^2\right) + l_7^2 + 2l_4l_6\,\mathbf{c}_2 - 2l_5l_6\,\mathbf{s}_2 \\ x_2^{0^2} + y_2^{0^2} + z_2^{0^2} &= l_4^2 + l_5^2 + l_6^2 + l_7^2 + 2l_6\left(l_4\,\mathbf{c}_2 - l_5\,\mathbf{s}_2\right) \end{aligned}$$

$$\begin{aligned} 2l_6\left(l_4\,\mathbf{c}_2 - l_5\,\mathbf{s}_2\right) &= x_2^{0^2} + y_2^{0^2} + z_2^{0^2} - \left(l_4^2 + l_5^2 + l_6^2 + l_7^2\right) \\ l_4\,\mathbf{c}_2 - l_5\,\mathbf{s}_2 &= \frac{x_2^{0^2} + y_2^{0^2} + z_2^{0^2} - (l_4^2 + l_5^2 + l_6^2 + l_7^2)}{2l_6} \\ l_4\,\mathbf{c}_2 &= \frac{x_2^{0^2} + y_2^{0^2} + z_2^{0^2} - (l_4^2 + l_5^2 + l_6^2 + l_7^2)}{2l_6} + l_5\,\mathbf{s}_2 \\ l_4\,\mathbf{c}_2 &= \frac{x_2^{0^2} + y_2^{0^2} + z_2^{0^2} - (l_4^2 + l_5^2 + l_6^2 + l_7^2) + 2l_5l_6\,\mathbf{s}_2}{2l_6} \\ \mathbf{c}_2 &= \frac{x_2^{0^2} + y_2^{0^2} + z_2^{0^2} - (l_4^2 + l_5^2 + l_6^2 + l_7^2) + 2l_5l_6\,\mathbf{s}_2}{2l_4l_6} \end{aligned} \tag{6.50}$$

Therefore, the values for $\mathbf{s}_2$ and $\mathbf{c}_2$ were as follows:

$$\begin{aligned} \mathbf{s}_2 &= \frac{l_5 - z_2^0}{l_6} \\ \mathbf{c}_2 &= \frac{x_2^{0^2} + y_2^{0^2} + z_2^{0^2} - (l_4^2 + l_5^2 + l_6^2 + l_7^2) + 2l_5l_6\,\mathbf{s}_2}{2l_4l_6} \end{aligned} \tag{6.51}$$

The isolated $\mathbf{s}_2$ and $\mathbf{c}_2$ equations (Equations 6.49, 6.50) are the arguments for the MATLAB function `atan2(Y,X)`—this function gives the four-quadrant inverse tangent (θ_2 is within the range $(-\pi, \pi]$), as opposed to the result that a standard arctangent computation would give: $(-\pi, \pi)$.

$$\theta_2 = \texttt{atan2}\left(\frac{l_5 + z_2^0}{l_6}, \frac{x_2^{0^2} + y_2^{0^2} + z_2^{0^2} - (l_4^2 + l_5^2 + l_6^2 + l_7^2) + 2l_5 l_6\, \mathbf{s}_2}{2l_4 l_6}\right) \tag{6.52}$$

In order to express the known position of the end effector with respect to the base frame, $\mathbf{T}_2^0$ can be calculated using the raw data from *sensor2* (the end effector) in the Aurora frame: $\mathbf{T}_{s_2}^A$. The homogeneous transformation matrix that was created in Section 6.2.2.1 (Equation 6.35, $\mathbf{H}_A^0$) was applied, starting from Equation 6.30:

$$\begin{aligned}
\mathbf{T}_2^0 &= \mathbf{H}_A^0 \cdot \mathbf{T}_{s_2}^A \\
&= \begin{bmatrix} -1 & 0 & 0 & \vec{d}_{0_x}^A \\ 0 & 0 & 1 & -\vec{d}_{0_z}^A \\ 0 & 1 & 0 & -\vec{d}_{0_y}^A \\ 0 & 0 & 0 & 1 \end{bmatrix} \cdot \begin{bmatrix} \mathbf{R}_{s_2}^A & \vec{d}_{s_2}^A \\ \vec{0} & 1 \end{bmatrix} \\
&= \begin{bmatrix} t_{11} & t_{12} & t_{13} & t_{14} \\ t_{21} & t_{22} & t_{23} & t_{24} \\ t_{31} & t_{32} & t_{33} & t_{34} \\ t_{41} & t_{42} & t_{43} & t_{44} \end{bmatrix},
\end{aligned} \tag{6.53}$$

where $\mathbf{R}_{s_2}^A$ was calculated using the Euler-to-rotation matrix conversion calculation given in Equation 6.36, and $\vec{d}_{s_2}^A$ is the transpose of the translation data from the raw Aurora sensor data, for each sample in the dataset. The variables $x_{2_{s2}}^0$, $y_{2_{s2}}^0$, and $z_{2_{s2}}^0$ from Equation 6.52 are elements t_{14}, t_{24}, and t_{34} of the above matrix, $\mathbf{T}_2^0$.

6.2.3 ATI Data and Synchronization

The data validation and preprocessing for the ATI force-torque data followed a similar process to that of the Aurora position data (section 6.2.2), though the raw data from the ATI sensor required less preprocessing to be viable.

The raw ATI datasets were imported using the `timetable` data structure. The datasets were filtered using the same Butterworth filter method as for the Aurora data: a 0.5 Hz cut off, sixth order Butterworth. The datasets were trimmed at the

start of Motion set A, using the same process as the Aurora data: finding the local minima and maxima (using `multiPT` and `findpeaks`), and choosing the correct peak or trough to clip at. The time vector was then re-set to start the time at the beginning of this clipped data, such that Time 0 occurred at the peak or trough that was chosen in the previous step.

The ATI data were split into its Set A and end portions—the end portion being Set B and the trailing data points—by comparing the `time` vector of the ATI data to the `time` vector for the Aurora Set A for the same experiment set. To isolate ATI Set A, the data points that occurred at a timestamp that was less than the last timestamp for the Aurora set (Set A) were retained. The end portion had the remaining data points, those being equal to or greater than the end point for Aurora Set A. ATI Set B was further isolated later during during the analysis, while synchronizing the two datasets in the `main2022.m` code.

Taking advantage of the `timetable` data structure, two `timetables` can be synchronized and linearly interpolated using the `synchronize` function. This was applied to both the Set A and Set B datasets to combine the Aurora and ATI data.

Since the ATI sensor measured in N and N·m (SI units) and the calculations derived from the Aurora sensor and SolidWorks models were in Millimetre-Gram-Second (mmgs), the ATI-measured torque was converted from kg·m/s^2 (N·m) to g·mm/s^2 (nN·m) using a factor of 10^{-9}.

The data from the force-torque sensor needed to be in the same frame as the theoretical world frame, which required a transformation of $-\pi/2$, as shown in Figure 6.31. As the only axis under consideration for the final torque is the Neck y axis, a transformation of -1 was multiplied to the M_x sensor data.

6.3 Analysis

The main code used for the analysis of the experiments—`main2022.m`—is included in the GitHub repository linked in Appendix A.

After the datasets from the Aurora were processed, the analysis code was used to calculate the head and cage angles: the position data of the system bodies. These data were verified using a small animation within `MATLAB`, using both the original Aurora frame and then the transformed Base frame, by plotting the positions of the various points of interest on a 3D plot. This included the sensors, the location of the Aurora, the location of the base, and the locations of the body

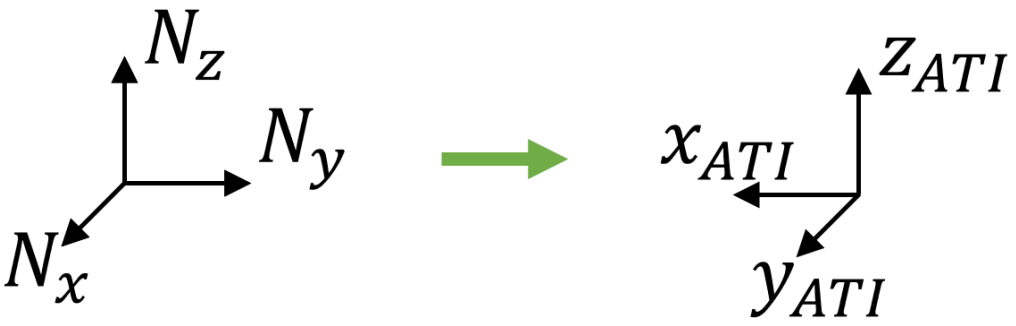

Figure 6.31: Transformation between the Neck System Frame and the ATI sensor frame.

COMs. A frame from the animation is shown in Figure 6.32. The code used for the animation—`animatedVerification.m`—is linked in Appendix A.

The position datasets were then differentiated twice to calculate both the velocity and the acceleration of the two bodies in question.

$$\text{vel} = \frac{\text{pos}(n) - \text{pos}(n-1)}{1/\text{freq}} \tag{6.54}$$

This equation translates to the following MATLAB pseudocode:

```
diff(calculated angles(:,1))/(1/aurora sampling frequency)
```

This was done for both the velocity (using position) and the acceleration (using velocity). These six variables (ϕ, $\dot{\phi}$, $\ddot{\phi}$, α, $\dot{\alpha}$, and $\ddot{\alpha}$) were fed into the τ_H and τ_G equations (Equation 4.2.5) from the example of the proposed method described earlier, as summarized in Section 4.2.5.

When comparing the calculated torque (from the theoretical dynamics) to the ATI measurements, the bias needed to be re-added to the ATI data, as the two graphed datasets were too similar in shape for the biasing from the experimental protocol to not be affecting the results. A side-by-side comparison of the torque comparisons before and after re-adding the bias can be seen in Figure 6.33. The bias was re-added as a torque equal to the initial torque in the x direction: the sum of the body masses multiplied by the respective y offset (e.g., $m_H \cdot y_H$). This bias was re-added to each data point in the ATI set. In a number of experiment

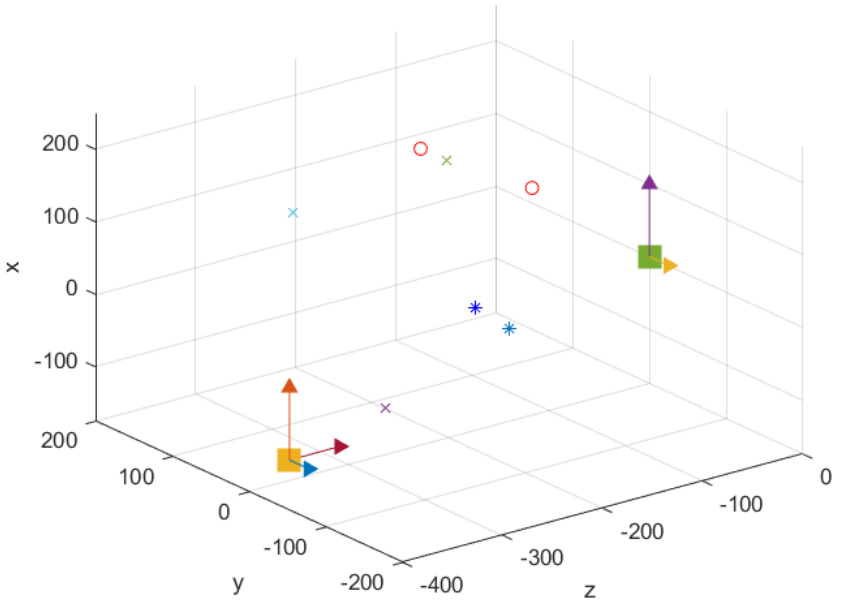

Figure 6.32: A frame of the animation showing the measured positions of the sensors with respect to the Aurora. The square on the right hand side is the aurora, located at $[0, 0, 0]$. The square on the left is the location of the base. The $\times$ are the landmark locations of the skull, *sensor*2, and the wheel. The $\star$ and $\circ$ are the initial locations and the current position of *sensor*1 and *sensor*2, respectively.

Table 6.5: Comparing the RMSE of the original, un-biased, and re-timed datasets.

	Dataset A: RMSE (Nm)			Dataset B: RMSE (Nm)		
	Original	Bias Added	Re-Timed	Original	Bias Added	Re-Timed
exp1-1	0.5584	0.1311	0.1255	0.4108	0.0958	0.0760
exp1-2	0.5669	0.1553	0.1272	0.4255	0.1641	0.0861
exp1-3	0.5423	0.1176	0.1180	0.3930	0.1007	0.0902
exp2-1	0.5033	0.0939	0.0941	0.3334	0.1449	0.1388
exp2-2	0.6040	0.1583	0.1579	0.4641	0.0672	0.0574
exp5-1	0.3553	0.1129	0.1098	0.2596	0.2235	0.2123
exp5-2	0.4239	0.0786	0.0780	0.3126	0.1603	0.1552
exp5-3	0.4124	0.0983	0.0955	0.3214	0.1742	0.1618
exp6-1	0.4334	0.0742	0.0723	0.2795	0.2107	0.1993
exp6-2	0.4849	0.0741	0.0742	0.3559	0.1310	0.1237
exp6-3	0.4516	0.0577	0.0577	0.3198	0.1734	0.1677
mean	0.4851	0.1047	0.1009	0.3523	0.1496	0.1335

sets, this aligned with the results well. When testing the root mean square error of the experiment before and after re-adding the bias, there was an average of 140 point decrease in the percent error for Dataset A and a 67 point decrease in the percent error for Dataset B.

The time synchronization also required a small adjustment, as the alignment was done manually for the two sensors. The difference between the first local extrema in the theoretical torque set (fully dependent on the Aurora data) and the measured dataset (fully dependent on the ATI data) was chosen to be the time offset. This offset was applied as an added offset to the theoretical `time` vector, and the two datasets (measured and theoretical) were re-synchronized using the `synchronize` function to linearly interpolate the two `timetable` datasets. These re-biased and re-synchronized sets were considered for the results below, show in Table 6.6. A second table, Table 6.5, shows the Root Mean Square Error (RMSE) across the various steps described above show that these changes do align the theoretical calculations better with the measured results. The changes are an improvement as the RMSE value trends towards zero; the closer the RMSE is to zero, the more accurate the model is at predicting outcomes.

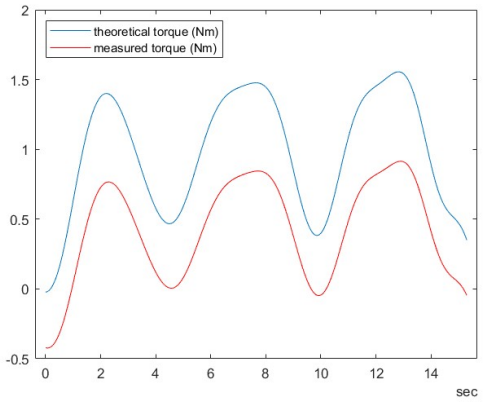

(a) Calculated (Theoretical) torque as compared to filtered sensor data (Measured).

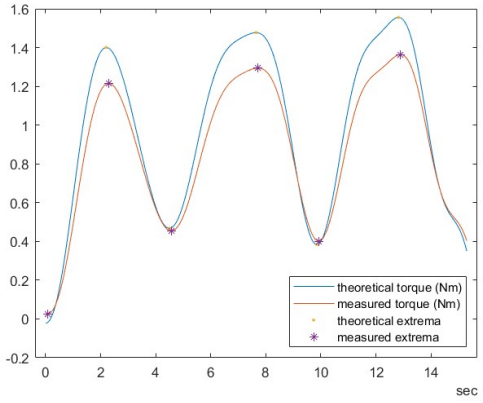

(b) Bias re-added to the sensor data (Measured), showing the local extrema for both plots.

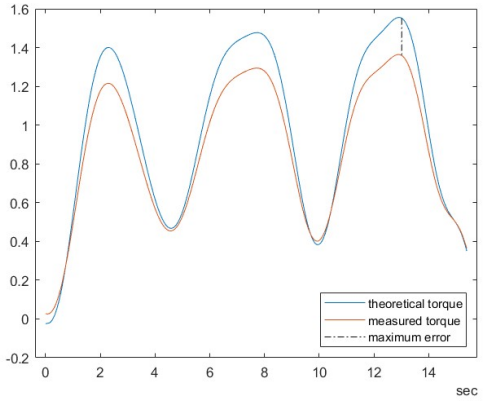

(c) Results after adjusting for the bias and synchronizing the time vector, showing maximum error location.

Figure 6.33: Figures outlining the process used to adjust the results after computation, showing the exp1-1 A set.

Table 6.6: A summary of the nRMSE and the maximum error measured for each dataset.

Experiment	Dataset A		Dataset B	
	nRMSE	Max Error (Nm)	nRMSE	Max Error (Nm)
exp1-1	9.37%	0.1923	8.17%	0.1493
exp1-2	12.61%	0.2156	7.23%	0.1490
exp1-3	11.22%	0.2012	9.61%	0.1563
exp2-1	8.92%	0.1638	17.22%	0.2457
exp2-2	25.81%	0.1996	6.11%	0.1245
exp5-1	16.61%	0.1709	26.57%	0.2937
exp5-2	7.17%	0.1598	18.56%	0.2283
exp5-3	8.38%	0.1757	15.03%	0.2401
exp6-1	8.36%	0.1460	19.72%	0.2674
exp6-2	7.89%	0.1383	12.57%	0.2104
exp6-3	6.68%	0.1110	13.93%	0.2622
mean	11.18%	0.1704	14.07%	0.2115

6.4 Results

The datasets, after being re-biased and re-timed, were compared using a Normalized Root Mean Square Error (nRMSE). The results for each experiment and dataset—the normalized RMSE (presented as a percent) and the maximum error (in Nm)—are presented in Table 6.6.

As stated previously, the data from a number of experiments were corrupted; either missing the data completely from one of the two Aurora sensors (Experiment Sets 2-3 through 4-3), or had too many data points requiring interpolation to be considered an accurate representation of the motion of the experiment. The cutoff for percent of interpolated points was 2%, leaving only Set A for Experiment Sets 1, 2-2, 5, and 6. As proof that the theoretical model holds up in the clockwise direction of neck motion, the Set B sets that had less than 10% interpolated points were analyzed as well. As seen in Table 6.7, the mean error across all the included experiments for set A is 11%, with a mean maximum error of 0.17 Nm. Set B, with a 10% cut off, has a mean error of 17% and a mean maximum error of 0.23 N·m. When only looking at the sets with no interpolation—an interpolated percent of zero—the mean error is 9%, with a mean maximum error of 0.15 N·m, as shown in Table 6.8.

Table 6.7: A summary of the nRMSE and maximum error for each dataset that met the inclusion criteria (less than 2% and 10% interpolation).

Experiment	Dataset A		Dataset B	
	nRMSE	Max Error (Nm)	nRMSE	Max Error (Nm)
exp1-1	9.37%	0.1923	–	–
exp1-2	12.61%	0.2156	–	–
exp1-3	11.22%	0.2012	–	–
exp2-1	–	–	–	–
exp2-2	25.81%	0.1996	–	–
exp5-1	16.61%	0.1709	–	–
exp5-2	7.17%	0.1598	18.56%	0.2283
exp5-3	8.36%	0.1757	15.03%	0.2401
exp6-1	8.36%	0.1460	–	–
exp6-2	7.89%	0.1383	–	–
exp6-3	6.68%	0.1110	–	–
mean	11.04%	0.1710	16.79%	0.2342

Table 6.8: Results for experiment sets with no interpolation in the data.

Experiment	Dataset A		Dataset B	
	nRMSE	Max Error (Nm)	nRMSE	Max Error (Nm)
exp1-1	–	–	–	–
exp1-2	–	–	–	–
exp1-3	–	–	–	–
exp2-1	–	–	–	–
exp2-	–	–	–	–
exp5-1	16.61%	0.1709	–	–
exp5-2	7.17%	0.1598	–	–
exp5-3	8.36%	0.1757	–	–
exp6-1	8.36%	0.1460	–	–
exp6-2	7.89%	0.1383	–	–
exp6-3	6.68%	0.1110	–	–
mean	9.18%	0.1503	–	–

6.5 Discussion

With the normalized RMSE, the results are scaled such that the closer a percent is to 0 (no error), the better a "fit" the theoretical model is. It can be seen that in all but one of the datasets with no sensor errors (no interpolation) that the nRMSE is below 10% (Table 6.8). Even in the sets that had significant interpolation, the nRMSE is below 30%, with all but two below 20% (Table 6.6).

While collecting the data, the sensor attached to the gyroscope cage—*sensor*2—had an error occur where the sensor was not recognized by the Aurora system. This affected experiments 2-3 through 4-3, before the system re-recognized the sensor and data collection was resumed for the sensor, starting with experiment set 5-1. It is worth noting that all of the experiment sets before the sensor error had error points in the Set A data, but there were no error points in the experiment sets after the system recognized the sensor again.

These first experiments are included in this analysis, since it is unknown the true effect on the data that the sensor error had, or if there was any affect at all. As mentioned in the Results section and shown in Table 6.8, when looking at the experiment sets with no interpolation (no error data points) there was an average error of 9%, with a maximum error of 0.15 N·m.

The results for all experiments under 2% interpolation (for Dataset A) and under 10% interpolation (Dataset B) can be seen in Table 6.7. The average error was 11%, which is slightly higher than the expected >10% error.

Looking at the range for the nRMSE for Dataset A, there is a wide spread of 6.68%–25.81%. After doing an analysis to see if there were any outliers in the results, an IQR analysis indicates that the 25.81% nRMSE observed in the exp2-2 dataset is an outlier, and can be removed from the analysis. An updated results table can be seen in Table 6.9.

After applying the outlier analysis to the results, only one result was removed from either Dataset A or B: exp2-2 (nRMSE of 25.81%). The median for nRMSE in Dataset A, including the outlier exp2-2, was 8.86%. The average error for Dataset A after removing the outlier set exp2-2 became 9.81%, with a maximum error of 0.17 N·m.

In looking at the resulting graphs of comparison—shown in Figures 6.34, 6.35, 6.36, 6.37 and 6.38—the largest areas of deviation occur during the peak of the motion: the theoretical model over estimates the expected torque. This is the ideal option for this use case: overestimating the torque experienced by the user,

Table 6.9: A summary of the nRMSE and maximum error for each dataset that both met the inclusion criteria (less than 2% and 10% interpolation), after removing any outliers.

Experiment	Dataset A		Dataset B	
	nRMSE	Max Error (Nm)	nRMSE	Max Error (Nm)
exp1-1	9.37%	0.1923	–	–
exp1-2	12.61%	0.2156	–	–
exp1-3	11.22%	0.2012	–	–
exp2-1	–	–	–	–
exp2-2	(25.81%)	(0.1996)	–	–
exp5-1	16.61%	0.1709	–	–
exp5-2	7.17%	0.1598	18.56%	0.2283
exp5-3	8.36%	0.1757	15.03%	0.2401
exp6-1	8.36%	0.1460	–	–
exp6-2	7.89%	0.1383	–	–
exp6-3	6.68%	0.1110	–	–
mean	9.81%	0.1679	16.79%	0.2342
median	8.86%			

to ensure no harmful resistance is experienced, as opposed to underestimating and having the user experience more torque than expected.

There are a number of sources of error that occurred in the experiments, as well as in the proposed model itself. It was assumed that there was no dissipation due to friction or other sources ($\mathcal{R} = 0$), despite there being no bearings used for the gimbals in the experimental setup. The model also assumed a rigid connection between the gyroscope and the user, where the experimental setup did not have a rigid connection. In terms of the data collection, the Aurora also sampled at a frequency too low to properly filter out electrical noise. The Aurora was also not fixed in place as compared to the experimental setup, so there is a chance that there is a small angle difference between the Aurora and the system (the Aurora frame and the Base frame were not parallel). The filtering of the data after collection did change the motion profile from something akin to a step to a signal that looked more like a sine wave. The system also assumes no significant twist between the neck joint and the gyroscope (the Base frame and the Cage/Wheel frames were not aligned).

In summary, both the nRMSE mean (removing the outlier) and the nRMSE median (including the outlier) for Dataset A are below the 10% that was expected if the proposed model was to predict the dynamics of the system accurately. Dataset

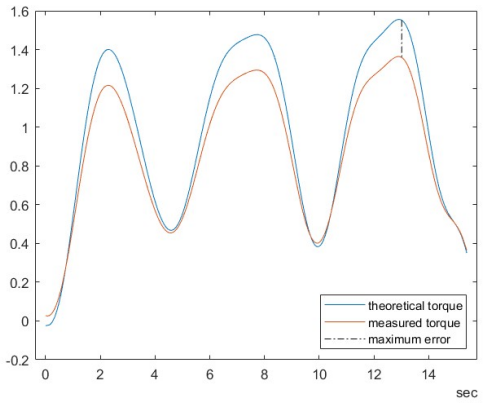

(a) Results for exp1-1 set A.

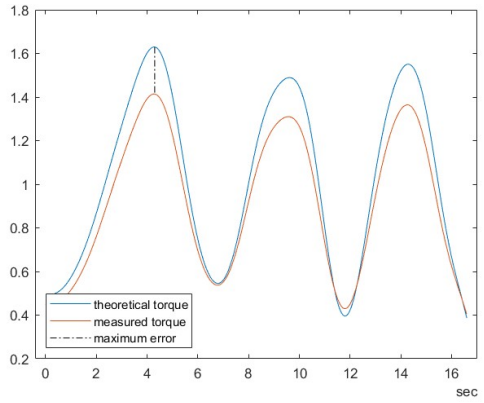

(b) Results for exp1-2 set A.

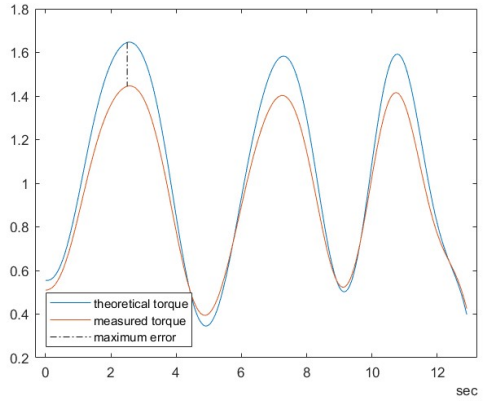

(c) Results for exp1-3 set A.

Figure 6.34: Results from the first experiment set that met the inclusion criteria.

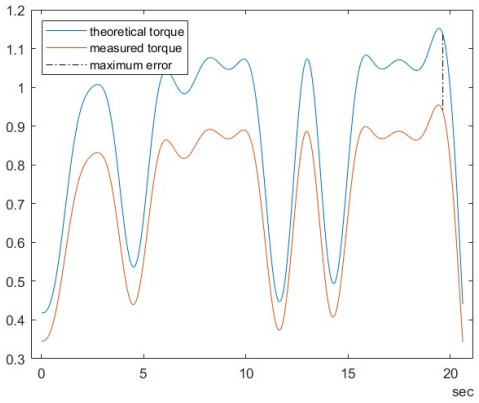

(a) Results for exp2-2 set A.

Figure 6.35: Results from the second experiment set that met the inclusion criteria.

B shows an average nRMSE of 17%, which is higher than expected, but this dataset also had significant interpolation.

6.6 Model Validation Conclusions

Using the experimental setup described in Chapter 5, the proposed method in Chapter 4, and the example one-gyroscope equations developed in Section 4.2, the proposed theoretical method was validated against the measured torque within 10%.

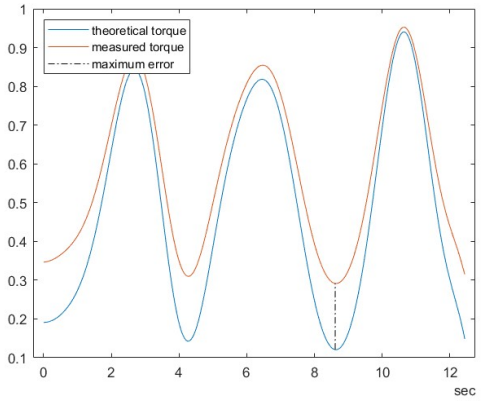

(a) Results for exp5-1 set A.

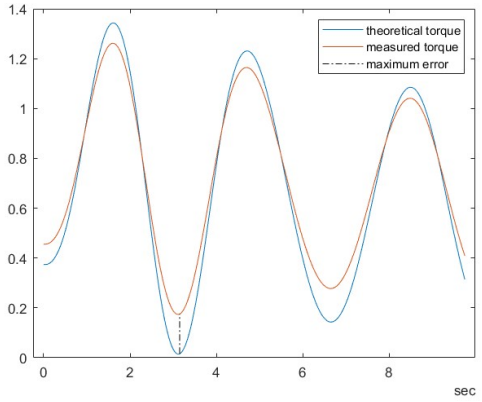

(b) Results for exp5-2 set A.

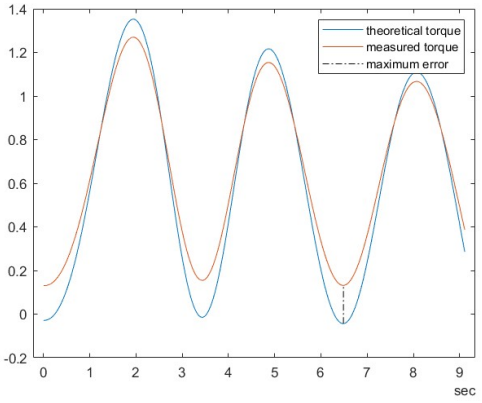

(c) Results for exp5-3 set A.

Figure 6.36: Results from the fifth experiment set that met the inclusion criteria.

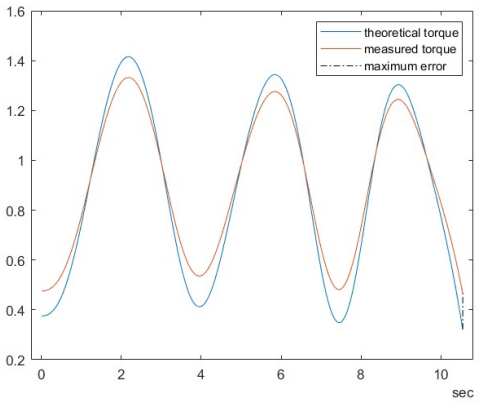

(a) Results for exp6-1 set A.

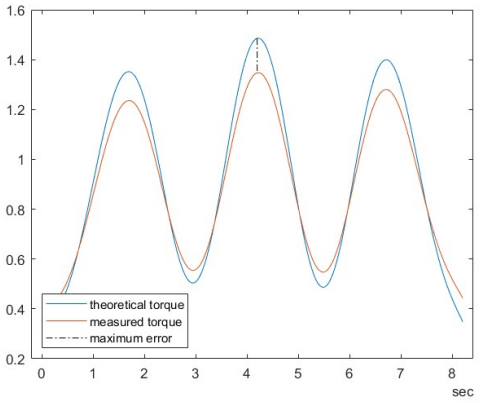

(b) Results for exp6-2 set A.

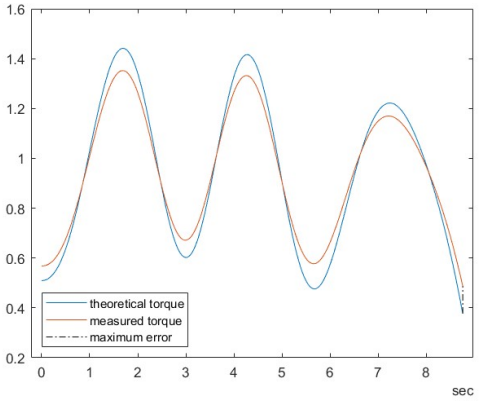

(c) Results for exp6-3 set A.

Figure 6.37: Results from the fifth experiment set that met the inclusion criteria.

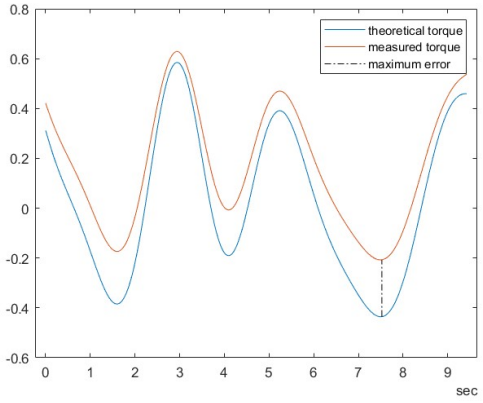

(a) Results for exp5-2 set B.

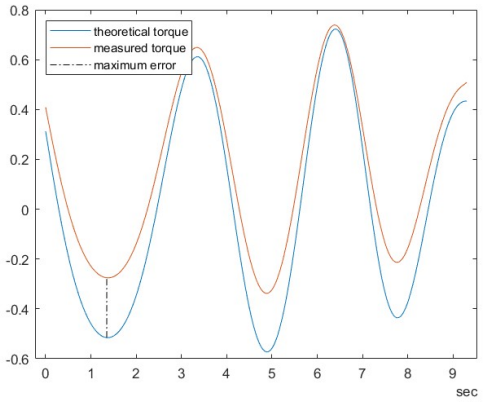

(b) Results for exp5-3 set B.

Figure 6.38: Results from the B Set experiment sets that met the inclusion criteria.

Chapter 7

Conclusions and Future Work

Neck pain can be a debilitating condition that affects a majority of people over the course of their life, and stems from various different causes, including trauma, degenerative disease, and/or mechanical factors. Current interventions for neck pain include, but are not limited to, manual interventions by a PT, at-home traction movements, exercise therapies, and strength training. The field of physiotherapy has also been looking into the gamification of therapy to increase adherence and ameliorate expected outcomes from treatments. For certain conditions, neck strengthening therapies have been shown to have significant impact in the pain and mitigation of disability in those that are affected. While the best results come from stricter regimens using exercise equipment-like devices at physiotherapy offices, even lower resistance, short duration resistance exercises have been shown in some cases to have statistically significant improvement in neck and shoulder pain. Take-home therapies are shown to be cost- and time-effective, but do have lower expected outcomes than in-office strength training options. This work aimed to lay the groundwork for developing a take-home device that could offer the same improvements as the office equipment, but with the convenience and ease of the take-home solutions.

One proposed method to accomplish this was combining a VR game with a tetherless take-home device: a gyroscope as a stabilizer to provide a known resistance to motion. This work specifically covers the gyroscope device and the dynamics that would model it in use. Wearable applications of gyroscopes are a relatively recent development, with the majority of papers being published on this topic within the last decade, but are seen in applications such as tremor suppression and fall prevention.

In order to develop this solution, optimal designs and control systems require modelling. Over the course of the work, models were needed for both the dynamics of the head–neck–gyroscope system and the anthropometric data that would be used to validate the dynamics model and for use in future optimization. A synthesis of the current anthropometric models that relate to the head or neck was undertaken to create a model that would include all the measurements and data that could be needed in future modelling work.

Modelling the dynamics of such a device brought about a new method for analyzing the dynamics of a neck–head–n-gyroscope system. Leveraging the relative simplicity of using the DH convention, as commonly used in robotics, a modified approach to calculating rigid link dynamics using the Euler–Lagrange method was developed. The Spry–Girard derivation in 2008 was the first to derive the equations with the Euler–Lagrange method for gryoscopic stabilizers. This derivation used inspection to calculate the velocities in the system, but the proposed method uses a modified application of the DH convention to attain the linear and angular velocities of each of the bodies, allowing for complex human motion to be easily modelled. The deviations from the DH convention allow for assumptions to be made to simplify the mathematical equations, such as treating the displacements as vectors and allowing the agnostic assignment of the wheel angle in the velocities. The method uses a number of rigid-link representations of portions of the system, and in summing the energies from each representation, can be analyzed as one cohesive system. Due to the nature of the proposed method, the specific location(s) or number of gyroscopes does not matter, which is one of the benefits of using this method: a device can be optimized or re-designed from the initial prototype without invalidating the method used to calculate the already-attained dynamics model. This method can also easily account for non-orthogonal orientations of gyroscopes, and multiple gyroscopes in the same or similar locations rotating with different rotation axes. This proposed method for calculating the dynamics and these equations can be used for future optimization of the proposed design.

In order to validate the above method, an initial prototype of the device was developed. An experiment and an experimental setup was also designed to test this prototype. This device was designed as a single gyroscope placed on the crown of the head with an axis of rotation perpendicular to the transverse plane, and without any optimization towards the size, weight, and rotational speed of the gyroscope. The device was designed with one gimbal on a harness with space for

five gyroscope locations. A dynamics model was calculated using the proposed method in Chapter 4 for this initial prototype. In addition, a to-scale model of a skull and C1 vertebra of a 50^{th} percentile male were created and 3D printed for the validation experiments.

The device was tested on a platform that could rotate the head–neck–gyroscope system in lateral flexion. The system was mounted to a F/T sensor and an electromagnetic position sensor was used to track the motion of both the head and the gyroscope cage. The position data was used as the inputs to the dynamics model, for which the output (τ_N) was compared to the measured torque at the neck. The results from this method showed that the dynamics model-calculated torques were within 10% of the measured values across nine sets of three consecutive left lateral flexion motions.

7.1 Contributions

The intent of this work was to complete the groundwork for a tetherless device that uses gyroscopes to apply resistance to a human head, in the context of strength training for neck rehabilitation therapies, interfaced with a VR game designed for neck rehabilitation. The specific contributions this thesis made towards that overarching goal were as follows:

- A proposed method for calculating the dynamics of a head–neck–n-gyroscope system. This method leverages the benefits of both the DH convention and the Spry–Girard derivation for Lagrangian mechanics [88]. The method allows for complex "base" movement of the vehicle or body(ies). This method will allow for the calculation of the dynamics of an n-gyroscope system in order to optimize both the gyroscope design, and any future use of a control system.

- The dynamics equations that describe the system with one gyroscope placed at the crown of the head, with the rotor axis perpendicular to ground and a gimbal axis perpendicular to the transverse plane. This model was validated in an experiment and deemed to accurately describe the dynamics within 10% across a number of trials.

- A synthesized model of anthropometric data describing the head–neck system. No one model available had all the measurements needed for this work,

so a compilation was made from a number of sources. The model describes a 50^{th} percentile male's dimensions.

- An initial prototype design for the gyroscope system, comprising of a harness and one gyroscope. The harness contained four placeholder mounts where additional gyroscopes could be placed, based on the first proposed design, which prioritized symmetry in the design and balanced weight. The gyroscope mount being a simple slot for the gimbal joint, and the cage being symmetric along all three planes.
- An experimental setup design that utilizes a modelled head and C1 vertebra. The models were based on an anatomical model skull and a CT scan of a neck, respectively.

7.2 Limitations and Future Work

With the work undertaken in this thesis, the research can be extended on this project in a number of ways. The proposed method can be further validated, the device can be optimized using the validated dynamics, the benefits of using a control system for the precession angle and/or rotation speed of the gyroscope(s) can be explored, as well as a number of experiments that can be undertaken to look at the feasibility, efficacy, and areas of improvement of the proposed design.

1. A number of experiments can be undertaken to ensure the validity of the proposed method of modelling the dynamics of the head–neck–n-gyroscope system. Due to the higher error in the right lateral flexion motions in the validation experiment, further experiments could be undertaken to confirm this direction does in fact work with the model for a single gyroscope design, as described in this work. This could be redesigning the experimental protocol or portions of the system to aid in blocking the interference, or simply rotating the experimental setup so that the field generator of the positions sensor is on the right side of the head, instead of on the left side (as is in the experiment described in this thesis). The proposed method can also be expanded to calculate the dynamics for a five-gyroscope model (or more), and tested for the validity of multiple gyroscopes acting on one head-neck system. This could be done using the same experimental protocol given in this thesis or one developed to test the right lateral flexion motion.

2. The validated dynamics equations derived from the proposed method for a one-gyroscope system can now be used to optimize the resultant user experienced torque, wheel weight, and motor speed. That is, future designs can be made that optimize such a device so that it meets the criteria for the resistance and the size and weight constraints for human use. This will allow for a resultant device that is optimized for use with therapies; the initial prototype designed for this thesis is bulky and provides very small resistance to motion in its current iteration.

3. More work into the anthropometry and related literature that are related to this work could be undertaken, to more accurately model the biomechanics related to the motion and the torques experienced.

4. Healthy subject testing can be completed, using either the optimized single gyroscope design, or a full five-gyroscope spread. This testing will likely be for qualitative feedback on the feeling of the motion and resistance experienced by the user. It has been shown in previous studies of wearable stabilizers that qualitative measures—such as predictability of the stabilization response—can have an impact on the performance of a task [108].

5. The dynamics of the single gyroscope system can also be used to look at developing a control algorithm for the system. An assumption was made at the beginning of the work that a passively controlled gyroscope would feel better to a user and be less likely to harm a user upon any form of failure. These assumptions could be erroneous, and can be tested in qualitative human trials—similar to the experiments suggested above—to see if the feel of a CMG, and a proposed control algorithm, would be better received than the passively controlled option, or if they are similar enough to continue without the extra layer of possibility of failure. At this point in the research, it is not yet known if the benefits of using a control system for this application will outweigh the drawbacks. The hesitancy to recommend a control system outright stems from the knowledge that the more complicated a system, the more possible ways there are for the system to fail. Since this device is to be used to exert forces on a human neck, a failure has more inherent risk than if the device was designed to work alongside or apart from humans. The benefits that could be seen from using a control system do have the ability to offset this, since research shows that an application can use lower speeds

and/or lighter rotors to achieve the same resistive force.

6. The device can be integrated for use with the VR system. This is the intended use for the tetherless resistive device, though the benefits of being a take-home solution for resistance training still exist without the VR component. Healthy subject testing could advance by interfacing with the VR system; both for qualitative and quantitative data on the effectiveness of the system as a whole.

7. Clinical trials can be undertaken to see the efficacy of the system when used to treat neck pain in various populations, looking for reductions in factors such as neck disability (e.g., the NDI), neck pain (e.g., the Numerical Rating Scale of Pain (NRS), and increases in neck strength measurements (such as isometric, flexion, extension, and lateral flexion).

8. From here, future work could be undertaken to look at creating a modular system to increase the forces to a higher range, as the current device is intended to work with small resistances in the 0–5 lbs force range. Increasing to the equivalent of resistance bands, which see an upper range in approximately 10–20 lbs force; or even upwards of 50 lbs force, as seen in the fitness machine-like devices. It is more likely that the higher the intended resistive force is, a control system will be needed in order to reduce the weight and speed that would be required of the gyroscopic stabilizer to produce that range.

References

[1] A. I. Binder, "Cervical spondylosis and neck pain," *British Medical Journal*, vol. 334, no. 7592, pp. 527–531, 2007.

[2] T. M. Kay, A. Gross, C. H. Goldsmith, S. Rutherford, S. Voth, J. L. Hoving, G. Bronfort, and P. L. Santaguida, "Exercises for mechanical neck disorders (Review)," The Cochrane Collaboration, Tech. Rep. 8, 2012.

[3] G. Jull, M. Sterling, J. Kenardy, and E. Beller, "Does the presence of sensory hypersensitivity influence outcomes of physical rehabilitation for chronic whiplash? – A preliminary RCT," *Pain*, vol. 129, no. 1, pp. 28–34, 2007.

[4] D. Rendant, D. Pach, R. Lüdtke, A. Reisshauer, A. Mietzner, S. N. Willich, and C. M. Witt, "Qigong versus exercise versus no therapy for patients with chronic neck pain," *Spine*, vol. 36, no. 6, pp. 419–427, 2011.

[5] T. Hall, H. T. Chan, L. Christensen, B. Odenthal, C. Wells, and K. Robinson, "Efficacy of a C1-C2 Self-sustained Natural Apophyseal Glide (SNAG) in the Management of Cervicogenic Headache," *Journal of Orthopaedic & Sports Physical Therapy*, vol. 37, no. 3, pp. 100–107, 2007.

[6] K. Mealy, H. Brennan, and G. C. C. Fenelon, "Early mobilisation of acute whiplash injuries," *BRITISH MEDICAL JOURNAL*, vol. 292, pp. 656–657, 1986.

[7] B. O. Ang, A. Monnier, and K. Harms-Ringdahl, "Neck/Shoulder Exercise for Neck Pain in Air Force Helicopter Pilots," *SPINE*, vol. 34, no. 16, pp. E544–E551, 2009.

[8] A. D. Bonk, R. Ferrari, G. D. Giebel, M. Edelmann, and R. Huser, "Prospective, Randomized, Controlled Study of Activity versus Collar, and the Nat-

ural History for Whiplash Injury, in Germany," *Journal of Musculoskeletal Pain*, vol. 8, no. 1/2, pp. 123–132, 2000.

[9] G. Allison, B. Nagy, and T. Hall, "A randomized clinical trial of manual therapy for cervico-brachial pain syndrome – a pilot study," *Manual Therapy*, vol. 7, no. 2, pp. 95–102, 2002.

[10] A. Helewa, C. H. Goldsmith, H. A. Smythe, P. Lee, K. Obright, and L. Stitt, "Effect of therapeutic exercise and sleeping neck support on patients with chronic neck pain: a randomized clinical trial." *The Journal of Rheumatology*, vol. 34, no. 1, pp. 151–158, jan 2007. [Online]. Available: http://www.ncbi.nlm.nih.gov/pubmed/17216683

[11] A. Gross, J. Miller, J. D'Sylva, S. J. Burnie, C. H. Goldsmith, N. Graham, T. Haines, G. Brønfort, and J. L. Hoving, "Manipulation or mobilisation for neck pain: A Cochrane Review," *Manual Therapy*, vol. 15, no. 4, pp. 315–333, 2010.

[12] B. Kuijper, J. T. J. Tans, A. Beelen, F. Nollet, and M. de Visser, "Cervical collar or physiotherapy versus wait and see policy for recent onset cervical radiculopathy: randomised trial," *BMJ (Clinical research ed.)*, vol. 339, no. 1, p. b3883, 2009. [Online]. Available: http://www.ncbi.nlm.nih.gov/pubmed/19812130 http://www.pubmedcentral.nih.gov/articlerender.fcgi?artid=PMC2758937

[13] J. Ylinen, E.-P. Takala, M. Nykanen, A. Hakkinen, E. Malkia, T. Pohjolainen, S.-L. Karppi, H. Kautiainen, and O. Airaksinen, "Active Neck Muscle Training in the Treatment of Chronic Neck Pain in Women," *JAMA*, vol. 289, no. 19, pp. 2509–2516, 2003.

[14] I. Lundblad, J. Elert, and B. Gerdle, "Randomized Controlled Trial of Physiotherapy and Feldenkrais Interventions in Female Workers with Neck-Shoulder Complaints," *Journal of Occupational Rehabilitation*, vol. 9, no. 3, pp. 179–194, 1999. [Online]. Available: http://link.springer.com/10.1023/A:1021301801292

[15] M. J. Walker, R. E. Boyles, B. A. Young, J. B. Strunce, M. B. Garber, J. M. Whitman, G. Deyle, and R. S. Wainner, "The Effectiveness of Manual

Physical Therapy and Exercise for Mechanical Neck Pain," *SPINE*, vol. 33, no. 22, pp. 2371–2378, 2008.

[16] L. Persson, M. Karlberg, and M. Magnusson, "Effects of Different Treatments on Postural Performance in Patients with Cervical Root Compression. A Randomized Prosective Study Assessing the Importance of the Neck in Postural Control," *Journal of Vestibular Research*, vol. 6, no. 6, pp. 439–453, 1996.

[17] H. G. Hoffman, T. L. Richards, T. Van Oostrom, B. A. Coda, M. P. Jensen, D. K. Blough, and S. R. Sharar, "The analgesic effects of opioids and immersive virtual reality distraction: Evidence from subjective and functional brain imaging assessments," *Anesthesia and Analgesia*, vol. 105, no. 6, pp. 1776–1783, 2007.

[18] G. Bronfort, R. Evans, B. Nelson, P. D. Aker, C. H. Goldsmith, and H. Vernon, "A Randomized Clinical Trial of Exercise and Spinal Manipulation for Patients with Chronic Neck Pain," *SPINE*, vol. 26, no. 7, pp. 788–799, 2001.

[19] T. T. Chiu, C. W. Hui-Chan, and G. Cheing, "A randomized clinical trial of TENS and exercise for patients with chronic neck pain," *Clinical Rehabilitation*, vol. 19, pp. 850–860, 2005.

[20] T. T. W. Chiu, T.-H. Lam, and A. J. Hedley, "A randomized controlled trial on the efficacy of exercise for patients with chronic neck pain." *Spine*, vol. 30, no. 1, pp. E1–7, 2005. [Online]. Available: http://www.ncbi.nlm.nih.gov/pubmed/15626966

[21] G. Kjellman and B. Oberg, "A Randomized Clinical Trial Comparing General Exercise, Mckenzie Treatment and A Control Group In Patients with Neck Pain," *Journal of Rehabilitation Medicine*, vol. 34, pp. 183–190, 2002.

[22] H. Brodin, "Cervical pain and mobilization - brief research report," *Int J Rehab Research*, vol. 7, no. 2, pp. 190–191, 1984.

[23] L. A. Mckinney, J. O. Dornan, and M. Ryan, "The role of physiotherapy in the management of acute neck sprains following road-traffic accidents," *Archives of Emergency Medicine*, vol. 6, pp. 27–33, 1989.

[24] K. Greenwood and R. De Nardis, "Melbourne whiplash centre outcome data. preliminary report," Melbourne Whiplash Centre, Tech. Rep., 2000.

[25] L. L. Andersen, C. A. Saervoll, O. S. Mortensen, O. M. Poulsen, H. Hannerz, and M. K. Zebis, "Effectiveness of small daily amounts of progressive resistance training for frequent neck/shoulder pain: Randomised controlled trial," *PAIN*, vol. 152, no. 2, pp. 440–446, 2011.

[26] I. B. C. Korthals-de Bos, J. L. Hoving, M. W. van Tulder, M. P. M. H. Rutten-van Molken, H. J. Ader, H. C. W. de Vet, B. W. Koes, H. Vondeling, and L. M. Bouter, "Cost effectiveness of physiotherapy, manual therapy, and general practitioner care for neck pain: economic evaluation alongside a randomised controlled trial," *British Medical Journal*, vol. 326, no. 7395, pp. 911–914, 2003.

[27] A. F. Burnett, F. L. Naumann, R. S. Price, and R. H. Sanders, "A comparison of training methods to increase neck muscle strength," *Work*, vol. 25, no. 3, pp. 205–210, 2005.

[28] O. Health and S. C. of Ontario (OHSCO), *Part 2: Resource Manual for the MSD Prevention Guideline for Ontario*, ser. Musculoskeletal Disorders Prevention Series, 2007, no. 5158A. [Online]. Available: https://www.wsib.ca/en/document/msd-prevention-guideline-ontario-part-2

[29] The Whiplash Prevention Campaign. (2023) Whiplash statistics. The Whiplash Prevention Campaign. BC, Canada. [Online]. Available: https://www.whiplashprevention.org/whiplashmatters/statistics/

[30] S. D. Acar, *NTSP Game*, Capstone project, The University of Western Ontario, London, ON, Canada, 2017, unpublished.

[31] S. Salim, "Quantifying the outcomes of a virtual reality (vr)-based gamified neck rehabilitation," M.Sc. thesis, Dept. of Health and Rehabil. Sci., Univ. of Western Ontario, London, Canada, 2019. [Online]. Available: https://ir.lib.uwo.ca/etd/6391/

[32] A. Gross, J. Paquin, G. Dupont, S. Blanchette, P. Lalonde, T. Cristie, N. Graham, T. Kay, S. Burnie, G. Gelley, C. Goldsmith, M. Forget,

P. Santaguida, A. Yee, G. Radisic, J. Hoving, and G. Bronfort, "Exercises for mechanical neck disorders: A cochrane review update," *Manual Therapy*, vol. 24, pp. 25–45, 2016. [Online]. Available: https://www.sciencedirect.com/science/article/pii/S1356689X16300078

[33] K. Greenwood and R. De Nardis, "Melbourne whiplash centre outcome data," Online, Melbourne Whisplash Centre, Melbourne, VI, Australia, Preliminary Report, 2000, unpublished. [Online]. Available: https://whiplashcentre.com/wp-content/uploads/outcome_data_summary.pdf

[34] L. G. W. Cox, K. T. Savur, R. J. De Nardis, and R. A. Iles, "Progressive resistance exercise for improving pain and disability in chronic neck pain: A case series," *Physiotheraphy Res. Int.*, vol. 25, no. 4, 2020.

[35] X.-x. Chen, X. Qi, and P. Lü, "Thera-band resistance exercise therapy for cervical spondylosis," *Chin. J. Tissue Eng. Res.*, vol. 16, 2012.

[36] C. Standing, S. Standing, M.-L. McDermott, R. Gururajan, and R. K. Mavi, "The paradoxes of telehealth: a review of the literature 2000–2015," *Syst. Res. and Behav. Sci.*, vol. 35, 2016.

[37] S. N. Gajarawala and J. N. Pelkowski, "Telehealth benefits and barriers," *The Journal for Nurse Practitioners*, vol. 17, no. 2, pp. 218–221, 2021. [Online]. Available: https://www.sciencedirect.com/science/article/pii/S1555415520305158

[38] P. J. Choi, R. J. Oskouian, and R. S. Tubbs, "Telesurgery: Past, present, and future," *Cureus*, vol. 10, may 2018.

[39] P. L. Nedelea, T. O. Popa, E. Manolescu, C. Bouros, G. Grigorasi, D. Andritoi, C. Pascale, A. Andrei, and D. C. Cimpoesu, "Telemedicine system applicability using drones in pandemic emergency medical situations," *Electronics*, vol. 11, no. 14, 2022. [Online]. Available: https://www.mdpi.com/2079-9292/11/14/2160

[40] F. Perez-Grau, R. Ragel, F. Caballero, A. Viguria, and A. Ollero, "Semi-autonomous teleoperation of uavs in search and rescue scenarios," in *2017 International Conference on Unmanned Aircraft Systems (ICUAS)*, 2017, pp. 1066–1074.

[41] A. Peretti, F. Amenta, S. K. Tayebati, G. Nittari, and S. S. Mahdi, "Telerehabilitation: Review of the state-of-the-art and areas of application," *JMIR Rehabil Assist Technol*, vol. 4, no. 2, p. e7, Jul 2017.

[42] R. Dickerman. (2018, May) Physical therapy for neck pain relief. Vertias Health, LLC. [Online]. Available: https://www.spinehealth.com/treatment/physical-therapy/physical-therapy-neck-pain-relief

[43] J. Miller, A. Gross, J. D'Sylva, S. J. Burnie, C. H. Goldsmith, N. Graham, T. Haines, G. Brønfort, and J. L. Hoving, "Manual therapy and exercise for neck pain: A systematic review," *Manual Therapy*, vol. 15, no. 4, pp. 334–354, 2010. [Online]. Available: https://www.sciencedirect.com/science/article/pii/S1356689X10000342

[44] BTE Technologies. (2023) Multi-Cervical Unit (MCU). [Online]. Available: https://www.btetechnologies.com/products/functional-rehabilitation/multi-cervical-unit/

[45] MedX, Inc. (2019) Core Spinal Fitness System - Four-Way Neck. [Online]. Available: http://medxonline.net/products/core-spinal-fitness-system/four-wayneck/

[46] N. Peake and A. Harte, "The effectiveness of cervical traction," *Physical Therapy Reviews*, vol. 10, no. 4, pp. 217–229, 2005.

[47] E. Lluch, J. Schomacher, L. Gizzi, F. Petzke, D. Seegar, and D. Falla, "Immediate effects of active cranio-cervical flexion exercise versus passive mobilisation of the upper cervical spine on pain and performance on the cranio-cervical flexion test," *Manual Therapy*, vol. 19, no. 1, pp. 25–31, 2014. [Online]. Available: https://www.sciencedirect.com/science/article/pii/S1356689X13000891

[48] E. Daly, A. J. Pearce, and L. Ryan, "A systematic review of strength and conditioning protocols for improving neck strength and reducing concussion incidence and impact injury risk in collision sports; is there evidence?" *J. Funct. Morphol. Kinesiol.*, vol. 6, no. 8, Jan. 2021.

[49] C. Hrysomallis, "Neck muscular strength, training, performance and sport injury risk: A review," *Sports Med.*, vol. 46, pp. 111–1124, 2016.

[50] S. J. Snodgrass, J. A. Cleland, R. Haskins, and D. A. Rivett, "The clinical utility of cervical range of motion in diagnosis, prognosis, and evaluating the effects of manipulation: a systematic review," *Physiotherapy*, vol. 100, no. 4, pp. 290–304, 2014. [Online]. Available: https://www.sciencedirect.com/science/article/pii/S0031940614000558

[51] D. Johnson, S. Deterding, K.-A. Kuhn, A. Staneva, S. Stoyanov, and L. Hides, "Gamification for health and wellbeing: A systematic review of the literature," *Internet Interv.*, vol. 6, pp. 89–106, Nov. 2016.

[52] J. Hamari, J. Koivisto, and H. Sarsa, "Does gamification work? - A literature review of empirical studies on gamification," in *Proceedings of the Annual Hawaii International Conference on System Sciences*, vol. 47, 2014, pp. 3025–3034.

[53] Duolingo. (2020) "Using Duolingo," Duolingo help center. [Online]. Available: https://support.duolingo.com/hc/en-us/sections/200829784-Using-Duolingo

[54] Snap Inc. (2020) "Friend emojis," Snapchat support. [Online]. Available: https://support.snapchat.com/en-GB/a/friend-emojis

[55] Nike, Inc. (2020) "How do I get the most out of Nike Run Club and Nike Training Club?" Nike get help. [Online]. Available: https://www.nike.com/help/a/nrc-ntc-apps

[56] Six to Start. (2020) Zombies, run! [Online]. Available: https://zombiesrungame.com/

[57] Habit RPG Inc. (2020) Habitica. [Online]. Available: http://www.habitica.com/static/front

[58] Snap Inc. (2017, April) Snapchat. Android, version 10.7.1.0.

[59] C. C. Abt, *Serious Games*. New York: The Viking Press, 1970. [Online]. Available: https://archive.org/details/seriousgames0000abtc/page/n7/mode/2up

[60] A. Lheureux, J. Lebleu, C. Frisque, C. Sion, G. Stoquart, T. Warlop, C. Detrembleur, and T. Lejeune, "Immersive virtual reality to restore

natural long-range autocorrelations in parkinson's disease patients' gait during treadmill walking," *Frontiers in Physiology*, vol. 11, 2020. [Online]. Available: https://www.frontiersin.org/articles/10.3389/fphys.2020.572063

[61] A. Garcia, N. Andre, D. Bell Boucher, A. Roberts-South, M. Jog, and M. Katchabaw, *Immersive Augmented Reality for Parkinson Disease Rehabilitation.* Berlin, Heidelberg: Springer Berlin Heidelberg, 2014, pp. 445–469.

[62] O. O'Neil, C. Gatzidis, and I. Swain, *A State of the Art Survey in the Use of Video Games for Upper Limb Stroke Rehabilitation.* Berlin, Heidelberg: Springer Berlin Heidelberg, 2014, pp. 345–370.

[63] E. Tsekleves, A. Warland, C. Kilbride, I. Paraskevopoulos, and D. Skordoulis, *The Use of the Nintendo Wii in Motor Rehabilitation for Virtual Reality Interventions: A Literature Review.* Berlin, Heidelberg: Springer Berlin Heidelberg, 2014, pp. 321–344.

[64] Y.-Y. Liao, Y.-R. Yang, S.-J. Cheng, Y.-R. Wu, J.-L. Fuh, and R.-Y. Wang, "Virtual reality–based training to improve obstacle-crossing performance and dynamic balance in patients with parkinson's disease," *Neurorehabilitation and Neural Repair*, vol. 29, no. 7, pp. 658–667, 2015, pMID: 25539782. [Online]. Available: https://doi.org/10.1177/1545968314562111

[65] G. Saposnik, R. Teasell, M. Mamdani, J. Hall, W. McIlroy, D. Cheung, K. E. Thorpe, L. G. Cohen, M. Bayley, and "the Stroke Outcome Research Canada (SORCan) Working Group", "Effectiveness of virtual reality using wii gaming technology in stroke rehabilitation," *Stroke*, vol. 41, 2010.

[66] L. Foucault, *Démonstration expérimentale du mouvement de la terre: addition aux communications faites dans les précédentes séances.* Gauthier-Villar, 1852.

[67] H. C. Ford, "The electrically driven gyroscope in marine work," *Transactions of the American Institute of Electrical Engineers*, vol. XXXIII, no. 1, pp. 857–872, 1914.

[68] E. A. Sperry, "Engineering applications of the gyroscope," *Journal of the Franklin Institute*, vol. 175, no. 5, pp. 447–482, 1913. [Online]. Available: https://www.sciencedirect.com/science/article/pii/S0016003213909820

[69] L. Goldmerstein, "The aeroplane," *Transactions (Society of Automobile Engineers)*, vol. 11, pp. 342–352, 1916. [Online]. Available: http://www.jstor.org/stable/44579451

[70] A. L. Callahan, "Reinventing the drone, reinventing the navy: 1919–1939," *Naval War College Review*, vol. 67, no. 3, pp. 98–122, 2014. [Online]. Available: http://www.jstor.org/stable/26397780

[71] P. P. Shīlovskiĭ, *The gyroscope: its practical construction and application: treating of the physics and experimental mechanics of the gyroscope, and explaining the method of its application to the stabilization of monorailways, ships, aeroplanes, marine guns, etc.* Spon, 1924. [Online]. Available: https://cir.nii.ac.jp/crid/1130000794422846080

[72] W. S. Franklin, "An important practical problem in gyrostatic action," *Phys. Rev. (Series I)*, vol. 34, pp. 48–52, Jan 1912. [Online]. Available: https://link.aps.org/doi/10.1103/PhysRevSeriesI.34.48

[73] B. L. Newkirk, "Nutation and the monorail car," *Journal of the Franklin Institute*, vol. 174, no. 3, pp. 265–278, 1912. [Online]. Available: https://www.sciencedirect.com/science/article/pii/S001600321291234X

[74] P. Schilowsky, "Monotrack-vehicle," U.S. Patent US1 041 680A, Oct. 15, 1912.

[75] "How new gyro car worked in london; passenger on odd two-wheeled vehicle says it was entirely steady," *The New York Times: Society*, p. 10, May 17, 1914.

[76] R. Chatys and Z. Koruba, "Gyroscope-based control and stabilization of unmanned aerial mini-vehicle (mini-uav)," *Aviation*, vol. 9, no. 2, pp. 10–16, 2005. [Online]. Available: https://www.tandfonline.com/doi/abs/10.1080/16487788.2005.9635898

[77] VEEM Marine. (2023) Veem marine. [Online]. Available: https://veemmarine.com/

[78] Seakeeper Inc. (2023) How it works. [Online]. Available: https://www.seakeeper.com/technology/

[79] TOHMEI Industries Co., Ltd. (2023) Anti rolling gyro. [Online]. Available: https://antirollinggyro.com/

[80] K.-S. Song, S.-M. Kim, M. K. Kwak, and W. Zhu, "Development of a control algorithm for active control of rolling motion of a ship using a gyrostabilizer," *Ocean Engineering*, vol. 280, no. 114669, 2023. [Online]. Available: https://www.sciencedirect.com/science/article/pii/S0029801823010533

[81] Z. Koruba, Z. Dziopa, and I. Krzysztofik, "Dynamics and control of a gyroscope-stabilized platform in a self-propelled anti-aircraft system," *J. Theor. and Appl. Math.*, vol. 48, no. 1, pp. 5–26, 2010. [Online]. Available: http://www.ptmts.org.pl/jtam/index.php/jtam/article/view/v48n1p5

[82] V. J. Lappas, W. H. Steyn, and C. I. Underwood, "Attitude control for small satellites using control moment gyros," *Acta Astronautica*, vol. 51, no. 1, pp. 101–111, 2002. [Online]. Available: https://www.sciencedirect.com/science/article/pii/S0094576502000899

[83] Honeywell International Inc. (2023) Hr04, hc7 & hc9 reaction wheel assemblies. [Online]. Available: https://aerospace.honeywell.com/us/en/products-and-services/product/hardware-and-systems/space/small-satellite-specific-bus-products/hr04-hc7-hc9-reaction-wheel-assemblies

[84] ——. (2023) Momentum control systems. [Online]. Available: https://aerospace.honeywell.com/us/en/products-and-services/product/hardware-and-systems/space/momentum-control-systems

[85] R. Votel and D. Sinclair, "Comparison of control moment gyros and reaction wheels for small earth-observing satellites," in *Proc. Small Satell. Conf.*, no. SSC12-X-1, Utah, USA, 2012. [Online]. Available: https://digitalcommons.usu.edu/smallsat/2012/all2012/74/

[86] H. Yetkin, S. Kalouche, M. Vernier, G. Colvin, K. Redmill, and U. Ozguner, "Gyroscopic stabilization of an unmanned bicycle," in *2014 American Control Conference*, 2014, pp. 4549–4554.

[87] S. Tamayo-León, S. Pulido-Guerrero, and H. Coral-Enriquez, "Self-stabilization of a riderless bicycle with a control moment gyroscope via

model-based active disturbance rejection control," in *2017 IEEE 3rd Colombian Conference on Automatic Control (CCAC)*, 2017, pp. 1–6.

[88] S. C. Spry and A. R. Girard, "Gyroscopic stabilisation of unstable vehicles: configurations, dynamics, and control," *Int. J. Vehicle Mechanics and Mobility*, vol. 46, pp. 247–260, 2008.

[89] A. Gaude and V. Lappas, "Design and structural analysis of a control moment gyroscope (cmg) actuator for cubesats," *Aerospace*, vol. 7, no. 5, 2020. [Online]. Available: https://www.mdpi.com/2226-4310/7/5/55

[90] D. J. Richie, V. J. Lappas, and G. Prassinos, "A practical small satellite variable-speed control moment gyroscope for combined energy storage and attitude control," *Acta Astronautica*, vol. 65, no. 11, pp. 1745–1764, 2009. [Online]. Available: https://www.sciencedirect.com/science/article/pii/S0094576509002835

[91] B. P. Redwood, "A sensorized instrument for minimally invasive surgery for the measurement of forces during training and surgery: Development and applications," Ph.D. thesis, Dept. of Mech. Eng., Univ. of Canterbury, Christchurch, New Zealand, 2014. [Online]. Available: https://ir.canterbury.ac.nz/items/c3348a07-ecd4-4b2a-9eb4-733df4f54cb8

[92] R. Schroer, "Stability and control [a century of powered flight 1903-2003]," *IEEE Aerospace and Electronic Systems Magazine*, vol. 18, no. 7, pp. 37–42, 2003.

[93] VEEM Ltd. (2023) Gyrostabilizers. [Online]. Available: https://veemmarine.com/gyro-stabilizer/

[94] B. Mashadi, M. Mokhtari-Alehashem, and H. Mostaghimi, "Active vehicle rollover control using a gyroscopic device," *Proceedings of the Institution of Mechanical Engineers, Part D: Journal of Automobile Engineering*, vol. 230, no. 14, pp. 1958–1971, 2016. [Online]. Available: https://doi.org/10.1177/0954407016641322

[95] P. CORMAC, "Wheels—ii," *Scientific American*, vol. 139, no. 6, pp. 526–528, 1928. [Online]. Available: http://www.jstor.org/stable/24965495

[96] H. Jin, T. Wang, F. Yu, Y. Zhu, J. Zhao, and J. Lee, "Unicycle robot stabilized by the effect of gyroscopic precession and its control realization based on centrifugal force compensation," *IEEE/ASME Transactions on Mechatronics*, vol. 21, no. 6, pp. 2737–2745, 2016.

[97] F. Ünker, "Proportional control moment gyroscope for two-wheeled self-balancing robot," *Journal of Vibration and Control*, vol. 28, no. 17-18, pp. 2310–2318, 2022. [Online]. Available: https://doi.org/10.1177/10775463211009988

[98] N. A. Kumar and P. Hur, "A handheld gyroscopic device for haptics and hand rehabilitation," *IEEE Transactions on Haptics*, vol. 15, no. 1, pp. 109–114, 2022.

[99] GyroGear Ltd. (2017) Blog. [Online]. Available: https://web.archive.org/web/20230131035308/http://gyrogear.co/blog-2

[100] S. Parkin. (2016, Jan. 14) Hope in a glove for parkinson's patients. MIT Technology Review. [Online]. Available: https://www.technologyreview.com/2016/01/14/163883/hope-in-a-glove-for-parkinsons-patients/

[101] J. F. Ong, B. Gan, B. Koh, X. L. Soler, W. Choong Ngan Lou, P. de Panisse Passis, Y. Ibrahim, J. Medeisis, T. Lasiman, and N. L. Vaklev, "Tremor stabiliastion apparatus and methods," European Patent EP3 237 081B1, Oct. 7, 2020.

[102] J. Mo and R. Priefer, "Medical devices for tremor suppression: Current status and future directions," *Biosensors*, vol. 11, no. 99, Mar. 2021.

[103] W. D. Hall, "Hand-held gyroscopic device," U.S. Patent US5 058 571A, Oct. 22, 1991.

[104] M. Kalvert, "Adjustable and tunable hand tremor stabilizer," U. S. Patent US20 030 236 475A1, May 4, 2004.

[105] H. Phan Van and H. Q. T. Ngo, "Developing an assisting device to reduce the vibration on the hands of elders," *Applied Sciences*, vol. 11, no. 11, 2021. [Online]. Available: https://www.mdpi.com/2076-3417/11/11/5026

[106] A. S. Bandsode and A. G. Thosar, "Parkinson's disease tremor suppression using gyroscopic effect," in *Proc. 7th ASRES Int. Conf. on Intell. Technol.*, ser. Lecture Notes in Networks and Systems, K. Arya, V. Tripathi, C. Rodriguez, and E. Yusuf, Eds., vol. 685, Jakarta, Indonesia, 2022, pp. 299–309.

[107] D. Li and H. Vallery, "Gyroscopic assistance for human balance," in *12th IEEE Int. Workshop Advanced Motion Control*, Sarajevo, Bosnia and Herzgovina, March 25-27, 2012.

[108] D. Lemus, A. Berry, S. Jabeen, C. Jayaraman, K. Hohl, F. C. T. van der Helm, A. Jayaraman, and H. Vallery, "Controller synthesis and clinical exploration of wearable gyroscopic actuators to support human balance," *Sci. Rep.*, vol. 10, no. 10412, 2020.

[109] B. T. Sterke, K. L. Poggensee, G. M. Ribbers, D. Lemus, and H. Vallery, "Light-weight wearable gyroscopic actuators can modulate balance performance and gait characteristics: A proof-of-concept study," *Healthcare*, vol. 11, no. 21, 2023. [Online]. Available: https://www.mdpi.com/2227-9032/11/21/2841

[110] *Man-System Integration Standards*, NASA Std. NASA-STD-3000, Rev. B, Jul. 1995. [Online]. Available: https://msis.jsc.nasa.gov/

[111] *NASA Spaceflight Human-System Standard Volume 2: Human Factors, Habitability, and Envrionmental Health*, NASA Standard Std. NASA-STD-3001, Sep. 2023.

[112] Human Factors Standardization SubTAG, *Human engineering design data digest*, Dept. Defense Human Factors Eng. Tech. Advisory Group Std., Apr 2000.

[113] *Basic human body measurements for technological design—Part 2: Statistical summaries of body measurements from individual ISO populations*, ISO Std. ISO/TR 7250-2:2010(E), 2010.

[114] N. Yoganandan, F. A. Pintar, J. Zhang, and J. L. Baisden, "Physical properties of the human head: Mass, center of gravity and moment of inertia," *Journal of Biomechanics*, vol. 42, no. 9, pp. 1177–1192, 2009. [Online]. Available: https://www.sciencedirect.com/science/article/pii/S0021929009001444

[115] *Anthropometric Source Book: Volume 1: Anthropometry for Designers.* NASA, Jul. 1978, no. NASA RP 1024.

[116] M. D. Burkhard and R. M. Sachs, "Anthropometric manikin for acoustic research," *J. Acoust. Soc. Amer.*, Jul. 1975.

[117] M. Izeki, M. Neo, M. Takemoto, S. Fujibayashi, H. Ito, K. Nagai, and S. Matsuda, "The O-C2 angle established at occipito-cervical fusion dictates the patient's destiny in terms of postoperative dyspnea and/or dysphagia," *Eur. Spine J.*, vol. 23, 2014.

[118] J. O. Karhu, R. K. Parkkola, and S. K. Koskinen, "Evaluation of flexion/extension of the upper cervical spine in patients with rheumatoid arthritis: an mri study with a dedicated positioning device compared to conventional radiographs," *Acta Radiologica*, vol. 46, no. 1, pp. 55–66, 2005.

[119] S. Matsunaga, T. Onishi, and T. Sakou, "Significance of occipitoaxial angle in subaxial lesion after occipitocervical fusion," *Spine*, vol. 26, Jan. 2001.

[120] P. Leitao and R. S. Nanda, "Relationship of natural head position to craniofacial morphology," *American Journal of Orthodontics and Dentofacial Orthopedics*, vol. 117, no. 4, pp. 406–417, 2000. [Online]. Available: https://www.sciencedirect.com/science/article/pii/S0889540600701600

[121] J. Denavit and R. S. Hartenberg, "A kinematic notation for lower-pair mechanisms based on matrices," *J. Appl. Mech.*, Jun. 1955.

[122] R. S. Hartenberg and J. Denavit, *Kinematic Synthesis of Linkages*, ser. Mechanical Engineering, R. M. Drake Jr. and S. J. Kline, Eds. New York, NY, USA: McGraw-Hill, Inc., 1964.

[123] R. P. Paul, *Robot manipulators : mathematics, programming, and control : the computer control of robot manipulators.* MIT Press, 1981.

[124] M. W. Spong, S. Hutchinson, and M. Vidyasagar, *Robot Modeling and Control*, 2nd ed. New York, NY, USA: John Wiley and Sons, 2020.

[125] A. L. Trejos, "Forward kinematics," 2022, lecture notes. Unpublished.

[126] G'llaume RBL. (2015, Aug.) Turnigy - D2836 1100KV. SolidWorks model. GrabCAD. [Online]. Available: https://grabcad.com/library/turnigy-d2836-1100kv-1

[127] M. Lidka, "Comparison of dc motors and dielectric elastomer actuators for wearable wrist exoskeletons," M.E.Sc. thesis, Dept. of Elect. and Comput. Eng., Univ. of Western Ontario, London, Canada, 2017. [Online]. Available: https://ir.lib.uwo.ca/etd/5032/

[128] M. Vettorello. (2014, Mar.) Anatomical Skull. STL model. Thingiverse. Creative Commons Attribution-NonCommercial 4.0 International. [Online]. Available: https://www.thingiverse.com/thing:280653

[129] A. L. Trejos, "A sensorized instrument for minimally invasive surgery for the measurement of forces during training and surgery: Development and applications," Ph.D. thesis, Dept. of Elect. and Comput. Eng., Univ. of Western Ontario, London, Canada, 2012. [Online]. Available: https://ir.lib.uwo.ca/etd/837

Appendix A

MATLAB Scripts

Available on GitHub: https://github.com/ndevos2/gyroscope-neck-model
A list of the available script is as follows:

1. Validation and Calculations for Dynamics Experiment
    - `animatedVerification.m`
    - `atiPreProcess.m`
    - `auroraPreProcess.m`
    - `checkError.m`
    - `eulerConv.m`
    - `filterTT.m`
    - `fixerrors.m`
    - `importData.m`
    - `initAvg.m`
    - `landmarkAvg.m`
    - `loadData.m`
    - `multiPT.m`
    - `plotATI.m`
    - `plotAurora.m`
    - `positionAvg.m`
    - `Rx.m`

- `Ry.m`
- `Rz.m`
- `testFilterScript.m`
- `testingFiltersN.m`

2. Analysis code

- `main2022.m`
- `loadConstants.m`
- `resultAnalysis.m`

Appendix B

Data Sheets

B.1 Turnigy D2836/9 950 KV Brushless Outrunner Motor

D2836 Out Runner Brushless Motor Instruction

Dimension

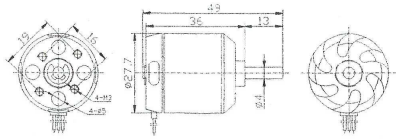

connection

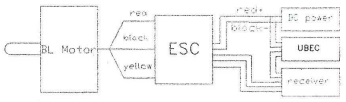

Congratulation for your purchase of high performance brushless outrunner motor series.
Our motors are designed to use perfectly with our own electronic speed controllers. But it is also possible to use them with most of other common electronic spee controllers. The motors are designed for running clockwise or counterclockwise. To change the turning direction you just simply exchange the red and yellow connection wir If you want to use other speed controllers, please refer to your controller instruction manual.

D2836（2217）BRUSHLESS MOTOR

Model	Volts	KV（rpm/v）	Max Pull	Weight	Motor size	Shaft size	Max Power	ESC	Battery/prop
D2836-6	7.4~11.1V	1500	1150g	70g	Φ28*36mm	Φ4.0*49mm	368watt	40A	LiPox2/9x6 LiPox4/7x3
D2836-8		1100	1130g				336watt		LiPox2/ 11x7 LiPox4/ 7x3
D2836-9		950	850g				243watt		LiPox2/2x6 LiPox4/9x6
D2836-11		750	800g				206watt		LiPox2/12x6 LiPox4/9x6

Product description

1. Mount your motor with the includes screws tightly on your front cover of model.
2. Our motors provide high effeciency stator design.
3. Small size, lightweight and long life.

ATTENTION:

1. Please make sure your motor has enough cooling while running. Consider to put a whole into your model motor cover to improve the ventilation.
2. Our motors providing best performance with the recommended propeller size. If you consider to change the propeller size be aware that motor can overheat an damaged.
3. Keep motors away from moisture, dust, scrap and small items to avoide damages.

We wish you many happy landings with our long life quality equipment.